Porins, VDACs and gating:
The role of conformational plasticity

A dissertation submitted
in fulfilment of the requirements for the degree of
DOCTOR IN NATURAL SCIENCES
(Dr. rer. Nat.)

Presented at the Department of Chemistry
Philipps University Marburg
by

Barbara Mertins
From Marburg, Germany
Fachbereich Chemie der Philipps-Universität Marburg

Marburg (Lahn) December 2014

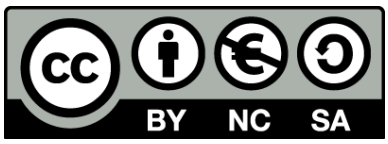

The present dissertation was prepared under the supervision of Prof. Dr Lars-Oliver Essen July 2011 to December 2014 at the Department of Chemistry, Philipps-University Marburg.

Received on December 19th, 2014 at the Chemistry Department, Phillips University Marburg (Hochschul-Kennziffer 1180)

First advisor: Prof. Dr Lars-Oliver Essen (Department of Chemistry, Unit Biochemistry, Marburg)
Second advisor: Prof. Dr Norbert Hampp (Department of Chemistry, Unit Physical Chemistry, Marburg)

Date of Examination: _____

I declare to the best of my knowledge and belief, that this thesis with the title:

“Porins, VDACs and gating: The role of conformational plasticity”

has not been accepted for any degree at any other university then the Philipps University Marburg. Furthermore, I declare that I wrote this thesis alone without further help of another person. This thesis contains no material previously published or written by another person, except where due references have been made.

Marburg, December 2014

_____

Barbara Mertins

Dedicated to my family

“Why, sometimes I've believed as many as six impossible things before breakfast.”

— Lewis Carroll, *Alice in Wonderland*

Summary

With about 10 000 copies per cell the voltage-dependent anion channels (VDACs) are the most abundant proteins of the mitochondrial outer membrane and are known to be involved in mitochondrial processes such as ATP-, calcium or ROS-transport. Beside this, they were identified as key players of mitochondrial physiology such as being involved in the mitochondrial related apoptotic pathway. Because of their strategic location as well as interaction with pro- and anti-apoptotic proteins, VDACs are involved in various diseases like Alzheimer, Down syndrome, cancer, stroke, and amylotrophic lateral sclerosis. Because of this multifunctionality, VDACs are important targets for medical approaches.

After their discovery, VDACs have been extensively studied in terms of their structural organisation and their gating mechanism. The N-terminal region in the pores interior fuelled further debates about the gating mechanism of VDACs. VDACs reply to an applied voltage in a symmetric manner showing one open and several closed states. In this work I classified the closed states into at least three major states. With these quantitative electrophysiological measurements I demonstrated for the first time that a conformational variability of the N-terminus is essential for VDACs function. Through engineering of double-cysteine mVDAC1-variants affixing the N-terminal segment at the bottom and midpoint of the pore I verified that the N-terminus is the major trigger of VDAC´s gating. Additionally, it was shown that channel transitions are not solely dependent on the N-terminus. By analysing EMP as minimal model system for β-barrel gating, I revealed that a loop-independent gating exists, similar to that observed in the double-cysteine mVDAC1 variants.

Given VDACs that interact with a plethora of effector proteins, I focused on the pro-apoptotic VDAC-effector Bid/tBid. Recent studies imply that Bid is a key player in neuronal cell death pathways. Accordingly, Bid seems to promote mitochondrial demise by release of death promoting proteins in the cytosol and the acceleration of oxidative stress. Furthermore, Bid-deficient neurons are highly resistant to cell death stimuli including oxygen-glucose deprivation (OGD) and glutamate-induced excitotoxicity *in vitro* and show reduced damage after cerebral ischemia and brain trauma *in vivo*. Here I could show a direct interaction between mVDAC1 and Bid/tBid and characterised the electrophysiological influence on VDAC in a quantitative manner. Biophysical analyse by SRCD, SROCD and EPR measurements give first insights into the structure of the VDAC-tBid complex. These data highlight the critical role for VDAC1 as a mitochondrial receptor for Bid thus providing a major control point of neuronal demise.

Zusammenfassung

Mit rund 10 000 Kopien pro Zelle sind die *voltage dependent anion channels* (VDACs) die am häufigsten vorkommenden Proteine der äußeren mitochondrialen Membran. VDACs regulieren mitochondriale Prozesse, wie z. B. ATP-, Calcium- und ROS-Transport. Neben dieser klassischen Rolle wurden VDACs als wichtigste Komponente der Mitochondrien-Physiologie und der damit verbundenen intrinsischen apoptotischen Signalwege identifiziert. Wegen ihrer strategischen Lage sowie der Interaktion mit pro- und anti-apoptotischen Proteinen, wurden VDACs mit verschiedenen Krankheiten wie Alzheimer, Down Syndrome, Krebs, Schlaganfall, und amylotrophischer lateraler Sklerose in Verbindung gebracht. Aufgrund dieser Multifunktionalität sind VDACs wichtige Ziele für medizinisch-therapeutische Behandlungsansätze.

Nach ihrer Entdeckung wurden VDACs in Bezug auf ihre Struktur und den Schaltmechanismus untersucht. Der N-Terminus im Inneren der Pore wurde als das verantwortliche Schalt-Element diskutiert. Durch Anlegen einer externen Spannung, können VDACs in einen offenen und mehrere geschlossene Zustände schalten die ein physiologisches Verhalten imitieren. In dieser Arbeit konnte ich diese geschlossenen Zustände in mindestens drei Haupt-Zustände unterteilen. Mit diesen quantitativen elektrophysiologischen Messungen habe ich zum ersten Mal deutlich gemacht, dass die konformationelle Variabilität des N-Terminus für VDACs Schaltverhalten entscheidend ist. Durch das Erzeugen von Doppel-Cystein Varianten, die den N-Terminus am unteren Rand und in der Mitte die Pore arretieren, konnte ich zeigen, dass der N-terminus den dominanten Teil beim Schalten von VDACs darstellt. Daneben wurde auch gezeigt, dass zusätzliche Schaltvorgänge in einen geschlossenen Zustand unabhängig vom N-terminus auftreten können. Durch die Analyse von EMP als minimales Modellsystem konnte ich solch ein *loop*-unabhängiges Schalten in Porinen demonstrieren.

VDACs interagieren mit pro- und anti-apoptotischen Effektorproteinen. Der Fokus meiner Arbeit lag auf der Aufklärung der VDAC-Bid/tBid Interaktion. Bid als pro-apoptotisches Effektorprotein wurde als wichtiger Akteur im neuronalen Zelltod identifiziert, indem es die Freisetzung von apoptotischen Proteinen in das Zytosol fördert. Darüber hinaus, zeigen Bid-defiziente neuronale Zellen eine hohe Resistenz gegen Zelltod-auslösende Reize wie z.B. Glutamattoxizität. Ich konnte die direkte Interaktion von VDAC1 und tBid zeigen und den funktionellen Einfluss mittels elektrophysiologischen Messungen quantifizieren. Biophysikalische Analysen (CD/OCD/EPR) ergaben erste Einblicke in den Protein-Komplex und verdeutlichen die Bedeutung der VDAC1-tBid Interaktion für die Viabilität von Neuronen.

Publications:

Oppermann S, Mertins B, Meissner L *et al*, *Interaction of Bid and VDAC1 determines mitochondrial demise and cell death in neurons,* EMBO, 2014 submitted

Mertins B, Psakis G, Essen L, *VDAC: the wizard of mitochondrial OM*, Biological Chemistry, 2014 Dec 1;395(12):1435-42. doi: 10.1515/hsz-2014-0203.

Grosse W, Psakis G, Mertins B *et al*, *Structure-Based Engineering of a Minimal Porin Reveals Loop-Independent Channel Closure*, Biochemistry, 2014; **53**(29); 4826-4838

Mertins B, Psakis G, Grosse W, *Flexibility of the N-terminal mVDAC1 segment controls the channel's gating behavior.* PloS one, 2012. **7**(10): p. e47938

Posters and Presentations:

Poster presentation "**Interaction of VDAC1 and Bid – Insights into mitochondrial fate**" at the CRC 807 International Symposium: Membrane Transport and Communication, Goethe University Frankfurt (2014)

Poster presentation "**Interaction of VDAC1 and Bid – Insights into mitochondrial fate**" at the 1st International Workshop on Interdisciplinary Approaches to Protein Structure-Function, University of Huddersfield (2014)

Poster presentation "**Interaction of VDAC1 and Bid – Insights into mitochondrial fate**" at the SFB 35 International Symposium: Transmembrane Transporters in Health and Disease, Vienna (2014)

Poster and oral presentation "**Interaction between VDAC1 and Bid - factors affecting mitochondrial integrity**" at the 9th International Transport Colloquium of the German Society for Biochemistry and Molecular Biology (GBM), Rauischholzhausen (2014)

Poster and oral presentation **"Conformational flexibility of VDAC and the influence of effectors"** at the molecular life science 2013, International Symposium of the German Society for Biochemistry and Molecular Biology (GBM), Frankfurt (2013)

Poster presentation **"Conformational flexibility of VDAC and the influence of effectors**" at the 541. Wilhelm und Else Heraeus Seminar on Transport through Nanopores: From Understanding to Engineering, Jacobs University, Bremen (2013)

Poster presentation **„Ion channel engineering with mVDAC1 and OmpG"**, Conference of Structural Biology of Molecular Transport, International Symposium of the study group "structural biology" of the German Society for Biochemistry and Molecular Biology (GBM), Murnau (2012), award for the best poster

Poster presentation "**Plasticity of the N-terminal mVDAC1 segment controls the channel's gating behaviour"** at the 8th International Transport Colloquium of the German Society for Biochemistry and Molecular Biology (GBM), Rauischholzhausen (2012), award for the best poster

Table of contents

1. Introduction

1.1 Biological membranes and membrane proteins

In cells, biological membranes ensure a proper metabolism by building compartments. These compartments are formed as bilayers of lipids providing a barrier for polar substances. Membranes are able to separate toxic or reactive substances that are formed during metabolism. Furthermore, membranes ensure different ion- or substrate concentration on both compartments that are needed for a proper metabolism. Accordingly, a harmonious flow equilibrium of energy, substrates or reagents is needed so that the membranes have to be permeable to these molecules or ions in a selective and regulated manner.[1] To guarantee selective transport membranes contain particular proteins. The protein content differs depending on the organism and the tissue. For example, myelin sheaths of the nerve cells obtain a protein to lipid ratio of 0.23 compared to a 3.2 ratio in the outer mitochondrial membrane.[2]

Membrane proteins ensure or catalyse transport processes through the membrane and are therefore essential for life itself. Mutations or the absence of particular membrane proteins lead to a changed or missing transport of substrates through the membrane and are therefore known to be responsible for various metabolic disturbances. For example, in the so called Hartnup-disease the sodium-dependent and chloride-independent neutral amino acid transporter SLC6A19 that is responsible for the transport of aromatic and hydrophobic amino acids is missing.[3] As consequence, these patients suffer of a systemic lack of amino acids in the organism. Another example is the altered expression of ATP-binding cassette (ABC) transporters at the blood-brain-barrier that accompanies several neuropathologies. For example, a reduced expression or transport of P-glycoprotein is associated with Alzheimer's, Creutzfeldt-Jakob or Parkinson's disease.[4] Because of these crucial functions membrane proteins are often targets of therapeutics and therefore gained interest in medicine and pharmacy.

Usually, membrane proteins can be classified into different classes depending on their location relative to the membrane. These classes are peripheral, lipid-bound and integral or

transmembrane proteins. An overview about the different membrane protein classes is shown in Figure 1.

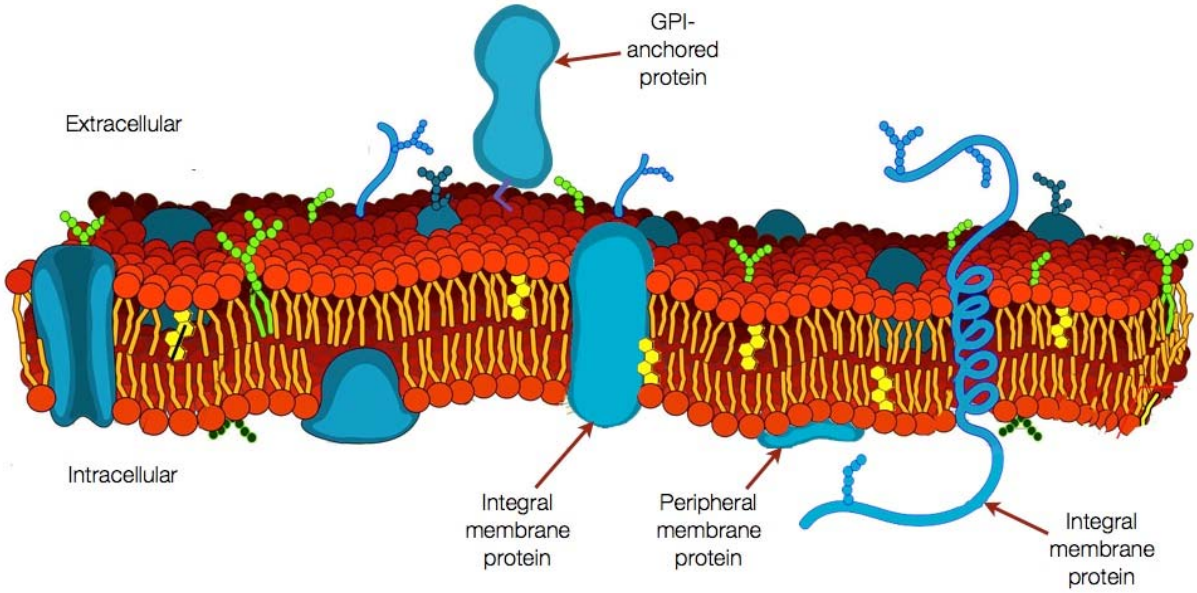

Figure 1:[5] Schematic view of the Singer-mosaic-model highlighting the membrane proteins. Usually membrane proteins are classified according to their location to the membrane. There are membrane-associated, peripheral, GPI-anchored and integral, i.e. membrane-spanning, membrane proteins.

Peripheral membrane proteins are located along the membrane surface and can therefore easily be extracted, *e.g.* by highly alkaline buffers. Lipid-bound membrane proteins are anchored to the membrane and therefore an extraction is only possible by the addition of detergents. The class of membrane proteins that are essential for metabolism and substrate transport are the integral or transmembrane proteins. These membrane proteins span the whole membrane and are therefore amphiphilic. The membrane-facing parts of these proteins are hydrophilic, whereas the membrane-embedded residues are lipophilic, to anchor and stabilise them in the membrane. Because of this transmembrane proteins can link two cell compartments and are therefore of special interest among the membrane proteins.[1]

Transmembrane proteins are built of either α-helices, β-barrels or a combination of both, and can be further subdivided according to their function to transporters, channels and pores. Transporters like the previously mentioned ABC transporters are transporting ions against a gradient by utilizing ATP hydrolysis as energy source.[6] In contrast, channels like the voltage dependent anion channel (VDAC) control the flux of ions by opening and closing.[7] Furthermore, pores are just able to provide a possibility for substrate flow without further

control. For example, aquaporins mediate the flux of water through cells to prevent osmotic swelling.[8]

Among the transmembrane channels there is a sub-class, the so called porins. Porins are β-barrel transmembrane proteins and represent the most abundant proteins in the outer membrane of gram-negative bacteria, chloroplasts and mitochondria. [9]

1.2 Mitochondria and the related apoptotic processes

Mitochondria (Greek: *mitos*: strand; *chondros*: grains) are cell organelles in eukaryotic cells, in which the oxidative metabolism takes place (Figure 2). In mitochondria, the pyruvate dehydrogenase, the enzymes of the citric acid cycle, the enzymes for fatty acid oxidation and the redox enzymes involved in the oxidative phosphorylation and electron transport can be found. Other important functions of the mitochondria are, *inter alia*, the synthesis of iron-sulphur clusters, the haem synthesis and a crucial role in programmed cell death (apoptosis) in the intrinsic pathway. Therefore the mitochondria are the central hub of the metabolic pathways.

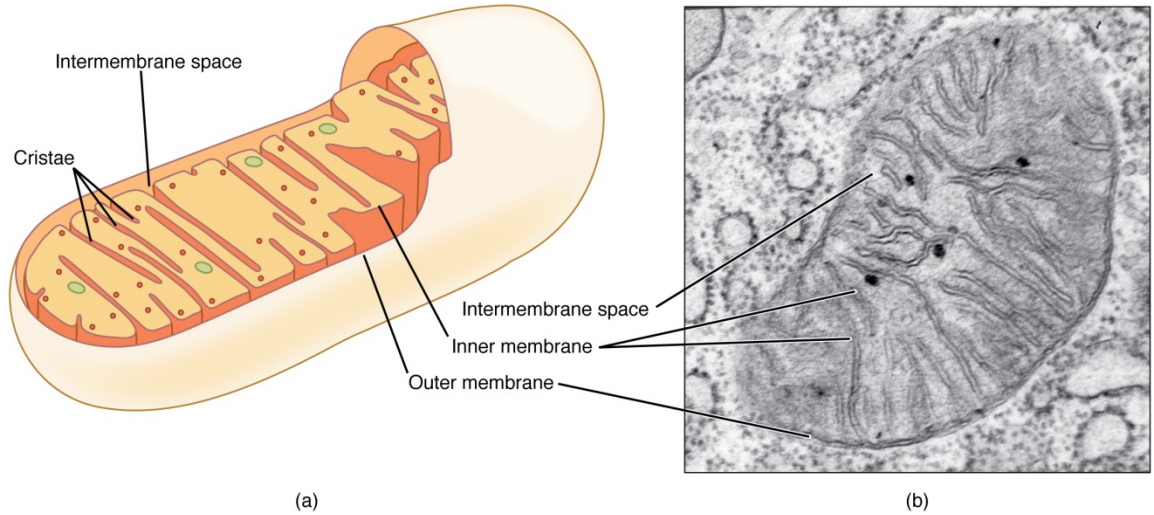

Figure 2:[10] Architecture of the mitochondria, (a) schematic view of the overall structure of mitochondria, (b) electron microscopic picture of a mitochondrion

According to the endosymbiont theory mitochondria as well as chloroplasts have developed by ingestion of prokaryotes in precursor eucytes, from which the similar structure of the mitochondrial membrane compared to the membrane of gram-negative bacteria can be explained. [11] The size of mitochondria varies significantly depending on their occurrences

and metabolic state. Usually, mitochondria are of elliptic shape of about 0.5 x 1.0 µm, which corresponds to the size of bacteria. [2]

The mitochondria are surrounded by a smooth outer membrane and an invaginated inner membrane, the so called christea (lat: *crista*: coxcomb). The space between the two membranes is called the intermembrane space and harbours proteins and substrates crucial for metabolism and apoptosis. The outer membrane of mitochondria contains, similar to the outer membrane of gram- negative bacteria, porins, which allow a free diffusion of molecules up to 5 kDa.[12] The inner membrane is composed of about three-quarters of proteins and thus is the membrane with the highest protein to lipid ratio. [13] The ion and substrate transport between the intermembrane space and the matrix is controlled by the proteins of the inner membrane. This strictly regulated permeability allows the formation of a concentration gradient between cytosol and matrix and therefore the induction of a membrane potential. Especially the membrane potential attracted further interest for regulation because some of the outer mitochondrial membrane proteins show a voltage response. For example, the most abundant mitochondrial outer membrane protein, the voltage dependent anion channel 1 (VDAC1), respond in a symmetric way to an applied voltage. Accordingly, the existence of a membrane potential along the outer membrane was questioned. As direct measurements of the mitochondrial membrane potential are difficult, there are currently only theoretical justifications of its existence. The first theoretical model was based on the *Donnan*-potential, where a potential is evolved by an ion gradient.[14, 15] As the outer membrane of mitochondria is highly permeable for ions, this theory is unlikely. Alternatively, metabolically derived potentials may complement the Donnan potential across the outer mitochondrial membrane, thus contributing to the generation of its membrane potential.[16] However, the calculated potential of this model is up to 30 mV and thus too low for a voltage response by VDACs. In later studies, Lemeshko [17, 18] postulated a non-Mitchell mechanism for driving the outer membrane potentials up to 80 mV, sufficiently high to trigger voltage-sensitive outer membrane proteins. When suitably coupled to the creatine-phosphate metabolism and the adenine nucleotide transport through the inner membrane, this model claims that the membrane-resident VDAC-hexokinase complexes could convert cytosolic glucose to glucose-6-phosphate under the generation of a transmembrane potential. Clearly, such a model would couple the VDAC transport activity to the metabolic flux, but suffers from a lack of direct experimental evidence. Still the origin and existence of membrane potentials along the outer mitochondrial membrane remain elusive.

1.2.1 Mitochondria as an interface for intrinsic cell death (apoptosis)

Beside the regulation of metabolic transport, the mitochondria are known to be a crucial interface in apoptotic processes. Apoptosis is essential for all multicellular life in growth and development. Cells that are no longer needed or are a threat to the organism are rebuilt by a rigorously regulated suicide process. Apoptosis can occur within either during normal cell growth (intrinsic) or upon cell damage (extrinsic). The intrinsic apoptotic pathway is initiated by cellular stress factors such as an excess of Ca^{2+}, the presence of reactive oxygen species (ROS) or DNA damage. After the initiation of apoptosis a rupture of the outer mitochondrial membrane occurs and as consequence apoptogenic factors like cytochrome c, the apoptosis inducing factor (AIF), Smac/DIABLO (second mitochondria derived activator of caspase/direct IAP-binding protein with low pI) or endonuclease G are released from the intermembrane space to the cytosol. Cytochrome c itself causes the activation of caspases by interacting with the apoptosis protease-activating factor-1 (Apaf-1) through assembly of caspase-3/cytochrome c/Apaf-1 comprising apoptosomes.[19] In the presence of caspases other pro-apoptotic proteins such as Bid (BH3-interacting death agonist) are activated and assemble at the outer mitochondrial membrane. This process induces the permeabilisation of the mitochondrial outer membrane (*e.g.* as a mitochondrial transition pore), which presents the point of no return in the intrinsic apoptotic pathway and causes finally cell death. A schematic view of apoptosis is shown in Figure 3.

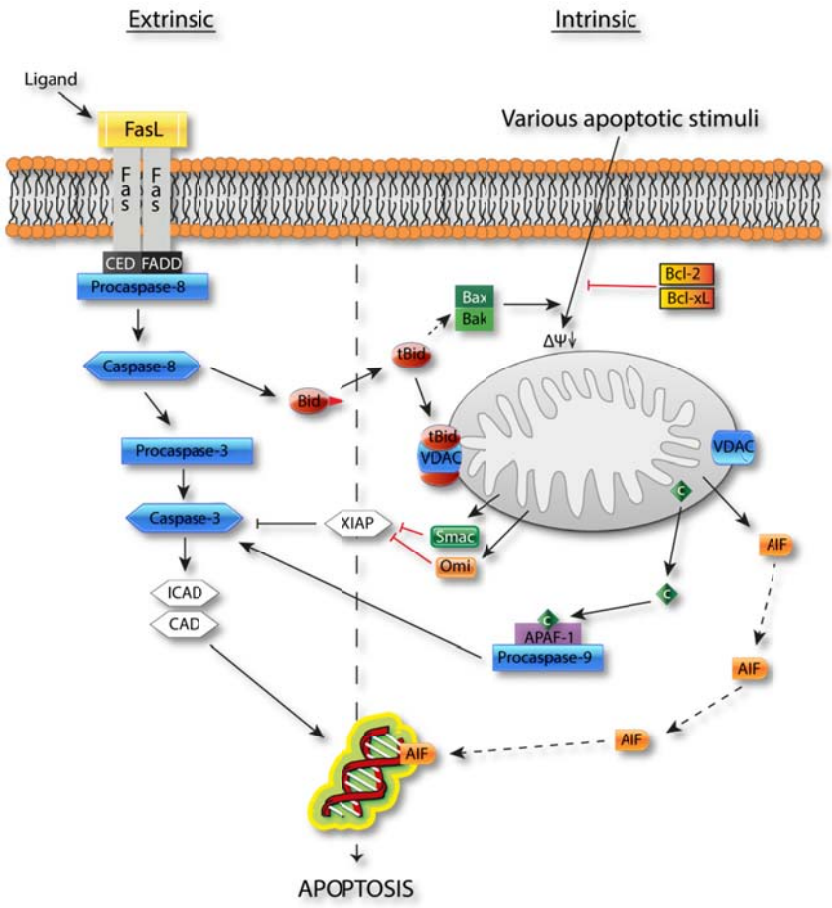

Figure 3: [(adapted from [20])] Intrinsic and extrinsic pathways of apoptosis. Apoptosis can occur by an extracellular extrinsic or an intracellular intrinsic pathway. In the extrinsic pathway, the death receptor Fas is activated by its ligand FasL. The signal is mediated to the Fas associated death domain (FADD), where procaspase-8 is associated with the death effector domain (CED). After the initial signal procaspase-8 is activated releasing the active caspase-8. Caspase-8 triggers the cleavage and activation of the downstream effector caspase-3 which induces the release of the caspase activated desoxyribonuclease (CAD) from its inhibitor (ICAD). As consequence CAD induces the nuclear DNA fragmentation, leading to apoptosis. The intrinsic mitochondrial pathway is triggered by various stimuli. The caspase-8 cleavage of Bid to its truncated and active form tBid connects both, extrinsic and intrinsic pathways. After activation of Bid, the pro-apoptotic effector translocates to the mitochondrial membrane, there inducing membrane permeabilisation by forming complexes with VDACs, or activation of pro-apoptotic proteins (Bak, Bax) to induce membrane rupture. After initial signalling the mitochondrial membrane potential $\Delta\psi$ decreases and cytochrome c (c) as well as apoptosis inducing factor (AIF), and Smac/DIABLO (second mitochondria derived activator of caspase / direct IAP-binding protein with low pI) are released from the intermembrane space. Smac/DIABLO or Omi (a mammalian homologue of the serine protease HtrA (high temperature requirement A)) remove the inhibitors of apoptosis (IAPs) such as XIAP, thereby enhancing caspase-3. Cytochrome, APAF-1 and procaspase-9 interact to form the apoptosome that enhances caspase-3 activation as well. Furthermore, after the release, AIF translocates to the nucleus where chromatin condensation and DNA fragmentation is initiated in a caspase-independent way.

How cytochrome c is released from the intermembrane space to the cytosol is still highly discussed. Lill *et al*. identified release systems for cytochrome c including the translocase of the outer membrane (TOM) and the translocase of the inner membrane (TIM).[21] Furthermore, VDAC1 was identified as crucial key player when releasing cytochrome c as well. It has been demonstrated that many pro- and anti-apoptotic proteins are able to bind to VDAC1[22] and that VDAC1 is classified to be pro-apoptotic.[23] Furthermore, VDACs are known to induce cytochrome c release over an unknown mechanism but depending on their oligomerisation grade. [24, 25] Nevertheless, VDAC1 as multi-functional protein in the outer mitochondrial membrane is a pharmaceutically relevant target to induce or prevent apoptosis.

1.3 Voltage dependent anion channel (VDAC)

With about 10 000 copies per cell the voltage-dependent anion channels (VDACs) are the most abundant proteins of the mitochondrial outer membrane (OM).[26] These porin-like channels attract considerable biochemical, biophysical and biomedical interest because of: a) their general occurrence in eukaryotes, b) the common physiological functions in terms of metabolite transport, c) their role in the induction of the intrinsic cell death (apoptosis) and d) the exceptional β-barrel architecture of their transmembrane domains. VDACs were first discovered in 1976 by Schein *et al* while working on the mitochondrial membrane of paramecium (*Paramecium aurelia*). [26] At this early stage the authors described VDAC as channel that a) has its maximum conductance when the potential is zero, b) responds symmetrically to positive and negative voltages, c) dwell times of the open state depends on the applied voltage, d) its high conductance state is about 5 nS in 0.1 to 1.0 M salt-solution and e) exhibits a preference for Cl^- that is 7 times higher than for K^+. Most of these early observations held true till today. Later, more isoforms of VDACs were discovered proving VDACs to be ubiquitous in eukaryotes. VDACs appear in eukaryotes in various isoforms, depending on the organism. Phylogenetic analyses show that the ancestral members of the multifunctional VDAC family separated early during eukaryotic evolution, where different VDAC paralougs were usually formed by gene duplication.[27] Metazoa, like fruit fly, human or fish harbour up to three mitochondrial isoforms, whereas higher plant genomes comprise up to ten paralogues.[27-30]

VDACs mediate the flow of energy-carrying molecules like ATP, ADP, pyruvate or succinate.[31] The current hypothesis is, that VDAC controls this transport by opening and closing of the channel as recognized in lipid bilayer measurements. Here, the channel shows multiple conductance states, a high conductance referred to as the open state, and several low conductance states referred to as closed or partly open.[25] The low conductance states are usually reported comprising a current of 40-60% to that of the high conductance state. Furthermore, in the high conductance state the channel is weakly anion selective, but exhibits weak cation selectivity when partly or fully closed.[32]

In 2008 first insights into the VDAC 3D-structure were obtained independently by three groups.[22, 25, 32] The solved X-ray structures of VDAC1 of mouse and human revealed an atypical 19-stranded β-barrel with an α-helix spanning the middle of the pore. As consequence of the 19 β-strands, the strands 1 and 19 have to align parallel. The VDAC1 channel has an elliptic shape with a maximum diameter of 27x24 Å and a molecular mass of 30 kDa. Based on the current structural data, it is accepted that alignment of the N-terminal α-helix with the barrel wall yields the "open" state although this helix constrict the pore to 27x14 Å. Despite the availability of structural information, the heterogeneity of the VDAC conductance states and the molecular mechanism underlying their transitions are poorly understood. Especially the N-terminus gained further interest to explain the observed current states. Current hypotheses favour control of the opening/closure of the channel through a complete or partial movement of the N-terminal helix with its flexible hinge region (T_{19}KGYGFG_{25}) into[33] or outside the pore[34] (Figure 4).

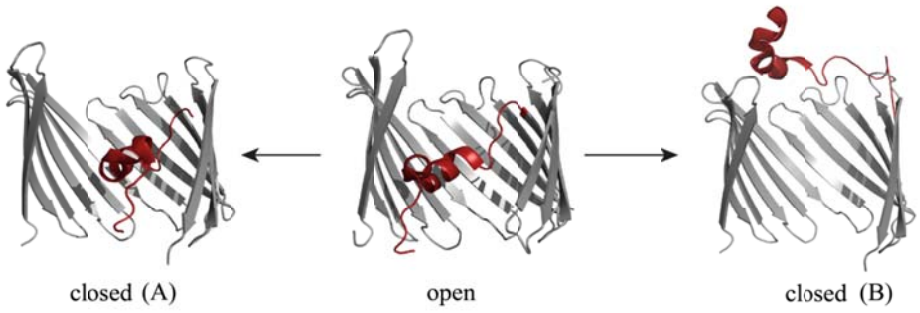

Figure 4: Proposed opening/closure mechanisms. VDAC (grey) open to closed transition can occur because of partial movement of the N-terminal α-helix (red) with its hinge region inside the pore (**A**)[33] or as complete movement outside the pore (**B**).[34]

Although an inward α-helical movement could control the channel's activity through blockage, it fails to account for the channel's ion selectivity, a situation that an outward-movement model claims to address more adequately.[34] None of the proposed models, however, has received strong experimental support.

Beside their function in metabolite regulation VDACs were determined to be involved in the intrinsic or mitochondrial apoptotic pathway. In the last decade, VDAC was identified to interact directly with a plethora of pro- or anti-apoptotic proteins with their N-terminus providing a putative interaction-site. [22, 35, 36] The participation of VDACs in the apoptotic cascade are discussed as a) a minor component incorporated into the mitochondrial transition pore complex, b) a major *a priori* component that creates the huge outer membrane pore itself by homo- or hetero-oligomerisation, c) an indirect trigger for pore formation, *e.g.* by chaperoning its assembly within the membrane, or d) an inducer for the formation of lipidic pores. Apart from their classic roles in metabolite regulation in the cytosol and apoptosis, mammalian VDACs were found to be involved in controlling the amount of reactive oxygen species (ROS) [37], *e.g.* by a closure of VDAC and simultaneous decrease of cytosolic ROS levels. Because of their multi-functionality VDACs are associated with a variety of diseases like Alzheimer, Down syndrome, cancer, stroke, and amyotrophic lateral sclerosis (reviewed in [29, 38]). Furthermore, certain VDAC isoforms are essential for reproductive functions. For example, VDAC3-deficient mice are infertile due to a lack of sperm mobility and VDAC1 knockdown mice show high embryonic mortality although the procreation seemed to be unaffected. [39, 40] Anyway, because of their importance in metabolite regulation and involvement in various diseases this thesis addresses the elucidation of VDACs gating as well as the interaction with the pro-apoptotic protein Bid.

1.4 The bacterial porins, OmpF, LamB, OmpG and OmpA and the toxin α-HL

The most abundant proteins of the outer membranes of gram-negative bacteria, mitochondria and chloroplast are the so called porins.[41] In bacteria, the outer membrane harbours up to 10^5 copies of different porins, that can be subdivided into 5 different subgroups. These subgroups are classified upon their ability to mediate substance transport. They are divided into common

porins as OmpF, specific porins as LamB, toxins as α-hemolysin, transporter porins as FhuA and pore-less porins as OmpA.[42, 43] Usually, porins harbour a β-barrel structure with a molecular mass of 30 - 50 kDa and occur as monomers (OmpG or OmpA) or trimers (OmpF or LamB). Porins are mediating the passive transport of charged substances like sugars, nucleotides, amino acids and small peptides up to 600 Da.[9] The number of β-strands varies in bacterial porins from 8-24 strands but the β-barrels are usually formed by an even number of β-strands. [44, 45] Beside the photoreaction centre of *Rhodopseudomonas vividris*[1], [46] porins were one of the first membrane proteins characterized by X-ray crystallography. In the next paragraph a selection of common and substrate-specific porins will be introduced.

One of the best studied porins is the trimeric outer membrane protein F (OmpF) (Figure 5). In 1995 its crystal structure was solved by Cowan *et al* [47]and since then OmpF suits as model systems for porins and ion-channel-engineering.[48] OmpF is mediating the passage of small molecules up to 600 Da including mono-, di- and trisaccharides to control the osmotic pressure. Additionally, if the cell is under osmotic pressure, the OmpF homologue OmpC is built to guarantee an appropriate flux of nutrients. The overall structure of OmpF consists of three separate monomers connected by a loop (loop2). The monomeric channels are formed by 16 β-strands of 340 amino acids, whereby the pore is constricted by an additional loop (loop 3, L3) located at the middle of each barrel (Figure 5).[47] The periplasmic regions are formed of small β-turns whereas the extracellular regions exhibit small loops. Loop 2 at the extracellular side of these porins is necessary to form the biological active trimers by hydrophobic interactions of its side chains. Loop 3 is found to affect the flux of substrates and constricts the channel to 7-11 Å depending on the loop position. [49]

[1] The first structure of a membrane protein was the photosynthetic reaction centre of *Rhodopseudomonas vividris* elucidated in 1984 by Michel, Huber and Deisenhofer. This first crystallization and x-ray structure determination was awarded in 1988 with the Nobel-prize for chemistry.

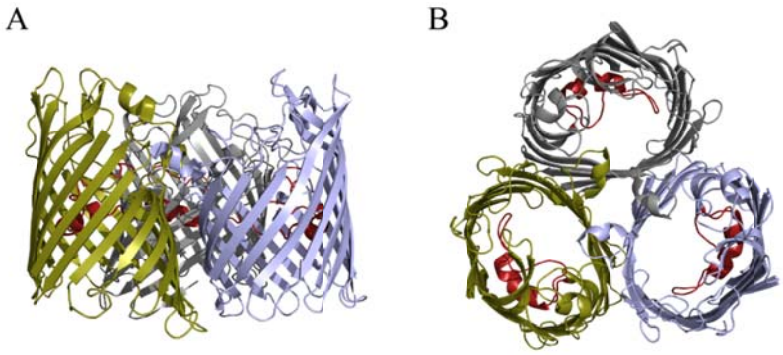

Figure 5: Trimeric structure of OmpF (pdb code 1OPF[47]), monomers are shown in grey, light blue and yellow, respectively, loop 3 (red) is responsible for the channels switching mechanism, **A** side view of the OmpF trimer (top: extracellular side, bottom: periplasmic side), **B** top view (extracellular) of the OmpF trimer.

LamB is an example for specific porins and is known to mediate the transport of maltose (342 Da) into the periplasma.[50] Like OmpF, LamB is built of three monomers. The monomers harbour an overall β-barrel structure of 18 β-strands formed by 446 amino acids with a molecular mass of 50 kDa (Figure 6).[50] In accordance to OmpF, LamB´s trimer is also stabilized by loop 2 and loop 3 constricts the pore. As specific porin, LamB is harbouring a so called "greasy slide". This region is built up of 6 aromatic amino acids providing a binding pocket for the transported sugars. Upon sugar binding at the channels surface, loop 3 is adapting another conformation and allows the substrate to pass the pore.[51] The distance of the amino acids in the "greasy slide" is slightly bigger than the size of the sugar, providing a stabilising effect during the transport without a tight binding.

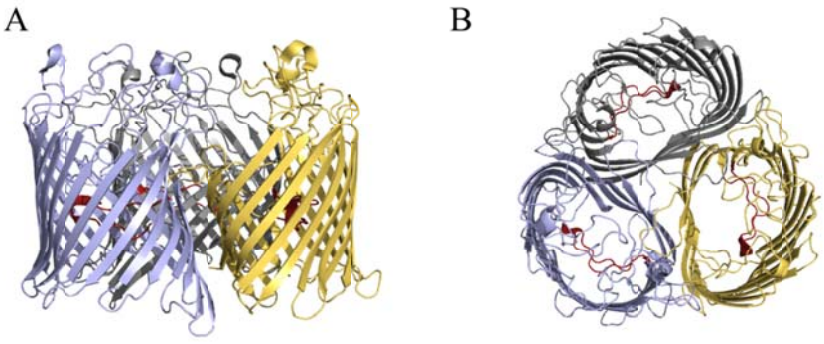

Figure 6: Trimeric structure of LamB (pdb code 1MAL [50]), monomers are shown in grey, light blue and yellow, respectively, loop 3 (red) is responsible for the channels switching mechanism, **A** side view of the LamB trimer (top: extracellular side, bottom: periplasmic side), **B** top view (extracellular) of the LamB trimer.

A common porin in the outer membrane of gram-negative bacteria is the monomeric outer membrane protein G (OmpG). OmpG consists of 14 β-strands, 280 amino acids and a molecular mass of 32 kDa.[45] In contrast to other porins, OmpG is only produced as stress response of the cell, and has therefore a unique function in the metabolism. OmpG was discovered in 1989 by Misra and Benson during mutagenesis experiments in the repression region of OmpG (cog – control of OmpG).[52] By mutations in this region, a LamB-like phenotype was found in LamB-deficient cells allowing them to grow on maltodextrines. Therefore, OmpG is only produced by LamB deficient cells as "emergency protein". [53, 54] OmpG assembles a straight β-barrel without any constrictions in its inside. In BLM measurements it is characterised by fast transitions between open and closed states. These fast channel transitions are often referred as flickering, thus their dwell times are in the ms range.[55-57] The structure of OmpG was solved in 2006 by two independent groups, revealing the typical β-barrel structure with a diameter of 12 x 15 Å, including long extracellular loops and short periplasmic turns (figure 7). [45, 58] In contrast to other porins, loop 2 is not involved in trimerisation and loop 3 is not constricting the pore. Instead, OmpGs gating is controlled by the flexible loop 6.[45] By deletion of loop 6 Grosse *et al* and Chen *et al* demonstrated the importance of this loop in voltage response.[59, 60] Because of the monomeric structure, OmpG has a central role in porin studies as well as in ion-channel engineering.[61] Therefore, OmpG was used as template for the enhanced minimal porin (EMP).

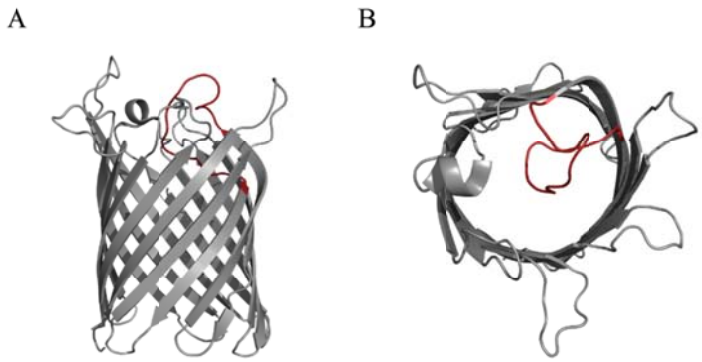

Figure 7: Overall structure of OmpG (grey) (pdb code 2IWW[45]), loop 6 (red) is responsible for the channels gating mechanism, **A** side view of the OmpG (top: extracellular side, bottom: periplasmic side), **B** top view (extracellular) of the OmpG.

One of the smallest known porins found in outer membranes of gram negative bacteria is the small outer membrane protein A (OmpA) (Figure 8). OmpA is formed of 8 β-strands by 172 amino acids and has a molecular mass of 19 kDa. It is crucial in the linkage of the outer

membrane to the periplasmic peptidoglycan layer in gram-negative bacteria.[62] The interior of the barrel is closed by hydrophobic amino acids. Interestingly, there are small water filled cavities in the channel, so that OmpA can be characterised as an inversed micelle. OmpA is a non-pore forming porin and has no extracellular loops that are involved in trimerisation or pore constriction. The existing extracellular loops are involved in bacterial conjugation or other recognition events. Interestingly, although the loops in OmpA are missing, it still can adopt high and low conductance states and therefore suits the definition of porin-gating. These transitions are considered to induce salt-bridges in the pores interior, providing transport of water in a unique manner. [63, 64]

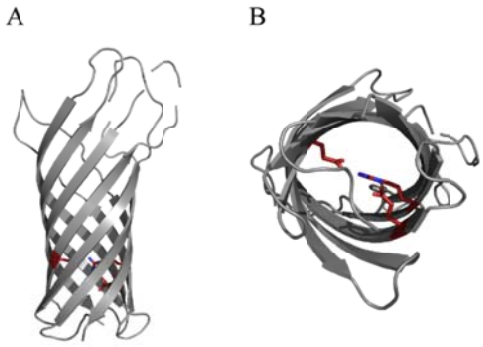

Figure 8: Overall structure (grey) and gating of OmpA (pdb code 1BXW[63]), the residues E52, R128 and R138 are responsible for OmpAs gating (red), **A** Side view of OmpA (top: extracellular side, bottom: periplasmic side), **B** Periplasmic view of OmpA.

One protein, enumerated among porins but with unique functions, is the toxin α-hemolysin (α-HL). Formation of transmembrane pores is a major mechanism by which exogenous proteins damage target cells. The membrane spanning α-HL heptamer is formed after the incorporation of the membrane bound monomers. As consequence, α-HL is destroying the membrane. [65] For the lysis of the cell, 1μM – 1mM of α-HL is needed depending on the membrane. The biologically active α-HL structure is built of a 14-stranded β-barrel cylinder with a β-strand hood (Figure 9). The N- and the C-terminus of every monomer are both located at the periplasmic side. In contrast to other porins, the membrane spanning β-barrel is built of 7 monomers whereas the β-barrel structure of other porins consists of just single polypeptide chains. α-HL gained interest in various medical studies, thus it is the major virulence determinant of *Staphylococcus aureus*.[66] It is also commonly used in ion-channel engineering because of its directed incorporation in membranes.

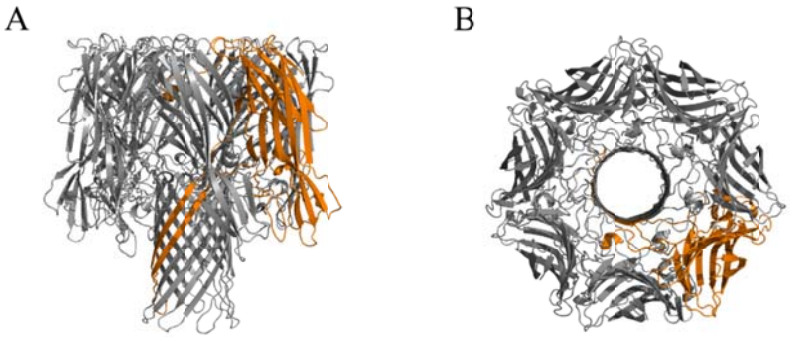

Figure 9: Overall structure of the heptameric toxin α-HL (grey) (pdb code 7AHL [65]), one monomer is depicted in orange. **A** Side view of α-HL (top: extracellular side, bottom: periplasmic side), **B** Periplasmic view of α-HL

1.5 The enhanced minimal porin and synthetic biology

Synthetic biology is an interdisciplinary field of research including biology, chemistry, engineering, physics and mathematics. It has two complementary objectives: on the one hand to improve the understanding of biological systems by mimicking a native structure and on the other hand construction of bio-orthogonal systems with new properties. [67]
For the construction of new proteins with defined properties, there are basically two strategies: the *de novo* synthesis and the re-design of proteins.[68] In *de novo* new amino acid sequences are engineered, which are capable to adopt a biologically active tertiary structure. To control these newly formed tertiary structures is not trivial, however, the number of *de novo* synthesized proteins increased steadily in the last years.[69] For porins, the second strategy, the so-called re-design, is more adequate. During re-design, existing proteins are manipulated by the exchange of individual amino acids so that the desired functional change occurs. This strategy is particularly suitable when only small changes in the protein are desired, enhancing the possibility of biocompatible proteins.

A special field in the synthetic biology is the work with ion channels, referred to as ion-channel engineering (ICE). Manipulations in ion channels can affect for example the ion selectivity or the gating characteristics. [70] ICE aims to alter the electrophysiological properties of biological pores or channels and to potentially evolve them into tuneable molecular switches, *e. g.* for the design of new biological tools [61, 71-74] or to develop them into alternative therapeutics.[72, 75-77] For rational engineering and applications like stochastic sensing the starting template is crucial. In this thesis the monomeric porin OmpG was used to

design a minimal pore. Current strategies on OmpG focus on pore deconstruction or on narrowing lumen permeability by introducing modulators at single or double attachment sites[57] to transform OmpG into a more ion- or substrate-specific porin. For engineering a minimal model-system for analysing β-barrel gating the first step included the deletion of the gating responsible loop 6, while the H-bonding network between strands β11 and β12 and the β-bulge remains intact.[59] As a second step all extra-membranous loops were shortened to simple β-turns gaining a minimal porin: the enhanced minimal porin (EMP) (Figure 10).

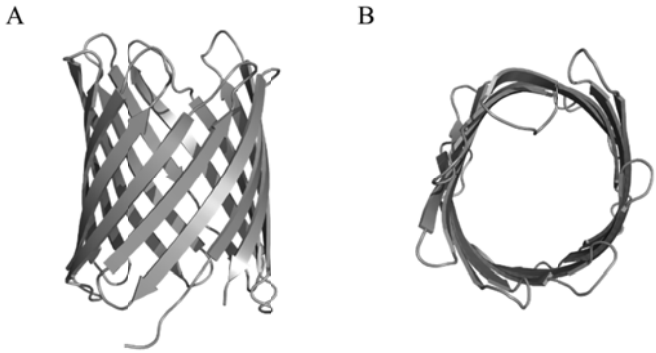

Figure 10: Structural model of the artificial porin EMP, the overall structure represents a β-barrel; **A** Side view of EMP (top: extracellular side, bottom: periplasmic side), **B** Periplasmic view of a-EMP. The model structure for EMP was generated by SWISS-MODEL (http://swissmodel.expasy.org) using the OmpG structure (PDB code 21WW) as template.

1.6 Aim

The first part of the thesis focuses on the elucidation of the gating mechanism of VDACs. Though the gating mechanism of VDACs is highly discussed the involvement of the N-terminal α-helix should be unravelled. After the clarification of the gating mechanism the interaction with the pro-apoptotic protein Bid/tBid should be addressed. By analysis of the VDAC-tBid complex further insights into VDACs role in apoptosis should be made available. The second part of this thesis focuses on the elucidation of loop-independent gating in β-barrels. Using the monomeric porin OmpG from *Escherichia coli* as template, an enhanced minimal porin (EMP) was developed, harbouring just the minimal required β-barrel structure. This pore should be analysed upon its temperature and pH stability. Furthermore, the electrophysiological behaviour should be analysed by lipid bilayer measurements to provide further insights into the gating characteristics of β-barrels.

2. Materials

2.1 Chemicals and consumables and equipment

All chemicals, not mentioned in tables 2 and 3, were ordered from Sigma Aldrich (Hamburg), VWR (Darmstadt) or Carl Roth GmbH + Co. KG (Karlsruhe).
All consumables, not mentioned in table 4 were ordered from Eppendorf AG (Wesseling-Berzdorf), Sarstedt AG & Co. (Nümbrecht) or Greiner Bio-One (Frickenhausen).
Chemicals for crystallization were ordered from Sigma Aldrich (Hamburg) with the highest possible purity.
Crystallization Screens were ordered from *Qiagen*.

All Enzymes not mentioned in Table 1 were ordered from *New England Biolabs* (*NEB*, Ipswich, MA, USA) and used following manufacturer's instructions.

2.1.1 Technical Equipment

Table 1: Technical equipment.

Device	Model (manufacturer)
LC systems	Äkta-Prime® P100 (*GE Healthcare*) Äkta-Purifier® 100 (*GE Healthcare*) NGC (*Biorad*)
BLM-device	Warner Instruments polystyrene cuvette: CP2A (*Warner Instruments*) bilayer chamber: BCH-22A (*Warner Instruments*) detector Multpatch 700B patch-clamp amplifier combined with a Digidata 1440A A/D converter with pClamp 10.2 software (*Axon Instruments*)
Digital-camera	D70s *(Nikon)*, lens: DX SWM ED *(Nikon)*, UV filter *(SEK)*
Electroporation device	MicroPulserTM *(Biorad)*
Fluidiser	EmulsiFlex C5 (*Avestin*)
French press	French-pressure cell-Version 5.1 (*Sim Aminco*) French-pressure cell (Philipps University

	Marburg unit for precision engineering)
Autoclave	T-line™ (*Fedegari*)
CD-spectrophotometer	J-810 or J-815 spectropolarimeter (*Jasco*)
Documentation systems	
Agarose gels	UV-transilluminator (*Herolab*)
Crystallisation	Rock Imager™ (*Formulatrix*)
Gelelectrophoresis	
SDS-PAGES trays/tanks	Mighty Small II SE250 (HoeferScientific Instruments), PerfectBlue two-gel system Twin M *(PEQLAB*)
Power boxes	Model 453 (ISCO), EPS 300 (*GE Health care)*
Crystallisation robot	Cartesian MicroSys™ 4004 (*Genomic Solutions*) Digilab Honeybee 963™ (*Zinsser analytic*)
pH-meter	Basic Meter PB-11 (*Sartorius*)
Homogenizer	After Potter-Elvehjem (*B. Braun*) KPG-stirrer (*Heidolph*)
Gel shaker	Model 3013 (*GFL*), Kottermann 4010 (*Kottermann*)
Incubator	Incubator (*Heraeus*), BFED-53 (*WTB Binder*)
Ultrapure water dispenser	Seralpur Pro90CN (Seral), Milli-Q (Millipore)
Peristaltic pump	P1 (GE Health care)
Shakers	CertomatR IS (Sartorius), G25 (New Brunswick Scientific), Multitron 2 (Infors), TH 25 (Edmund Buhler)
Centrifuges	2K15 (*Sigma*), Biofuge 13R (*Heraeus*), Biofuge fresco/pico (*Heraeus*), Centrifuge 5417C/5910R (*Eppendorf*), DiscoveryTM 90SE (*Sorvall*), EvolutionRC (*Sorvall*), J2-HS / J2-21 M/E (*Beckmann*), Minifuge GL (*Heraeus Christ*)
UV/Vis-spectrophotometer	Ultrospec™ 3100pro (Biochrom) Nanodrop® ND-1000 (peqLab)
Quartz glass cuvettes	110-QS 10 mm, Suprasil 10 mm (*Hellma*)

2.1.2. Consumables

Table 2: Consumables.

Consumable	Model (manufacturer)
Cuvettes	REF 67.742 (Sarstedt)
FPLC columns	Fractogel® EMD SE Hitrap M (*Merck*) Fractogel® DEAE- Hitrap (*Merck*) Superdex 200 Size-exclusion-column 16/60 (*GE Healthcare*) Ni-NTA Protino column (*MACHERY-NAGEL*) TALON metal affinity column (*GE Healthcare*)
Desalting column	PD Mini Trap G-25 desalting column (*GE Healthcare*)
Protein concentration devices	Amicon ultra - 15 Centrifugal Filter Devices Amicon ultra - 30 Centrifugal Filter Devices Amicon ultra- 0.5 Filter Devices 10000 / 3000 Da MWCO(*Milipore*)
Crystallisation consumables	Cover slides O = 22 mm (*Hampton Research*) 96-well inovaplate (*Innovadyne*) SilverSeal (Greiner Bio-one), VIEWsealTM adhesive sheets (*Greiner Bio-one*) CryoCaps with Data Matrix (Molecular Dimension) Cryschem Plate (*Hampton Research*) CrystalCap HAT (*Hampton Research*) CrystalCap HT Vial (*Hampton Research*) Crystal Clear Sealing Tape (*Hampton Research*)
Dialysis cassettes	Slide-A-LyzerR Mini Dialysis Units 10000 MWCO (*Pierce*)
Dialysis membrane	Pore size 0.025 µm, O = 25 mm (*Millipore*)
Disposable cuvettes	Cuvettes REF 67.742 (*Sardstedt*)
Sterilisation filters	Filtropur S 0.2, (*Sarstedt*) Filtropur S 0.45, (*Sarstedt*) Ultrafree®-MC (*Milipore*) Steritop Bottletop MF-Membrane Filters 0.025 µm VSWP (*Milipore*)
Electroporation cuvettes	400 µL, 2 mm gap (VWR))
Molecular biology consumables	QIAprep Spin Miniprep Kit (*Qiagen*) QIAquick PCR Purification Kit (*Qiagen*)

2.1.3 Chemicals

Table 3: Chemicals.

Chemical	Company
Acetonitrile HPLC-grade	*J.T.Baker*
Bacto® trypton	*Becton, Dickinson and Company*
Bacto® yeast extract	*Becton, Dickinson and Company*
Coomassie-brilliant blue G250	*Serva*
D(+)-glucose	*Merck KGaA*
Dichloromethane	*Merck KGaA*
Dipotassium hydrogenphosphate	*Merck KGaA*
Dithiothreitol	*Biomo*
Guanidiniumchloride	*Merck KGaA*
Urea	*Merck KGaA*
Potassium dihydrogen phosphate	*KMF optichem*
Lauryl-dimethylamin-oxide (LDAO)	*Fluka*
Sodium dodecyl sulfate	*Serva*
Sodium hydroxide	*Fluka*
Protein markers	*SM0431 Unstained Protein Molecular Weight Marker (Fermentas)*
Hydrochloric acid	*Riedel de Haën*
Virkon®	*Antec International*
(1-Oxyl-2,2,5,5-tetramethylpyrroline-3-methyl)methanethiosulfate (MTSSL)	*Enzo Life Science*
Alexa Fluor® 532 C5-maleimide	*Inivitrogen*
Isopropyl-β-*D*-thio-galacto-pyranoside	*Duchefa*
Ampicillin (sodium salt)	*Applichem GmbH*
Asolectin (from soybeans)	*Avanti Polar Lipids*
BC Assay Protein Quantification Kit	*Uptima by Interchim*
1,2-Diphytanoyl-*sn*-glycero-3-phosphocholine (DPhPC)	*Avanti Polar Lipids*
Mass Ruler DNA-Ladder-Mix (SM0403)	*Fermentas GmbH*
n-Octyltetraoxyethylene (C8E4)	*Bachem AG*
***n*-Octyl-β-*D*-glucopyranoside (n-OG)**	*Glycon Biochemicals*
1,2-Dimyristoyl-*sn*-glycero-3-phosphocoline (DMPC)	*Avanti Polar Lipids*
n-Decyl-β-maltoside (DM)	*Glycon Biochemicals*
n-Decyl-β-D-gluco-pyranoside (n-DG)	*Glycon Biochemicals*
n-Octyl-β-D-thio-gluco-pyranoside (OTG)	*Glycon Biochemicals*

2.1.4 Enzymes

Table 4: Enzymes.

Enzymes and antibodies	Company
Lysozyme	Boehringer Mannheim GmbH
Phusion High Fidelity DNA Polymerase	Finnzymes
Caspase 8	Merck Milipore
Trypsin Gold (Mass Spectrometry Grade)	Promega Corp.

2.2 Biological Materials

2.2.1 *E. coli* strains

E. coli DH5α

Genotype: F^-, Φ80*lac*ZΔM15, Δ(*lac*ZYA-*arg*F) U169, *recA*.1, *end*A1, *hsd*R17 (rk^-, mk^+), *pho*A, *sup*E44, λ^-, *thi*-1, *gyr*A96, *rel*A1

E. coli DH5α cells (*Invitrogen*) harbour a very high yield of plasmid DNA because of high replication rates. The cells were used as propagation strains because they are mutated for recA and rK^- which means that they do not restrict the foreign modified genetic material (e.g. plasmid). They are therefore well suited for preparation and isolation of recombinant DNA. These cells were used for all tasks of plasmid construction and preparation.[78]

E. coli BL21 (DE3) omp9

Genotype: F^-, ompT, $hsdS_B$ (r_B^- m_B^-), gal dcm (DE3), ΔlamB, ompF: :Tn5, ΔompA, ΔompC, ΔompN

E. coli BL21 (DE3) cells (*Novagen*) are designed for gene expression using T7-polymerase vectors like the pET series. These cells harbour the λ-prophage region encoding a T7 RNA polymerase, which is required for recognition of the T7 promoter on the used vectors, but is

itself under the control of the lac UV5 promoter. Therefore an IPTG based gen-expression for the production of recombinant proteins is possible.
E. coli BL21 (DE3) omp9 cells are based on *E. coli* BL21 (DE3) (*Novagen*), suitable for the expression of outer membrane proteins because of several incorporated gene deletions for the major *E. coli* porins. Namely, they lack the genes for a) the maltose-maltodextrin transporter LamB, b) the outer membrane-protease VII OmpT and c) the outer membrane proteins OmpA, OmpF, OmpC and OmpN. These cells ensure the lack of unwanted contaminants following the target protein´s gene expression.[79, 80] In addition, this strain harbours genes encoding for kanamycin and streptomycin resistances.
This strain was provided by Ralf Koebnik *et al.* (Biozentrum Universität Basel) and was used for the recombinant overproduction of all membrane proteins used in this work.

***E. coli* Rosetta (DE3)**

Genotype: F^-, ompT, hsdSB (r_B^- m_B^-), gal dcm (DE3), pRARE (Cam^R)

E.coli Rosetta (DE3) cells are based on the *E.coli* BL21 (DE3) strain (see above). They were designed for the overexpression of eukaryotic proteins whose genes contained codons rarely used by the bacterial host. Rosetta cells provide tRNAs for the rare codons AGG, AGA, AUA, CUA, CCC and GGA on an extra-chromosomal plasmid resistant to chloramphenicol.[81] In this work, this cell line was used for the expression of *BID* in pET-15b(+).

2.2.2 Vectors

pET-20b(+)®

The pET-20b(+) vector *(Novagen)* in combination with *E. coli* DH5α and *E. coli* BL21 (DE3) Omp9 was used for cloning, mutagenesis and recombinant overproduction of all membrane proteins in this thesis. Wildtype and *mVDAC1-variants* were inserted in pET-20b(+) using HindII and NdeI whereas EcoRI and NdeI sites were used for the wildtype *mVDAC2-variants*. The *minimal porin-gene* was inserted using XhoI and NdeI as restriction sites. pET-20b(+) has a length of 3716 bp and is a medium copy plasmid harbouring ampicillin resistance. The

expression cassette is under the control of the T7 promoter and the lac operator, which ensures IPTG controlled gene-expression.[82, 83] This vector is capable to introduce a C-terminal hexahistidine-Tag (His_6) for purification and a *peIB*-signal sequence needed for membrane insertion of membrane proteins. Both features were not used in this work.

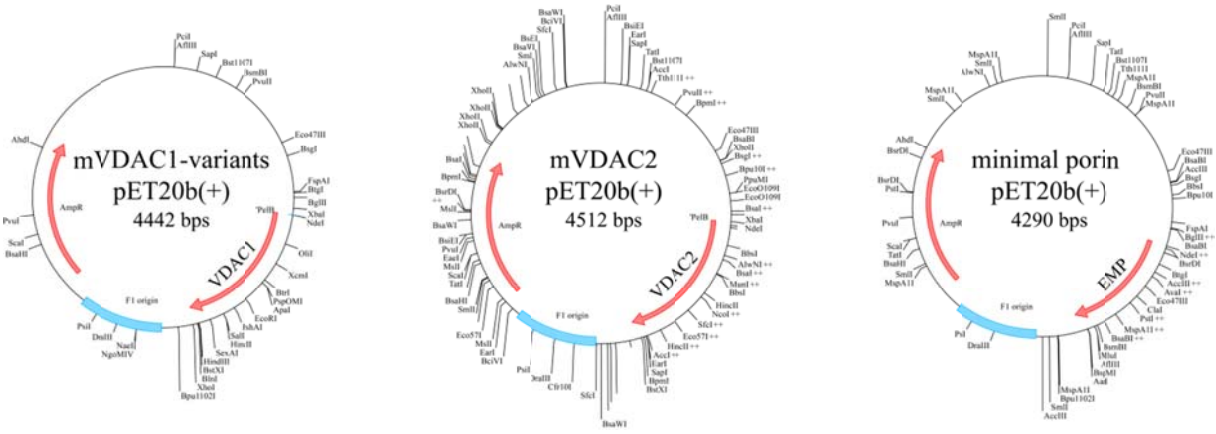

Figure 11: Vector maps for recombinant membrane proteins in pET-20b (+).

pET-15b(+)®

The pET-15b(+) vector *(Addgene)* was used for the heterologous overexpression of the *BID* using *E.coli* Rosetta (DE3) cells. *BID* had been subcloned in pET-15b(+) vector by Dr Sina Oppermann in.[20] The gene was inserted using NdeI on both cloning sites. pET-15b(+) has a length of 5708 bp and is a high copy plasmid harbouring an ampicillin resistance. The expression cassette is under control of the T7 promoter and the lac operator which ensures IPTG-controlled gene-expression. [82, 83] *BID* was fused to an N-terminal hexahistidine-tag (His_6) for purification.

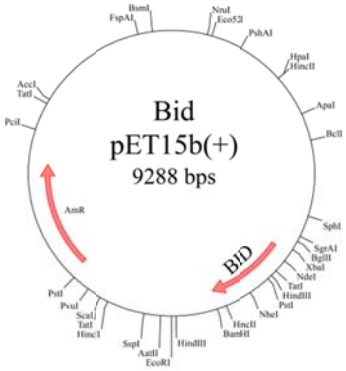

Figure 12: Vector map of Bid in pET 15b (+)

2.2.3 Primers

Sequencing of all constructs was performed by GATC or Qiagen using following oligonucleotides:

T7-Primer: 5' TAATACGACTCACTATAGGG
pET-RP: 5’ CTAGTTATTGCTCAGCGG

Primers for VDAC variants used in this work are listed in table 5, melting temperatures were calculated using the OligoAnalyzer 3.1 from IDTDNA.[84] Primers 1-5 were designed for *de novo* cloning whereas primer 6-25 were designed for mutagenesis of cloned genes. All primers were ordered from Metabion. Upon arrival the lyophilized primers were dissolved in EB to achieve 100 µM of oligonucleotide solution. The stock solutions were stored at -20 °C until further use. All stock solutions were diluted to 10 µM before use. When possible, an analytical restriction site was introduced. Analytical restrictions sites are underlined, mutations are represented in bold.

Table 5: Primers for de novo and quick change mutagenesis cloning.

Nr	Primer	Tm	Analytical restriction side	mutation
1[1]	• **5´**-TTAATACTCGAGTTATGCTTGAAATTCCAGTCCTAGGC • **5´**-TATACGCATATGAGAGGATCGCATCACCATCAC	• 61.5 °C • 61.9°C	XhoI NdeI	mVDAC1
2[1]	• **5’-**GCACATCAACCTCGGGGCTGACGTGGACTTTGAC • **5’-**GTCAAAGTCCACGTCAGCCCCGAGGTTGATGTGC	• 68.4 ºC	---	C127A
3[1]	• **5’-**CCAAGTATCAGGTGGATCCTGATGCCGCCTTTTCGGCCAAAG • **5’-**CTTTGGCCGAAAAGGCGGCATCAGGATCCACCAGATACTTGG	• 69.4 ºC	---	C232A
4[1]	• **5´**-TTAATACTCGAGTTATGCTTGAAATTCCAGTCCTAGGC • **5´**-TATAGACATATGTGTTCCGCCAGGGATGTCTTC	• 61.5 °C • 61.8 °C	XhoI NdeI	Δ1-11-K12C
5[1]	• **5´**-TTAATACTCGAGTTATGCTTGAAATTCCAGTCCTAGGC • **5´**-ATAAATCATATGTGCGGCTTTGGCTTAATAAAACTTGATTTGAAAAC	• 61.5 °C • 62.0 °C	XhoI NdeI	Δ1-21-Y22C
6[1]	• **5´**-TTAATACTCGAGTTATGCTTGAAATTCCAGTCCTAGGC	• 61.5 °C	XhoI	Δ1-25-

	• **5′**-AGAGATCATATGTGTATAAAACTTGATTTGAAAACGAAGTCAGAGAATG	• 61.5 °C	NdeI	L26C
7[1]	• **5′**-GAAGGAGATATCCATATGTGCGTGCCTCCCAC • **5′**-GTGGGAGGCACGCACATATGGATATCTCCTTC	• 64.2 ºC	EcoRV	A2C
8	• **5′**-GAAGGAGATATCCATATGGCC**TGC**CCTCCCACATACG • **5′**-CGTATGTGGGAGG**GCA**GGCCATATGGATATCTCCTTC	• 66.4 °C	EcoRV	V3C
9[1]	• **5′**-CGCCGATCTTGGC**TGC**TCCGCCAGGG • **5′**-CCCTGGCGGA**GCA**GCCAAGATCGGCG	• 70.8 °C	---	K12C
10[2]	• **5'**-CTTGGCAAGTCC**TGC**AGGGATGTCTTC • **5'**-GAAGACATCCCT**GCA**GGACTTGCCAAG	• 63.0 ºC	PstI	A14C
11	• **5′**-TTTGGCTTAATA**TGT**CTTGATTTAAAAACGAAG • **5′**-CTTCGTTTTTAAATCAAG**ACA**TATTAAGCCAAA	• 55.4 °C	DraI	K28C
12	• **5′**-GGCTTAATAAAGCTT**TGT**TTGAAAACGAAG • **3′**-CCGAATTATTTCGAA**ACA**AACTTTTGCTTC	• 56.0 °C	HindIII	D30C
13	• **5′**-TTAATAAAGCTTGATT**TGT**GTACGAAGTCAGAG • **5′**-AATTATTTCGAACTAAAC**ACA**TGCTTCAGTCTC	• 57.2 ºC	HindIII	K32C
14	• **5′**-AAAACGAAGTCA**TGT**AATGGATTGGAATTCACCAGCTCAGGC • **5′**-GCCTGAGCTGGTGAATTCCAATCCATT**ACA**TGACTTCGTTTT	• 65.4 ºC	EcoRI	E36C
15	• **5′**-AAAGTGAACGGC**TGT**CTAGAAACCAAGTAC • **5′**-TTTCACTTGCCG**ACA**GATCTTTGGTTCATG	• 60.1 °C	XbaI	S57C
16[1]	• **5′**-CCAAAGTGAACGGAAGCTTG**TGC**ACCAAGTACAGATGG • **5'**-CCATCTGTACTTGGT**GCA**CAAGCTTCCGTTCACTTTGG	• 66.3 °C	HindIII	E59C
17	• **5′**-AAGTGGAACACA**TGC**AACACCCTGGGC • **5′**-GCCCAGGGTGTT**GCA**TGTTCCACTT	• 65.2 °C	---	D78C
18	• **5′**-GAGATCACTGTG**TGT**GACCAGCTTGCT • **5′**-AGCAAGCTGGTC**ACA**CACAGTGATCTC	• 62.3°C	DraIII	E88C
19	• **5′**-CAAGACAGGGTAC**TGC**AGGGAGCACATCAACC • **5′**-GGTTGATGTGCTCCCT**GCA**GTACCCTGTCTTG	• 66.0 ºC	---	K119C
20[1]	• **5'**-GGGTACAAGAGG**TGC**CACATCAACCTCGG • **5'**-CCGAGGTTGATGTG**GCA**CCTCTTGTACCC	• 65.4 ºC	---	E121C
21	• **5′**-GACTTTGACATC**TGT**GGGCCCTCGATCCGCGGCGCTCTGGTG • **5′**-CACCAGAGCGCCGCGGATCGAGGGCCC**ACA**GATGTCAAAGTC	• 73.0 °C	AccII	A134C
22	• **5′**-GAGGGTTGGCTAGCTGGCTACTGTATGAATTTTGAG • **5′**-CTCAAAATTCATACAGTAGCCAGCTAGCCAACCCTC	• 63.6 °C	NheI	Q154C

23	• **5´**-TGGCTATAAGACA**TGT**GAATTCCAGCT • **5´**-AGCTGGAATTC**ACA**TGTCTTATAGCCA	• 58.0 °C	PciI	D176C
24[1]	• **5´**-CAGAGTTTGGTGGC**TGC**ATTTACCAGA AGG • **5´**-CCTTCTGGTAAAT**GCA**GCCACCAAACTC TG	• 62.7 ºC	---	S193C
25	• **5´**-AATCTCGCCTGGACGGCAGGA**TGC**AGT AACACTCGC • **5´**-GCGAGTGTTACT**GCA**TCCTGCCGTCCAG GCGAGATT •	• 69.6 °C	BglI	N214C
26	• **5´**-TCAGCCCTGCTC**TGT**GGCAAGAACGTC AACGCGGGTGGCTTT • **5´**-AAAGCCACCCGCGTTGACGTTCTTGCC**A CA**GAGCAGGGCTGA	• 73.3°C	HincII	D264C

[1] Primer planned by Dr Wolfgang Grosse

2.3 Recombinant proteins

mVDAC1 and the cysteineless variant *mVDAC1-C127A-C232A* were cloned into the pET-20b(+) vector using XhoI and NdeI as restriction sides. All other *VDAC1* variants were cloned based on one of these templates using the primers of table 5. For further notion all VDAC1 constructs with cysteine mutations were based on the cysteineless variant *mVDAC1-C127A-C232A* and are therefore designated as CL. *mVDAC2* and *EMP* were ordered from GeneArt and their gene sequence were optimised for *E.coli* based expressions. *mVDAC2* was supplied in the donor vector pMT-R whereas the *EMP* was delivered in the pMA vector. Both vectors encoded for ampicillin resistance. The inserts were flanked with EcoRI/NdeI (*mVDAC2*) and XhoI/NdeI (*EMP*) allowing cloning into pET-20b(+) using EcoRI/NdeI and XhoI/NdeI respectively. A *BID* coding pET-15b(+) vector was kindly provided by Prof. C. Culmsee. Cloning details as well as usage of recombinant proteins are provided in Table 6.

Table 6: VDAC variants, EMP and BID produced with the pairs of primers used in the PCR-based mutagenesis.

Nr	Recombinant protein	description	Primers used for cloning
1[1]	mVDAC1	wildtype	1
2	mVDAC2	wildtype	---
3[1]	mVDAC1-C127A-C232A (CL)	cysteineless variant (CL)	2 / 3
4[1]	Δ1-11-mVDAC1-K12C	N-terminal deletion variant	4
5[1]	Δ1-21-mVDAC1-Y22C	N-terminal deletion variant	5
6[1]	Δ1-25-mVDAC1-L26C	N-terminal deletion variant	6
7[2]	mVDAC1-CL-A2C-E121C	cysteine variant to fix the N-terminus in an open state	7 / 20
8[3]	mVDAC1-CL-V3C-K119C	cysteine variant to fix the N-terminus in an open state	8 / 19
9	mVDAC1-CL-K12C	cysteine variant for *cw*/ DEER measurements	9
10	mVDAC1-CL-K12C-D30C	cysteine variant for *cw*/ DEER measurements	9 / 12
11	mVDAC1-CL-K12C-K32C	cysteine variant for *cw*/ DEER measurements	9 / 13
12	mVDAC1-CL-K12C-S57C	cysteine variant for *cw*/ DEER measurements	9 / 15
13[2]	mVDAC1-CL-K12C-E59C	cysteine variant for *cw*/ DEER measurements	9 / 16
14[2]	mVDAC1-CL-A14C-S193C	cysteine variant to fix the N-terminus in an open state	10 / 24
15	mVDAC1-CL-K28C-Q154C	cysteine variant for *cw*/ DEER measurements	11 / 22
16	mVDAC1-CL-K32C	cysteine variant for *cw*/ DEER measurements	13
17	mVDAC1-CL-E36C-D176C	cysteine variant for *cw*/ DEER measurements	14 / 23
18[2]	mVDAC1-CL-E59C	cysteine variant for *cw*/ DEER measurements	16
19	mVDAC1-CL-E59C-S193C	cysteine variant for *cw*/ DEER measurements	16 / 24
20	mVDAC1-CL -D78C-N214C	cysteine variant for *cw*/ DEER measurements	17 / 25
21	mVDAC1-CL-E88C-K119C	cysteine variant for *cw*/ DEER measurements	18 / 19
22	mVDAC1-CL-A134C-D264C	cysteine variant for *cw*/ DEER measurements	21 / 26
23[4]	Minimal porin	optimized porin for ion channel engineering	---
24	BID	pro-apoptotic effector protein for VDAC	---

[1] Cloned by Anastasia Salisowski[85], [2] Cloned by Kathrin Back[86], [3] Cloned by Dr Georgios Psakis, [4] Constructed and cloned by Dr Wolfgang Grosse.

2.4 Media, stock solutions and buffers

2.4.1 Media

Lysogeny-broth (LB) media were employed for heterologous expression of genes listed above.[87] In addition LB-media were used in all molecular biological experiments (liquid cultures and agar plates). All components listed in table 7 were dissolved in dH_2O and autoclaved immediately after preparation (30 min at 121 °C and 2 bar).

Liquid media were stored under sterile conditions at room temperature until further use. For recombinant overproduction of membrane proteins (*mVDAC1* variants, *mVDAC2* and *EMP*) glucose (1% w/v) and ampicillin (100 µg/mL end concentration) were added prior to inoculation. For recombinant overproduction of *BID* only ampicillin (100 µg/mL end concentration) was added prior to inoculation.

The solid media were heated and cooled to approximately 50 °C before addition of ampicillin (100 µg/mL end concentration). The media were poured into petri dishes under sterile conditions and stored at 8 °C until further use.

Table 7: Composition of LB based media.

LB-media	**LB-agar**
10 g/L Bacto®-tryptone	10 g/L Bacto®-tryptone
5 g/L Bacto®-yeast-extract	5 g/L Bacto®-yeast-extract
10 g/L NaCl	10 g/L NaCl
400 µL/L NaOH (10M)	400 µL/L NaOH (10M)
	15 g/L agar-agar

2.4.2 Stock solutions

The following solutions were regularly prepared as stocks:

Table 8: Diverse stock solutions.

Stock solutions	
Ampicillin	100 mg/mL (in ddH_20)
DTT	1 M (in ddH_20)
EDTA	0,1 M (in ddH_20)
IPTG	1 M (in ddH_20)
PMSF	0.2 M (in isopropanole)
Glucose	20% w/v (in ddH_20)
TCA	72% w/v (in ddH_20)

2.4.3 Protein buffers

2.4.3.1 Buffers for molecular biological experiments

The following table contains the buffer compositions for standard molecular biological techniques.

Table 9: Agarose gel electrophoresis stock solutions.

Agarose gel	TBE buffer (10x)
1 % (w/v) agarose in TBE	1 M Tris
	1M boric acid
	20 mM EDTA

2.4.3.2 Buffers for protein analysis

The compositions of buffers used for analysis of the proteins generated in this work are shown below:

Table 10: SDS-PAGE gel buffers

SDS resolving gel buffer	SDS stacking gel buffer
1.125 M Tris / HCl, pH 8.8	625 mM Tris / HCl, pH 6.8
30% (w/v) sucrose	

Table 11: SDS-PAGE buffers

SDS running buffer (10x)	SDS sample buffer
0.25 M Tris	62.5 mM Tris / HCl, pH 6.8
2 M glycine	15% (v/v) glycerol
1% (w/v) SDS	15% (w/v) SDS
	0.001% (w/v) bromo-phenol-blue
	4% (v/v) 2-mercaptoethanol

Table 12: BN-PAGE running-buffer

BN-PAGE buffer
0.25 M Tris (pH 8.6 – 9.0)
1.94 M glycine
2 mM EGTA

Table 13: SDS-PAGE stainer and destainer

SDS-Stainer	SDS-Destainer
25% (w/v) Coomassie brilliant blue G250	5% (v/v) acetic acid
5% (v/v) acetic acid	28% (v/v) 2-propanol
50% (v/v) ethanol	

2.4.3.3 Buffers for protein purification

All buffers for protein purification were prepared according to the compositions mentioned in chapter 3 (methods) using dH_2O. All buffers were sterile filtered (0.025 µm) before use and stored at 8°C.

3. Methods

3.1 Molecular biology

The following section will describe the methods used to manipulate, modify and obtain DNA. mVDAC1 genes were cloned by Anastasia Salisovsky[85], Katrin Back[86], Georgios Psakis or myself (see Table 6 for details).

3.1.1 mVDAC1 constructs

Plasmid vectors, harbouring the mVDAC1 gene, were kindly provided by Dr Jeff Abramson (University of California LA). The *mVDAC1* gene was amplified by PCR according to the manufacturer´s instructions, using the primers 1 (see table 5), introducing the XhoI and NdeI restriction sites respectively. PCR products were digested and PCR cleaned. The acceptor vector pET-20b(+) was pre-digested with the same enzymes and dephosphorylated with alkaline phosphatase (*NEB*) (1 unit for every pmol of DNA ends) to obtain complementary restriction sides. Subsequent ligation was performed with T4-ligase (*NEB*) according to the manufacturer's instructions. DH5α cells were transformed with the ligated product.
The N-terminal deletion variants (constructs 4-6) were PCR amplified using the primers 3, 4 or 5 which contained XhoI and NdeI restriction sides. The PCR product was digested with XhoI/NdeI according to the manufacturer's instructions and PCR cleaned. Subsequent ligation was performed with T4-ligase (*NEB*) in a 3:1 ratio with pre-digested and dephosphorylated pET-20b(+) vector. DH5α cells were transformed with the ligated product.
To obtain the cysteineless mVDAC1-C127A-C232A construct the PCR-based QuickChange mutagenesis method was used. QuickChange™ mutagenesis is a quick and easy way for *in vitro* site-specific mutation. During this procedure complementary primers harbouring the desired mutation are used to amplify the entire circular molecule. For this, primers 2 were used and PCR was performed according to QIAGEN quick change kit´s manual with the exception that DpnI (*NEB*) treatment was prolonged relative to the manufacturer's instructions.[88] Following confirmation of the first mutation by DNA sequencing the second

was introduced using the same protocol but using primers 3 and mVDAC1-C127A as template. The identity of the final construct was also confirmed by DNA sequencing (GATC or Qiagen).
All other VDAC1 genes were cloned by the QuickChange PCR-based mutagenesis using the cysteine-free mVDAC1 plasmid as template. All primers for the different constructs are listed in table 5 and the protocol as described above was similarly used for all mVDAC1 genes. The identity of all constructs was confirmed by DNA sequencing (*Qiagen* and *GATC*).

3.1.2 mVDAC2 construct

The *mvdac2-gene* was ordered from GeneArt as an *E.coli* optimized gene construct. The pMT-R vector containing the mVDAC2 gene flanked with NdeI and EcoRI restriction sides was transformed in DH5α cells to amplify the desired plasmid (see section 3.1.5 for details). The *mvdac2-gene* was digested using NdeI and EcoRI according to manufacturer's instruction. The ligation was performed with T4-ligase in a 3:1 ratio with pre-digested and dephosphorylated pET20b(+) vector. DH5α cells were transformed with the ligated product.

3.1.3 Minimal porin

The molecular biological work for EMP was conducted by Dr Wolfgang Grosse. The *EMP-gene* was ordered from GeneArt in pMA donor vector. The gene sequence had been optimised for expression in *E.coli*. The desired *EMP-gene* was flanked with NdeI and XhoI restriction sites and DH5α were transformed with the donor plasmid (see section 3.1.5 for details). The *EMP-gene* was digested using NdeI and XhoI according to manufacturer's instruction and the ligation was performed with T4-ligase in a 3:1 ratio with a pre-digested and dephosphorylated pET20b(+) vector. DH5α cells were transformed with the ligated product.

3.1.4 Preparation of competent *E.coli* cells

For the preparation of *E.coli* competent cells two different methods are commonly used, electro transformation and chemical transformation using a heat shock.[89] Competent *E.coli* cells are able to uptake plasmid DNA. This ability is needed while working with manipulated

DNA. After preparation the competency of the cells was determined using the following formula.[90]

$$\text{transformants per microgram of plasmid DNA} = \frac{number\ of\ transformants\ (colonies)}{microgram\ of\ plasmid\ DNA} \cdot \frac{final\ volume\ at\ recovery\ (mL)}{volume\ plated\ (mL)} \quad \text{(Eq 1)}$$

3.1.4.1. Preparation of chemically competent cells

Chemically competent cells were prepared using the RbCl method.[91] The RbCl method is basically the same method than the $CaCl_2$ method but yields better DNA uptake efficiencies.[92, 93] Chemically competent DH5α cells were used for re-transformations of plasmids and chemically competent BL21 (DE3) Omp9 and Rosetta cells were used for recombinant gene expression.

To prepare a new batch of chemically competent cells 5 mL of liquid LB medium was inoculated with a single colony from a LB-agar plate. Cells were grown over night at 37 °C. 100 mL of liquid LB-medium was inoculated with 1 mL of the overnight culture and was left to grow at 37 °C and 225 rpm until an OD_{600} of 0.5 – 0.6 was reached. The cells were then cooled in ice-water and pelleted (12300 g, 10 min, 4 °C). The pellet were resuspended in 30 mL TFBI buffer (100 mM RbCl, 50 mM $MnCl_2$, 30 mM KOAc, 10 mM $CaCl_2$, 15% (v/v) glycerine) and incubated for 2h on ice. Following the incubation, cells were again pelleted (12300 g, 10 min, 4 °C) and resuspended in 4 mL precooled TFBII buffer (10 mM MOPS, 10 mM RbCl, 75 mM $CaCl_2$, 15% (v/v) glycerine). The cells were then immediately divided in 50 µL aliquots and shock-frozen in liquid nitrogen. Aliquots were stored at -80 °C until further use.

3.1.4.2 Preparation of electro-competent cells

Compared to chemically competent cells, electro-competent cells may achieve a higher yield of DNA uptake. The efficiency of a transformation using a heat shock is about 10^6-10^8 colonies per µg DNA, whereas the transformation efficiency using the electroporation methods is up to 10^{10} colonies per µg DNA.[89] Thus, electro-competent DH5α cells were used

for all transformations following the QuickChange mutagenesis or ligations. The method is based on a protocol from Dower (1988).[94]

To prepare a new batch of electro-competent cells 50 mL of liquid LB-media were inoculated with a single colony from a fresh LB-Agar plate and were left to grow at 37 °C and 225 rpm overnight. 1L pre-warmed LB medium was inoculated with 10 mL of overnight culture and were left to grow until an OD_{600} of 0.8 was reached. The cells were immediately cooled in ice-water for 20 min and pelleted afterwards (12300 g, 10 min, 4 °C). The pellet was resuspended in 450 mL ice-cold water and again pelleted (12300 g, 10 min, 4 °C). This step was repeated once. After this the pellet was resuspended in 450 mL of ice cold glycerol solution (10% v/v) and pelleted again (12300 g, 10 min, 4 °C). Finally the pellets were resuspended in 2.5 mL of ice cold glycerol solution (10% v/v) and immediately divided in 50 µL aliquots. The aliquots were shock frozen in liquid nitrogen and stored at -80 °C until further use.

3.1.5 Transformation of competent cells

The uptake of foreign DNA in prokaryotic cells is known as transformation. Generally speaking, there are different methods to force competent cells to uptake plasmid DNA. In this thesis two different methods were used, the chemical transformation and the electroporation. As mentioned above the chemical transformation was used for all gene expressions whereas the electroporation was used following the PCR-based and QuickChange mutagenesis.

3.1.5.1 Transformation of electro-competent cells

During electroporation the competent cells were treated with a short but high voltage pulse. Although the mechanism is not completely understood,[95] this pulse allows DNA to enter the cytoplasm of the cell.

10 µL of the ligation and 10 µL of the QuickChange mutagenesis assay were dialyzed for at least 4 h. 50 µL of chilled DH5α cells were treated with 4 µL of the dialyzed solution and transferred to an electroporation cell. The sample was then pulsed with a surge of 1-2 keV for 3.0 -6.0 ms and 950 mL liquid LB-medium was added immediately. The cells were then grown at 37 °C for 1.5 h with shaking (225 rpm). Cells were subsequently harvested

(centrifuged), resuspended in approximately 20 µL and plated on LB agar plates containing ampicillin as selection marker. The plates were incubated at 37 °C overnight.

3.1.5.2 Transformation of chemically competent cells

During chemical transformation the cells are treated with a heat shock to weaken the cell walls allowing the DNA to enter the cytoplasm.[92]
Chemically competent DH5α were used for re-transformation, whereas BL21 (DE3) Omp9 and Rosetta cells were used for gene expressions.
50 µL of chilled cells were treated with 1 µL of plasmid DNA and incubated for 30 min on ice. The cells were warmed for 90s at 42°C and cooled on ice immediately after the heat shock. 950 µL liquid LB-media were added and the cells were left for recovery at 37°C and 225 rpm for 1h. Afterwards the cells were plated on an LB-agar plate containing ampicillin as selection marker. The plate was left overnight in the incubator at 37°C.

3.1.6 Preparation of plasmid DNA

3.1.6.1 Qiagen method

The preparation of plasmid DNA was performed using the QIAprep Spin Miniprep Kit (*QIAGEN*) according to manufacturer's instructions.[96] 4 mL of pelleted overnight culture were used. The cells were lysed with NaOH and chromosomal DNA as well as proteins and cell particles were precipitated. The plasmid purification was performed using a silica matrix with a capacity for duplex DNA of ≤ 10 kbp. The supernatant of the lysed cells were added to the column under high salt conditions and washed with EtOH containing buffer. The purified plasmid DNA was then eluted under low salt conditions.

3.1.6.2 "Quick and dirty" method

The "quick and dirty" method is based on the alkaline lysis of cells.[97] The "quick and dirty" method is a cheap method for the isolation of high amounts of plasmids but a final purification is often needed for further work with isolated plasmids. All plasmids isolated

with this method were analysed using agarose gel electrophoresis (see chapter 3.1.8) and putatively positive clones were PCR-cleaned before being sent to sequencing.
4 mL of pelleted overnight culture were resuspended in 300 µL P1-buffer (50 mL Tris/HCl, pH 8.0, 10 mM EDTA, 100 µg/mL RNaseA) and 300 µL of P2-buffer (200 mM NaOH, 1% (w/v) SDS) were added. The sample was inverted carefully and incubated for 5 min at room temperature. 300 µL P3-buffer (2.55 M KOAc) were added to neutralize the solution and the whole sample was incubated for 15 min on ice. Chromosomal DNA as well as proteins and cell particles were precipitated (25402 g, 15 min, 4°C) and the supernatant was transferred to a new 1.5 mL Eppendorf reaction cup. 600 µL isopropanol were added and the whole solution was vortexed to precipitate the plasmid DNA. The precipitated plasmids were pelleted (25402 g, 30 min, 4°C) and washed twice with EtOH and water. The plasmid pellet was dried at 37 °C and 50 µL EB buffer (10 mM Tris/HCl, pH 8.5) was added for redissolution.

3.1.6.3 PCR purification using the Qiagen method

Isolated plasmids were purified using the QIAprep Spin PCR-purification Kit (*QIAGEN*) following the manufacturer's instructions.[96] The purification is based on the separation of plasmid DNA and contaminants on a silica matrix with a capacity of ≤ 10 kbp. The plasmids were added to the column under high salt conditions and washed with EtOH containing buffer. The purified plasmid DNA was then eluted under low salt conditions.

3.1.7 Determination of DNA concentration

The concentration of DNA was determined by absorption at 260 nm. Contaminants like proteins and RNA could be identified from the proportion of the absorbance at 280 nm and 230 nm respectively. All measurements were done at the ND-1000 Spectrophotometers (*peqlab*). Concentration calculation for double-stranded DNA were based on the following equation.[89]

$$c_{DNA} = OD_{260} \times 50\frac{ng}{\mu L}$$

(Eq 2)

3.1.8 Agarose gel electrophoresis

The agarose gel electrophoresis was used to separate and analyse DNA fragments after the cleavage by restriction enzymes. Accordingly, 1% (w/v) agarose in TBE-buffer (100 mM Tris, 100 mM boric acid, 2 mM EDTA) was melted and poured to an electrophoresis equipment (mechanics tool shop, Philipps University Marburg). Following cooling of the agarose gel, 6x loading dye were added to the DNA solution and samples were applied onto the gel. The electrophoresis was performed at 100 V with constant current for 75 minutes. The resulting DNA bands were stained with ethidium bromide (0.5 µg/mL) and detected under UV light (λ = 254 nm).[98]

3.2 Biochemical methods

3.2.1 Overnight liquid cultures for microbiology

For identification of VDAC1 variant clones as well as for the retransformation of plasmids, *E.coli* DH5α cells were used.
5 mL LB-medium containing 100 µg/mL ampicillin was inoculated with a single colony from an LB-agar plate of transformants. The cell culture was grown at 37 °C over night and the plasmids were isolated as described in section 3.1.6.

3.2.2 Recombinant gene expression

Recombinant gene expression in *E.coli* was used for the production of proteins for further structural and functional analysis.

3.2.2.1 Recombinant protein overproductions

mVDAC1 variants, mVDAC2 and the minimal porin were produced as inclusion bodies using *E.coli* BL21(DE3) omp9 cells.[59, 99] For this, cells were transformed with pET-20b(+) plasmids harbouring the genes of interest without the signal sequence. All transformants were

tested for their expression efficiencies in a small scale before embarking on preparative scale experiments.

3.2.2.2 Recombinant protein overproductions on an analytical scale

Transformants were grown in 5 mL liquid LB-medium containing 100 µg/mL ampicillin and 1% glucose (w/v) at 37°C and 225 rpm for approximately 4h. After this 100 µL of the culture were transferred to 5 mL of fresh liquid LB-medium containing 100 µg/mL ampicillin and 1% glucose (w/v) and were incubated at 37°C and 225 rpm until further usage. With the remaining initial culture a small scale expression was performed. For this, 4 µL IPTG (c_{end} = 1 mM) was added to the cell suspension and the expression was performed for 1.5 h at the same conditions. An SDS sample before and after induction was taken and analysed by an 12% SDS-PAGE. The SDS-samples was prepared by taking 1 mL cell solution and precipitating the cells (25402 g, 3 min). The cell pellets were resuspended in 20 µL SDS-sample buffer, heated for 5 min at 98°C and loaded on an 12% SDS-PAGE gel to identify the best expression clone for preparative recombinant protein overproduction (see section 3.3.1). 10 µL of the best expressing clone was therefore transferred to 100 mL of liquid LB-medium containing 100 µg/mL ampicillin and 1% glucose (w/v) and were left to grow at 37°C and 225 rpm overnight.

3.2.2.3 Recombinant protein overproductions on a preparative scale

The preparative overproduction of VDAC1-variants, VDAC2 and EMP variant was done in 6 L liquid LB-medium to produce inclusion bodies.

The liquid LB-medium was divided in 2 L medium in 5 L conical-flasks to ensure optimal supply of oxygen. 30 mL of starter culture (see chapter 3.2.2.2) was added to 2L of liquid LB medium containing 100 µg/mL ampicillin and 1% glucose (w/v). Induction was performed at an OD_{600} of ~ 0.6 by the addition of 1 mM IPTG. After induction the cells were grown for 4h at 37°C and 125 rpm before harvesting (6400 g, 15 min, 4°C). The cell pellets were resuspended in TEN-buffer (50 mM Tris/HCl, pH 8.0, 100 mM NaCl) and shock frozen in liquid nitrogen. The cell suspension was stored at -80°C until cell disruption.

3.2.2.4 *BID* expression in a preparative scale

The *BID* expression was performed in Rosetta cells. Transformants were grown overnight in 100 mL liquid LB-medium containing 100 µg/mL ampicillin and 34 µg/mL chloramphenicol. The preparative gene expression was done in 6 L liquid LB-medium.

The liquid LB-medium was divided in 2 L medium in 5 L conical-flasks to ensure optimal supply of oxygen. 30 mL of starter culture was added to 2 L of liquid LB medium containing 100 µg/mL ampicillin and 34 µg/mL chloramphenicol. Induction was performed at an OD_{600} ~ 0.6 by the addition of 1 mM IPTG. After induction the cells were grown for 4h at 37°C and 125 rpm before harvesting (6400 g, 15 min, 4 °C). The cell pellets were resuspended in Bid IEC-buffer (20 mM Tris/HCl, pH 7.5, 250 mM NaCl and 10 mM β-mercaptoethanol). Protease inhibitor cocktail (1mL per 100 mL of cell lysate, #P8849 *Sigma Aldrich*) was added and the cell suspension was shock frozen in liquid nitrogen. The cell suspension was stored at -80 °C until cell disruption.

3.2.3 Cell disruption

Cells were disrupted using either a high pressure homogeniser (Emulsifier EmulsiFlex C5, *Avestin*) or a French press (*Sim Amico*) device. Cell disruption is facilitated by the explosive decompression of cells (approx. 8 MPa) which inevitably leads to their lysis. [100]

Before disruption of cells used for the recombinant overproduction of membrane proteins (VDAC1, VDAC2 and EMP) PMSF (c_{End} = 0.375 mM) and EDTA (c_{End} = 0.1 mM) was added. The cell disruption was performed twice (~ 1000 psi) and the insoluble inclusion bodies were separated from the soluble parts by centrifugation (25402 g, 30 min, 4 °C). The crude cell extract was discarded and the inclusion bodies were washed to obtain the denatured membrane proteins.

The soluble Bid protein was disrupted using the French press device. Especially for soluble proteins it is important to ensure a proper cooling of the devices so that the protein remains in the native fold. Before cell disruption a spatula tip DNAseI (*Applichem*) was added and the cell solution was incubated for 5 min at room temperature. The cells were disrupted twice (~ 1000 psi) to ensure complete lysis. The supernatant containing the soluble Bid protein was separated via centrifugation (25402 g, 30 min, 4 °C) from the insoluble parts of the cell,

filtered using a syringe sterile filter (0.2 µm, *Sarsted*) and applied to a Ni-NTA Protino column (*MACHERY-NAGEL*) for further purification.

3.2.4 Preparation of inclusion bodies

The separation of *inclusion bodies* from *E.coli* lipids and other proteins was done by a multi-step washing protocol using a homogeniser after Potter-Elvjhem (*Braun*).[101, 102]
The protein-containing pellet from the cell disruption was washed three times in a detergent containing Triton-TEN Buffer (50 mM Tris/HCl, pH 8.0, 100 mM NaCl, 10 mM EDTA, 2.5% (v/v) Triton-X-100) and three times in TEN buffer (50 mM Tris/HCl, pH 8.0, 100 mM NaCl) to get rid of the detergent (TEN buffer). The protein pellet was finally resuspended in TEN buffer, flash-frozen in liquid nitrogen and stored at −80 °C until further use.
The protein content of the inclusion bodies was determined spectroscopically monitoring the absorbance of proteins at 280 nm. At this wavelength mainly trypthophans and tyrosines are absorbing. The extinction coefficients were calculated using ProtParam (ExPASy) [103].
10 µL of washed inclusion bodies were denatured in 1 mL potassium-buffer (20 mM K_3PO_4 pH 6.5, 6 M guanidinium chloride). The absorbance was measured three times and the protein concentration was determined using the following equation.

$$c_{Prot} = \frac{\mathrm{E}}{\varepsilon_{red}} \cdot 100 \qquad \text{(Eq 3)}$$

3.2.5 Refolding of membrane proteins

mVDAC1-variants, mVDAC2 and the minimal porin were produced as insoluble inclusion bodies. A two-step rapid dilution protocol according to Bayrhuber *et al.*[25] and Hiller *et al.*[32] was used to restore the native conformation. The first step of this refolding procedure is the full denaturation of the membrane proteins by high concentrations of chaotropic salts. The following two steps of dilution in the presence of detergent-containing buffers are necessary to reduce the amount of chaotropic salts and to ensure the refolding in the native conformation.

3.2.5.1 Refolding of membrane proteins in an analytical scale

A variety of different lipids and folding aids are commercially available. To find the right conditions for proper refolding, a refolding screen for mVDAC1 and the minimal porin was performed. In these screens different detergents, proteins concentrations as well as folding aids were tested to find the optimal refolding conditions.

The refolding screen for mVDAC1 in detail is provided in table 14 and the refolding screen of the minimal prion is provided in table 15.

Table 14: Refolding screen for mVDAC1.

Protein concentration	Folding aid	Detergent
1, 5 and 10 mg/ mL		LDAO
1, 5 and 10 mg/ mL		n-OG
1, 5 and 10 mg/ mL		C8E4
1, 5 and 10 mg/ mL		DM
1, 5 and 10 mg/ mL		n-DG
1, 5 and 10 mg/ mL		DDM
5 and 10 mg/ mL	Glycerol (5-20%)	LDAO
5 and 10 mg/ mL	Sucrose (1-25 mg/mL)	LDAO
5 and 10 mg/ mL	Prolin (10 – 1000 mM	LDAO

Table 15: Refolding screen for the minimal porin.

Proteinconcentration	Folding aid	Detergent
10 mg/ mL		LDAO
10 mg/ mL	Glycerol 10%	LDAO
10 mg/ mL	Xylitol 10%	LDAO
10 mg/ mL		n-OG
10 mg/ mL	Glycerol 10%	n-OG
10 mg/ mL	Xylitol 10%	n-OG
10 mg/ mL		C8E4
10 mg/ mL	Glycerol 10%	C8E4
10 mg/ mL	Xylitol 10%	C8E4
10 mg/ mL		DM
10 mg/ mL	Glycerol 10%	DM
10 mg/ mL	Xylitol 10%	DM
10 mg/ mL		n-DG
10 mg/ mL	Glycerol 10%	n-DG
10 mg/ mL	Xylitol 10%	n-DG
10 mg/ mL		OTG
10 mg/ mL	Glycerol 10%	OTG
10 mg/ mL	Xylitol 10%	OTG

The inclusion bodies were separated from the buffer by centrifugation (13 krpm, 3 min) and the pellets were resuspended in denaturation-buffer (25 mM NaH_2PO_4/Na_2HPO_4, pH 7.0, 100

mM NaCl, 1 mM EDTA, 10 mM DTT, 6 M guanidinium chloride). To ensure optimal denaturation of the inclusion bodies, the solution was heated for 10 min at 60°C. Insoluble parts were separated by centrifugation (25402 g, 3min) and the supernatant was added drop wise to a ten-fold dilution of refolding-buffer 1 (25 mM NaH_2PO_4/Na_2HPO_4, pH 7.0, 100 mM NaCl, 1 mM EDTA, 10xCMC detergent, folding aid). The samples were gently mixed over night at 10 °C. The precipitate was removed (25402 g, 3 min 4 °C) and the supernatant was applied drop-wise to a ten-fold excess of refolding-buffer 2 (25 mM NaH_2PO_4/Na_2HPO_4, pH 7.0, 10 mM NaCl, 1 mM EDTA, 1 mM DTT, 5xCMC detergent, folding aid). The refolding solution was mildly mixed overnight at 10 °C. The insoluble parts were again removed by centrifugation (25402 g, 3 min 4 °C) and the supernatants were analysed via SDS-PAGE (section 3.3.1).

3.2.5.2 Refolding of membrane proteins in a preparative scale

After identifying the right refolding conditions the membrane proteins were refolded in a preparative scale. The protein refolding was accomplished by rapid dilution in a two-step process.

The inclusion bodies (10 mg/mL) were denatured in denaturation-buffer (25 mM NaH_2PO_4/Na_2HPO_4, pH 7.0 for VDAC1, pH 7.4 for EMP and pH 6.0 for VDAC2, 100 mM NaCl, 1 mM EDTA, 10 mM DTT, 6 M guanidinium chloride) and heated for 10 min and 1250 rpm at 60 °C. The insoluble parts were separated by centrifugation (25402 g, 3 min) and the supernatant was added drop wise to a 10-fold excess of refolding-buffer 1 (25 mM NaH_2PO_4/Na_2HPO_4, pH 7.0 for VDAC1, pH 7.4 for EMP and pH 6.0 for VDAC2, 100 mM NaCl, 1mM EDTA, 2.22% (v/v) lauryldimethylamine-oxide (LDAO), and 10% glycerol for EMP). The mixture was gently stirred overnight at 4°C and the insoluble parts were removed by centrifugation (12300g, 10 min, 4 °C) and the supernatant was added drop wise to a tenfold dilution of refolding-buffer II (25 mM NaH_2PO_4/Na_2HPO_4, pH 7.0 for VDAC1, pH 7.4 for EMP and pH 6.0 for VDAC2, 10 mM NaCl, 1 mM EDTA, 0.1% (v/v) LDAO, and 10% glycerol for EMP). The solution was mildly stirred overnight and the insoluble parts were removed by a sterile filter before being applied onto a pre-equilibrated column for further purification.

3.2.6 Truncation of Bid

The soluble Bid protein is the inactive form of the pro-apoptotic protein. The activation of Bid to tBid, the truncated form of Bid, is achieved by cleavage of the premature protein by Caspase8.[104] For binding assays and functional analysis studies it was necessary to activate Bid. Following Bid truncation, hydrophobic parts become solvent-exposed.[105] Therefore, a buffer containing detergents was used to hinder tBid from precipitation.
The cleavage was performed in cutting buffer (50 mM HEPES / NaOH, pH 7.5, 100 mM NaCl, 10 mM DTT 1 mM EDTA, 10 % Sacharose) to ensure full activity of Caspase8. 200 µL of purified Bid in SEC-buffer (20 mM Tris / HCl pH, 7.4, 50 mM NaCl) was diluted in cutting-buffer to 10 mg/mL and 1 µL (5 units) of Caspase 8 (*Merck Milipore*) was added. The mixture was incubated for 30 min – 72 h at 30 °C until the Bid protein was completely cleaved. The success of cleavage was analysed via SDS-PAGE (section 3.3.1). The cleaved tBid solution was again diluted to 5 mg/mL in tBid-SEC-buffer (50 mM Hepes / NaOH pH 7.5, 300 mM NaCl, 0.2 mM DTT, 1% OG) to prevent precipitation and further purified by size-exclusion chromatography.

3.2.7 Protein purification

3.2.7.1 Ion-exchange chromatography

Ion-exchange chromatography is commonly used during protein purification. The purification is achieved through the interaction of charged side chains of the amino acids residues with the charged column material. The choice of the ion-exchange material is based on the pI of the protein and the pH of the buffer solution.

mVDAC1-variants were purified using a pre-equilibrated Fractogel EMD-SE Hicap cation-exchange column (5 mL volume, *Merck*) operated at an ÄKTA prime purification system (*Amersham Biosciences*) or an NGC system (*Biorad*). This special material enhances the protein to column interaction by providing the charged groups on flexible linkers. Especially for membrane proteins in detergent micelles the interaction between column material and protein is not trivial. Therefore the Fractogel material was found to produce the best separation results. [106]

After refolding, the sterile-filtered mVDAC1-variants were applied onto the pre-equilibrated Fractogel EMD-SE Hicap cation-exchange column. The cation-exchange column was used because of the theoretical pI of the VDAC1-variants (8.3-8.8) in combination with the buffer at pH 7.0. Because of the large volume obtained after refolding the column was loaded overnight using a peristaltic pump under circular back flow. Elution was performed using a multi-segment gradient of 10 - 1000 mM NaCl in elution-buffer (25 mM NaH_2PO_4/Na_2HPO_4, pH 7.0, 1 mM EDTA, 1 mM DTT and 0.1% (v/v) LDAO) and purification was detected at 280 nm. The mVDAC1-containing fractions were analysed on an 12% SDS-PAGE (section 3.3.1), pooled and concentrated using a 10-kDa Amicon concentrator (*Millipore*).

mVDAC2 variants were purified using a pre-equilibrated Fractogel DEAE anion-exchange column using an adapted protocol of mVDAC1 purification. The refolding of mVDAC2 was performed in refolding buffer II buffer (25 mM NaH_2PO_4/Na_2HPO_4, pH 6.0, 10 mM NaCl, 1 mM EDTA, 1 mM DTT and 0.1% (v/v) LDAO) at an pH of 6.0. The pH of the refolding solution was then carefully raised from 6.0 to 8.5 using 1 M NaOH and controlled by an pH meter. mVDAC2 was applied onto a pre-equilibrated Fractogel DEAE anion-exchange column operated at an NGC device (*Biorad*). Elution was performed using a continuous gradient of 10 - 1000 mM NaCl in Elution buffer (25 mM NaH_2PO_4/Na_2HPO_4 (pH 8.0), 1 mM EDTA, 1 mM DTT and 0.1% (v/v) LDAO) and purification was detected at 280 nm. The mVDAC2-containing fractions were analysed on an 12% SDS-PAGE (section 3.3.1), pooled and concentrated using a 10-kDa Amicon concentrator (*Millipore*).

3.2.7.2 Metal affinity chromatography

The minimal porin as well as the soluble Bid protein was fused with an N-terminal His-tag compatible with the purification by metal affinity chromatography. The hexa-histidine tag has a high affinity for either Ni^{2+} when complexed to tetradentate ligand nitrilotriacetate (Ni-NTA) or Co^{2+} when complexed to carboxymethylated aspartate (TALON™).[107, 108] The histidine residues are able to coordinate the metal-ion at the remaining coordination sites and elution is done by different concentrations of imidazole.

EMP was purified using a TALON metal affinity column (*GE Healthcare*). The TALON-column has a higher affinity towards His-tagged proteins although it is more sensitive to other

substances like EDTA or DTT. Use of the TALON-matrix was required because the detergent micelle was preventing a satisfying binding of EMP to the Ni-NTA resin. After refolding, the sterile-filtered (0.025 µm) minimal porin was applied overnight onto a pre-equilibrated Talon-column using a peristaltic pump under circular back flow. Elution was performed using a continuous gradient of 0 - 150 mM imidazole in elution-buffer (25 mM NaH_2PO_4/Na_2HPO_4, pH 7.4, 10 mM NaCl, 10% glycerol and 0.1% (v/v) LDAO) and purification was detected at 280 nm. The protein-containing fractions were analysed using an 12% SDS-PAGE (section 3.3.1), pooled and concentrated by a 10-kDa Amicon concentrator (*Millipore*).

For the soluble protein Bid a Ni-NTA Protino column (*Machery-Nagel*) was used. After cell disruption, the lysate was sterile filtered and applied onto a pre-equilibrated Ni-NTA-column. Elution was performed using a continuous gradient of 0 - 400 mM imidazole in Elution-buffer (20 mM Tris / HCl (pH 7.5), 250 mM NaCl, 10 mM β-mercaptoethanole) and purification was detected at 280 nm. The protein-containing fractions were analysed using a 12% SDS-PAGE (section 3.3.1), pooled and concentrated via a 3-kDa Amicon concentrator (*Millipore*).

3.2.7.3 Size-exclusion chromatography

Size-exclusion chromatography (SEC) separates proteins in terms of their hydrodynamic radii. The column matrix is a polymer of cross-linked agarose or dextran with variously sized pores. The separation is based on diffusion through these pores with larger proteins eluting earlier than smaller proteins. The reciprocal of a calibration curve of the eluted volumes and the logarithm of the molecular mass standards enables the calculation of the unknown particle size.

An analytical SEC-column was used to analyse small amounts of proteins. For example the protein-protein complex of mVDAC1 with Bid/tBid was analysed using a Superdex™ 200 in 150/10GL column (*GE Healthcare*) with a column volume of 3 mL. For preparative protein purification a Superdex™ 200 XK 16/60 column (*GE Healthcare*) with a bed volume of 120 mL was used. The purification over a SEC was used as a polishing step and a measure of monodispersity for all proteins purified in this work. All proteins were sterile filtered (0.025 µm) before application onto the pre-equilibrated column. Elution profiles were detected at 280 nm. The protein-containing fractions were analysed using a 12% SDS-PAGE

(section 3.3.1), pooled and concentrated via a 10-kDa (3-kDa for Bid and tBid) Amicon concentrator (Millipore). Protein concentrations were determined from the UV-Vis absorbance of tested samples at 280 nm (Nanodrop ND-1000, *peqLab*), using extinction coefficients as predicted by ProtParam.[103] Purified samples were stored at 4 °C until further use. The SEC-buffer compositions are provided in table 16:

Table 16: SEC-buffers.

VDAC1-variants	**VDAC2**	**minimal porin**	**Bid**	**tBid**
10 mM Tris/HCl, pH 8.0	10 mM Tris/HCl, pH 8.0	25 mM Tris/HCl, pH 7.4	20 mM Tris/HCl, pH 7.4	50 mM HEPES/NaOH, pH 7.5
100 mM NaCl	100 mM NaCl	100 mM NaCl	50 mM NaCl	300 mM NaCl
0.05% LDAO	0.05% LDAO	10% (v/v) glycerol		0.2 mM DTT
		0.05% (v/v) LDAO		1% OG

3.2.7.4 Desalting

The PD Mini Trap G-25 desalting column (*GE Healthcare*) was used both for desalting of purified proteins as well as for the removal of excess of label according to manufacturer's instruction. For several experiments like microscale-thermophoresis or EPR measurements it is necessary to label the proteins. Following site-specific labelling of proteins an excess of label would interfere with further analytical methods. The purification is based on the principle of the size-exclusion chromatography. The column matrix is made of Sephadex™-G25, too small for proteins to enter. Therefore, proteins are eluted very fast, whereas labels diffuse into the pores and elute later.[81]

3.2.8 Precipitation of VDAC-variants

For quantitative analysis of refolding efficiencies, proteins were precipitated. The precipitation of proteins has two major advantages, a) the concentration of the sample is increased and b) agents that interfere with the analytical methods like detergents are removed. In this work, the acetone precipitation was used. A 4-fold excess of acetone was added to the

protein solution and samples were incubated for 1h at -20 °C. Samples were centrifuged (25402 g, 3 min, 4 °C) and pellets were washed with dH_2O and EtOH respectively. The pellets were dried at 37 °C and resuspended in SDS-sample buffer for further analysis.

3.2.9 Labelling of mVDAC1-variants

For analytical methods like microscale-thermophoresis or EPR measurements mVDAC1-variants were labelled at specific sites. The labelling methods were aiming for the reactive thiol groups of cysteines whether with iodoacetamides, maleimides or activated thiols as reaction partners.
The challenges in every protein labelling steps are a) to achieve quantitative labelling of all available cysteines and b) to preserve the native fold and function of the protein of interest.

3.2.9.1 Labelling of mVDAC-variants for microscale-thermophoresis

mVDAC1, Δ1-11-mVDAC1-K12C, Δ1-25-mVDAC1-L26C and mVDAC2 were labelled using Alexa Fluor® 532 C5-maleimide (*Invitrogen*). 1 mM TCEP (*AppliChem*) was added to 100 µM protein solution and the sample was incubated for 30 min at 10°C. After incubation 1 mM label (c_{end}) was added and the solution was incubated over night at 10°C and 350 rpm in a Thermomixer (*Eppendorf*). Excess of label were removed (see chapter 3.2.7.3) and protein concentration as well as label efficiency were determined using a Nanodrop ND-1000 spectrophotometer (*peqLab*). The label efficiency was calculated using the following equation.

$$\frac{A_x}{\varepsilon} \cdot \frac{molecular\ mass\ of\ protein}{mg\ of\ protein/mL} = \frac{\text{moles of dye}}{\text{moles of label}}$$

(Eq 4)

A_x = absorbance value of the dye at absorption maximum wavelength (here 532 nm)
ε = molar extinction coefficient of dye at absorption maximum wavelength (here 81.000 $L \cdot mol^{-1} \cdot cm^{-1}$

3.2.9.2 Labelling of mVDAC-variants for EPR measurements

Electron-pulse-resonance measurements are based on the repulsion of unpaired electrons. For this unpaired electrons must be available in the protein. Cysteine site-specific spin-labels were introduced to mVDAC1-variants because of the lack of unpaired electrons. For this the spin label (1-oxyl-2,2,5,5,-tetramethylpyrroline-3-methyl)methanethiosulfate (MTSSL) (*Enzo life science*) was used. 10 mM DTT was added to 300 µM protein solution and the sample was incubated overnight at 10°C. Following the overnight incubation, DTT was removed from the solution, to prevent rapid loss of the MTSSL-label by extensive washing (five buffer exchanges) using a 10-kDa Amicon concentrator (*Millipore*). The protein-solution was diluted to 5 mL with SEC-buffer (10 mM Tris/HCl (pH 8.0), 100 mM NaCl 0.05% LDAO) and concentrated to ca. 300 µL. This was repeated four times. After removal of the DTT, 1 mM label (c_{end}) was added and the solution was incubated overnight at 10°C and 350 rpm in a thermomixer (*Eppendorf*). Excess label was removed (see chapter 3.2.7.3) and protein concentration was determined using a Nanodrop ND-1000 (*peqLab*). The labelling efficiency was qualitatively analysed using an iodoacetamide-dansyl label (Figure 12). The iodoacetamide-dansyl label was kindly provided by Menekse Cebi and Boris Hirsch (working group of Prof. Koert, University of Marburg). Dansyl is a fluorescent molecule and the emitted light can therefore be detected under UV illumination (λ = 254 nm). In this thesis the iodoacetamide-dansyl label was used to analyse the label efficiency of the EPR label in a qualitative manner.

1 mM of iodoacetamide-dansyl label was added to 10 µL of labelled and unlabelled protein solution and incubated for 2h at 10°C. The sample was mixed with 5 µL SDS-sample buffer and analysed on an 12% SDS-PAGE (section 3.3.1). Before staining, the SDS-PAGE was exposed under UV light (λ = 365 nm) to determine binding of the dansyl label.

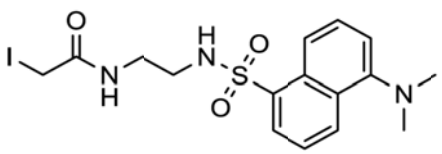

Figure 12: Iodoacetamide-dansyl label.

3.2.10 Oxidation and reduction of mVDAC1-variants

For effective induction of disulphide cross-linking in mVDAC1 variants, purified proteins were treated with 100 mM copper-phenanthroline (CuX_2Ph).[109] CuX_2Ph was freshly prepared using $CuSO_4$ und 1,10-phenanthroline in a molar ratio of 1 to 3.5 in a DMSO solution. 50 - 100 µL of purified mVDAC1-variants were treated with 1.3 mM CuX_2Ph and incubated for 1h at 10°C. CuX_2Ph reactions were quenched by addition of 5 mM EDTA and incubated for additional 30 min at 10°C. Disulphide bond reduction was mediated by addition of 10 mM DTT followed by an incubation for 1h at 10°C. Excess of oxidative or reductive agents were removed using an Amicon Ultra-0.5 Centrifugal Filter Devices (*Millipore*) after manufacturer's instructions. [84] The presence or absence of disulphide bonds was confirmed independently by non-reducing SDS-PAGE and peptide mass fingerprint spectrometry. The excess of DTT was removed to prevent potential interference of CuX_2Ph or DTT with the subsequently performed assays, treated protein samples were further purified using an Amicon Ultra-0.5 mL Filter Device (*Millipore*) according to the manufacturer's instructions.

3.2.11 Reconstitution into lipid vesicles

For SRCD and SROCD measurements, reconstitution of refolded and purified mVDAC1 and EMP into DMPC liposomes was necessary. The reconstitution was performed after an adaption of the Klamm et al 2007 and Neves et al 2009 protocols.

For SRCD or SROCD measurements the removal of all interfering agents like Cl^- or non-aliphatic detergents from purified porins was essential. As described in 3.2.7.3 mVDAC1 was desalted using a variation of refolding buffer II (25 mM NaH_2PO_4/Na_2HPO_4, pH 7.0, 10 mM NaF, 0.05% (v/v) LDAO). The CHAPSO:DMPC bicelles were prepared in a molar ratio of 1:2.8 mM as previously described. [22] 100 µL of desalted protein was reconstituted in 1 mM CHAPSO:DMPC bicelles and incubated once for 1h at 30 °C and once overnight at 10 °C. Excess of detergent was removed using biobeads as previously described. [110, 111] 750 mg of biobeads were washed once with 10 mL methanol, trice with water and twice with 25 mM NaH_2PO_4/Na_2HPO_4, pH 7.0, 10 mM NaF. 1 mL of washed biobeads were incubated for 30 min at room temperature with 100 µL lipid suspension. 1 part of mVDAC1 in bicelles was added to 10 parts of biobeads and incubated overnight at 30°C or 10°C. The supernatant was transferred to fresh, lipid-saturated biobeads and again incubated for 6 h at 30 °C or 10 °C.

The supernatant was centrifuged (25402 g, 2h) and protein-containing liposomes were carefully resuspended.

Purified EMP was reconstituted into DMPC liposomes following previously established protocols by Dr Georgios Psakis. [110, 111] As described before, preformed liposomes (50 mg/ml) were mixed with the refolded minimal porin at a molar ratio of 2000:1 and incubated at 30 °C for 2 h. Detergent was removed with washed lipid saturated biobeads in 25 mM NaP_i pH 7.4, 25 mM NaCl, 10% (v/v) glycerol. Biobeads were mixed with the protein bicelles in a ratio of 100:1 and the absorbance of detergents was performed overnight at 30 °C. For identification and quantification of lipid in the proteoliposomes, and for confirmation of complete detergent removal, thin layer chromatography was performed as previously described. [112]

3.3 Protein analytics

3.3.1 Sodium dodecylsulfate-polyacrylamide gel electrophoresis (SDS-PAGE)

The sodium dodecylsulfate-polyacrylamide gel electrophoresis (SDS-PAGE) was used to identify proteins, control the purity, asses refolding efficiencies and assess labelling/crosslinking. The method was described by *Laemmli et al.* 1970.[113] The gels were stained using either Coomassie Brilliant Blue (R) or silver staining. All analysed proteins were applied to SDS-PAGES containing whether 12% or 16% acrylamide in the separation gel. The electrophoreses were performed at 30 mA per gel and constant voltage for 45 minutes in SDS running buffer (25 mM Tris, 0.2 M glycine, 0.1% (w/v) SDS) using a Mighty Small II (*Hoefer Inc.*, Holliston, MA, USA) or a PerfectBlue Twin M device (*peqlab Biotechnologie GmbH*, Erlangen). The mixture of the gels is described in table 17.

Coomassie Brilliant Blue (R) staining was performed in SDS-PAGE staining solution (section 2.4.3.2 table 13) and the background was destained using SDS-PAGE destaining solution (section 2.4.3.2 Table 13).

If the protein concentration was too low to identify single protein bands on the Coomassie Brilliant Blue (R) stained gel, a silver staining was performed as described previously.[114] In

short, a Coomassie Brilliant Blue (R) stained SDS-PAGE was destained completely using destaining solution (section 2.4.3.2 table 13) and incubated overnight in dH_2O. The gels were sensitized for 2 min using sensitizer (0.02% (w/v) $Na_2S_2O_3$). Following, the gels were washed trice in dH_2O for 5 min and the gels were stained for 20 min in silver solution (0.2 % (w/v) $AgNO_3$, 0.076% (v/v) formalin). The gels were again washed twice for 1 min in dH_2O and developed (6% (w/v) Na_2CO_3, 0.05% (v/v) formalin, 0.0004% (w/v) $Na_2S_2O_3$) until brownish protein bands became visible. The staining reaction was stopped (50% (v/v) MeOH, 12% (v/v) HOAc) for 5 min. The gel could be stored at 4 °C in 1% HAc.

Table 17: Components of SDS-PAGE gels.

Component	12% separation gel (60 mL)	4% stacking gel (25 mL)
30% acrylamide solution	24 mL	3,33 mL
10% SDS solution	600 µL	250 µL
dH_2O	15,18 mL	16,43 mL
SDS resolving gel buffer	20 mL	-
SDS stacking gel buffer	-	5 mL
TEMED	60 µL	250 µL
30% APS	300 µL	25 µL

Beside the denaturing SDS-PAGE for a quick and simple protein analysis a blue native PAGE (BN-PAGE) was used for the determination of protein complexes.[115] BN-PAGES are non-invasive and therefore protein-complexes can be detected as intact complexes whereas a SDS-PAGE separates the components. The mixture of BN-gels is described in table 18.

Table 18: Components of BN-PAGE gels.

Component	Volume
10 x BN-running buffer	6 mL
Acrylamide solution 30%	20 mL
EGTA solution 0.2 M	60 µL
APS solution 30%	300 µL
TEMED	40 µL
Water	60 mL

3.3.2 Peptide mass fingerprinting

For the identification of protein as well as free cysteines and disulphide-bridges oxidized or reduced samples were analysed using the peptide mass fingerprint method. [116, 117] This method was performed following the tryptic digestion of target proteins, to allow detection of certain protein fragments by ESI-mass spectrometry. To cap free cysteines 2-iodoacetamide (*Applichem*) was added in a final concentration of 1 mM to the mVDAC1 samples and stirred over night at 8 °C. To remove free 2-iodo-acetamide the protein was precipitated as described in chapter 3.2.8. Pellets (341 µg each) were dried at 37 °C. Further digestion and analyses were done by Dr Uwe Linne and Natalia Fritzler of the mass-spectrometry unit of the Philipps University Marburg. The dried pellets were dissolved in 100 µL 10% acetonitrile and digested over night at 37 °C with 10 µg sequencing grade trypsin (*Promega*) containing 25 µL 50 mM NH_4HCO_3 buffer at pH 8.0. For chromatographic separation of the tryptic peptides an 1100 Agilent HPLC system was used with a 150x3 mm Kinetex 2.6 µm C18 column (*Phenomenex*) at a temperature of 40 °C and a flow rate of 0.2 mL/min. UV-detection of the peptides was carried out at 215 nm. The following gradient of water (solvent A) and acetonitrile (solvent B) each containing 0.1% TFA was applied: 5% B for 10 minutes, linear increase to 60% B within 150 minutes, linear increase to 90% B in additional 5 minutes and then holding B at 90% for 10 minutes. Mass spectrometric detection of the peptides was done by online electrospray-ionisation-mass spectrometry (ESI-MS) with an LTQ-FT mass spectrometer (*ThermoScientific*). An FTMS scan was carried out in the mass range of 400-2000 m/z, followed by three automated ion trap MS/MS scans.[118] The disulphide-bridged peptides were identified from comparisons of predicted and actual masses.

3.3.5 Protein concentration using bicinchoninic acid assay (BCA)

The concentration of liposome-containing samples or labelled proteins was determined using the BC-assay (*Uptima* by *Interchim*). The protein concentration is determined via a copper (I) protein complex build by an *in situ* Biuret reaction with bicinchoninic acid.[119] The BC-assay is compatible with detergents and lipids and was therefore used for the analyses of membrane proteins.[120]

1000 µL of reagent A was mixed with 20 µL of reagent B and 50 µL protein solution. As reference a sample with 50 µL buffer instead of protein solution was added. Both samples were incubated for 30 min at 37 °C. If the protein concentration was too low the incubation

temperature was raised to 60 °C according to manufacturer's instructions. The absorbance was measured at 562 nm (Ultrospec 3100pro UV Visible Spectrometer, *GE Healthcare*) and the concentration could be determined using a calibration curve. From the calibration the following equation could be calculated and were used for all BC-assay determined protein concentrations.

$$c = \frac{A - 0.01353}{0.00102} \cdot \frac{1}{1000} \cdot dilution \left[\frac{mg}{mL}\right]$$

(Eq 5)

3.3.6 Single channel conductance recordings

Single channel conductance recordings were performed using the Black Lipid Membrane (BLM) technique. [57, 121-125] This technique is based on the measurement of current (pA) when a certain voltage (mV) is applied. The chamber for BLM-measurements comprises two compartments (polystyrene cuvette: CP2A, bilayer chamber: BCH-22A, *Warner Instruments*) separated with a small 200 µm circular hole. The chambers are filled with suitable buffer and a lipid bilayer is painted over the hole. Upon reconstitution of membrane proteins into the lipid bilayer, a current can be detected after voltage is applied by two Ag/AgCl electrodes (Figure 13).The membrane proteins are acting as Ohmic resistance and therefore their conductivity can be calculated using an Ohm Plot.

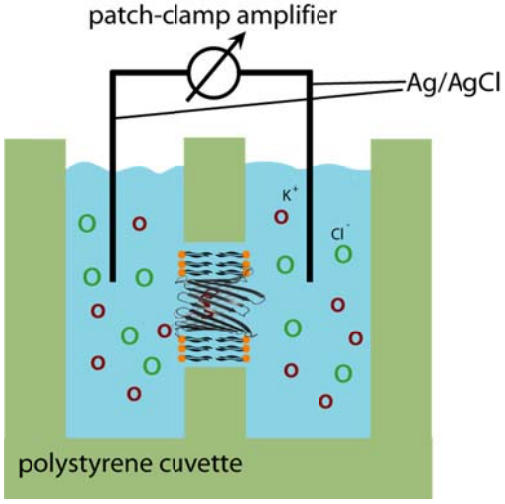

Figure 13: Schematic view of a chamber for BLM measurements, the chamber (green) comprises two compartments separated by a 200 µm hole. A lipid bilayer (headgroups of the lipids are shown in orange, lipophilic tails are shown in grey) is painted over the hole. Both compartments are filled with ion containing solution (*e.g.* K^+, red circles and Cl^-, orange circles). The refolded membrane protein incorporates into the bilayer (*e.g.* mVDAC1, structure shown as cartoon) and by application of voltages using the Ag/AgCl electrodes the corresponding conductance is recorded.

BLM measurements were performed in 1,2-diphytanoyl-*sn*-glycero-3-phosphocholine (DPhPC) and asolectin (*Avanti polar lipids*) as described previously. [57, 59, 99, 126] A sample of *n*-decane-solubilised diphytanoyl phosphatidylcholine membrane mixture (25 mg/mL) was painted over a 200 µm circular hole, separating the chamber compartments equally filled with BLM buffer (10 mM Tris/HCl, pH 7.4, 1 M KCl, 5 mM $CaCl_2$ for mVDAC1-variants and mVDAC2, 10 mM Tris/HCl, pH 7.4, 1 M NaCl, or 10 mM sodium acetate/acetic acid, pH 5.0, 1 M NaCl for the minimal porin). Protein (7.5-15 µg) was added to one compartment next to the planar lipid layer and a voltage-gradient was imposed across the membrane whilst waiting for insertion of single channels. Voltages in a range of up to ±80 mV were applied and electric current was recorded using a Multipatch 700B patch-clamp amplifier connected to a Digidata 1440A A/D converter. Current traces were analysed using the Clampex 10.2 software (*Axon Instruments*), from a data collection frequency of 5 kHz and a sampling rate of 200 Hz; conductances are given ± SEM. Only traces with a spontaneous insertion of up to 5 channels were analysed. For each measurement, high and low conductance states were defined relative to a clear baseline, and their corresponding differences to the baseline were evaluated by the software. Linear regressions and 2D event distribution plots for the +80 mV traces were calculated by Origin 7 (*Origin Lab*). Open probabilities as well as dwell times were defined as the time the analysed porin remains in the open state (> 90% of I_0) divided by

the total recording time. BLM measurements and first analyses were done by Dr Philipp Reiss (Group of Prof Koert, University of Marburg).

3.3.7 ThermoFluor assay

The ThermoFluor assay is a quick and easy method to determine the thermal stability of proteins. It can be used as an alternative to CD-measurements when analysing the melting temperature of a protein or protein-protein/-ligand complex.[127] ThermoFluor assays have the main advantage that optically active samples such as detergents and liposomes do not interfere with this method compared to CD.[128] The method is based on the binding of a fluorophor dye (SYPRO Orange) to the hydrophobic patches of the protein resulting in a fluorescent signal. Upon unfolding, the protein is presenting more hydrophobic patches and the dye will therefore bind to the newly accessible patches. As a consequence the fluorescence will increase. The measurements were done in a Rotor-Gene Q (*Qiagen*) and data were analysed using Rotor-Gene Q series High-resolution melting analysis (HRM) software (*Qiagen*). The analysis of the melting curves includes the subtraction of the background (buffer + dye) and signal integration, with the inflection point representing the sample´s melting temperature (Tm).
0.6 mg/ml of purified mVDAC1 was mixed with Bid / tBid in a molar ratio of 0.5 to 2. 5 µL SYPRO Orange 5000 (*life technologies*, # S-6650) was added to detect the fluorescence change during melting. Melting curve analysis was performed in a Rotor-Gene Q (*Qiagen*). Fluorescence was detected at 510 ± 5 nm and data were analysed using Rotor-Gene Q series High-resolution melting analysis (HRM) software (*Qiagen*). By comparing the different melting curves with and without the effector-protein Bid/tBid the complex stability could be inferred.

3.3.8 Thermophoresis

A temperature gradient in aqueous solution can induce a flow of molecules depending on their mass. This effect is also known as Ludwig-Sorret effect or thermophoresis.[129] It is argued that thermophoresis is a local non-equilibrium effect depending on fluid dynamics, force fields and particle solvent potentials. There is a great influence of the solvent-particle interface and particle charge to describe the thermophoretic effect. Although the effect is not

fully understood, thermophoresis can be phenomenologically explained by the linear drift response.[130] According to this, the molecule velocity (v) is linearly dependent on the temperature gradient (gradT) with a proportionality constant D_T (thermal diffusion coefficient or thermophoretic mobility).[131]

$$v = -D_T gradT$$

(Eq 6)

The velocity is dependent on the particle concentration as well as on diffusion constants for every particle in solution. To overcome dependency on concentrations, microscale thermophoresis is done at a nanomolar scale. The diffusion coefficients (D) depend on solvent interaction and therefore the whole thermophoretic assay is influenced by protein solvent interaction as described by the Sorret coefficient S_T.

$$S_T = {}^{D_T}/_{D}$$

(Eq 7)

In general the Sorret coefficient depends on the molecule size, it´s charge and the interaction with solvents. If one of these parameters is changed, the thermophoretic migration is altered.
In terms of experiments, thermophoresis detects the thermophoretic migration of labelled proteins in a temperature gradient hypothesizing that protein and protein complexes are migrating differently due to their size.[132, 133] In theory larger proteins and protein-complexes should migrate slower whereas smaller proteins or protein-complexes should migrate faster in a temperature gradient. [2] Using this, binding assays were performed to determine dissociation constants (K_D-values). The experimental setup consists of an infrared laser coupled into the path of fluorescence excitation/emission. Upon a measurement, the laser heats a small spot of the capillary where the fluorescently labelled analyte is present. The analyte is migrating in the thermal field depending on its Sorret coefficient. A schematic view of the microscale thermophoresis (MST) is provided in Figure 14.

[2] This is the most prevalent case, known as positive thermophoretic effect.

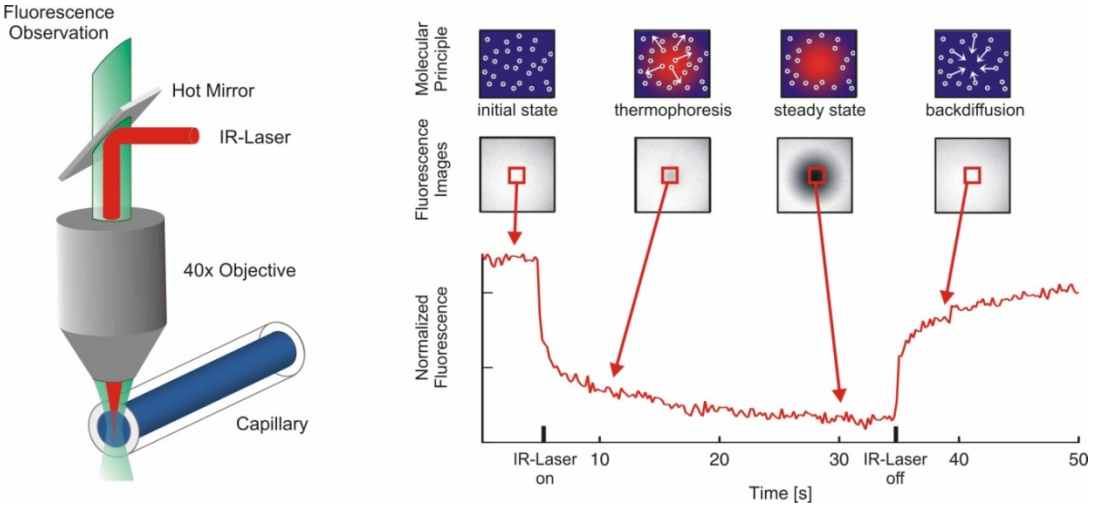

Figure 14:[131] (A) MST is measured in a capillary, upon laser irradiation the change of the fluorescence is measured through the same optical element (B) typical MST signal for one capillary. After laser (30s) irradiation the fluorescence signal drops (detected as thermophoresis). After the steady state region is reached the laser is turned off and backdiffusion as driven by mass diffusion can be detected.

mVDAC1-variants and mVDAC2 were labelled using Alexa Fluor® 532 C5-maleimide (*Invitrogen*) and excess of label was removed by a PD Mini Trap G-25 desalting column (*GE Healthcare*). Protein concentration and label efficiency were measured at 280 nm and 532 nm by a Nanodrop ND-1000 (*peqLab*) spectrophotometer. Thermophoresis measurements were performed using the Monolith NT.115 instrument (*Nano Temper*). mVDAC1-variants and mVDAC2 concentrations were kept constant at 50 nM and Bid/tBid were added to the solution ranging from 15 nM to 500 µM. The protein solution was incubated in the dark for 20 min at room temperature and centrifuged (25402 g, 5 min) to remove precipitated proteins. Capillaries (standard grade, *Nano Temper*) were filled with 8-10 µL of the protein solution and MST curves were recorded. K_D values were calculated using the NT-Analysis software.

3.3.9 Circular dichroism spectroscopy

Circular dichroism (CD) spectroscopy is an optical method to analyse secondary structure elements. It is based on the absorption of circular-polarized light by chiral molecules. Chiral molecules are absorbing left and right polarized light in a different manner and therefore the difference in these absorbance characteristics is generating a CD signal which can subsequently be detected.[134] A schematic view of a CD-spectroscopic instrument is shown in Figure 15.

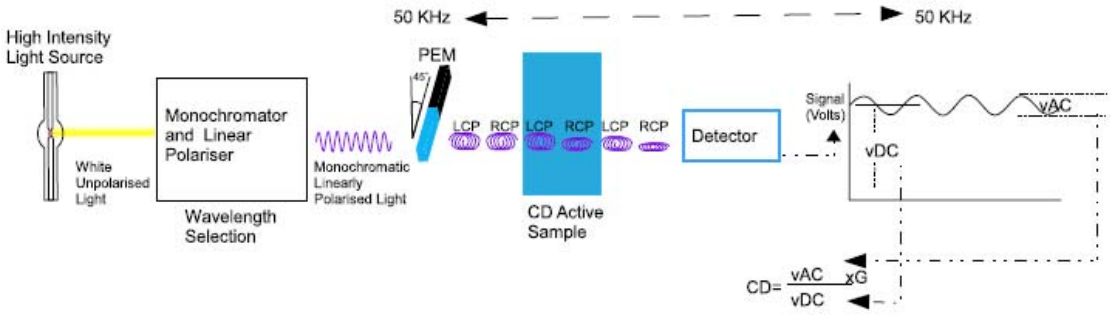

Figure 15: schematic view of a CD-spectroscopic instrument, the white unpolarised light from a high intensity light source is linear polarised by a monochromator. The monochromatic linear polarised light is transformed to left (LCP) and right (RCP) circular polarised light by the photo-elastic modulator (PEM). The absorbance of an optically active sample (blue square) is measured by a detector as average light intensity over time. The CD signal is calculated by the division of vAC through vDC to give units of millidegress of Δabsorbance. Plotting CD signals vs. wavelengths result in the CD spectrum. [135]

The characteristic spectrum of the CD measurements is achieved by plotting the CD-signals against the wavelength. Not only simple chiral molecules cause a CD-signal as secondary structures of proteins show distinct polarized-light-interactions that can be analysed with this method as well. The secondary structures of proteins, like α-helix and β-sheets as well as random coils, show distinct CD-spectral signatures. Therefore the overall secondary structure of a protein or the change of secondary structure upon effector binding can be calculated on the basis of a CD spectrogram.

The quality of a CD-spectrum depends on the quality of the sample. Interfering agents, such as optically active detergents or light scattering agents like liposomes can´t be used during normal CD-measurements. For this purpose another method of CD spectroscopy was developed. The light source, in conventional CD devices, is a wolfram lamp, enabling good emission in the near UV (260 – 320 nm) but inadequate emission in the far UV regions (170 – 260 nm). To overcome the unwanted interference with buffer components as well as providing better data for the far UV region a synchrotron light source was used. A synchrotron source with its higher light intensity has the main advantage that lipids do not interfere with the absorption pattern and that much smaller protein concentrations and volumes can be used. Another analytical technique based on CD-spectroscopy was used at the ANKA source of the Karlsruher Institute for Technology (KIT), oriented CD spectroscopy that offers an additional analytical method for membrane proteins. With this method it is

possible not only to analyse secondary structures but determine the orientation of theses structural elements relative to the membrane-normal. This provides information on how a membrane protein is oriented in the membrane plane and whether it´s structure is changing upon effector binding.

Beside pure structural analysis the stability and dynamics of proteins can be detected by melting curve analysis. During a melting curve analysis the measured ellipticity is plotted against the temperature giving information about the denaturation and spontaneous refolding during the heating and cooling circles. As ellipticity depends on the proteins structure the stability of proteins as indicated by the melting point can be calculated.[136] In this work CD measurements were done using a conventional J-810 or J-815 spectropolarimeter (*Jasco*) or the CD12-beamline at the ANKA synchrotron source of KIT.

CD studies on refolded and purified EMP were done by Dr Georgios Psakis using a J-810 or J-815 spectropolarimeter (*Jasco*) as previously described (Psakis et al 2009, Windisch et al 2010). Protein samples in LDAO micelles were analysed at 20 °C and spectra of samples in DMPC were recorded above (35 °C) and below (20 °C) the phase transition temperature of DMPC (23 °C). Scans were collected in a 1 mm quartz cell (110-QS, *Hellma*), at a speed of 10 nm/min, 8 s response time, and 1 nm bandwidth. Thermal denaturation was followed at the corresponding CD minima and the temperature was varied by 0.5 °C/min from 10 °C to 95 °C. CD spectra were collected at 20 °C before heating and after cooling. Averaged spectra (three accumulations) were smoothed by the adaptive smoothing algorithm (*Jasco*). The concentration of the samples was determined either by UV-Vis measurements at 280 nm (NanoDrop ND-1000, *PEQLAB*) or by the bicinchoninic acid assay (BCA).
CD–studies on mVDAC1-variants in liposomes were performed at the CD12 beamline of the ANKA synchrotron. To detect a structural rearrangement of mVDAC1 in liposomes upon tBid binding both proteins were measured alone as well as the protein-protein complex in molar ratios of 1:1 and 1:2. From the separate measurements a combined CD curve could be calculated. By comparison of the calculated and measured protein-protein CD spectra a qualitative statement about the structural state was made. Scans were collected between two quartz-glass slides with a pathlength of 0.012 mm from 270-170 nm in 0.5 nm steps and a dwell time of 1500 ms.
Secondary structure predictions of the analysed protein samples were performed using the CONTIN-LL [137, 138] algorithm of the DICHROWEB server [139-141] with the reference set

SP175.[142, 143] Confident predictions showed a normalized-root-mean-square deviation (NRMSD) of <0.1 for the comparison of experimental and back-calculated data. [139]
For OCD studies of mVDAC1-variants and the minimal porin a 50-100 µl aliquot of the lipoprotein sample (maximum 0.2 mg lipid in 10 mM KP_i, pH 7.4) was deposited on a quartz glass plate with a 20 mm diameter. The sample was dried at room temperature under a gentle stream of air, leaving a circular spot of ~12 mm diameter. Following the assembly of the OCD cell, samples were subsequently hydrated at the desired temperature for 15 hours, by using a saturated K_2SO_4 solution, until their relative humidity was between 97-99%.[144, 145] For reduction of artefacts, three spectra were recorded for every 45° rotation of the cell around the beam axis using the same acquisition parameters as for normal CD measurements.[145, 146] Baseline subtraction used the average of eight spectra from empty liposomes. Secondary structure predictions from the DMPC reconstituted samples were performed as described above.

3.3.10 Electron pulsed resonance (EPR) spectroscopy

EPR spectroscopy of site-directed spin-labelled proteins is a useful technique to study structural and conformational dynamics of protein and protein complexes. This technique is very useful in terms of membrane proteins, as lipids and detergents are not interfering with the EPR-signal.[147] The spin label (often a paramagnetic nitroxide group) can be introduced by various ways. The most common one is the labelling of sulfhydryl-groups of free cysteines. The cysteines can be introduced in recombinant proteins by site-directed mutagenesis. There are two different EPR methods to obtain structural and conformational dynamics information, a) the continuous wave (*cw*) and b) the pulsed EPR (DEER) techniques. These two methods differ by their ability to detect inter-spin-spin distances. The *cw* method is able to analyse distances up to 2 nm whereas in pulsed EPR distances up to 8 nm can be determined. *cw* measurements yield information about the nitroxide chain mobility, solvent accessibility and the polarity of the direct environment of the label. In addition the distances between the nitroxide and another paramagnetic residues can be detected.[148]
EPR sensitivity is limited due to the reorientational motion of the nitroxide side chain. The motion as well as the dynamics of the nitroxide incorporated into a protein is characterized by three correlation times, a) the rotational correlation time for the whole protein, b) the effective correlation time of the rotational isomerization of the label and c) the effective correlation

time for the segmental motion of the backbone. All these motions can be described using the Stokes-Einstein equation:

$$\tau_R = \frac{\eta V}{k_B T} = \frac{\eta}{k_B T} \cdot \frac{\bar{V} M}{N_A}$$

(Eq 8)

η = viscosity of the solution

k_B = Boltzmann constant

T = absolute temperature

V = volume of the protein

$\overline{V}$ = the partial specific volume of the protein

M = molecular mass of the protein

N_A = Avogadro constant

This parameter is crucial for the spectral line width and therefore for the sensitivity of the EPR spectrum itself. A second semi-empiric parameter connected to the spectral line width and therefore responsible for the sensitivity is the spectral breadth, represented by the second moment $\langle H^2 \rangle$:

$$\langle H^2 \rangle = \frac{\int (B - \langle H \rangle)^2 S(B) dB}{\int S(B) dB}$$

(Eq 9)

$\langle H^2 \rangle$ is defined by the mean geometrical centre of the spectrum (first moment) $\langle H \rangle$:

$$\langle H \rangle = \frac{\int B\, S(B) dB}{\int S(B) dB}$$

(Eq 10)

B = magnetic field

S(B) = absorption spectrum of the spin-labelled protein

The numeric values of the second moment increase, if the reorientational motion of the nitroxide label is reduced by either sterical hindering after structural rearrangement or by overall changes in the hydrophobic environment of the label.

Another EPR method is the determination of interspin-distances between two spin labels or one spin label and a paramagnetic centre in the protein. In this work interspin-distance-measurements upon two spin labels were performed. The spin-spin interaction is composed of the static dipolar interaction, the modulation of the dipolar interaction by the protein residues and exchange interactions. The distance of two nitroxides can be found as a statistical distribution due to their mobility. Simulations of spin-spin distances can be performed using the EPR simulation program DIPFIT.[149, 150] The upper limit is as already mentioned up to 8 nm due to the pulsed EPR technique. The lower limit is about 0.8 nm due to the increasing modes of exchange interaction by the two overlapping π-orbitals of the nitroxide. For a quantitative analysis of interspin distances the differences between the two second moments of the singly- and doubly- labelled protein can be calculated by the following formula.

$$\langle \Delta H^2 \rangle = \frac{\int (B - \langle H \rangle)^2 S_D(B) dB}{\int S_D(B) dB} - \frac{\int (B - \langle H \rangle)^2 S_S(B) dB}{\int S_S(B) dB}$$

(Eq 11)

S_D = absorption spectrum of the doubly-labelled protein

S_D = absorption spectrum of the singly-labelled protein

Using this equation, the analysis of interspin exchanges is independent of exchange interactions and therefore less sensitive towards incomplete labelling. Using two radical pairs equation 12 yields the interspin distance r.

$$r = 2.32 \, \langle \Delta H^2 \cdot 10^8 \rangle^{-1/6} \, nm$$

(Eq 12)

The spin labelling was done with the (1-oxyl-2,2,5,5,-tetratmethylpyrroline-3-methyl)methanethiosulfate (MTSSL).[151] This label is suitable for EPR analysis because the flexible chain of the label is not interfering with the protein structure and the size resembles a tryptophan residue. Nevertheless it has to be checked whether the protein characteristics and the overall fold are not affected by incorporation of the label. For this issue the BLM technic was used and BLM traces of mVDAC1-variants with and without the spin label were compared.

mVDAC1-variants were labelled (see chapter 3.2.9.2) and *cw* and DEER-EPR measurements were performed by Katharina Rudi and Dr Johann Klare (group of Prof Dr Steinhoff, Physics department, University of Osnabrück).

Continuous wave EPR experiments were performed using X-band EPR spectrometers (constructed by the physics department, university of Osnabrück) equipped with an AEG H_{103} rectangular cavity or a dielectric resonator (*Bruker*). The magnetic field was measured with a B-NM 12 B-field meter (*Bruker*). Samples were loaded into EPR quartz capillaries (150 µM). Spectra were recorded with a modulation amplitude of 1.5 G, and microwave power adjusted to between 0.1 and 0.6 mW. A modified Oxford ESR 9 variable temperature accessory allowed stabilization of the sample temperature between 80 and 330K.

DEER measurements were accomplished at X-band frequencies (9.3-9.4 GHz) with a BrukerElexsys 580 spectrometer equipped with a Bruker Flexline split-ring resonator ER 4118XMS3 and a continuous flow helium cryostat ESR900 (Oxford Instruments) controlled by an Oxford Intelligent temperature controller ITC 503S. Measurements were performed using the four-pulse DEER sequence:[152, 153]

$$\pi/2\ (\nu_{obs})\ -\ \tau_1\ -\ \pi\ (\nu_{obs})\ -\ t'\ -\ \pi\ (\nu_{pump})\ -\ (\tau_1 + \tau_2 - t')\ -\ \pi\ (\nu_{obs})\ -\tau_2-\ \text{echo} \qquad \text{(Eq 13)}$$

A two-step phase cycling (+ ⟨x⟩,-⟨x⟩) was performed on $\pi/2$ (ν_{obs}). Time t' is varied, whereas τ_1 and τ_2 are kept constant. The dipolar evolution time is given by $t = t'-\tau_1$. Data were analysed only for $t > 0$. The resonator was overcoupled to $Q \approx 100$; the pump frequency ν_{pump} was set to the centre of the resonator dip and coincided with the maximum of the nitroxide EPR spectrum, whereas the observer frequency ν_{obs} was ~ 65-75 MHz higher, coinciding with the low field local maximum of the spectrum. All measurements were performed at a temperature of 50 K with observer pulse lengths of 16 ns for $\pi/2$ and 32 ns for π pulses and a pump pulse length of 12 ns. Proton modulation was averaged by adding traces at eight different τ_1 values, starting at $\tau_{1,0}$= 200 ns and incrementing by $\Delta\tau_1$ = 8 ns. Data points were collected in 8-ns time steps. The total measurement time for each sample was 24–48 h. Data analysis was performed with the software package DeerAnalysis2013 in the distance range 1.0 – 8.0 nm with a regularization parameter (α) of 100, according to the L-curve criteria.[153]

Inter-spin label distance distributions were simulated using a rotamer library of spin labelled residues as described in Polyhach *et al*., 2011.[154] The rotamer library implemented in the software package MMM2011 consisted of 210 rotamers of MTSSL bound to cysteine, which have been used to replace the native residues at the positions of interest in the RocCOR structural model. Energies and resulting populations for individual rotamers were calculated by means of a Lennard–Jones potential at 175 K (the glass transition temperature for a water–glycerol mixture), and have been used as weights in the simulation of the distance distributions.

3.4 Protein crystallisation

One of the most important methods for determining the 3D structure of proteins is the x-ray diffraction analysis of protein crystals. The diffraction quality of protein crystals is perhaps the most limiting factors during structure determination by X-ray crystallography. The formations of well diffracting crystals depend on various factors like buffers, temperatures, precipitants and additives. To obtain initial crystallization conditions a sparse matrix screening is performed.[155] After initial hits a fine screening is performed to increase size and quality of the obtained crystals.

Especially for membrane proteins, well diffracting crystals are not that easy to obtain. This is due to detergents that cannot be excluded because of the hydrophobic pattern in membrane proteins. To overcome this problem there are various methods for membrane protein crystallisation. In this work crystallisation trials were done with mVDAC1-variants incorporated in bicelles as previously described. [22] Bicelles are discs composed of lipids and detergents and are therefore suitable to increase the protein stability so that a single crystal can be obtained. Another very promising method is the crystallisation in lipidic-cubic-phases (LCP).[156] Here the proteins are incorporated in LCP and single crystals are growing on the surface of the LCP. The disadvantage here is the difficulty in picking and extracting the crystals from the LCP.

The preparation of bicelles was mainly the same as for the incorporation of proteins into liposomes and was conducted as described by Sanders *et al.* [157] 10 mM CHAPSO and 10 mM DMPC were dissolved in dH_2O and mixed in a molar ratio of 1:2.8 mM (CHAPSO:DMPC). The clear bicelles-solution were mixed with four volume parts of refolded and purified protein-solution (c = 10 mg/mL) in SEC-buffer (10 mM Tris/HCl (pH

8.0), 100 mM NaCl, 0.05% LDAO) and incubated overnight at 10°C under mild shaking. The bicelles solution was mixed with nanoparticles and the pipetting to the sparse matrix screen was done by the Digilab Honeybee 963TM (*Zinsser analytic*). Crystals were obtained by vapour-diffusion using the sitting drop method.

Crystallisation trials were performed with mVDAC1 and the oxidized mVDAC1-V3C-K119C- C127A-C232A and mVDAC1-A14C-C127A-S193C-C232A variants. For all three variants a sparse matrix screen as well as a fine screen was performed. Accordingly, 2 mL of the crystallisation solutions were transferred to a 96-deep-well plate for automatically pipetting using the Digilab Honeybee 963^{TM} (*Zinser analytic*). The device pipetted at first 80 µL reservoir into the Innova plates (*Hampton Research*). Following, 300 nL reservoir and 300 nL protein solution were mixed in the wells and the plates were sealed using VIEWseal^{TM} (*Greiner Bio-one*). The plates were stored at either 18°C or 4°C as temperature affect crystal growth. The sparse matrix screens were performed using JCSG core suite I-IV, PACT, JCSG+, Classics, Cryos, MBC I-II AmSO4 and Anions suites (*QIAGEN*). The best hits were obtained using an optimisation screen as provided in table S1 (section 9.5).

4. Results

4.1 Functional characterisation of mVDAC1

Although VDACs were discovered in 1976 a detailed molecular characterisation was missing for the next three decades.[26] Early observations revealed VDACs as voltage responsive ion channels in 1989 by Colombini. He characterized VDAC as voltage dependent ion-channel which exhibits two different states, an open and a closed state.[158] VDAC exerts a weak anion preference in the open ($P(Cl^-)/P(K^+)$: 1.7-1.9) and a strong cation preference in the closed states ($P(K^+)/P(Cl^-)$: 2-8). Further observations showed that VDACs switch between a high conductance state at low voltages and several reduced conductance states at high voltages. A structural explanation for this behaviour was missing. In 2009, one year after the release of VDAC1´s crystal structure, the first model was proposed trying to explain this switching behaviour. In this model, Hiller and Wagner described the N-terminal α-helix located in the middle of the pore to be responsible for the observed switching.[33] The first part of this thesis is dealing with the elucidation of the switching mechanism though the crystal structures, as well as the switching mode, are still under debate. Most of the results shown in this chapter were already published in Mertins, Psakis, Grosse *et al* (2012).[99]

4.1.1 Expression, refolding and purification of mVDAC-variants

In this work all VDAC variants were expressed as inclusion bodies as described in chapter 3.2.2.3. The used method was further optimized from the one used in my diploma thesis.[106] There are two ways to express and purify recombinant membrane proteins: a) produce membrane proteins in the membrane followed by a detergent-mediated extraction and b) or production as denatured proteins in the form of inclusion bodies, which can then be refolded in the presence of detergents or lipids. The expression of VDAC variants as inclusion bodies revealed yields of about 50 – 90 mg protein per litre medium. Refolding procedures of mVDAC1 variants were established before but still needed some optimisation.[106] Accordingly, an optimisation screen was performed to obtain efficient refolding conditions.

At first several detergents were checked in a two-step rapid dilution assay (first step 10 fold CMC and second step 5 fold CMC). The supernatants, where refolded protein is present, were analysed on an SDS-PAGE.

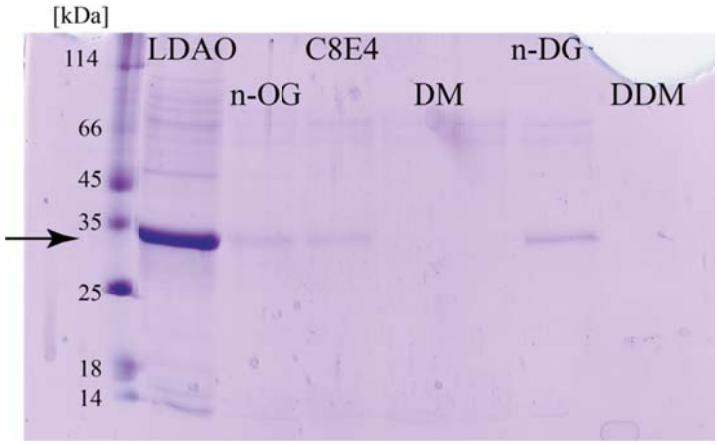

Figure 16: 12% Coomassie-stained SDS-PAGE analysis of the second step of the rapid dilution refolding screen for mVDAC1. LDAO, n-OG, C8E4, DM, n-DG and DDM were tested, the arrow indicates the presence of refolded mVDAC1.

The refolding screen revealed LDAO (first step 2.22% second step 0.1%) as best detergent for the quantitative refolding of mVDAC1. Based on the refolding screen all other protein refoldings were done using 2.22% and 0.1% LDAO respectively in a two-step rapid dilution protocol as described in chapter 3.2.5.2.

In addition, the refolding of membrane proteins can be enhanced by folding aids. [159] Folding aids are small compounds that prevent protein aggregation during refolding since folding intermediates are produced at intermediate denaturant concentrations. The tested folding aids in the presence of 2.22% and 0.1% LDAO respectively in a two-step rapid dilution protocol are described in chapter 3.2.5.1. The protein-containing supernatants were precipitated and analysed on an SDS-PAGE (Figure 17).

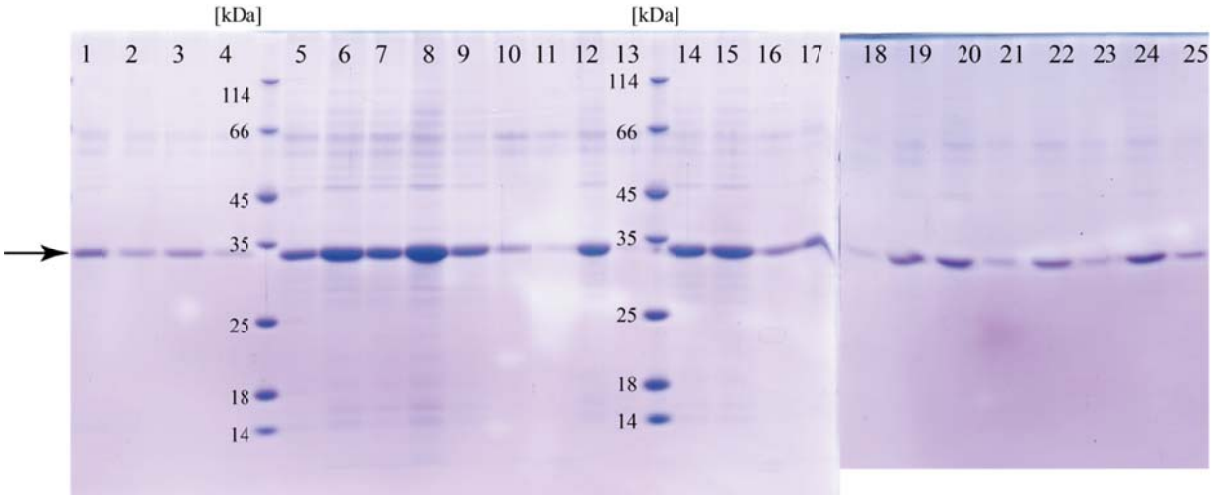

Figure 17: 12% Coomassie-stained SDS-PAGE analysis of the second step of the rapid dilution refolding screen for mVDAC1 with folding aids in the presence of LDAO as detergent, 1-4: mVDAC1 concentration 5 mg/ml; glycerol 5%, 10%, 15% 20%, 5-8: mVDAC1 concentration 10 mg/ml; glycerol 5%, 10%, 15% 20%, 9-13: mVDAC1 concentration 5 mg/ml; sucrose 1 mg/mL, 5 mg/mL, 10 mg/mL, 20 mg/mL, 25 mg/mL, 14-17: mVDAC1 concentration 10 mg/ml; sucrose 1 mg/mL, 5 mg/mL, 10 mg/mL, 20 mg/mL, 18-21: mVDAC1 concentration 5 mg/ml, prolin 10 mM, 100 mM, 500 mM, 1000 mM, 22-25: mVDAC1 concentration 10 mg/ml, prolin 10 mM, 100 mM, 500 mM, 1000 mM, the arrow indicates the presence of refolded mVDAC1

Based on this refolding screen, the presence of 15% glycerol appears to be optimal to prevent aggregation. Most of the refolding experiments of VDAC variants were done without glycerol because of the interference with other analytical experiments.

All VDAC1 variants were purified in two steps, first ion-exchange-chromatography (IEC) followed by a size-exclusion-chromatography (SEC). During IEC the interaction of membrane proteins with the column resin is diminished because of the presence of detergents or lipids. Accordingly, the purification of mVDAC1 variants was established in my diploma thesis using Fractogel-EMD-SE Hicap (M) (*Merck*) with a multisegment gradient of 0-1000 mM NaCl.[106] A representative IEC run and the corresponding SDS-PAGE are shown in Figure 18.

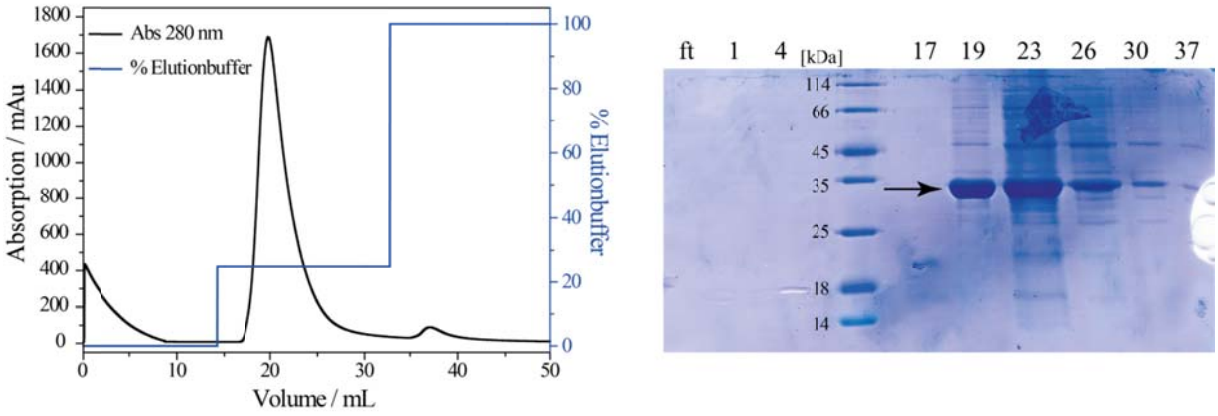

Figure 18: Representative IEC-chromatogram and 12% Coomassie-stained SDS-PAGE analysis of VDAC1-variants, SDS-PAGE lanes correspond to the elution volume (ft = flow through), the arrow marks purified mVDAC1.

Although most of the impurities could be removed during refolding and IEC, a SEC was performed as polishing step, yielding pure VDAC1-protein. In addition SEC verified a monomeric protein fraction. A representative SEC is shown in Figure 19.

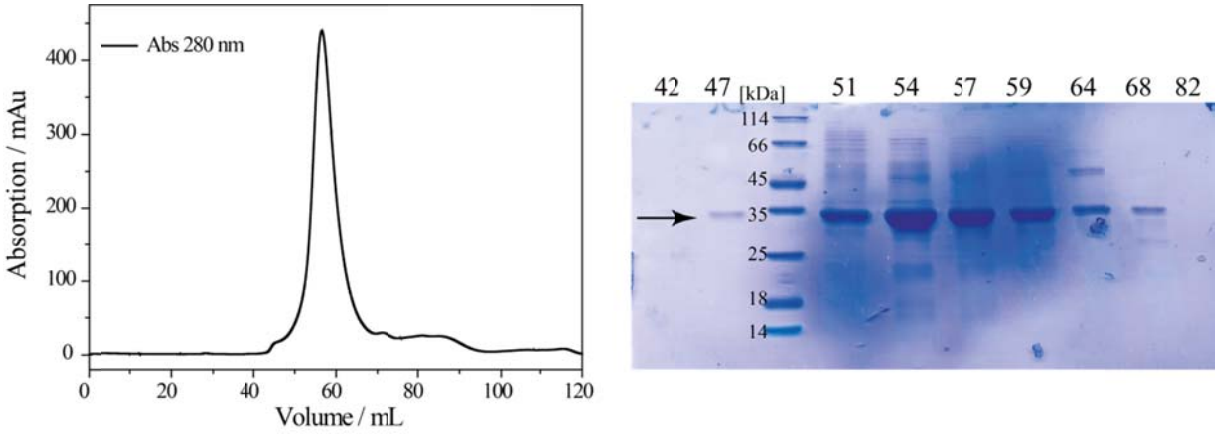

Figure 19: Representative SEC-chromatogram and 12% Coomassie-stained SDS-PAGE analysis of VDAC1-variants, Coomassie stained SDS-PAGE lanes correspond to the elution volume (ft = flow through), the arrow marks purified mVDAC1.

The refolding and purification of mVDAC1 from inclusion bodies yielded 12-18 mg mVDAC1 per litre culture.

For refolding and purification of mVDAC2 a slightly adapted refolding protocol of mVDAC1 was used, where the buffers were changed to pH 6.0 to create the same pH / pI difference as for mVDAC1. Using these conditions, it was possible to refold VDAC2 in comparable, good

yields, 2-5 mg mVDAC2 per litre culture. Interestingly, mVDAC2 failed to bind to the formerly used Fractogel EMD SE Hicap (M) (*Merck*) matrix. Accordingly, the pH was carefully adjusted to pH 8.5 to ensure proper binding to the Fractogel DEAE anion exchanger. Elution was performed using a continuous gradient of 10-1000 mM NaCl in elution buffer. A representative chromatogram of the IEC is shown in Figure 20.

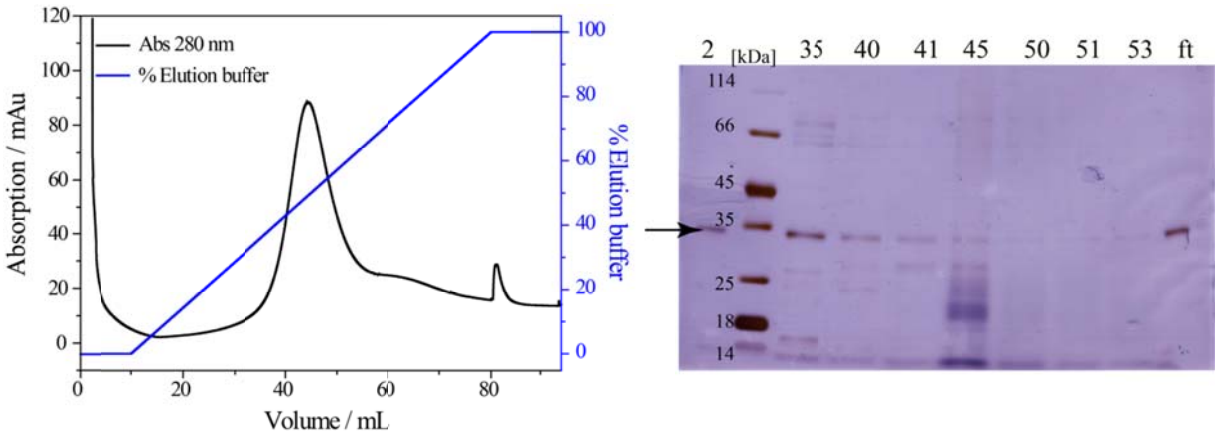

Figure 20: Representative IEC-chromatogram and 12% Coomassie-stained SDS-PAGE analysis of mVDAC2, silver stained SDS-PAGE lanes correspond to the elution volume (ft = flow-through), the arrow marks the presence of mVDAC2.

Although the flow-through indicates that the binding of refolded mVDAC2 to the column was incomplete, the yield of pure mVDAC2 was suitable for functional studies.

As second step for mVDAC2 purification, a SEC was done to separate mVDAC2 from the remaining impurities. The SEC run as well as the SDS-PAGE is shown in Figure 21, proving that refolding and purification of mVDAC2 was successful.

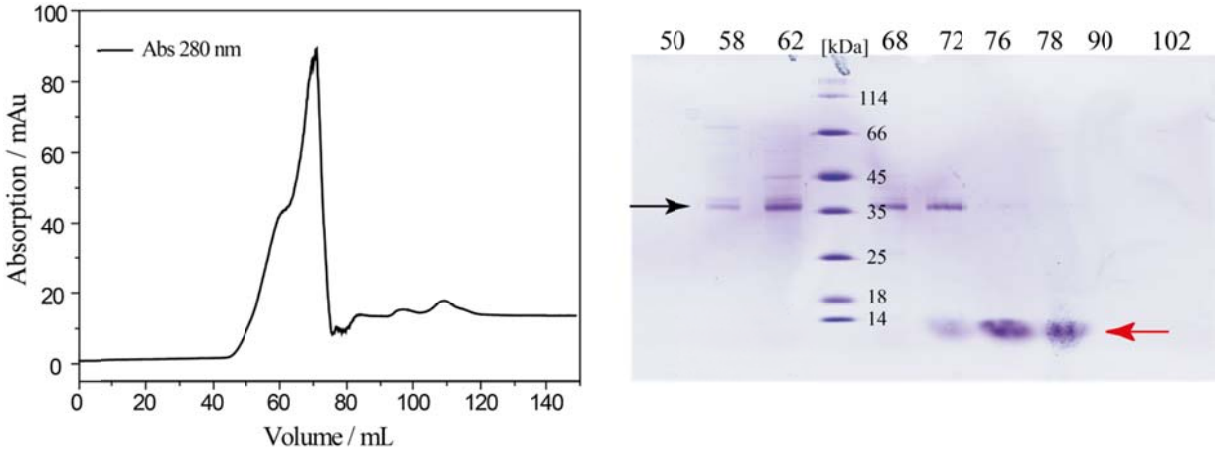

Figure 21: Representative SEC-chromatogram and 12% Coomassie-stained SDS-PAGE analysis of mVDAC2, SDS-PAGE lanes correspond to the elution volume (ft = flow through) the black arrow marks purified mVDAC2, the red arrow marks the separated impurities.

4.1.2 Disulphide link formation in mVDAC1 variants

To get deeper knowledge of the origin of the switching mechanism in mVDAC1 three different variants were engineered for fixing the N-terminal segment to the inner barrel wall. We expected to control the gating behaviour and unravel the role of the N-terminal segment during switching.

Following the successful refolding and purification of mVDAC1 variants containing appropriate paired cysteine mutations at the positions A2-E121, A14-S193 and V3-K119, disulphide-bridge formation was performed in the presence of copper-phenanthroline (CuX_2Ph). Full oxidation and therefore a quantitative disulphide-bridge formation was confirmed by denaturing SDS-PAGE electrophoresis. Hence, mVDAC1-variants with intact disulphide-bridge migrate faster due to their compacter shape compared to the reduced state of double cysteine variants (Figure 22B).

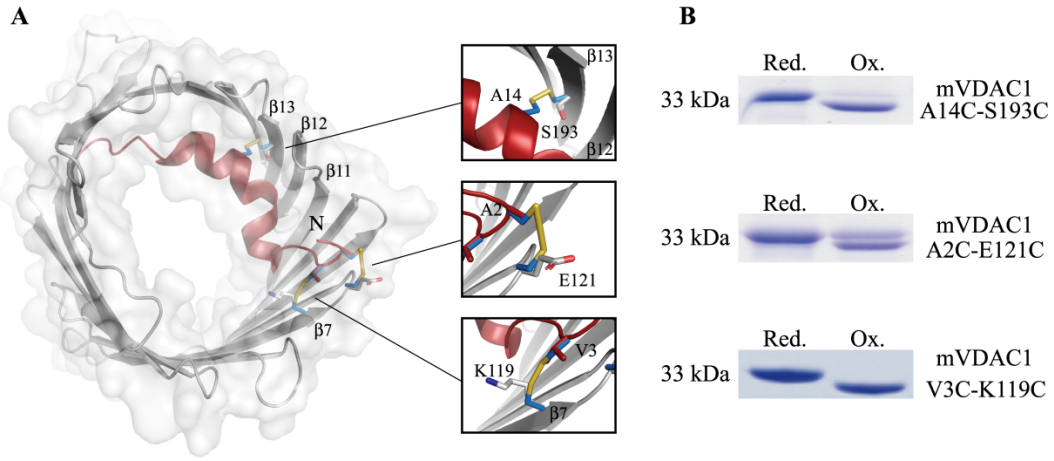

Figure 22: [99] Cysteine mutagenesis on mVDAC1 and cross-linking of the N-terminal segment to the barrel wall. (**A**) Cartoon representation of mVDAC1, based on the 3EMN structure [22], Location of the engineered cysteines and expected formation of disulphide bonds are shown as inlays. (**B**) 12% Coomassie-stained, non-reducing SDS-PAGE analysis of native and engineered mVDAC1 variants.

Due to the disulphide-bond formation complete mVDAC1-CL-V3C-K119C and mVDAC1-CL-A14C-S193C were used for analytical studies whereas the mVDAC1-CL-A2C-E121C variant could not be fully oxidized and was not further used (Figure 22B). For the latter the formation of the disulphide bridge may be structurally disfavoured. To get further proof of the intactness of the mVDAC1-CL-V3C-K119C and mVDAC1-CL-A14C-S193C disulphide bridges, peptide mass fingerprinting was performed. Here the oxidized A14C-S193C variant confirmed quantitative disulphide formation by detection of the S13-R15/T175-Y197 fragment as shown in Figure 23.

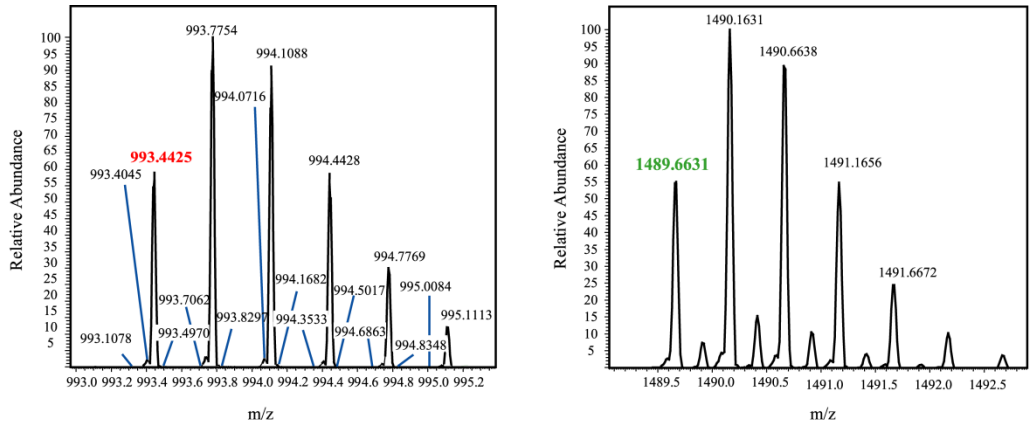

	Amino acids	Peptide	Mass predicted [m/z]	Mass found [m/z]	Mass [Da]
Oxidized Fragment	13-15 175-197	SCR TDEFQLHTNVNDGTEFGGCIQK	M^{3+}: 993.4401 M^{2+}: 1489.6563	**993.4425** **1489.6631**	**2979.33**

Figure 23: [99] MALDI-MS tryptic peptide mass fingerprint of A14C-S193C-mVDAC1. Detected masses for the +3 and +2 ionization states are labelled (red and green) and are compared to the expected masses in the table below. Calculations were performed with the Peptide Mass Calculator v3.2.

The peaks of the obtained chromatograms reveal the ionization profile of two cross-linked fragments for the 993.0-995.4 and 1489-1493 mass range (m/z) of the three- and twicefold ionized state respectively, confirming the quantitative oxidation of this variant. The corresponding fragment of the V3C-K119C variant could not be detected, most likely due to lack of sufficient ionization for ESI-MS analysis.

Having confirmed the cross-linked mVDAC1-variants, functional analyse to elucidate the role of the N-terminal segment during switching could be performed.

4.1.3 Electrophysiological (BLM) measurements of mVDAC1-variants

To get information about the switching mechanism of mVDAC1 it was necessary to characterize at first the behaviour of unmodified mVDAC1. Although many different studies about mVDAC1´s switching characteristics were performed, no study explained in detail the observed behaviour. A high conductance state of ~ 4 nS was accepted to represent the open state (S0), whereas the low conductance state was defined by ~ 50% of the high conductance state. [22, 32, 35, 158, 160-162] By closer inspection of the previous reports the reduced conductance state can be apparently further divided to at least two substates, S1 and S2. Therefore, we

thoroughly characterised the electrophysiological features of mVDAC1 before heading to the next challenge, explaining its gating behaviour.

In our studies, mVDAC1 responds linearly to the application of both positive and negative potentials, alternating between high and low conductance states (Figure 15B). In addition, the switching behaviour was characterized by its dwell times, *i.e.* the times where mVDAC1 stays arrested in one state before switching to another. Dwell times were calculated at an applied voltage of +30 mV and the analysis for the high conductance state (S0) revealed an average dwell time of 10.3 s. The channels´ conductances were determined by analysis of the corresponding Ohm plots (channel currents in response to voltages from -40 to +40 mV. The open state (S0) observed in a total of 680 measurements with a conductance of 3.94 ± 0.04 nS, was consistent with previous reports, whereas the closed state could be assigned to at least two distinct states, unlike most previous reports (Table 24, section 5.1.2.1 Figure 24A). The main question in this case was, whether the two closed states represent just one, as described in literature before, or truly two distinct states. Averaging both closed states resulted in a conductance of 2.34 ± 0.06 nS, significantly different to previously determined values (Table 24, section 5.1.2.1). By fitting the distribution of the low conductance states to a sum of two Gaussians (Figure 24A) we confirmed the existence of the two closed states, S1 (66% of the open S0 state) and S2 (48% of the S0 state) (Figure 24A). Furthermore, it appears that the S2 state (0.8-2.2 nS) can be further subdivided to two additional substates (S2A and S2B) as proven by an additional double Gaussian fit (Figure 24A). Hence, the conductance of the closed conformation seems to be composed of at least three separate, low conducting states, S1, S2A and S2B (Table 19). This observation was strengthened by T-test analyses confirming a statistically significant difference between the observed states ($P = 10^{-4}$).

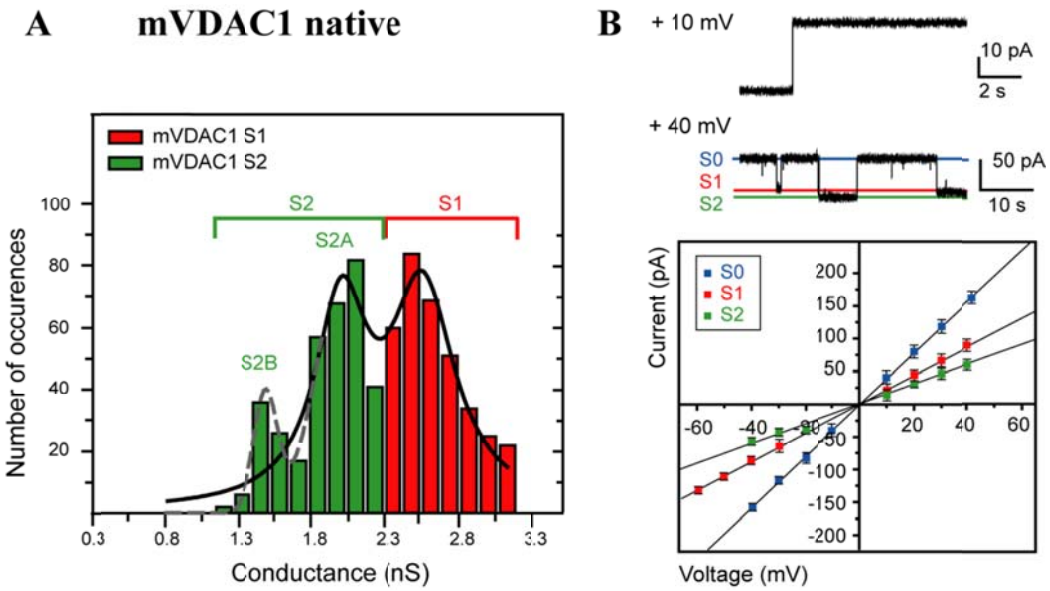

Figure 24:[(adapted from [99])] (**A**) Histogram of occurrences of low conductance values for native mVDAC1. The sum of two Gaussians indicated the presence of two possible low conductance states for the native channel, S1 (red) and S2 (green) with an R^2 value of: 0.91. (**B**) Gating profiles of native mVDAC1. Corresponding U/I-plots from collected data, used for the determination of conductance values, are provided below panel B. Bars represent standard errors.

Further mVDAC1 characterisations were based on the cysteineless mVDAC1 variant. Accordingly, the electrophysiological characterisation of this variant was necessary to prove that the lack of two cysteines are not interfering with the channels´ switching behaviour. The cysteine-less mVDAC1 variant closely resembles the mVDAC1 wild type behaviour. We observed the open S0 state with a conductance of 3.78 ± 0.09 nS (n = 170), S1 state with a conductance of 2.50 ± 0.12 nS (n = 72) and the S2 closed state with a conductance of 1.78 ± 0.09 nS (n = 30) (Table 19). Additionally, native and cysteineless mVDAC1 variants occupied the observed states with the same average dwell-times (Figure 25). Based on this result, it was obvious that any change in the gating behaviour of further modified mVDAC1 variants just occurred by the incorporated disulphide bridges.

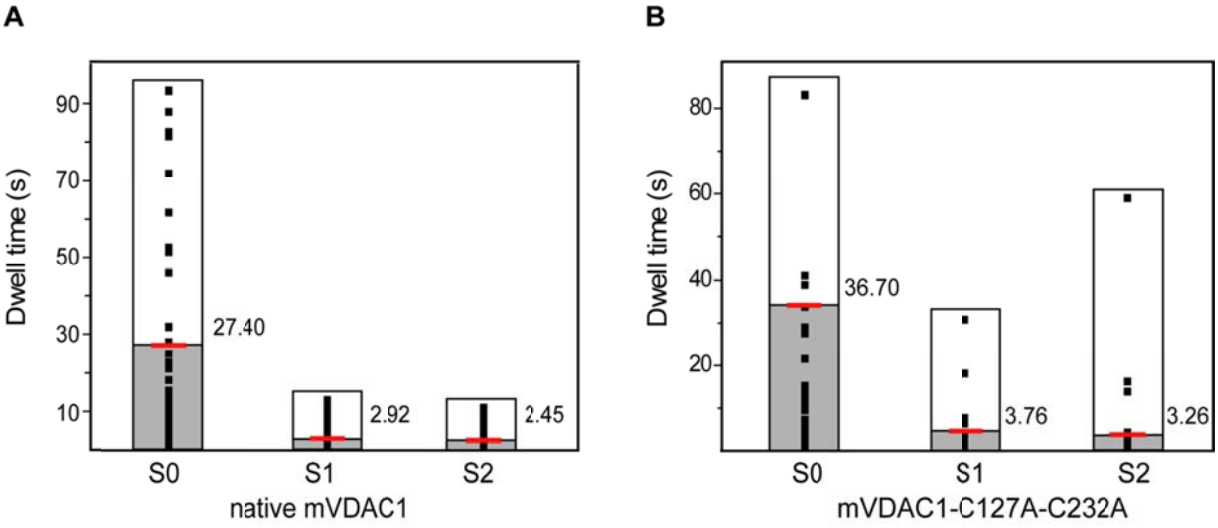

Figure 25: (adapted from [99]) The dwell times of native (**A**) and cysteineless (**B**) mVDAC1 were analysed and separated in the different switching states. Native channel and cysteineless variant occupy the S0 state longer than the closed states S1/S2.

To prove the dominant role of the N-terminal α-helix in any gating behaviour of mVDAC1, the N-terminal truncation variant Δ1−21-Y22C-mVDAC1 (Δ21-mVDAC1) was analysed. BLM measurements revealed a permanent open pore with a conductance of 4.00 ± 0.04 nS (n = 276) in agreement with the reported observations of Abu-Hamad *et al*. [35] and De Pinto *et al*. (see table 24 section 5.1.2.1). [163]

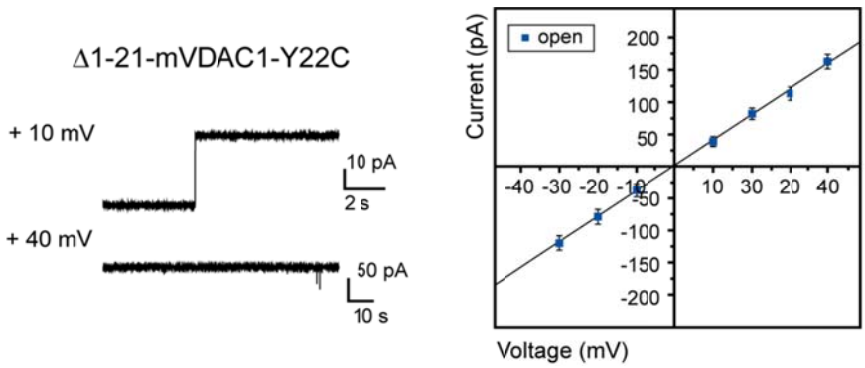

Figure 26: (adapted from [99]) Gating profiles of the Δ21-mVDAC1 deletion variant. Corresponding U/I-plots from collected data, used for the determination of conductance values, are provided. Bars represent standard errors.

After determining the switching behaviour of native, cysteineless and truncated mVDAC1 the cysteine-variants mVDAC1-CL-A14C-S193C and mVDAC1-CL-V3C-K119C were analysed expecting a different gating behaviour. For that BLM measurements were performed with

oxidized and reduced mVDAC1-variants. As expected, fully reduced mVDAC1-CL-A14C-S193C revealed almost the same switching behaviour than mVDAC1. The reduced mVDAC1-CL-A14C-S193C showed a high conductance state at 3.70 ± 0.01 nS high (S0) and low conductance states at 1.67 ± 0.09 nS (S2) comparable to the wild type (Figure 24B, Table 19). Unlike the native mVDAC1, pre-oxidized mVDAC1-CL-A14C-S193C showed almost a lock in the S0 conductive state (3.74 ± 0.05 nS, Table 19). In a minority of measurements (27/355), a switch to a low conductance state (1.85 ± 0.07 nS) could be observed (Table 19). This state was observed only after several minutes, where the channel remained in the S0 state and finally switched to a state equivalent to S2 of mVDAC1 (P = 0.868). Interestingly, this mVDAC1 variant avoided the S1 state and failed to reopen. Furthermore, the dwell time for the oxidized A14C-S193C variant in the S0 state (30.6 min) was 180 times longer in comparison to native mVDAC1 (0.17 min) (Figure 27B).

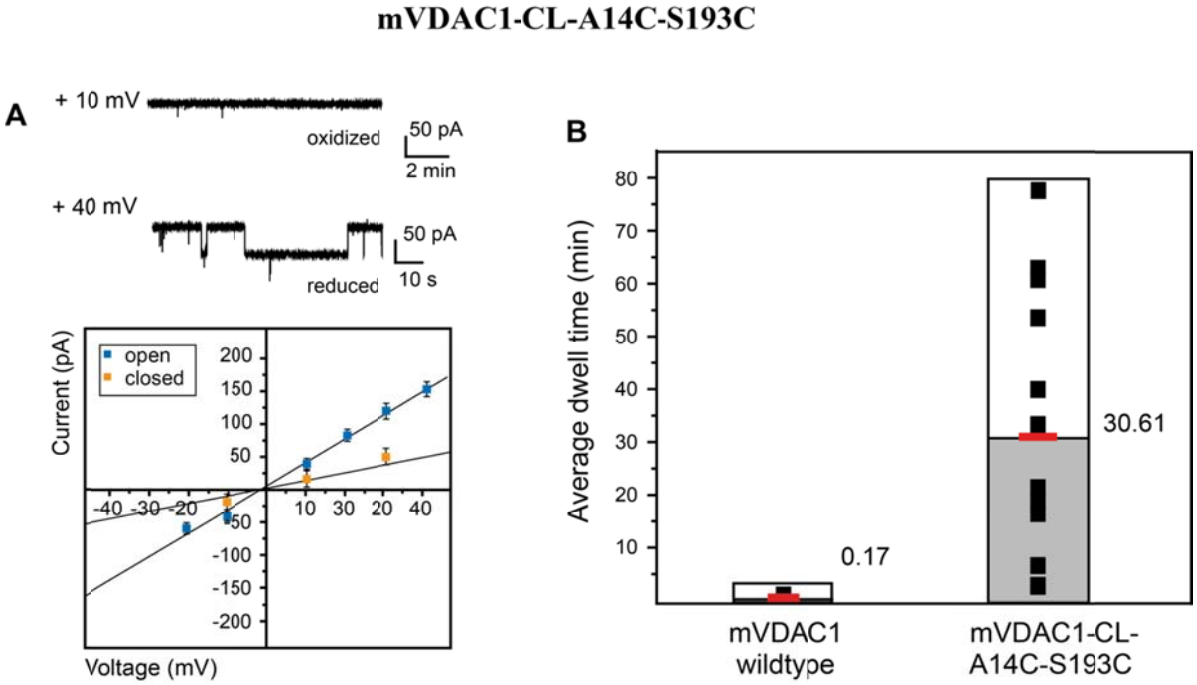

Figure 27: [adapted from [99]] (**A**) Gating profiles of native mVDAC1-CL-A14C-S193C. Corresponding U/I-plots from collected data, used for the determination of conductance values, are provided. Bars represent standard errors. (**B**) Comparison of mVDAC1 wild type and mVDAC1-CL-A14-S193C´s dwell times.

The analysis of pre-oxidized mVDAC1-CL-V3C-K119C revealed an asymmetric switching behaviour. BLM measurements unveiled a channel opening under both positive and negative potentials, but closing just under the reversed (Figures 28). The type of potential required for the closure depends on the orientation of the mVDAC1 variant within the BLM set-up. For

instance, channel incorporation during positive potentials in the sample chamber resulted in a permanent open pore. By application of the reversed (negative) potential the mVDAC1 variant switched to a low conductance state. Likewise, channel incorporation at negative potentials in the sample chamber resulted in an open pore until positive voltages were applied. It appears that the incorporation of the first channel is random as mVDAC1-CL-V3C-K119C channel closure was observed at positive and negative voltages in different series of measurements. Additionally, further channel incorporation followed the orientation of the first one, as proven by the gating profile observed in all measurements and in harmony with earlier observations [164-167]. Otherwise, a closing at both voltage signs would have been observed in all series of measurements if the incorporation of the second or third channel was random. Because of the observed asymmetry we gained confidence that the incorporation of more than one mVDAC1 is channel-assisted.

Pre-reduction of the disulphide bond restored the native switching behaviour (Figure 28A). When analysing the dwell times of mVDAC1-CL-V3C-K119C an immense difference depending on the potential sign was observed. Accordingly, the dwell time of the initial potential was 7.85 s, comparable to the wild type, whereas the dwell times of the reversed potential was 78.5 s, significantly prolonged with respect to native mVDAC1 (Figure 28B). During switching the lowest closed state (1.77 ± 0.09 nS) was similar to the S2 state of the native channel (n = 50) but the S1 state was avoided like in mVDAC1-CL-A14C-S193C (Table 19). Additional S0-to-S1 transitions occurred only in 5% of the events and were independent of S2.

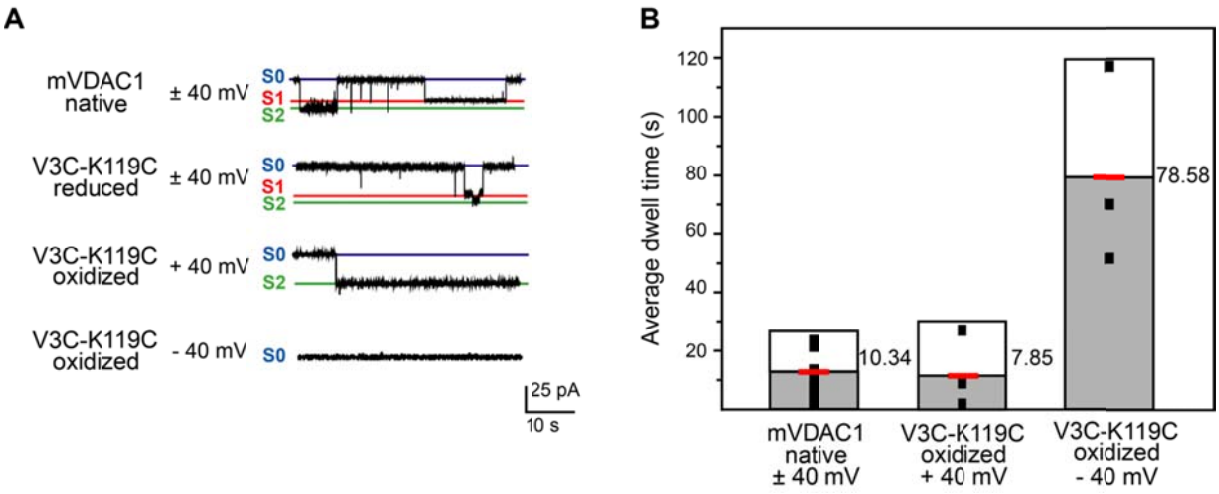

Figure 28: [99] (**A**) Gating profiles of native mVDAC1-CL-V3C-K119C. (**B**) Comparison of mVDAC1 wild type and mVDAC1-CL-V3C-K119C´s dwell times.

Table 19: Conductance values for mVDAC1 variants following their reconstitution in planar lipids. Adapted from [99]

Protein	**Open State (nS)**	**Closed state (nS)**	**Salt composition**
mVDAC1	3.94 ± 0.04[a](S0)	2.61 ± 0.01[a](S1) 1.90 ± 0.06[a] (S2)	1 M KCl 5 mM $CaCl_2$
Δ1-21mVDAC1-Y22C	4.00 ± 0.04[a](S0)	---	
mVDAC1-C127A-C232A	3.78 ± 0.09[b](S0)	2.50 ± 0.12[a] (S1) 1.78 ± 0.09[a] (S2)	
mVDAC1-A14C- C127A-S193C -C232A (oxidized)	3.74 ± 0.05[a](S0)	1.85 ± 0.07[a] (S2) low probability	
mVDAC1-CL-A14C- S193C (reduced)	3.70 ± 0.01[a] (S0)	1.95 ± 0.08[a] (S1) 1.67 ± 0.09[a] (S2)	
mVDAC1-CL-A14C- S193C (oxidized)	3.28 ± 0.04[a] (S0)	1.77 ± 0.09[a] (S2)	
mVDAC1-CL-V3C-K119C (reduced)	3.98 ± 0.04[a] (S0)	~2.70 (S1) 2.05 ± 0.13[a] (S2)	

[a] values given with their standard error.

4.1.4 Electrophysiological (BLM) measurements of mVDAC2

To understand the switching behaviour of mVDAC2 the following BLM measurements were performed. This chapter gives first insights in the electrophysiological characteristics of mVDAC2.

mVDAC2 responds linearly to the application of both positive and negative potentials, alternating between high and low conductance states (Figure 29). In addition and contrary to mVDAC1, mVDAC2 adopts at pH 8.6, the same pH as in BLM measurements with mVDAC1, a conductance state around 0.86 ± 0.02 nS whereas a lower state resulted in a conductance of 0.20 ± 0.01 nS. The reduced conductivity compared to mVDAC1 is caused by an irregular switching behaviour of mVDAC2, probably because of the presence of cysteines in mVDAC2´s sequence. The presence of cysteines in the sequence, especially in the N-terminal region, may allow the formation of disulphide bridges under oxidative conditions, analogous to the situation of the double-cysteine-mVDAC1 variants.

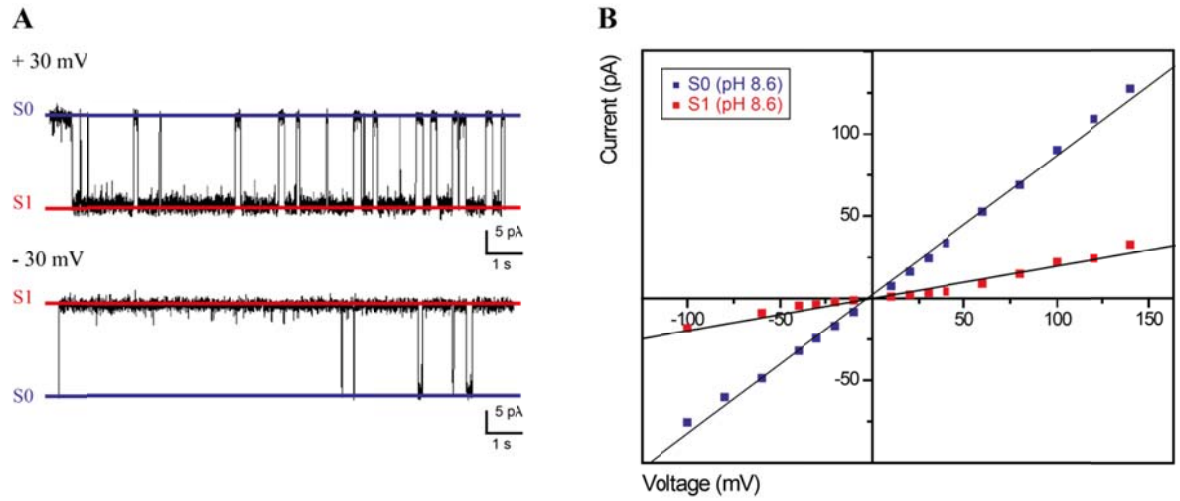

Figure 29: (**A**) Gating profiles of mVDAC2 at +30 mV and -30 mV, (**B**) U/I-plots of native mVDAC2 at pH 8.6 from data (n = 57), used for the determination of conductance values, are provided.

In all BLM measurements the open probability of the channel was quite low. During the measurements the open probability changed apparently towards the applied voltage. For example, in one measurement the channel lingered in the closed state at negative voltages whereas the highest open probability was found at ~ +75 mV (Figure 30). Interestingly, because of the asymmetric distribution of the open probability a directed insertion of mVDAC2 into the lipid bilayer can be assumed.

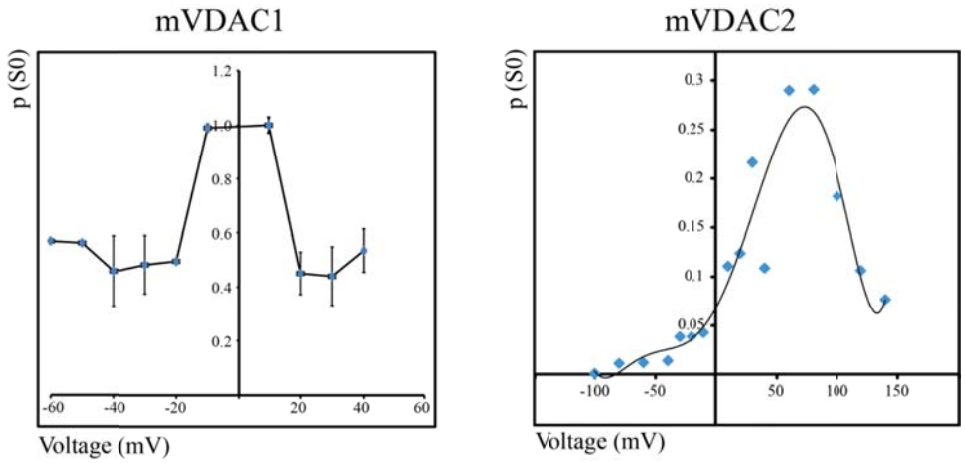

Figure 30: Open probabilities of mVDAC1 (left) and mVDAC2 (right) at pH 8.6; mVDAC1 exhibits the highest open probability at 0 mV, whereas mVDAC2 shows an increased open probability at ~ +75 mV.

Interestingly mVDAC2´s gating characteristic is pH-dependent. At pH 6.2 the high conductance state is about 3.48 ± 0.03 nS and comparable to the open state of mVDAC1, although the closed state is extraordinary low (0.63 ± 0.03 nS) (Figure 31).

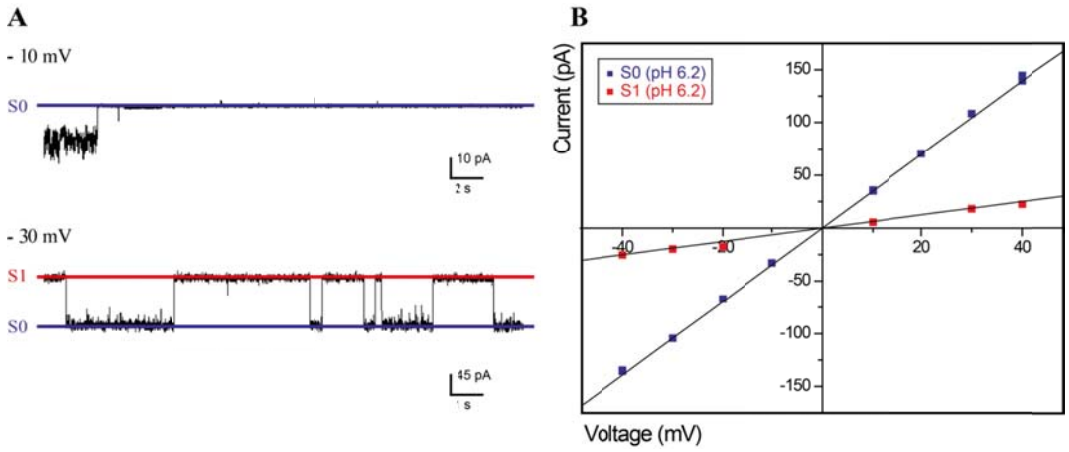

Figure 31: (**A**) Channel incorporation of mVDAC2 at +10 mV (top) and gating profile at -30 mV (bottom), (**B**) U/I-plots of native mVDAC2 at pH 8.6 from data (n = 173), used for the determination of conductance values, are provided.

The gating characteristics of mVDAC2 at pH 8.6 reminds of the behaviour of mVDAC1-CL-V3C-K119C whereas the gating behaviour at pH 6.2 reminds on mVDAC1. It can be easily assumed, that the presence of the cysteines in mVDAC2´s N-terminus and β-barrel caused this behaviour. Without any doubt the behaviour of mVDAC2 has to be characterized more extensively than it has been done in this thesis. To date, these are the first BLM measurements of refolded recombinant mVDAC2 incorporated into lipid bilayers.

4.1.5 Crystallisation trials

Beside a functional analysis of mVDAC1, the 3D-structure should be characterized as well. Especially the structure of mVDAC1 variants used during BLM studies desired considerable interest. Unfortunately, it was not possible to solve the structure of mVDAC1 variants due to the poor diffraction quality of the obtained crystals. There were some promising crystallisation trials resulting in protein crystals with diffraction properties, which may be further optimised. The best results are provided in Table 20.

Table 20: Results of the crystallisation trials on wild type mVDAC1

Screen	Composition	Picture
Classics 4°C	0.2 M Calcium chloride 0.1 M HEPES pH 7.5 28% (w/v) PEG 400	
Core II	0.1M Tris pH 8.5 20% (v/v) ethanol	
Core III	0.2M Tri-sodium-citrate 0.1M HEPES pH 7.5 10% (v/v) isopropanol	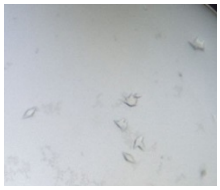
Fine screen	0.1M HEPES pH 7.5 0.2M $MgCl_2$ 18% EtOH	

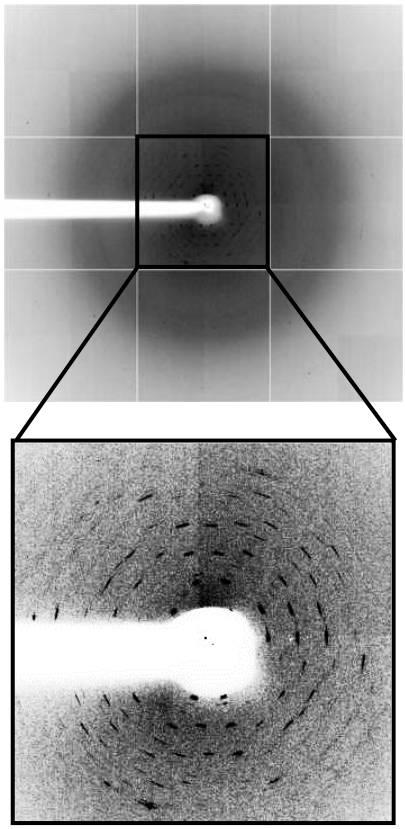

Figure 32: X-ray scatter of an mVDAC1 crystal. Crystals were diffraction to 6-10 Å.

The crystals shown in Table 20 were measured at the beam line ID 23-2 of the ESRF synchrotron source (Figure 32). The obtained crystals were very small and fragile. Therefore a proper handling during crystal harvest was very difficult. In addition, the best observed crystals were grown under alcoholic conditions making reproducibility difficult. Some of the crystals were diffracting to 6-10 Å, still low to solve mVDAC1´s structure.

4.2 Influence on VDAC by the pro-apoptotic effector Bid

VDAC isoforms are able to mediate the traffic of <5 kDa metabolites through the outer mitochondrial membrane. Beside this feature mammalian VDAC isoforms have been identified as key players in apoptotic processes. Apoptosis is essential for all multicellular life and occurs because of either normal cell growth (intrinsic) or cell damage (extrinsic). In the intrinsic apoptotic pathway cellular stress factors cause activation of pro-apoptotic proteins which assembles in the outer mitochondrial membrane. The thereby induced rupture of the outer mitochondrial membrane releases apoptogenic factors like cytochrome c, AIF or Smac/DIABLO from the intermembrane space to the cytosol and causes finally cell death. VDACs have been identified to interact directly with a variety of pro- and anti-apoptotic factors, either members of the Bcl-2 protein family such as Bcl-xL [168, 169], Bid/tBid[170], Bax/Bak, [171] and hexokinases [172], or Bnip3 [173]. The precise molecular functions and stoichiometries of these VDAC/apoptotic factor complexes are poorly understood, although structural predictions for several VDAC/effector complexes have been suggested [174].

This section is focussing on the structural and functional behaviour of VDAC1 and VDAC2 in the presence of the activated pro-apoptotic effector protein tBid. tBid is the caspase 8 truncated and thereby activated form of Bid. Dr Sina Oppermann demonstrated in cell line experiments, that the presence of VDAC1 is necessary for the glutamate- and tBid-induced apoptosis in neuronal cell lines (Figure 33).[20] The main question was, whether a direct interaction of both proteins occurs during the apoptotic process or whether these results relate to another cellular pathway.

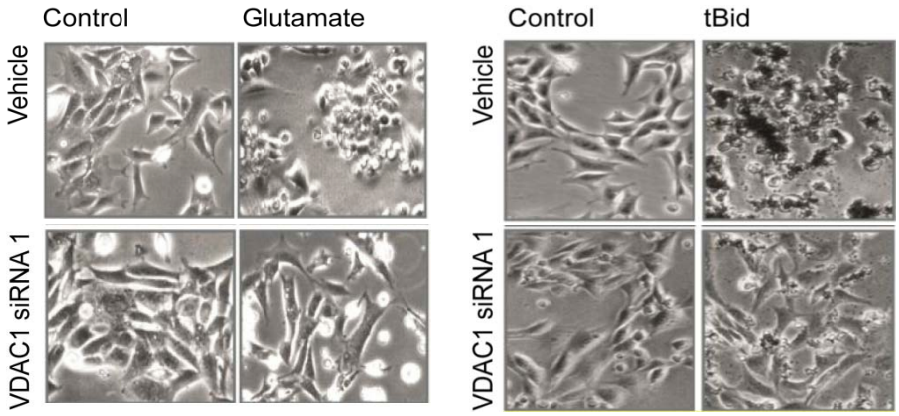

Figure 33: [175] Visualization of cell viability as done by Dr Sina Oppermann.[20] The photomicrographs (10 x 0.25 NA objective) show non-transfected HT-22 cells (vehicle, left panels) and cells transfected with VDAC1 siRNA 1 (20 nM, lower panel) 16 h after glutamate or tBid challenge (right panels). The cells undergo apoptosis after glutamate (right) or tBid (left) treatment (upper panels) whereas silencing of VDAC1 (lower panels) leads to cell survival.

4.2.1 Expression and purification of Bid

Bid was expressed in *E.coli* Rosetta cells as described before.[176] To yield highly purified protein the cell lysate was first separated by Ni-NTA chromatography followed by a SEC. The yields of recombinant Bid were 25 mg protein per litre expression culture after purification (Figure 34 and 35).

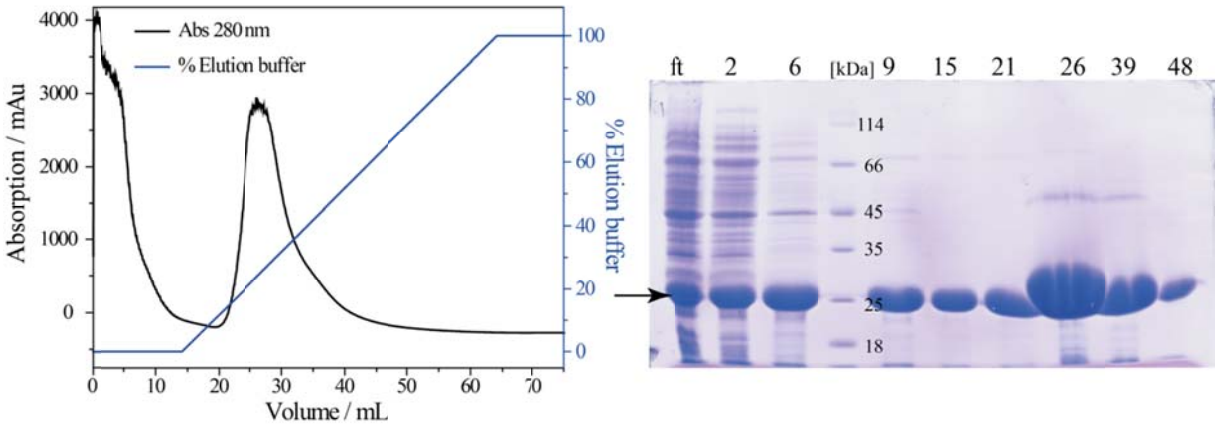

Figure 34: Representative Ni-NTA-chromatogram and 12% Coomassie-stained SDS-PAGE analysis of Bid, SDS-PAGE lanes correspond to the elution volume (ft = flow through); the arrow marks purified Bid.

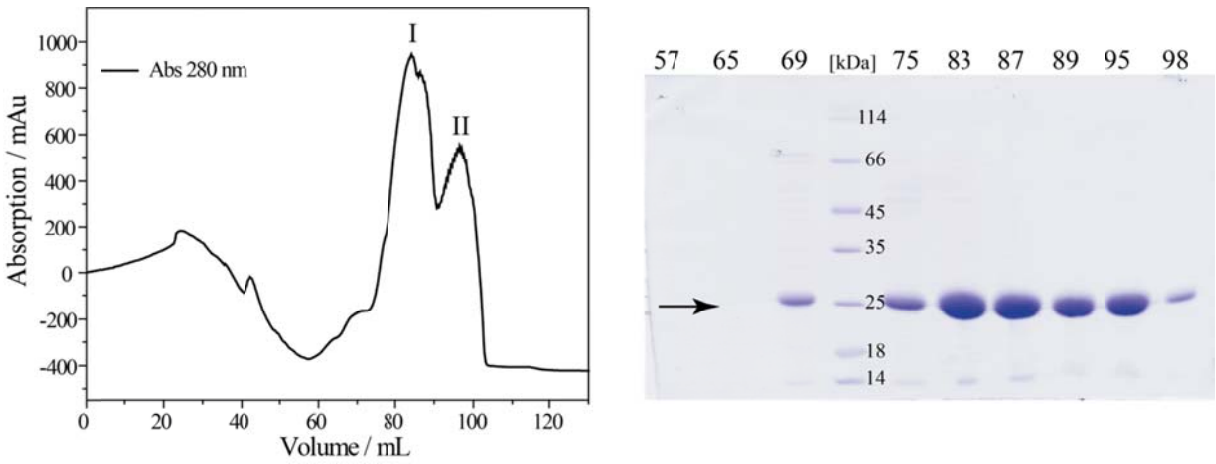

Figure 35: Representative SEC-chromatogram and 12% Coomassie-stained SDS-PAGE analysis of Bid, SDS-PAGE lanes correspond to the elution; arrow marks purified Bid.

Although there were two peaks (I, II) during size exclusion chromatography, the SDS-PAGE analysis confirmed the presence only of Bid. The apparent molecular mass of the purified Bid in the two peaks can be determined by the following calibration equation:

$$\lg(MW\ (kDa)) = -0.0338x + 4.5421 \quad \text{(Eq 15)}$$

The first peak in size exclusion occurs at 86 mL and corresponds to a molecular mass of ~ 43.1 kDa. The second peak occurs at 95 mL and corresponds to a molecular mass of ~ 21.4 kDa. Bid has a molecular mass of about 22.0 kDa and therefore it seems that Bid was purified as both monomer and dimer. Both peaks were collected and concentrated but only monomeric Bid was used for further mVDAC1-Bid interaction studies.

4.2.2 Truncation of Bid and purification of tBid

The active form of Bid is truncated tBid. As a mixture of truncated and full length protein is not useful for interaction studies, the truncated Bid was generated and purified as described in chapter 3.2.7.2. The cutting efficiency was estimated to be over 95% according SDS-PAGE analysis. The purification of tBid was achieved by SEC with a 2% OG (5xCMC) containing buffer to prevent tBid´s precipitation. The purification step yielded 11 mg of purified tBid from 14 mg Bid. A representative SEC-chromatogram and the corresponding SDS-PAGE is shown in Figure 36.

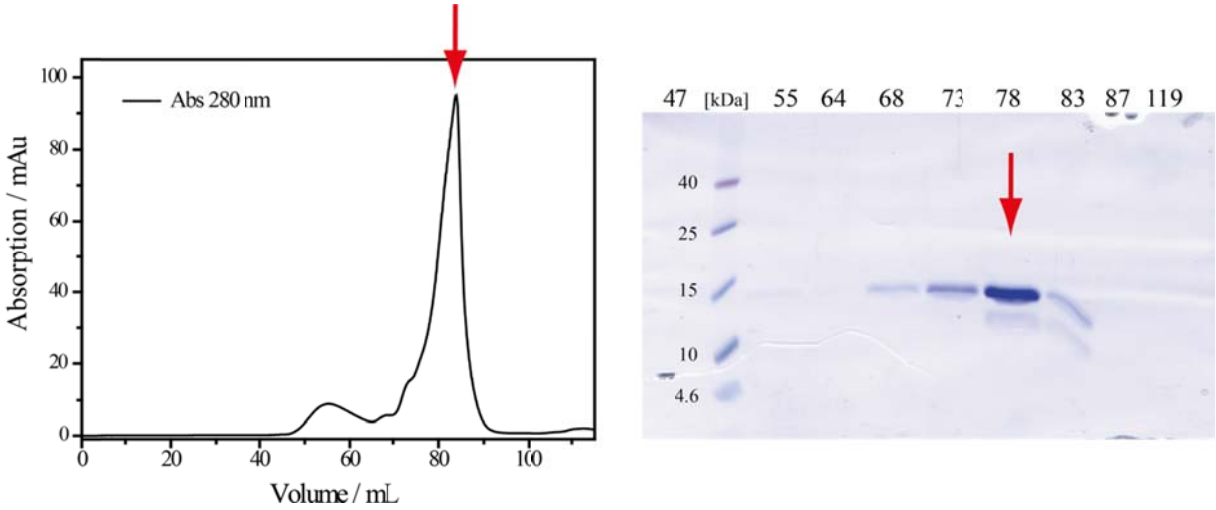

Figure 36: SEC chromatogram and corresponding 12% Coomassie-stained SDS-PAGE analysis of tBid purification. Red arrow indicates the main peak and pure tBid.

4.2.3 Influence on VDAC

From cell line experiments, it was known, that the pro-apoptotic effect of tBid was only observed when VDAC1 was expressed. Accordingly, different techniques were established to prove a direct interaction of the recombinant proteins. Especially, the affinity of tBid towards mVDAC1, the influence on mVDAC1´s gating characteristics and the structural rearrangement of the overall complex were of major interest.

4.2.3.1 Establishment of an analytical method for the VDAC1-tBid-interaction

To establish an analytical method for the VDAC1-tBid interaction first SEC and thermofluor analysis was performed. Accordingly, SEC gives first information about the existence of a stable mVDAC1-tBid complex, whereas thermofluor measurements were used to determine the stability of the mVDAC1-tBid complex.

Though the molar ratios of the mVDAC1-tBid complex were unknown, mVDAC1 and tBid, as well as Δ11-mVDAC1 and tBid were mixed in an equimolar ratio. The protein samples were then purified by SEC using mVDAC1´s SEC buffer. In addition, it was evaluated whether the inactive Bid also binds to mVDAC1 and it´s variant. A comparison of the SEC

chromatograms is shown in Figure 37. The fractions were analysed on a native and a denaturing PAGE (section 9.5).

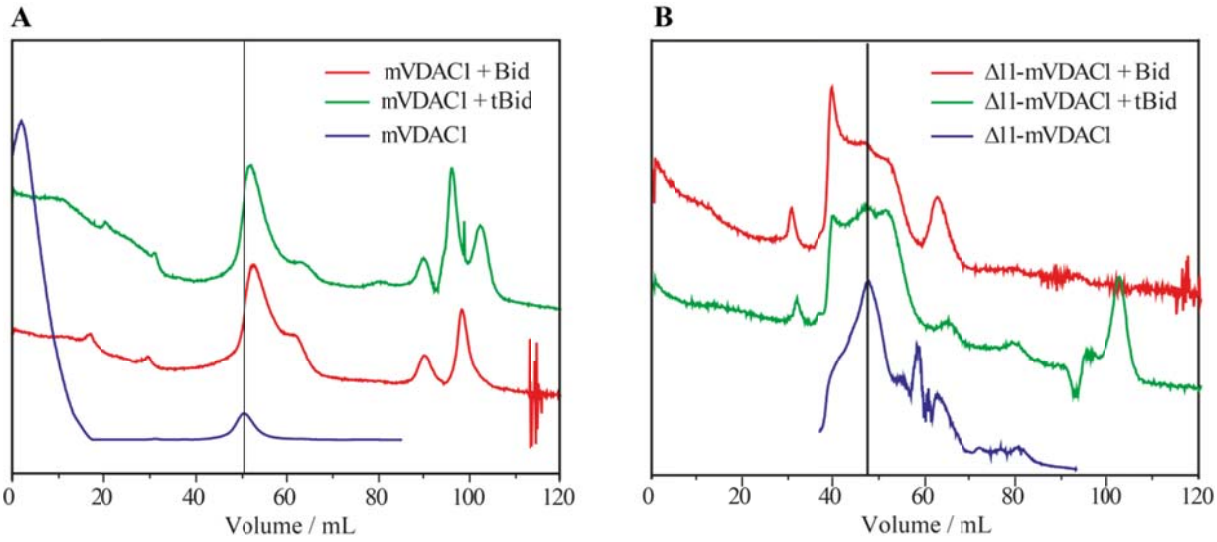

Figure 37: SEC chromatogram of the VDAC1-Bid/tBid and Δ11-VDAC1-Bid/tBid complexes (**A**) Comparison of mVDAC1 (blue), mVDAC1+Bid (red) and mVDAC1+tBid (green) elution profiles, the black line indicates the mean elution volume of mVDAC1. (**B**) Comparison of Δ11-mVDAC1 (blue), Δ11-mVDAC1+Bid (red) and Δ11-mVDAC1+tBid (green) elution profiles, the black line indicates the mean elution volume of Δ11-mVDAC1.

The results of the SEC of mVDAC1-tBid, mVDAC1-Bid as well as Δ11-mVDAC1-tBid and Δ11-mVDAC1-Bid indicate that the elution profiles of the protein complexes unexpectedly shift to higher elution volumes. In SEC higher elution volumes correspond to smaller molecular masses, indicating that the protein complex appears to be smaller than mVDAC1 alone. This is indeed not the case, but while working in a detergent buffer the size of the micelles surrounding VDAC may be affected by the binding of Bid/tBid. The SEC analyses are hence not giving a clear proof of the direct interaction of mVDAC1 and its variant but a stable mVDAC1-tBid complex cannot be excluded.

As another setup, the thermal stability of VDAC1 was determined in dependency of the presence of Bid/tBid by thermofluor analysis. For this attempt mVDAC1 was mixed in a 0.5, 1 and 2 molar ratio of Bid /tBid and melting curves were performed. The results are shown in Figure 38.

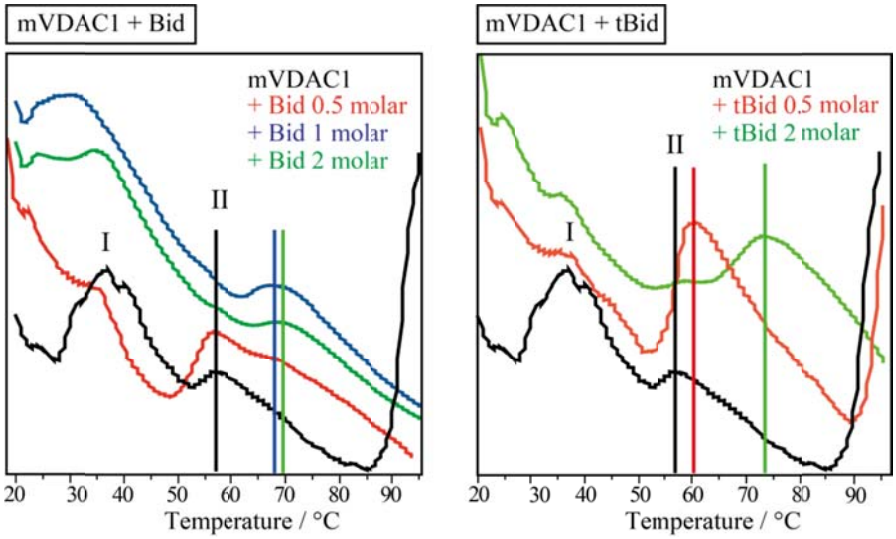

Figure 38: Thermofluor analysis of mVDAC1-Bid/tBid complex. Bid/tBid was added in different molar ratios to gather information about the thermic behaviour of the protein complex. Vertical lines indicates the assumed melting temperature of mVDAC1 alone (black) and the protein complex with 0.5 molar (red), 1 molar (blue) and 2 molar (green) Bid/tBid.

During the thermal denaturation of mVDAC1 there are two major peaks around 37°C (I) and 57°C (II) indicating two melting points. It is likely that peak I occurs from the detergents, thus providing more hydrophobic residues, where the dye can bind. Peak II around 57°C tends to be the melting point of mVDAC1 in agreement with previous CD studies (T_m = 68°C [86]). After addition of 0.5 molar Bid to the mVDAC1 solution, peak II remains at 57°C (Figure 38 left panel). Interestingly, 1 and 2 molar Bid induced a thermal shift of peak II to 67°C (1 molar Bid) and 69°C (2 molar Bid). Therefore, one can assume a higher melting temperature of the VDAC1-Bid complex. Furthermore, the thermal shift of peak II is even more pronounced by the addition of tBid in 0.5 and 2 molar ratios (Figure 38 right panel). At a molar ratio of 0.5:1 (tBid:mVDAC1) peak II is shifted to 61°C indicating binding of tBid to mVDAC1. After addition of 2 molar tBid to 1 molar mVDAC1, peak II shifts to 74°C. Taken together, the results hint to a) a direct interaction because of the changed thermic behaviour b) a higher specificity of tBid to mVDAC1 then Bid and c) an increased thermal stability of the protein complex compared to mVDAC1 alone.

4.2.3.2 Microscale thermophoresis analysis proofs a direct interaction of Bid/tBid and VDAC1

Microscale thermophoresis (MST) is an alternative to isothermal calorimetric measurements (ITC). Both experimental setups provide binding affinities of proteins in complexes with small compounds or other proteins. Because of the presence of lipids or detergents, binding affinities of the mVDAC1-Bid/tBid complex could not be determined by ITC. Therefore MST experiments were performed. tBid is commonly used to identify VDAC1 activity but K_D values were missing.[170] For this, mVDAC1 was labelled with a fluorophor and Bid/tBid was added in concentrations of 15 nM to 500 µM to the mVDAC1 solution. Based on the diffusion and migration characteristics of the labelled mVDAC1, binding affinities can be calculated as described in chapter 3.3.8. Thermophoresis analyses gave different dissociation constants for the full length Bid and the cleaved tBid. Here, tBid binds to mVDAC1 with a K_D of 26.9 ± 0.6 µM (Figure 39), whereas Bid interacts with mVDAC1 with a strongly reduced affinity (K_D = 1420 ± 30.7 µM). By comparing these findings with the lack of binding of Bid to OmpG nonspecific interaction with β-barrels was excluded.

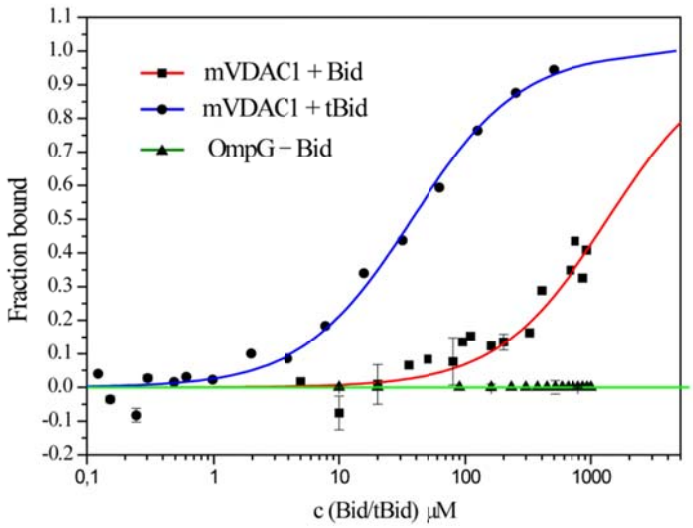

Figure 39:[175] To determine the affinity of Bid/tBid to fluorescently labelled mVDAC1 (c = 75 nM, 5xCMC LDAO containing SEC buffer) and OmpG (c = 75 nM, 5xCMC C_8E_4 containing SEC buffer), titration series were performed. The change in the thermophoretic signal leads to a K_D of 26.9 ± 0.6 µM for tBid (dots, blue line) and 1420 ± 30.7 µM for Bid (squares, red line). The interaction with fluorescently labelled OmpG leads to no significant change in the thermophoretic signal (triangle, green line) and therefore an unspecific interaction between tBid and β-barrels can be excluded. Bars represent standard errors of three independent measurements.

After confirming the direct interaction of mVDAC1 with Bid/tBid additional measurements were performed to elucidate the role of the N-terminus towards effector binding. For this titration series of tBid (c = 15 nM - 500 µM) to fluorescently labelled mVDAC1 deletion variants (c = 50 nM) were performed. During thermophoresis measurements K_D values for both of deletion variants were determined. Surprisingly, tBid interaction with Δ11-mVDAC1 resulted in K_D values of 1.83 ± 0.17 µM, 16 fold higher compared to full-length mVDAC1 (Figure 40 and Table 31). Furthermore, tBid binds to Δ26-mVDAC1 with a decreased affinity compared to the wild type (K_D = 63.2 ± 3.4 µM). Though the only difference of these variants is the shortening of the N-terminus, the distinct K_D values just occur upon this change.

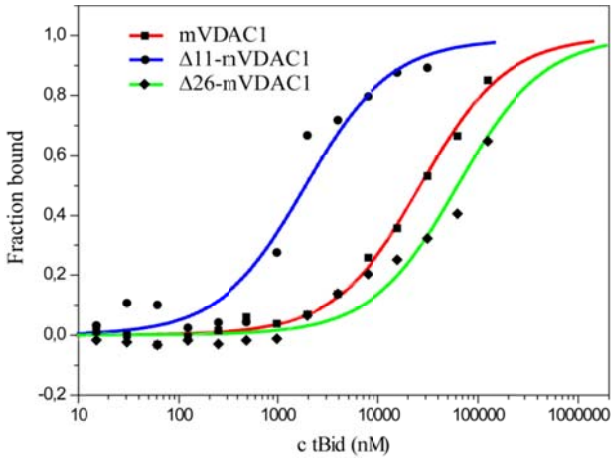

Figure 40: To determine the affinity between tBid and fluorescently labelled mVDAC1 (c = 75 nM, 5xCMC LDAO containing SEC buffer) and mVDAC1 deletion variants (c = 55 nM, 5xCMC LDAO containing SEC buffer) a titration series was performed. The change in the thermophoretic signal leads to a K_D of 26.9 + 0.6 µM for mVDAC1 (squares, red line), 1.83 + 0.17 µM for Δ11-mVDAC1 (dots, blue line) and 63.2 + 3.4 µM for Δ26-mVDAC1 (triangle, green line).

To prove whether the N-terminus promotes the effector binding, additional MST measurements were performed with mVDAC2. mVDAC2 has, compared to mVDAC1, a prolonged N-terminus and therefore one may expect weaker binding of tBid. During thermophoresis measurements a K_D value of 92 ± 1 µM for mVDAC2 was determined (Figure 41), three fold lower than the wild type.

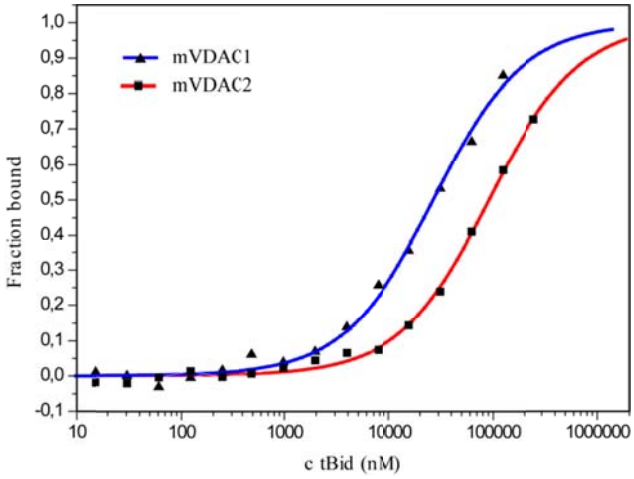

Figure 41: To determine the affinity of tBid and fluorescently labelled mVDAC1 and mVDAC2 a titration series was performed. The change in the thermophoretic signal leads to a K_D of 26.9 + 0.605 µM for mVDAC1 (triangles, blue line) and 92 + 0.952 µM for mVDAC2 (squares, red line).

Taken together, the results demonstrate that VDACs and Bid/tBid are capable of interacting in a direct manner. Interestingly, the deletion variant Δ11-mVDAC1 has the highest affinity towards tBid whereas the deletion variant Δ26-mVDAC1 has the lowest. Accordingly, the binding motif of mVDAC1 for tBid may not be entirely located in the N-terminus, which may hence indirectly affect binding.

Table 31: Results of the thermophoretic analysis.

Protein	Kd
mVDAC1 (tBid)	26.9 ± 0.605 µM
mVDAC1 (Bid)	1420 ± 30.7 µM
Δ11-mVDAC1-K12C	1.83 ± 0.174 µM
Δ25-mVDAC1-Y26C	63.2 ± 3.4 µM
mVDAC2	92 ± 0.952 µM

4.2.3.3 tBid addition to mVDAC1-containing planar lipid bilayers reduce the channel's conductance

After confirming, that tBid binds in a direct and specific manner to mVDAC1 (see chapter 4.2.3.2), the functional effect of tBid binding to mVDAC1 examined. In previous reports, VDAC1 closure after addition of tBid was described.[170] Based on our results, a detailed analysis of this closed state was performed. Native mVDAC1 exhibited the expected gating

behaviour, responding linearly to the application of both positive and negative potentials, and alternating between high and low conducting states [177-183].

Overall channel currents were recorded in the -40 - +40 mV voltage range and conductances were calculated from the corresponding Ohm plots. As shown above [99], native-like mVDAC1 occupied the fully open S0 state with a conductance of 3.94 ± 0.04 nS and the closed S1 and S2 states with conductances of 2.61 ± 0.01 nS and 1.90 ± 0.06 nS respectively (Figure 24 chapter 4.1.3). Following tBid addition (Figure 42 A and B), the channel´s conductance suffered a 23% reduction (3.05 ± 0.24 nS, N = 131) with respect to that of the S0 state (unpaired T-test: $P = 10^{-4}$). This lowered conductance differed from all closed-state conductances (unpaired T-test: $P = 10^{-4}$), a fact suggesting that the tBid-VDAC interaction may be caused by a deformation of the channel or partial occluding by tBid rather than a full closure (Figure 42 C and D).

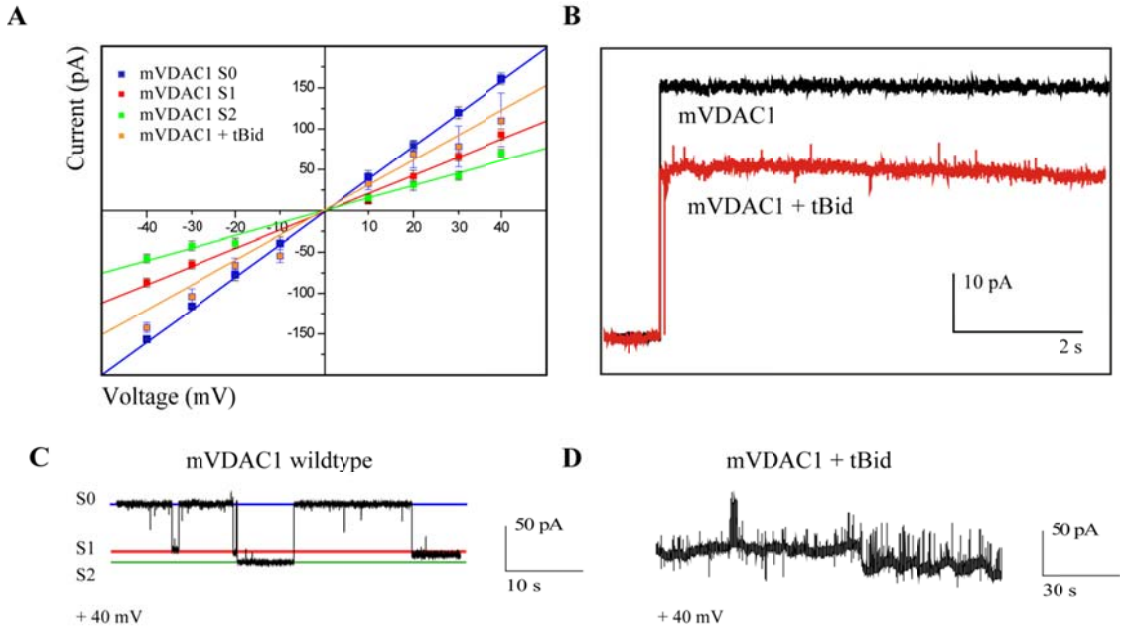

Figure 42: (adapted from [175]) (**A**) Ohm-plot used for the determination of the conductance values of the corresponding states. Reconstituted native mVDAC1 (5xCMC LDAO in SEC Buffer) responded linearly to application of both positive and negative potentials, alternating between an open (S0; blue) and two major (S1; red and S2; green) closed states. After tBid (5xCMC OG in SEC Buffer) addition to the *cis*-side the overall conductance of the channel drops to 77% compared to S0 (orange). (**B**) Representative traces of mVDAC1 before and after tBid addition. The overall current is reduced by incorporation of the mVDAC1-tBid channel complexes, (**C**) Representative trace of the mVDAC1 gating activity at +40 mV. The observed S0, S1 and S2 states, in the +40 mV trace, are indicated by blue, red and green lines respectively. (**D**) Representative trace of mVDAC1 after addition of tBid at +40 mV. The channel shows now minor, yet atypical fast channel switching transitions.

4.2.3.4 tBid binding to mVDAC1 induces structural changes in the protein complex

To get first structural insights in the mVDAc1-tBid-complex synchrotron radiation CD measurements were performed. For this, mVDAC1 was reconstituted in DMPC liposomes (see chapter 3.2.11) and CD spectra were measured using the ANKA synchrotron. The usage of a synchrotron source has the advantage that non-optical active lipids, providing a native-like environment for membrane proteins, do not interfere with this method.

At first the secondary structure contents of mVDAC1 and tBid in liposomes were determined and the mVDAC1-tBid-complex structure contents were compared with the predicted values. The analysis of the CD and OCD spectra was done by Dr Dirk Windisch (Karlsruher Institute for technology).

As expected and in accordance with the crystal structure, a CD analysis of monomeric mVDAC1 indicates an overall β-barrel structure (49 % β-sheet) with a small α-helical part (7% α-helix). The rest of the secondary structure is composed of turns (9%) and random coil (35%) (Figure 42A). In addition a CD analysis of tBid was performed to confirm structural stability of tBid in the presence of DMPC. CD analyses of tBid confirmed the overall α-helical structure of tBid (58% α-helix, 5% β-strand, 10% turn, and 26% random coil) as shown by the NMR structure.[105] In addition the structural stability of tBid in the presence of DMPC was confirmed by comparing the CD spectra before and after DMPC addition (Figure 43B).

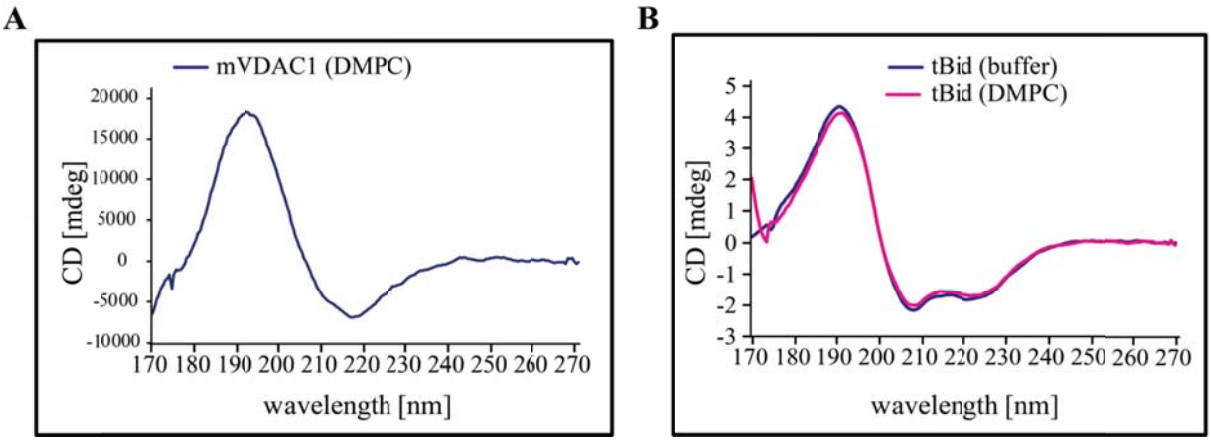

Figure 43: CD spectra of mVDAC1 and tBid, (**A**) CD spectrum of mVDAC1 in DMPC liposomes was recorded above (30°C) the DMPC phase transition temperature (**B**) CD spectra of tBid was recorded at 30°C in 5xCMC OG containing buffer (blue) and in the presence of DMPC (pink).

The mVDAC1-tBid complex was measured in different molar ratios. 1 and 2 molar equivalents of tBid were added to an equivalent of 1 molar mVDAC1 and the CD spectrum was recorded. The theoretical spectrum was simulated by combining both single CD spectra in the same ratios. If the simulated and measured spectra are different one can assume that there is a structural rearrangement in the tBid-mVDAC1 complex upon association.

CD analyses of the mVDAC1-tBid complex in a molar ratio of 1:1 revealed no significant structural deviations as indicated by the predicted and recorded spectra (Figure 44A). The analyses of CD spectra of mVDAC1-tBid complexes in a molar ratio of 1:2 revealed a sizeable structural difference suggesting rearrangements within the mVDAC1-tBid complex (Figure 44B). The difference spectrum of mVDAC1-tBid 1:2 resembles a random coil spectrum suggesting a partial unfolding of one of the complex partners (Figure 44C).

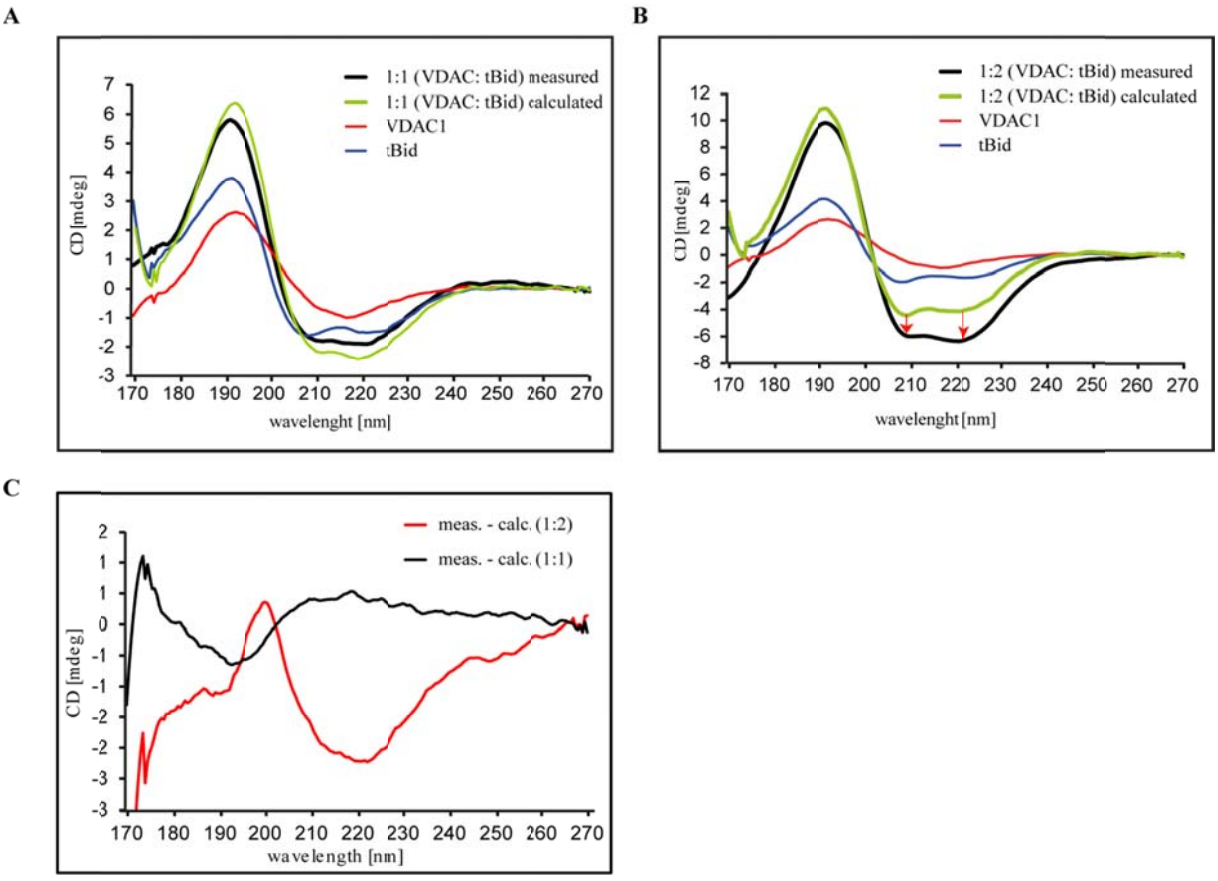

Figure 44: CD spectra of mVDAC1-tBid-complex in DMPC liposomes was recorded above (30°C) the DMPC phase transition temperature, (**A**) CD analyses of mVDAC1-tBid (1:1) as predicted (green) and recorded (black) spectrum, CD analyses of mVDAC1 (red) as well as tBid (blue) are shown for comparison, (**B**) CD analyses of mVDAC1-tBid (1:2) as predicted (green) and recorded (black) spectrum, CD analyses of mVDAC1 (red) as well as tBid (blue) are shown for comparison, the red arrows indicate significant differences between predicted and recorded spectrum, (**C**) difference spectrum recorded-predicted of the mVDAC1-tBid complex in 1:1 (black) and 1:2 (red) molar ratio.

OCD analyses of mVDAC1 in DMPC vesicles revealed that mVDAC1 is incorporated and preferentially orientated in the bilayer. When comparing the maximum and minimum of the OCD spectrum one can determine the orientation of the β-strands towards the membrane. If the max:min relation is about 1:1, all β-strands will align parallel to the membrane.[59] Another mark for the orientation of β-strands is the signal at 205 nm. If the signal is solely positive, a high max:min relation will occur and therefore a β-strand orientation vertical to the membrane can be predicted. To determine the orientation of α-helices towards the membrane the signal at 208 nm can be analysed.[184] Positive signals at 208 nm indicates that the α-helices are vertical to the membrane whereas a strong negative signal indicates a parallel orientation of the α-helices relative to the membrane plane.

The max:min relation of the mVDAC1 CD spectra reveals a value of 2,6/0,98 = 2,65 indicating a tilt of the β-strands in the liposomes. In the oriented liposomes the strands seem to be even more tilted indicated by a max:min relation of 7,09/2,2 = 3,22 (Figure 45A) . The mVDAC1-tBid complex was analysed in OCD in the same manner than in CD spectroscopy by comparing the recorded and predicted spectra. OCD analyses of the 1:1 mVDAC1:tBid-complex revealed no significant change in the max:min relation and in consequence no change upon the orientation of the complex in the membrane (max:min = 3.4) Contrary, the analyses of the 1:2 molar ratio mVDAC1-tBid complex showed a clear reorientation in the membrane (max:min = 2.58). Because the relation after tBid addition is closer to 1 one may conclude that the β-strands are more tilted (Figure 45B). The difference-spectrum of the 1:2 mVDAC1-tBid complex reveals a random coil-like structure, suggesting a partial unfolding upon tBid binding. In addition the signal at 208 nm indicates that one α-helix inserts into the membrane in a vertical manner (Figure 45C).

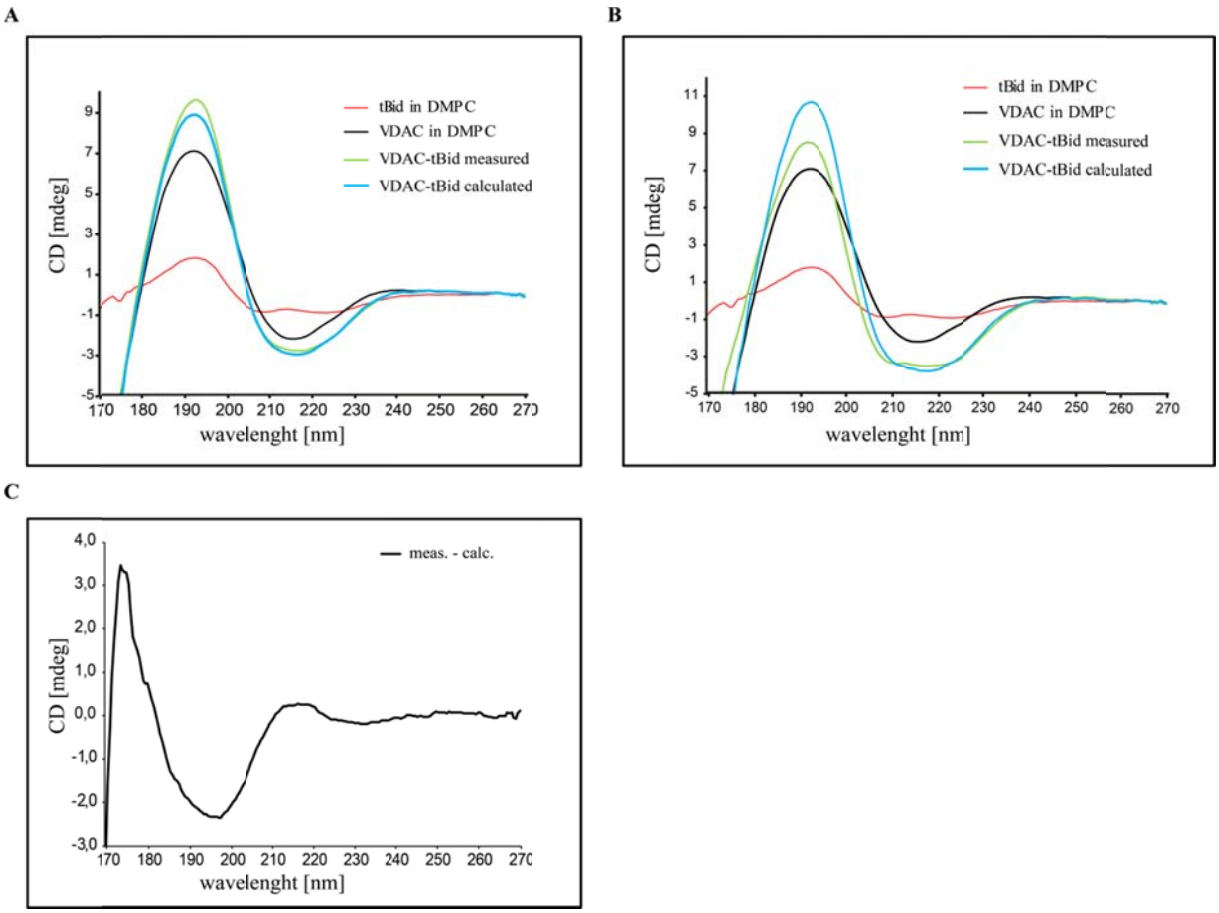

Figure 45: OCD spectra of mVDAC1-tBid-complex in DMPC liposomes was recorded above (30°C) the DMPC phase transition temperature, **A**: OCD analyses of mVDAC1-tBid (1:1) as predicted (blue) and recorded (green) spectra, OCD analyses of mVDAC1 (black) as well as tBid (red) are shown for comparison, **B**: OCD analyses of mVDAC1-tBid (1:2) as predicted (blue) and recorded (green) spectrum, OCD analyses of mVDAC1 (black) as well as tBid (red) are shown for comparison, **C**: Difference spectrum of the recorded-predicted 1:2 mVDAC1-tBid complex.

4.2.3.5 The structural change after tBid binding occurs in mVDAC1´s N-terminus and at its cytosolic side

Following a qualitative analysis of the structural rearrangement of the mVDAC1-tBid complex, a more precise analysis was performed by EPR measurements. All shown *cw* and DEER measurements were performed and analysed by Katharina Rudi and Dr Johann Klare (University of Osnabrück). For this, double-cysteines mVDAC1-variants were prepared and labelled according to chapter 3.2.9. A qualitative analysis of the label efficiency was performed by a second labelling step with dansyl-iodo-acetamide as described before.[57] A lack of light scattering in the MTSSL-labelled variants indicates a quantitative binding of the

MTSSL label. The analysis was performed for all mVDAC1-variants. A representative result of the qualitative labelling analysis is shown in Figure 46.

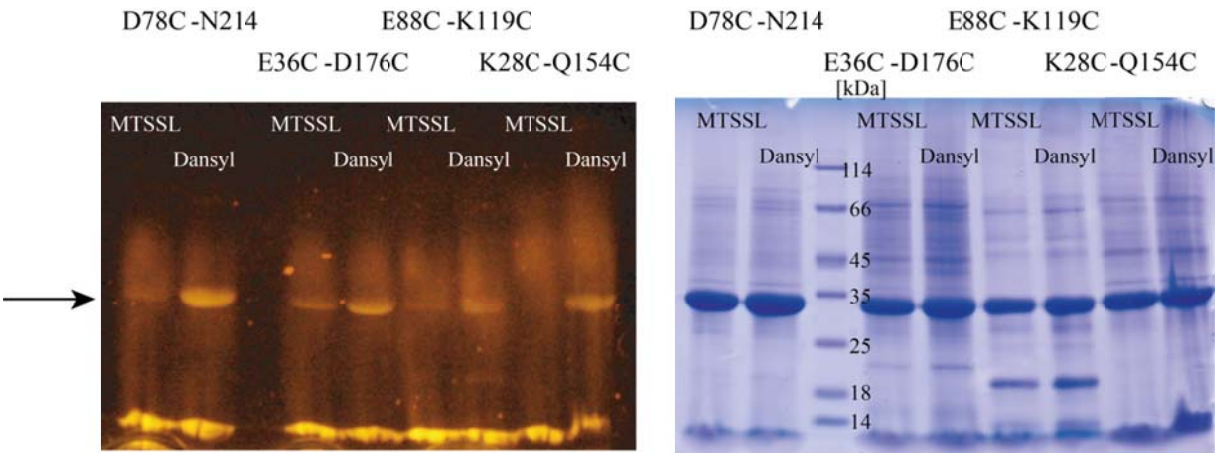

Figure 46: Qualitative analysis of the EPR-labelling. Double-cysteine mVDAC1 variants (200 µM) were labelled with MTSSL (c_{end} = 1 mM) in DMSO. To confirm the quantitative binding of the spin-label, the previously labelled mVDAC1-variants as well as unlabelled variants were treated with dansyl-iodo-acetamide (c_{end} = 1 mM). Left panel: SDS-PAGE under UV light, "MTSSL" marks the EPR-labelled mVDAC1-variant, "Dansyl" mark the dansyl-iodo-acetamide labelled mVDAC1-variant, the black arrow marks the height of mVDAC1, a lack of light scattering in MTSSL lane indicates a quantitative labelling. Right panel: Corresponding 12% Coomassie-stained SDS-PAGE.

The labelling efficiency of mVDAC1 was also analysed by *cw* EPR-measurements. For this a *cw* spectrum of a solution of 100 µM MTSSL label was measured and compared to the *cw* spectra of labelled mVDAC1-variants. The results of the label efficiency are shown in Table 22.

Table 22: Labelling efficiency of the mVDAC1-variants used for EPR measurements.

No.	mVDAC1-variant (cysteineless)	Position of the label in mVDAC1	Distance	Label efficiency %
1	mVDAC1-K12C	helix	--	46
2	mVDAC1-E59C	helix	--	109
3	mVDAC1-K32C	helix	--	28
4	mVDAC1-K12C-D30C	helix	17.9	220
5	mVDAC1-K12C-K32C	helix	17.6	150
6	mVDAC1-K12C-S57CC	helix	19.6	140
7	mVDAC1-K12C-E59C	helix	18.8	170
8	mVDAC1-E88C-K119C	IMS	8.3 Å	81
9	mVDAC1-E36C-D176C	IMS	23.4 Å	93
10	mVDAC1-E59C-S193C	middle of the pore	29.4 Å	24
11	mVDAC1-K28C-Q154C	middle of the pore	30.6 Å	107
12	mVDAC1-D78C-N214C	cytosolic side	35.9 Å	94
13	mVDAC1-A134C-D264C	cytosolic side	39.5 Å	14

At first, *cw* and DEER measurements were performed without the addition of tBid to map the initial state of mVDAC1 in detergent micelles. For this, 10 double-cysteine mVDAC1-variants and 3 single-cysteine mVDAC1-variants were analysed (Figure 47). Comparison of the measured and calculated distance distributions shows reasonable agreement, indicating that the crystal structure appropriately reflects the structure of the protein in LDAO micelles. Interestingly, the deviations between theory and experiment suggest a slightly different and mainly more flexible arrangement of the α-helix relative to the β-barrel.

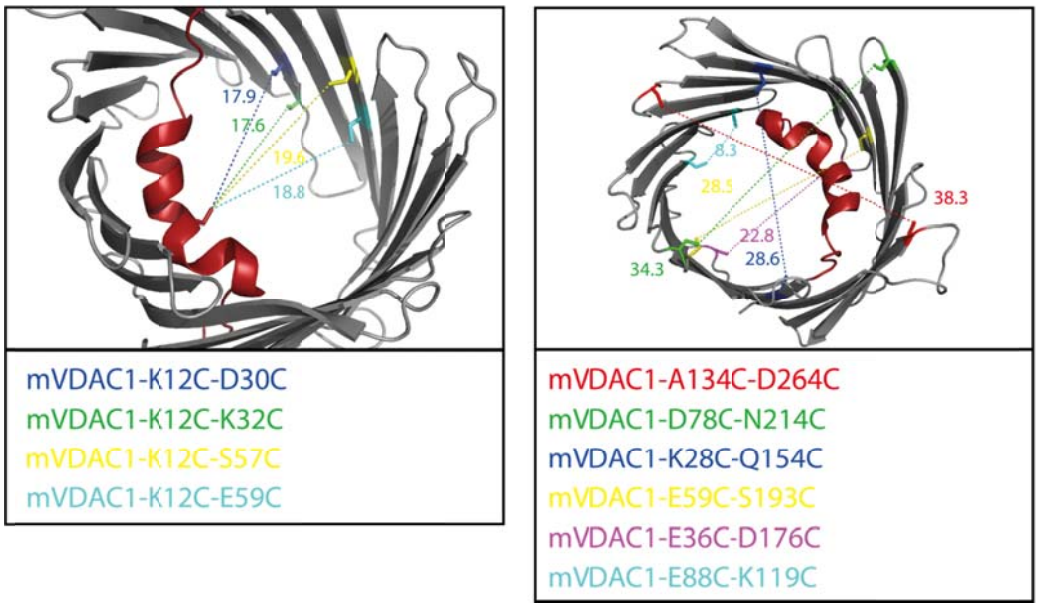

Figure 47: mVDAC1-variants used for EPR measurements. Left panel: double-cysteine variants to determine the involvement of the α-helix upon tBid interaction. Right panel: double-cysteine variants to determine an overall structural rearrangement of the β-barrel.

After the initial mapping of mVDAC1-variants, *cw* and DEER measurements were repeated in the presence of tBid in a one-to-two molar ratio. *cw* measurements show slight changes in the chemical environment of the MTSSL label in several variants indicating a structural change. In detail, the mVDAC1-variants 1-7 (Table 22), where a spin label is attached to the helix, show increased spin label mobility. Especially the variants mVDAC1-K12C and mVDAC1-K12C-E59C provide the largest changes after tBid binding (Figure 48). The increase of the spin label mobility can be explained by a change of the chemical environment of the label that is induced by a structural change, *e.g.* tBid forcing the spin label in a specific orientation. With the specific orientation, the labels loose some of their degrees of freedom and thereby the *cw* signature altered. In addition a titration series of 1:1, 1:2, 1:3 and 1:4 (mVDAC1:tBid) was performed using mVDAC1-K12C-E59C to determine the molar ratio of the interaction partners. *cw* measurements revealed the largest alteration in spin label mobility after addition of one part tBid. Furthermore, the spin label mobility still changes until a 1:2 ratio is achieved. Further addition of tBid has no influence on the spin label mobility indicating that mVDAC1 and tBid are interacting in a 1:2 molar ratio. Additionally, the influence of glycerol was checked using mVDAC1-K12C-E59C, as all DEER measurements were performed in the presence of 20% glycerol. *cw* analysis revealed no influence of glycerol in tBid binding (Figure 48).

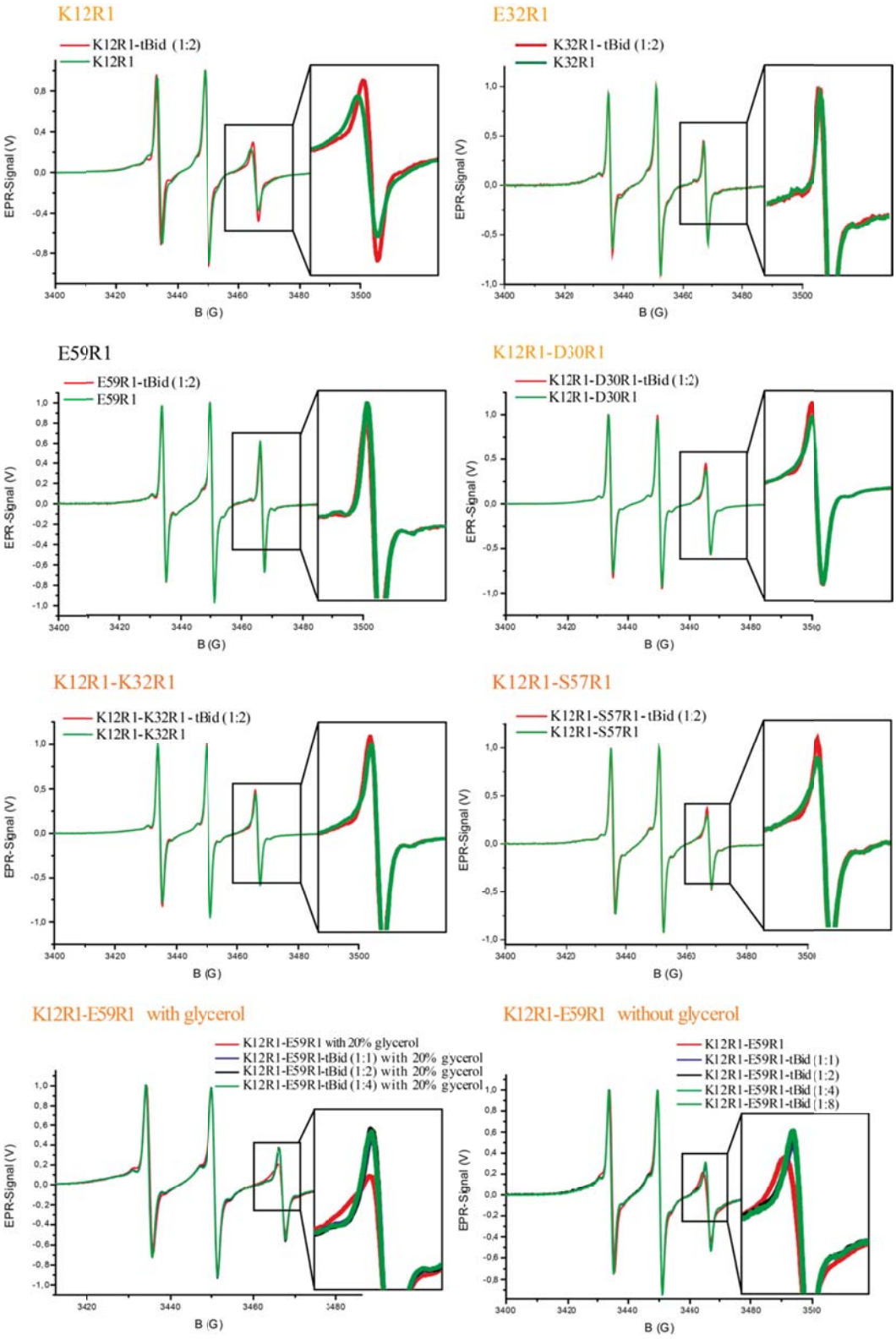

Figure 48: *cw* measurements of the mVDAC1-variants for determination of the influence of the α-helix upon tBid binding. Spectra were recorded for 20 min with a modulation amplitude of 1.5 G using X-band EPR spectrometers with an AEG H_{103} rectangular cavity or a dielectric resonator (*Bruker*). The magnetic field was measured with a B-NM 12 B-field meter (*Bruker*). *Cw* measurements were performed without (green) and with the addition of tBid (red). Inlays show *cw* signal change in detail. Orange variant names indicate significant changes in the spin label mobility.

The remaining six double-cysteine mVDAC1-variants 7-13 (Table 22) for analysing the influence of tBid on the β-barrel structure were characterised by *cw* measurements using the same setup. Interestingly, only an influence on the spin-label mobility could be detected in variants, where it was attached to the cytosolic side or located in the middle of the pore. The *cw* analysis suggests that the interaction of tBid occurs from the cytosolic side and influences the position of the α-helix (Figure 49).

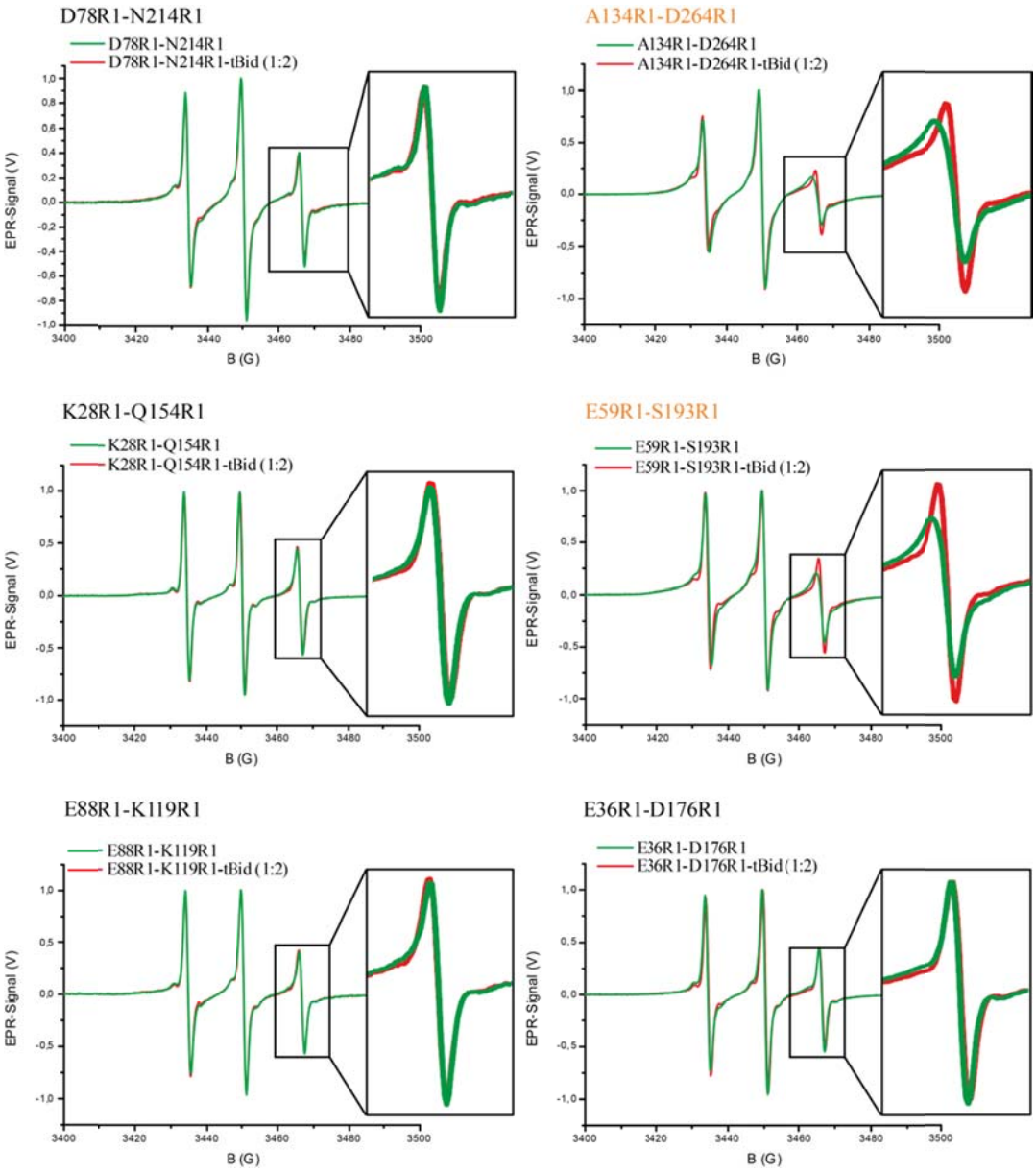

Figure 49: *cw* measurements of the mVDAC1-variants for determination of the influence of the α-helix upon tBid binding. Spectra were recorded for 20 min with a modulation amplitude of 1.5 G using X-band EPR spectrometers with an AEG H_{103} rectangular cavity or a dielectric resonator (*Bruker*). The magnetic field was measured with a B-NM 12 B-field meter (*Bruker*). *Cw* measurements were performed without (green) and with the addition of tBid (red). Orange variant names indicate significant changes in the spin label mobility.

Beside *cw* measurements the distance distributions of the spin labels in all mVDAC1-variants were determined. The measurements were performed with and without the addition of tBid to gather information about the structural rearrangement in mVDAC1. DEER analyses of the mVDAC1-variants for the α-helix involvement revealed that the helix becomes less flexible upon tBid binding as indicated by the form factor of the DEER measurements (Figure 50). For example, mVDAC1-K12C-E59C shows a broad distance distribution of the labelled positions. After tBid addition distances over 1.7 nm disappear, suggesting that the α-helix becomes less flexible.

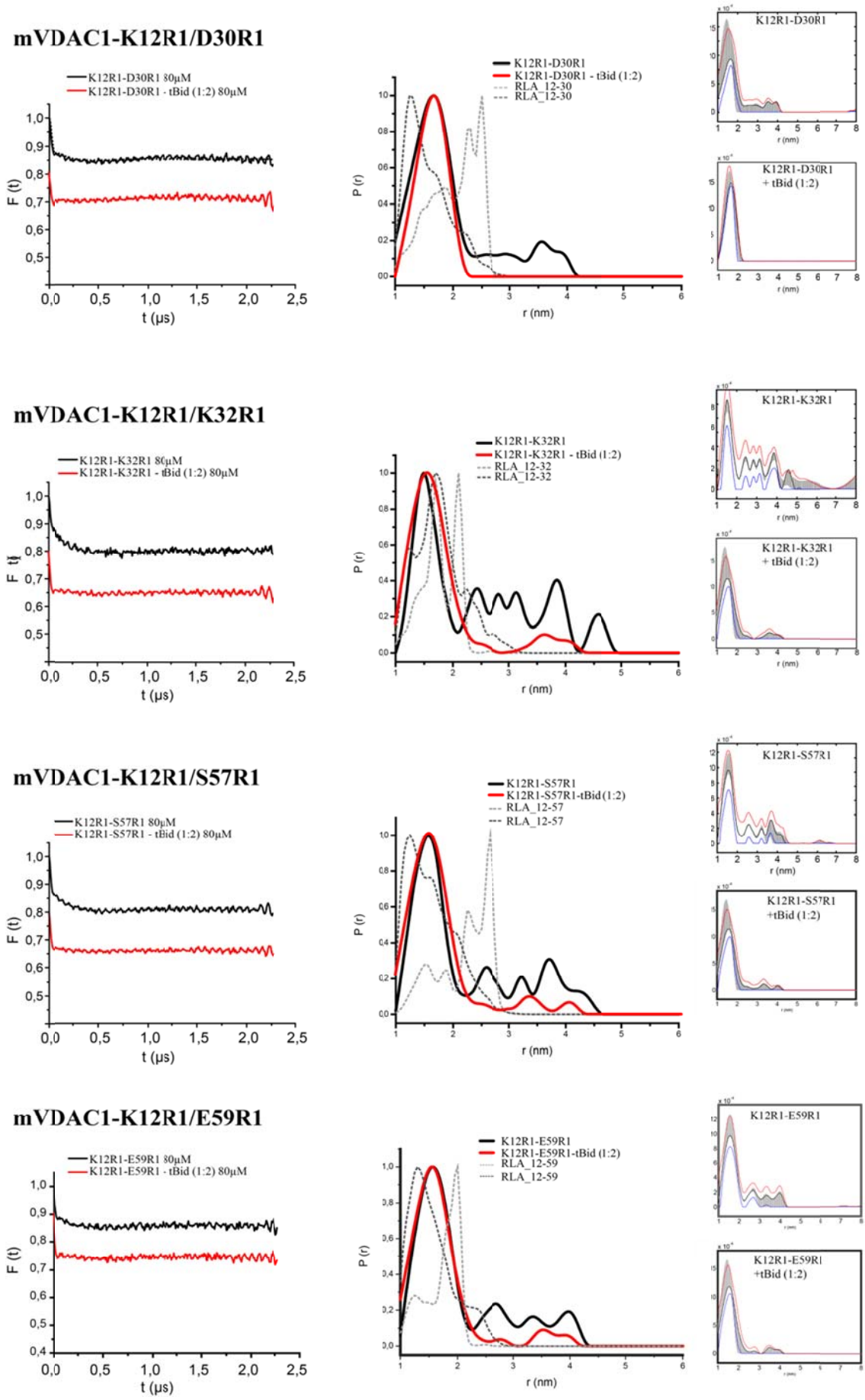
mVDAC1-K12R1/D30R1
K12R1-D30R1 80µM
K12R1-D30R1 - tBid (1:2) 80µM
F (t)
t (µs)
K12R1-D30R1
K12R1-D30R1 - tBid (1:2)
RLA_12-30
RLA_12-30
P (r)
r (nm)
K12R1-D30R1
K12R1-D30R1 + tBid (1:2)
mVDAC1-K12R1/K32R1
K12R1-K32R1 80µM
K12R1-K32R1 - tBid (1:2) 80µM
K12R1-K32R1
K12R1-K32R1 - tBid (1:2)
RLA_12-32
RLA_12-32
K12R1-K32R1
K12R1-K32R1 + tBid (1:2)
mVDAC1-K12R1/S57R1
K12R1-S57R1 80µM
K12R1-S57R1 - tBid (1:2) 80µM
K12R1-S57R1
K12R1-S57R1-tBid (1:2)
RLA_12-57
RLA_12-57
K12R1-S57R1
K12R1-S57R1 +tBid (1:2)
mVDAC1-K12R1/E59R1
K12R1-E59R1 80µM
K12R1-E59R1 - tBid (1:2) 80µM
K12R1-E59R1
K12R1-E59R1-tBid (1:2)
RLA_12-59
RLA_12-59
K12R1-E59R1
K12R1-E59R1 +tBid (1:2)

Figure 50: DEER analyses of mVDAC1-variants (c= 80 µM) that were used for the elucidation of mVDAC1´s α-helix involvement in tBid interaction before and after tBid (160 µM) addition. DEER measurements were accomplished at X-band frequencies (9.3-9.4 GHz) with a BrukerElexsys 580 spectrometer equipped with a Bruker Flexline split-ring resonator ER 4118XMS3 and a continuous flow helium cryostat ESR900 (Oxford Instruments) controlled by an Oxford Intelligent temperature controller ITC 503S for 24-36h. Left panels: DEER form factor (background-corrected dipolar evolution data) and fit (dashed line) before (black) and after (red) tBid addition. Middle panels: DEER distance distribution before (black) and after (red) tBid addition and theoretical distance distribution obtained by a Rotamer Library Analysis (RLA) (dashed lines) of the mVDAC1 crystal structure (pdb: 3EMN). Right panels: Validation of the DEER-analysis. Uncertainties in the distance distributions arise from (i) noise, and (ii) insufficient background correction. The reliability of the distance distributions is tested by systematic variation of the background. Grey shaded areas in the validation plots represent contributions in the distance distribution that depend on the background correction.

The remaining six double-cysteine mVDAC1-variants 7-13 (Table 22) for analysing the influence of tBid on the β-barrel structure were characterised by DEER measurements using the same setup. In accordance to the *cw* measurements, an influence on the form factor is observed when tBid binds to variants, where the spin-labels were attached to the cytosolic side or located in the middle of the pore. The variants, where the spin labels are located in the IMS, appear to be not affected in their overall structure (Figure 51). Basically, the influence on the β-barrel is not significant so that it can be postulated, that the overall β-barrel structure remains unchanged.

mVDAC1-E88R1-K119R1

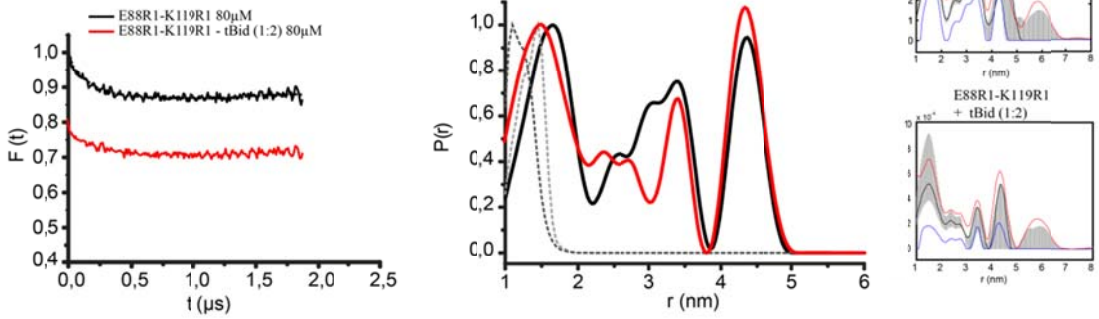

mVDAC1-E36R1-D176R1

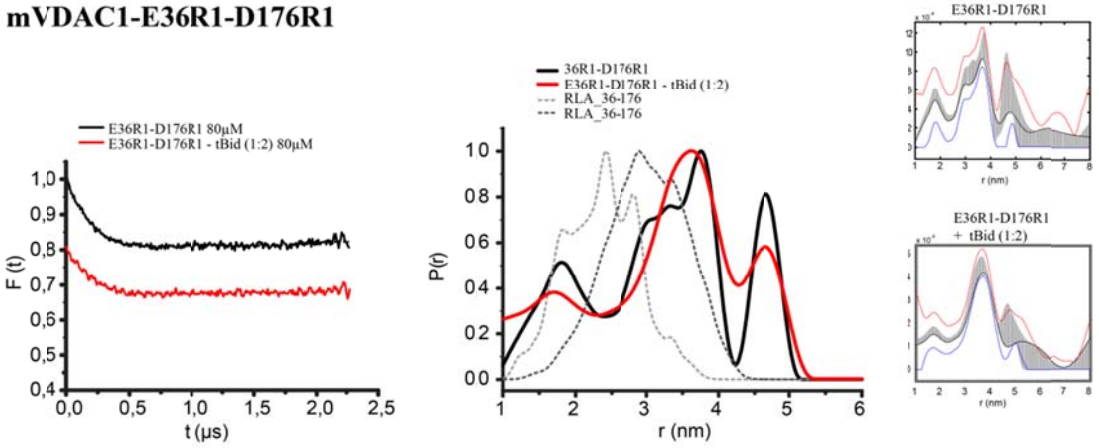

mVDAC1-E59R1-S193R1

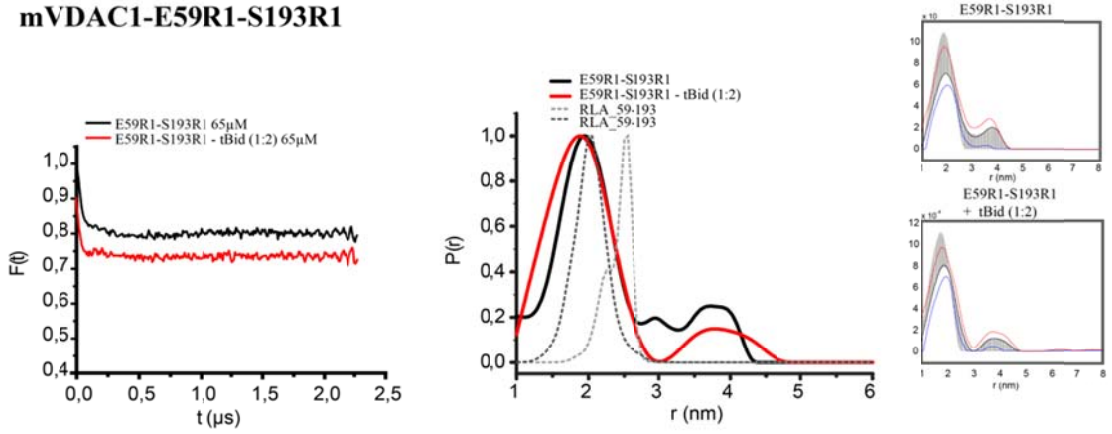

mVDAC1-K28R1-Q154R1

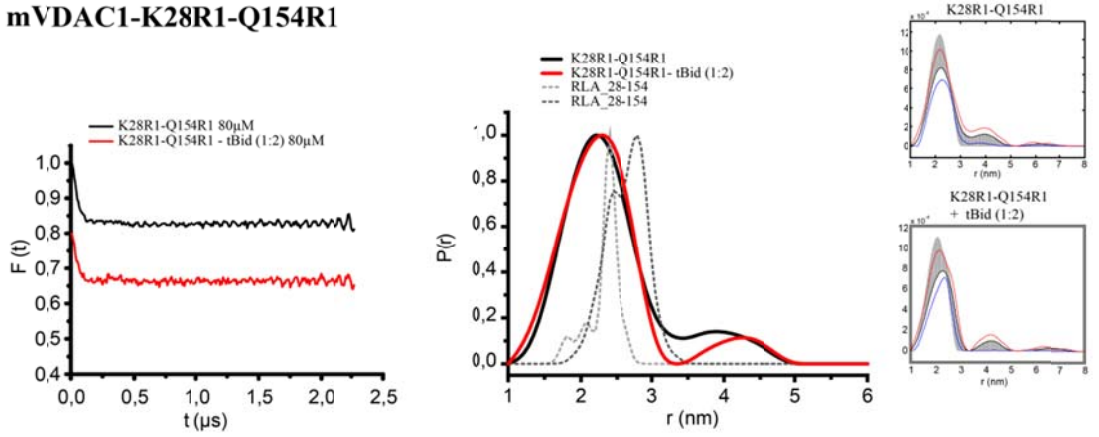

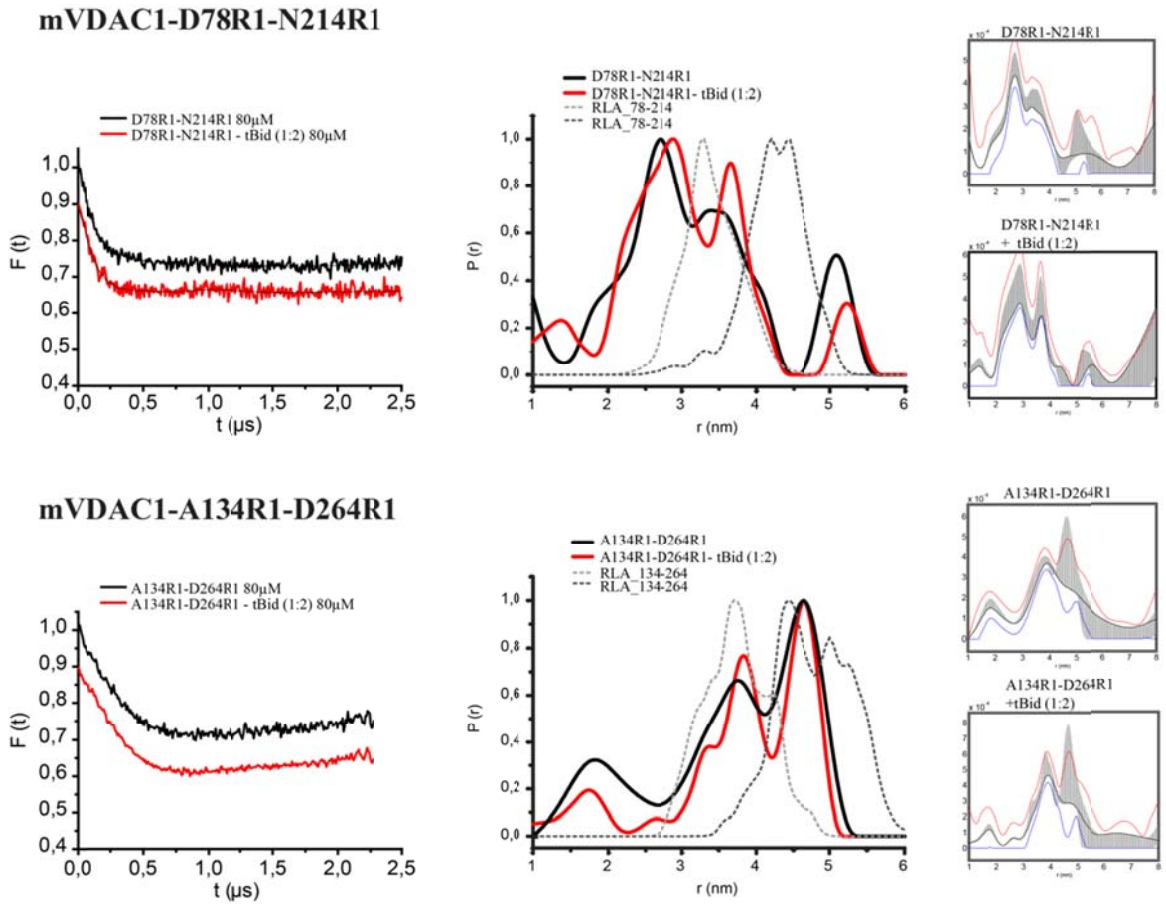

Figure 51: DEER analyses of mVDAC1-variants (65-80µM) that were used for the elucidation of mVDAC1´s β-barrel structure before and after tBid (130-160 µM) addition. DEER measurements were accomplished at X-band frequencies (9.3-9.4 GHz) with a Bruker Elexsys 580 spectrometer equipped with a Bruker Flexline split-ring resonator ER 4118XMS3 and a continuous flow helium cryostat ESR900 (Oxford Instruments) controlled by an Oxford Intelligent temperature controller ITC 503S for 24-36h. Left panels: DEER form factor (background-corrected dipolar evolution data) and fit (dashed line) before (black) and after (red) tBid addition. Middle panels: DEER distance distribution before (black) and after (red) tBid addition and theoretical distance distribution obtained by a Rotamer Library Analysis (RLA) (dashed lines) of the mVDAC1 crystal structure (pdb: 3EMN). Right panels: Validation of the DEER-analysis. Uncertainties in the distance distributions arise from (i) noise, and (ii) insufficient background correction. The reliability of the distance distributions is tested by systematic variation of the background. Grey shaded areas in the validation plots represent contributions in the distance distribution that depend on the background correction.

Additionally, EPR measurements revealed a tendency for mVDAC1 oligomerisation. E.g. mVDAC1-E59C DEER measurements resulted in a distance distribution of 2.1 nm, the distances in a predicted oligomer. Furthermore, even longer distances were recorded where a higher oligomerisation grade can be assumed. Taken this into account of the previous DEER results, the disappearance of the longer distances, observed in several mVDAC1 variants,

could also hint to a disruption of mVDAC1-oligomers by tBid. In detail, the mVDAC1-K12C-E59C variant shows the main distance distribution at 1.7 nm and several other distance distributions between 2.7 nm and 4.2 nm. The short distance resembles the measured distance between the two spin label positions in the crystal structure whereas 2.7 nm and 4.2 nm can be inferred a hypothetical mVDAC1 oligomer. The shift to smaller distances after tBid addition was also observed in the IMS mVDAC1-E88C-K119C variant. This variant shows likewise large distances, hinting to mVDAC1 oligomerisation. After tBid addition this kind of oligomerisation tendency disappears and only small distance distributions remain. In summary, mVDAC1 can apparently adopt a transient oligomeric state in detergent micelles that become disrupted by tBid binding (Figure 52).

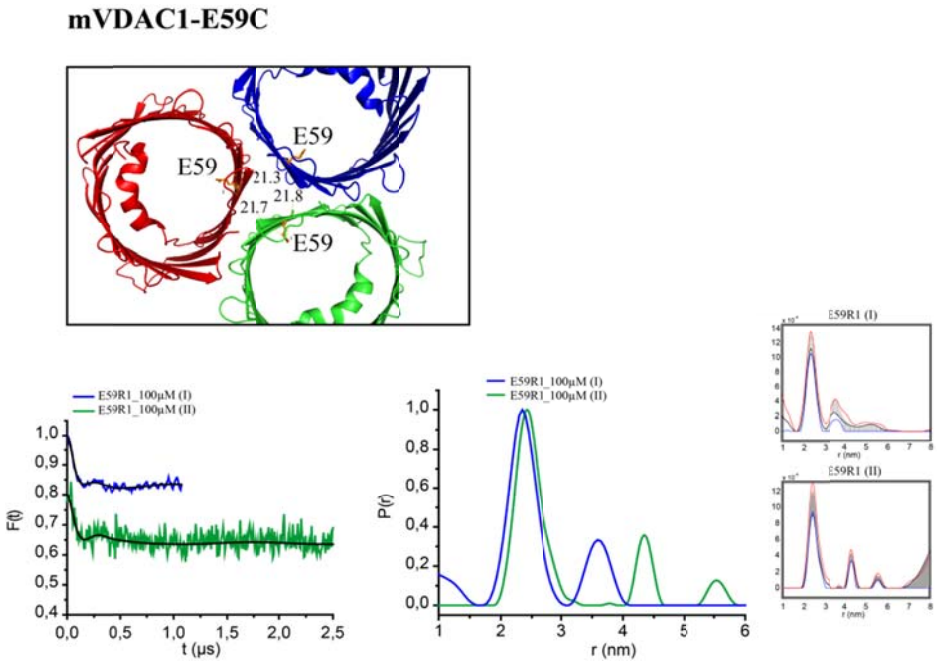

Figure 52: DEER analyses of mVDAC1-E59C (100 µM). DEER measurements were accomplished at X-band frequencies (9.3-9.4 GHz) with a BrukerElexsys 580 spectrometer equipped with a Bruker Flexline split-ring resonator ER 4118XMS3 and a continuous flow helium cryostat ESR900 (Oxford Instruments) controlled by an Oxford Intelligent temperature controller ITC 503S for 24-36h. Upper panel: Cartoon of mVDAC1-trimer based on the crystal structure (3EMN). Lower left panel: DEER form factor (background-corrected dipolar evolution data) and fit (black line). Lower middle panel: DEER distance distribution. Lower right panel: Validation of the DEER-analysis. Uncertainties in the distance distributions arise from (i) noise, and (ii) insufficient background correction. The reliability of the distance distributions is tested by systematic variation of the background. Grey shaded areas in the validation plots represent contributions in the distance distribution that depend on the background correction.

Taken together the EPR analysis demonstrates a clear structural change of mVDAC1 after tBid binding. Interestingly, mVDAC1´s N-terminus is somehow involved in the interaction as

indicated by the change in *cw* and DEER signals. In addition, the helix is less flexible after tBid binding corroborating the previously postulated interaction. In agreement with previous results, the binding side seems to be at the cytosolic side of mVDAC1 as indicated by *cw* and DEER measurements of the mVDAC1-β-barrel variants. Beside this, DEER measurements of the single-cysteine variants indicate a tendency of mVDAC1 for oligomerisation. After tBid addition the oligomerisation becomes disrupted, although further experiments have to be done.

4.3 A minimal porin reveals loop-independent channel closure

Beside VDAC1 as exceptional porin because of a) the presence of an N-terminal α-helix and b) the odd β-strand number, an engineered minimal porin (EMP) was analysed in terms of gating characteristics and structure stability. Porins, like the outer membrane protein G (OmpG) of *Escherichia coli*, are ideal templates amongst ion channels for protein and chemical engineering due to their robustness and simple architecture. Though OmpG shows fast transitions between open and closed states, which were attributed to loop 6 (L6), it tends to be not an optimal template. Therefore, EMP was engineered with all remaining extra membranous loops being truncated to provide a stable pore as ideal template for further ion-channel-engineering. Most of the results shown in this chapter were published in Grosse, Psakis, Mertins et al (2014).[59]

4.3.1 Expression, refolding and purification of the minimal porin

The minimal porin was overproduced as inclusion bodies analogous to mVDAC1, yielding 80 – 150 mg EMP per litre medium. Following cell disruption, the inclusion bodies were washed as previously described and a refolding screen was performed to determine the optimal refolding conditions. Accordingly, different detergents and refolding aids were tested in a two-step rapid dilution procedure similar to mVDAC1 (section 4.1.1). Supernatants were treated with acetone and the pellets were analysed by 12% SDS-PAGE (Figure 53).

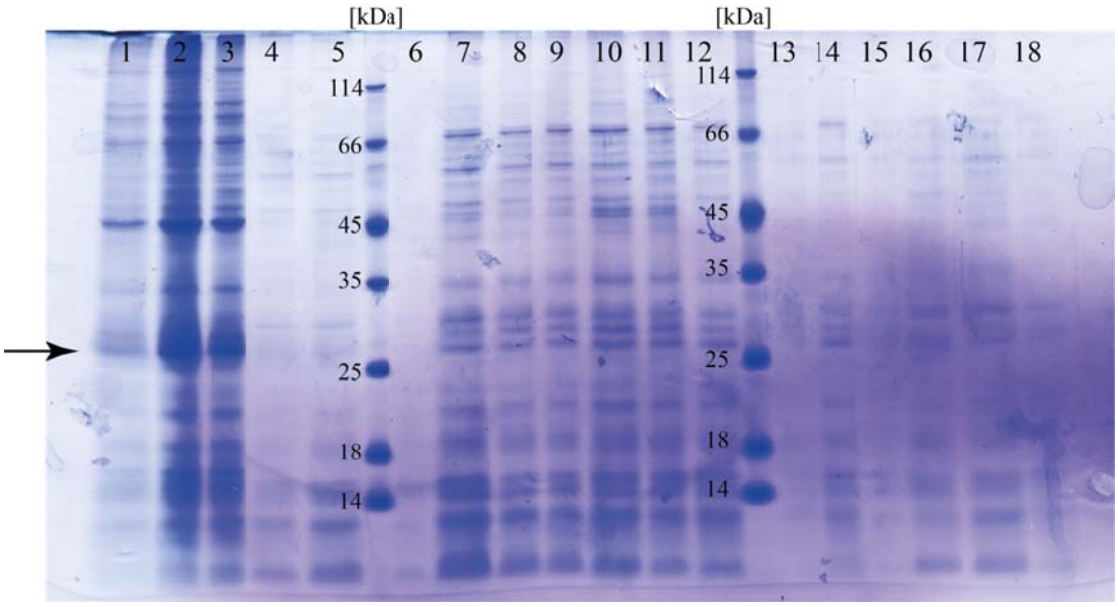

Figure 53: 12% Coomassie-stained SDS-PAGE analysis of the second step of the rapid dilution refolding screen for EMP, initial protein concentration was 10 mg/mL, 1: LDAO, 2: LDAO, 10% glycerol, 3: LDAO 10% xylitol, 4: n-OG, 5: n-OG, 10% glycerol, 6: n-OG, 10% xylitol, 7: C8E4, 8: C8E4, 10% glycerol, 9: C8E4 10% xylitol, 10: DM, 11: DM, 10% glycerol, 12: DM 10% xylitol, 13: n-DG, 14: n-DG, 10% glycerol, 15: n-DG 10% xylitol, 16: OTG, 17: OTG, 10% glycerol, 18: OTG, 10% xylitol; the arrow indicates the presence of refolded EMP.

The refolding screen revealed the presence of LDAO 10% glycerol as being optimal for a two-step rapid dilution protocol. All further preparative refoldings of the minimal porin were performed under these conditions. Interestingly, refolding attempts in other mild detergents such as β-OG, DM or C_8E_4 failed to yield monomeric EMP.

EMP was purified in two steps using IMAC and SEC. Because of the presence of LDAO micelles, IMAC purification was performed by a TALON-column. The high affinity of the cobalt ion enhances protein binding so that pure EMP was obtained. Elution was performed using a continuous gradient of 0-150 mM imidazole. A representative chromatogram and the corresponding 12% SDS-PAGE are shown in Figure 54.

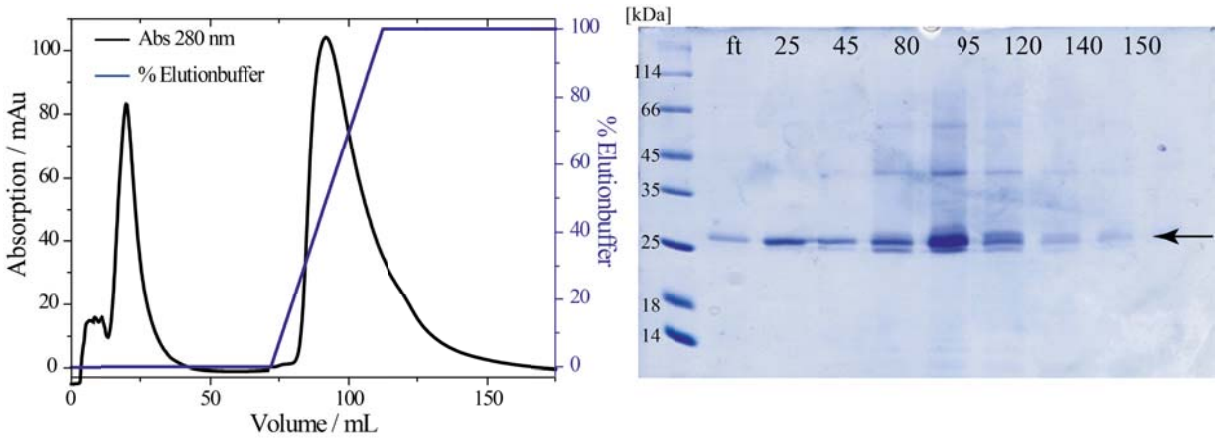

Figure 54: Representative IMAC-chromatogram and 12% Coomassie-stained SDS-PAGE analysis of EMP, SDS-PAGE lanes correspond to the elution volume (ft = flow through); the arrow marks purified minimal porin.

SEC was used for further purification and analysis of homogeneity and oligomerisation. In SEC, recombinant EMP, refolded in LDAO micelles, eluted as a mixture of dimers and monomers as indicated by a broad elution peak (I) and the later narrow peak (II). The retention of the peak II (60 ml) corresponds to an apparent molecular mass of 85 kDa, so that a monomeric species of EMP in LDAO micelles can be assumed (26 kDa EMP + 59 kDa LDAO micelle). Peak I (45-58 ml) indicates the presence of a dimeric species of EMP. Western blotting and mass spectrometry confirmed the identity of refolded/purified EMP monomers. The SEC and SDS-PAGE/western blot analysis is shown in Figure 55.

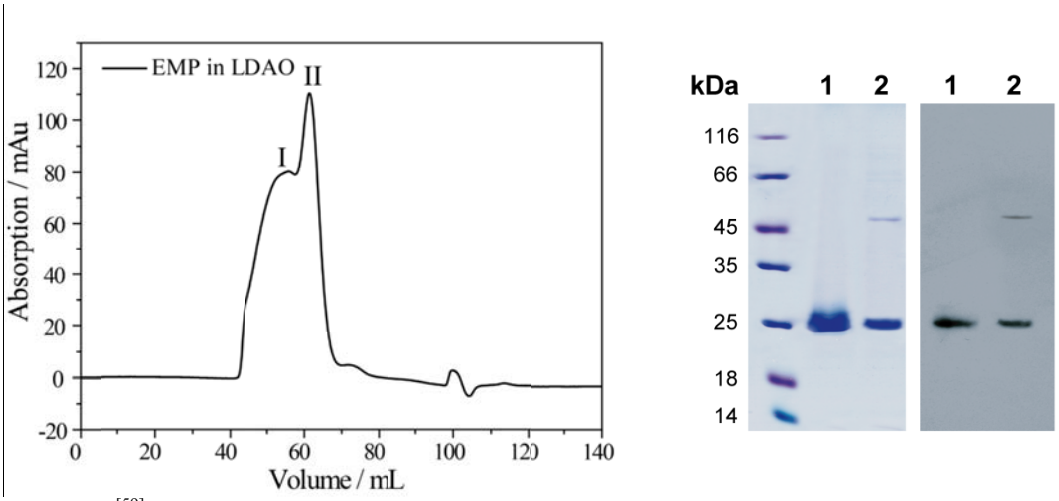

Figure 55:[59] Left panel: Elution profile of EMP-LDAO micelles from the Superdex 200 size-exclusion-column 16/60 (*GE Healthcare*). The expected size for EMP was 26 kDa. Right panel: 12% SDS-PAGE and Western blot of peak II (lane 1; 0.5 µg) and I (lane 2; 0.2 µg) fractions with micelle-embedded EMP.

In addition, EMP tends to further dimerise dimers is increased by time. An additional SEC after two days revealed only EMP-dimers as indicated by a sharp elution peak (45-58 ml) (Figure 56).

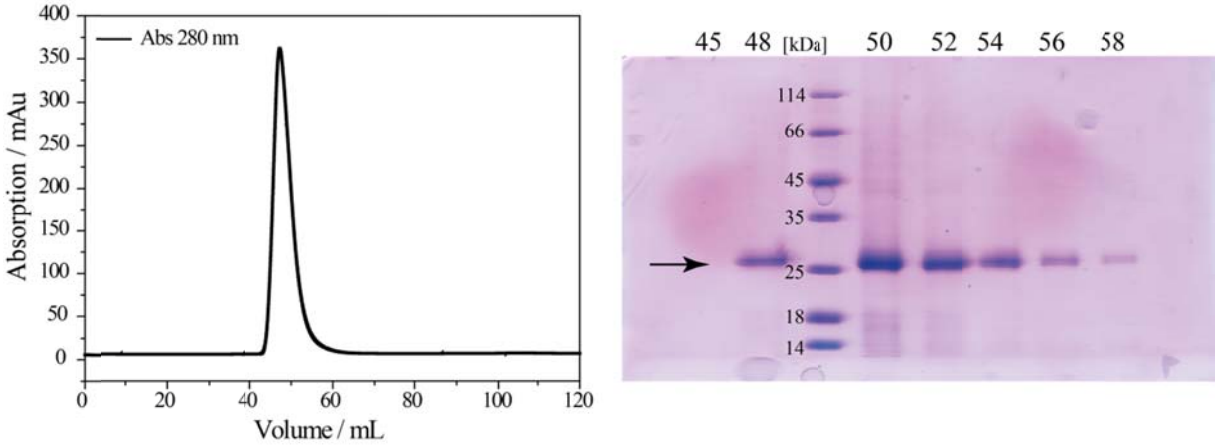

Figure 56: SEC-chromatogram and 12% Coomassie-stained SDS-PAGE analysis of EMP after two days at 8°C, the sharp peak indicates the presence of a stable EMP dimer; Coomassie-stained SDS-PAGE lanes correspond to the elution volume; the arrow marks purified minimal porin.

For all analytical experiments, EMP was characterized immediately after purification, assuming the prevalence of monomeric EMP.

4.3.2 Structural characterization of EMP

All structural characterisations were done using monomeric EMP. The structural characterisation of EMP by CD and OCD was done by Dr Georgios Psakis (University of Huddersfield) and Dr Dirk Windisch (Karlsruher Institute of Technology). For comparison, the results of OmpG and the deletion variant L6 are shown here as well. All of these OmpG variants were produced, purified and analysed by Dr Wolfgang Grosse. As expected, CD analyses of monomeric EMP indicate a β-barrel conformation, being highly comparable to those of OmpG and its L6 variants (Figure 57).

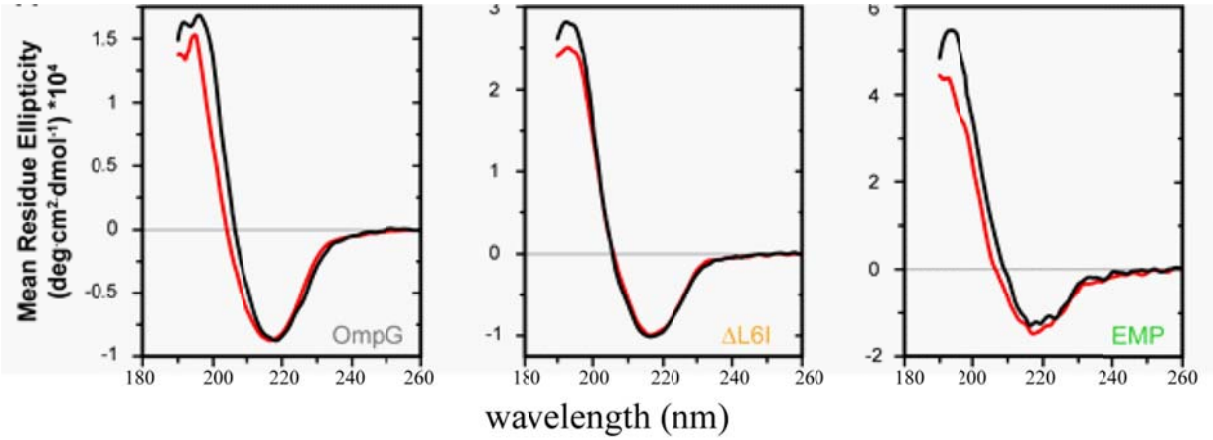

Figure 57: (adapted from [59]) Far-UV CD spectra of OmpG, ΔL6I variant and EMP in DMPC. Spectra were recorded below (20 °C, black) and above (35 °C, red) the DMPC phase transition temperature.

After first CD measurements a thermal unfolding scan by CD was performed. The analysis of its melting curve indicates that thermal unfolding of EMP is cooperative and irreversible. Confidence about this was gained by the strong hysteresis upon cooling as well as the hypsochromically shifted CD spectrum of heat-denatured EMP. Interestingly, the thermal stability of monomeric EMP is about 10° C higher compared to OmpG so that an exact determination of its T_m is impeded (Figure 58).

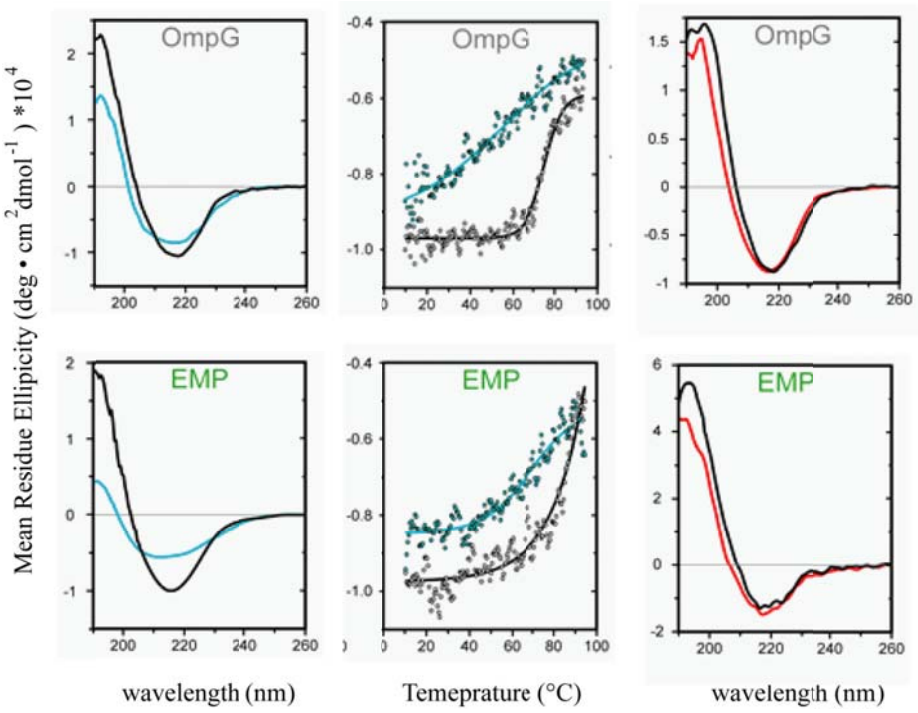

Figure 58: (adapted from [59]) CD analysis of OmpG and EMP in detergent micelles and isotropic vesicles. Left: Far-UV spectra of proteins (0.03-0.07 mg/ml) in 10 mM KP_i, 0.05% v/v LDAO, pH 7.4, at 20 °C, before (black) and after thermal denaturation (cyan). Middle: Heating (black), cooling (cyan) denaturation of OmpG and EMP. Right: Far-UV spectra of proteins in DMPC, in 10 mM KP_i, pH 7.4, at 20 °C (black) and 35 °C (red).

Another difference to OmpG is the stronger tendency of monomeric EMP to aggregate at high temperatures as indicated by the ~60% reduced intensity of the CD spectrum after thermal unfolding and cooling. This mild protein aggregation is strengthened by the observation of increased high *voltage*/dynode signals of the spectrometer´s photomultiplier during heating as well (particle-generated light scattering) (Figure 59). Nevertheless, EMP is a highly robust porin as it can be stored over weeks at 4 °C without apparent aggregation.

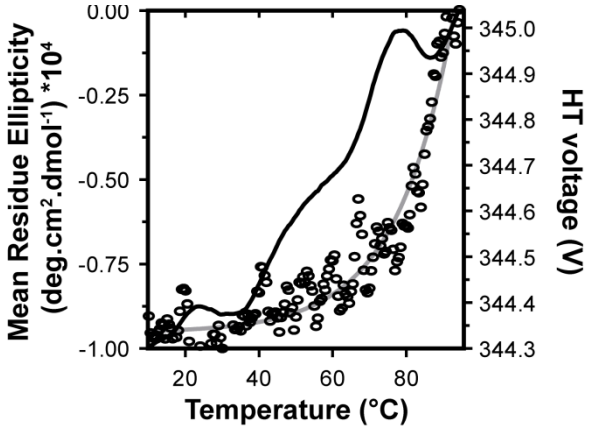

Figure 59: (adapted from [59]) Heat denaturation profile of EMP (0.03 mg/ml) in LDAO (0.05%, v/v) (open circles). The dynode voltage signal (HT, solid black line) increases following the gradual denaturation of EMP, as a result of aggregate-generated scattering. The HT signal reaches its maximum at 80 °C. Then, following a short decrease, indicative of partial protein precipitation, the voltage rises again until 90 °C is reached.

OCD analyses of EMP in DMPC vesicles (Figure 60) revealed that EMP is changing its orientation when inserted in bilayers below (20 °C) and above (35 °C) the lipid-phase transition temperature. Below the transition phase, the DMPC membrane is thicker and therefore EMP incorporates as expected in a tilted manner as indicated by the strong positive band at 190 nm. Interestingly, above the phase transition EMP seems to be even more tilted as indicated by the drop of the 190 nm band. This is not further surprising though the membrane is thinner and therefore EMP cannot incorporate in an upright manner. In addition the negative band at 218 nm is significantly increased. Therefore, and as mentioned for mVDAC1, the max:min relation is closer to 1, indicating that the β-strands are more tilted. These OCD results demonstrate clearly that EMP is sensitive to bilayer thickness.

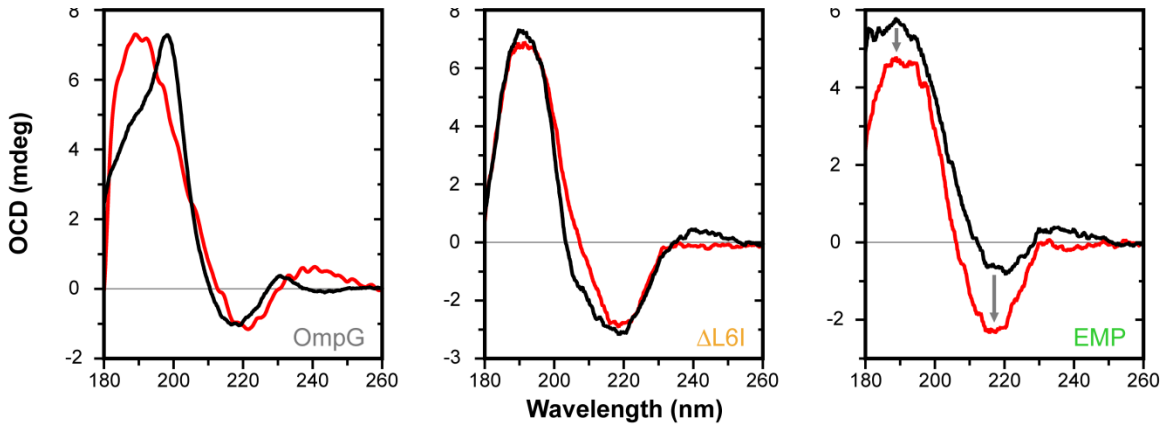

Figure 60: [adapted from [59]] OCD spectra of OmpG, ΔL6I variant and EMP in DMPC; OCD spectra were recorded using a J-810 or J-815 spectropolarimeter (*Jasco*). For reduction of artefacts, three spectra were recorded for every 45° rotation of the cell around the beam axis. Grey arrows indicate directional changes in the EMP spectra.

4.3.3 Electrophysiological properties of EMP

In BLM measurements EMP channels showed 1.2-fold higher conductances (N = 38, P $<10^{-3}$) compared to OmpG. Interestingly the EMP conductances were found in a range of 0.86 ±0.02 nS to 1.06 ±0.04 nS and dependent on pH and the type of lipids (Figure 61). For example, EMP showed higher conductances in DMPC than in asolectin and at pH 7.4 than at pH 5.0. EMP was thought to represent a permanent open pore as all essential parts for OmpG gating were removed. Surprisingly, distinct partly closed states of EMP were observed, where the pore suffered a 26-66% reduction of conductance relative to the open state. As mentioned above, switching to these closed states was pH- and lipid-dependent. In detail, in asolectin at pH 7.4, EMP channels achieved only two partly closed states with conductances of 0.64 ±0.02 nS (S1: N = 19) and 0.38 ±0.01 nS (S2: N = 9). At pH 5.0, an open state (S0: 0.92 ±0.03 nS, N = 19) and two partly closed states (S1: 0.47 ±0.02 nS, N = 23; S2: 0.24 ±0.02 nS, N = 11) were observed. The same conductances for open and closed states were observed in DPhPC indicating a strong pH and a minor lipid influence on EMP. In detail, in DPhPC and neutral pH EMP switched between the open (S0: 1.06 ±0.04 nS, N = 21) and two partly closed states (S1: 0.67 ±0.05 nS, N = 17; S2: 0.42 ±0.05 nS, N = 8). Again the conductance of EMP at acidic pH was reduced to 0.86 ±0.02 nS (S0, N = 35), 0.52 ±0.03 nS (S1, N = 24) and 0.28 ±0.02 nS (S2, N = 30), respectively (Figure 61).

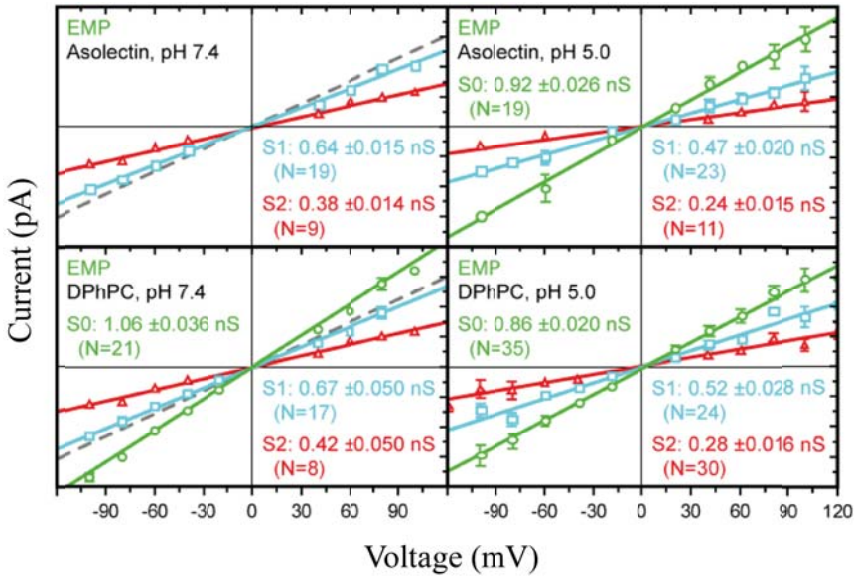

Figure 61: (adapted from [59]) Ohm plots for conductances of EMP. EMP conductance varies with pH and type of lipid. In asolectin and at neutral pH EMP occupies only partially closed states (S1 cyan, S2 red), under acidic pH it additionally acquires a fully open state (S0 green). In DPhPC, EMP behaviour is inverted as it conducts more strongly at neutral rather than acidic pH. OmpG conductance appears in all graphs as a dashed grey line for comparison.

The conductances of EMP appear to be independent of the lipid bilayer but dependent on the pH. Furthermore, the open probabilities for EMP depend on the composition of the bilayer. In asolectin membranes and at pH 7.4, EMP channels have a 6-fold reduction of their open probability and a 5-fold reduced gating transition frequency compared to OmpG (Figure 62C). Accordingly, the 2D event distribution plots as derived from current recordings of EMP in asolectin membranes (+80 mV), revealed few gating events with duration in the 31 ms to 1 s range (Figure 62B). On the other hand, the influence on open probabilities and transition frequency is reduced in DPhPC bilayers. Here the open probability at pH 7.4 is reduced by the factor 2 and the transition frequency showed just a three-fold reduction. Nevertheless a strong effect on EMPs gating is observed (Figure 62C). As with asolectin, the mean dwell times of EMP gating in DPhPC ranged from 1 ms to 31 s (Figure 62). Furthermore, under acidic conditions the previous effects were inverted, and EMP channels displayed now stronger gating characteristics in asolectin than in DPhPC membranes.

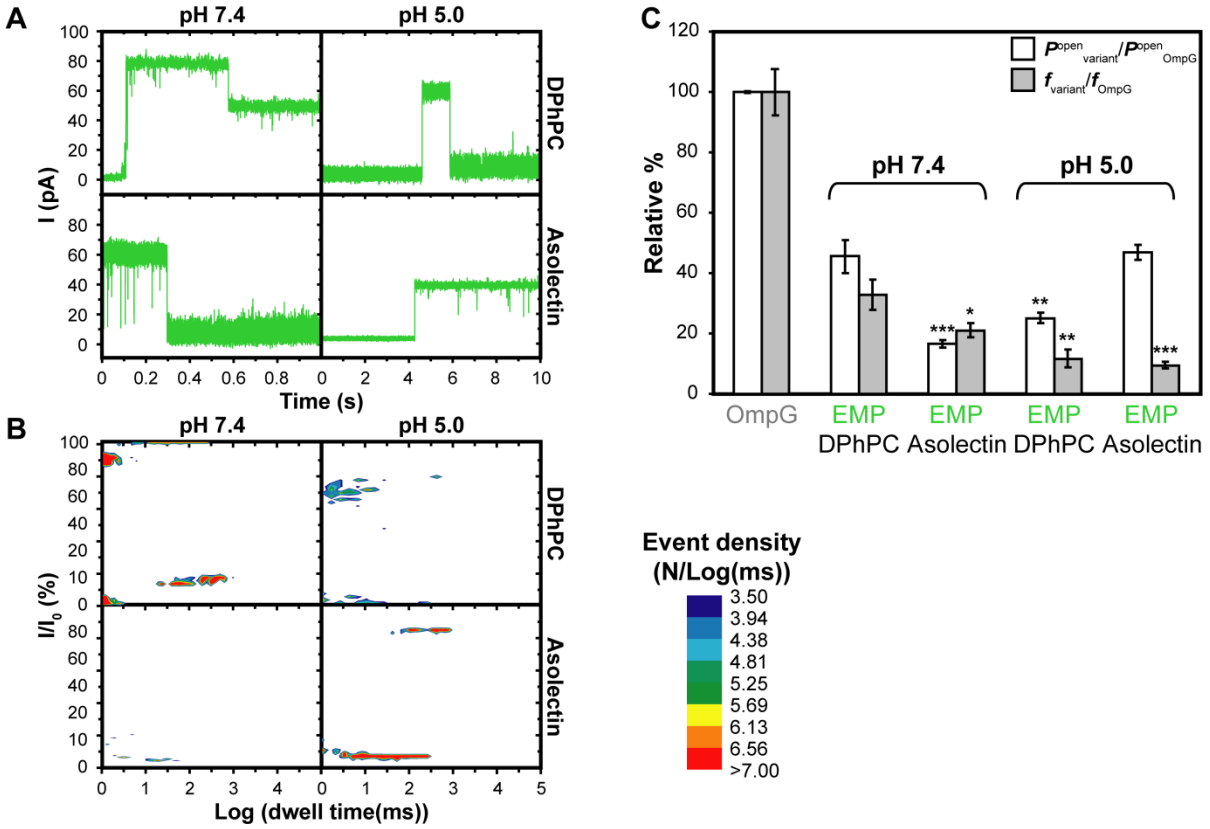

Figure 62: (adapted from [59]) Influence of pH and type of lipid on gating characteristics of EMP. (**A**) Typical +80 mV single-channel recordings of EMP at pH 7.4 or pH 5.0 in asolectin and DPhPC, used for the generation of the 2D distribution plots in (**B**) 2D event-distribution plots of the switching behaviour of EMP. Distribution of events for 30 s of recorded time is plotted according to the current intensity *I* and dwell times. *I* (colour code on the right) is expressed as a percentage of the highest intensity I_o. (**C**) Comparison of the gating behaviour of OmpG and EMP (Table S2). *f* and the P_o of EMP are expressed as a percentage of OmpG. Bars denote standard errors of triplicate measurements, stars statistically significant differences (paired t-test: * $P \geq 0.069$; ** $P < 0.0232$ and *** $P \leq 0.0067$) with respect to EMP in DPhPC (pH 7.4) values.

.

5. Discussion

5.1 VDACs are the most important porins of the outer mitochondrial membrane

With about 10 000 copies per cell the voltage-dependent anion channels (VDACs) are the most abundant proteins of the mitochondrial outer membrane (OM).[26] VDACs can be found in three isoforms in *metazoa* and can occur in up to 11 isoforms in plants. Although all isoforms are thought to share the same overall structure, their specific functions remain unclear.

VDACs are located in the outer mitochondrial membrane (OMM) and are known to be involved in mitochondrial processes such as ATP-, calcium or ROS-transport. Beside this, they were identified as key players of mitochondrial physiology such as being involved in the mitochondria-related apoptotic pathway. Accordingly, they are acting as docking platform for pro and anti-apoptotic proteins. Furthermore, VDACs were found to be involved in various diseases like Alzheimer, Down syndrome, cancer, stroke, and amylotrophic lateral sclerosis (reviewed in [29, 38]) (Figure 63). As crucial exchange pore in the OMM VDACs exhibit a high medical relevance as being potential pharmaceutical targets. Although the key players of apoptosis seem to be identified the exact mechanism remains largely unclear. For this, elucidation of VDACs´ involvement in apoptosis and related diseases has a high relevance.

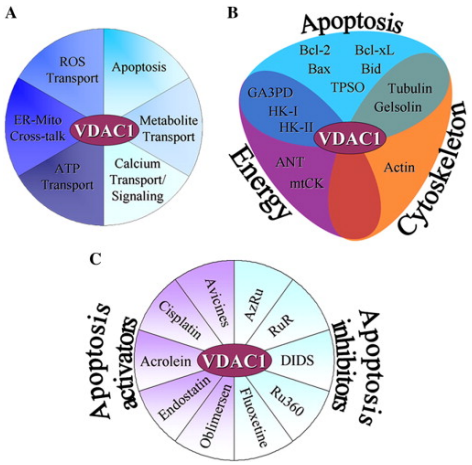

Figure 63:[29] Schematic representation of VDAC1´s multiple functions and interactions with associated proteins or drugs. (**A**) Cellular processes in which VDAC is involved, illustrating its multifunctional properties. (**B**) Proteins interacting with VDAC include proteins involved in processes such as apoptosis, energy production and regulation, and structural proteins of the cytoskeleton. Some proteins are involved in more than one function. (**C**) Several drugs act *via* VDAC as either inductors or inhibitors of apoptosis.

In the past years an increasing number of proteins have been identified to interact with VDACs. These proteins were found to be pro- or anti-apoptotic or even pro-survival as found in cancer cells. It is not yet proven whether all these interactions happen directly with a specific VDAC isoform or whether the nature of these interactions is unspecific towards VDACs. In addition, the structural modes of interaction remain elusive although structures for individual components are already available.

By characterising VDAC1´s gating mechanism and defining its distinct interaction pattern with the pro-apoptotic protein tBid, I highlight the critical role for VDAC1 as a mitochondrial receptor. Accordingly, the VDAC1-tBid complex provides a major control point in neuronal demise.

5.2 Gating mechanism in porins

A major class of membrane proteins are the so called porins. These large channels are located in the outer membrane of gram negative bacteria (OmpG, OmpF, OmpA, OmpX),[42, 185] as well as mitochondria (VDACs).[158] or forms parts of microbial toxins that assemble on membranes to form oligomeric transmembrane channels (α-HL).[65] Apart from the VDACs with their 19-stranded β-barrels, all prokaryotic porins possess a β-barrel structure with an

even number of β-strands. As consequence of the odd-numbered strands of VDACs their N- and C-termini are both facing inside the mitochondrial inter-membrane space.[22]

The switching between high and low conductances observed in transmembrane channels is called “gating”. This gating occurs because of a change in the transmembrane voltage and its mechanism is assumed to be basically the same in all porins. A link between the observed gating in patch clamp and lipid bilayer measurements and a physiological relevance is not proven yet but may mainly reflect the distinct conformational substates adoptable by porins.

5.2.1 Voltage-responsive β-barrels: Small structural changes - large effects

Porins are classified in high-specific (LamB, ScrY), low-specific (OmpF, OmpG, PhoE) as well as non-specific porins (OmpX, OmpA) due to the substrates, which are capable to pass these channels. Additionally, there are porins formed by the polypeptide chains of toxins (α-HL, TolC). Because of the increasing number of solved β-barrel structures this classification appears to be a bit archaic. A contemporary classification scheme may arrange the β-barrel porins according to their gating behaviour to demonstrate common and different features.

One of the best studied porins is the trimeric outer membrane protein F (OmpF) (Figure 64). The overall structure of OmpF consists of three separate channels connected by a loop (loop 2, L2). The monomeric channels are constricted by an additional loop (loop 3, L3) located at the middle of the barrels.[47] Interestingly, L3 is built of a small helix, whereas loops of other porins are folded as random coil. OmpF adopts open or closed conformations, depending on the applied voltage. To explain the achievement of these states two fundamentally different mechanisms have been hypothesized. One of these mechanisms involves the movement of L3 restricting the diameter of the pore and thereby closing it.[186] The second mechanism focuses on a redistribution of charges in the channel resulting in closure of the pore.[187] Although a structural rearrangement of L3 seems to be the most obvious and easiest explanation of OmpF´s closure, this hypothesis turned out to be invalid. Prilipov *et al* demonstrated by deletion variants and mutations in the loop 3 that gating is not dramatically affected by L3.[187] Furthermore, multiple small rearrangements of fixed charges

in the lumen of the channel appear to cause diminished metabolite flux. Overall, OmpF is a porin, where the switch between an open and closed conformation is caused by small structural changes and a charge rearrangement.

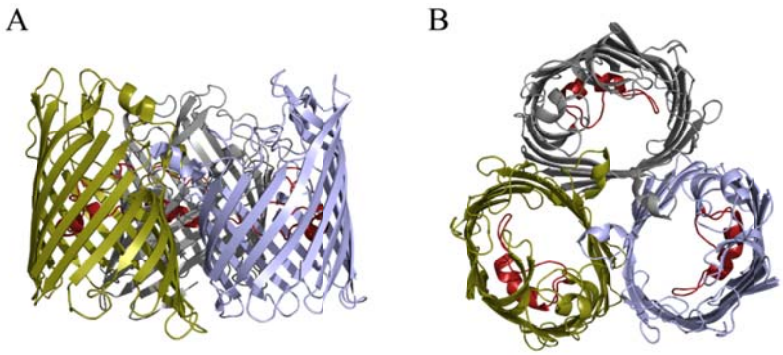

Figure 64: Trimeric structure of OmpF (pdb code 1OPF[47]), monomers are shown in grey, light blue and yellow, loop 3 (red) is responsible for the channels switching mechanism, **A** side view of the OmpF trimer, **B** top view (extracellular) of the OmpF trimer.

Another prominent porin found in outer membranes of gram-negative bacteria is the small outer membrane protein OmpA (figure 65 **A** and **B**). OmpA is formed of 8 β-strands and has a role in the linkage of the outer membrane to the periplasmic peptidoglycan layer.[62] Furthermore, the extracellular loops are involved in bacterial conjugation or other recognition events. Interestingly, it was found that OmpA switches between a high and a low conductance state and therefore suits the definition of gating. These gating events apparently occur because of side-chain-side-chain interactions in its barrel. Additionally, the same side-chain-side-chain interactions were found in the crystal structure that represents the closed state.[63] a new model for the gating mechanism of OmpA was indicated by MD simulations and displayed an involvement of salt bridges in the channels side-chains. By conformational flickering of Arg138, that forms alternate salt bridges with Glu52 and Glu128, the closed and the open state are achieved (Figure 65C). [64] Taken together OmpA shows a switching pattern based on transient salt bridge formation.

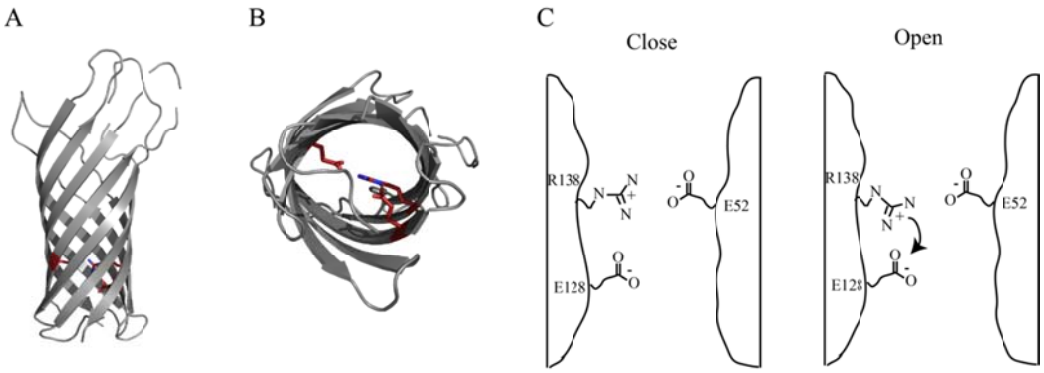

Figure 65: Structure (grey) and gating of OmpA (pdb code 1BXW[63], the residues E52, R128 and R138 are responsible for OmpAs gating (red), **A** Side view of OmpA, **B** Periplasmic view of OmpA, **C** Proposed gating mechanism.(adapted from [64])

A third type of gating is exemplified by the monomeric porin OmpG (Figure 66), which is produced upon stress response. OmpG consists of 14 β-strands forming a straight barrel without any constrictions in the inside. Interestingly, and contrary to OmpF and OmpA, OmpGs gating is controlled by the flexible loop 6. The crystal structure of OmpG in the closed state allows further insights in the loop 6-dependent gating.[45] OmpG exhibits fast channel transitions between open and closed states in planar lipid bilayer recordings. By deletion of loop 6 Grosse *et al* demonstrated the importance of this loop in voltage response.[59]

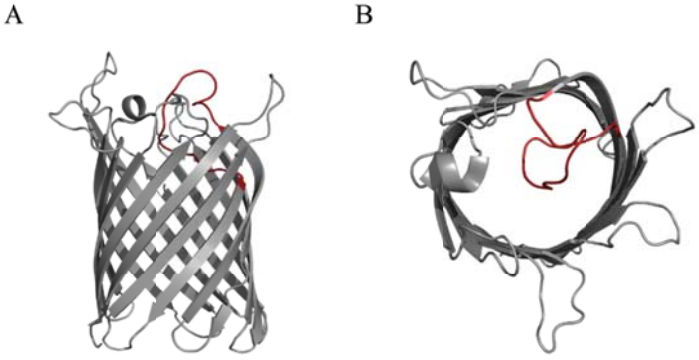

Figure 66: Structure of OmpG (grey) (pdb code 2IWW[45]), loop 6 (red) is responsible for the channels gating mechanism, **A** side view of the OmpG, **B** top view (extracellular) of the OmpG.

Taking together, these porins show three major gating mechanisms, a) small structural rearrangements of amino acids leading to a rearrangement of charges, b) formation and breakage of salt bridges and c) big structural rearrangements leading to a mechanical closing of the pore. Of course also a combined mechanism can occur as formation of salt-bridges result in a rearrangement of charges within the pore as well.

5.2.2 The N-terminus as a crucial element of VDAC´s gating

Among the class of β-barrel transmembrane proteins, the VDAC-like porins represent one of 27 known superfamilies [188] showing remarkable differences to all other β-barrel transmembrane superfamilies. After their discovery, VDACs have been extensively studied in terms of their structural organisation and their gating mechanism. [26, 189] Before the elucidation of VDACs´ 3D-structure, various hypotheses about the gating were proposed for rationalising the known gating patterns. For example, it was proposed that VDAC achieves the different conductance states by a loop region, comparable to OmpG´s gating.[34] After publishing of the 3D structures of mVDAC1 and hVDAC1 by three independent groups using either X-ray crystallography, solution-state NMR or a hybrid X-ray/NMR approach (Table 23) the formerly proposed mechanisms had to be rejected. VDAC1 is commonly described as a 19 β-stranded pore - yet atypical for porins - with overall dimensions of 27 x 24 Å. As consequence of the odd numbers of β-strands β19 and β1 are aligning in a parallel way. [22, 25, 32] The N-terminal part of VDAC is α-helical and aligns to the inner barrel wall [22] or at least localizes in the pore's interior, constricting the channel to an inner diameter of 14 Å. [32] All these structures are assigned as the open state and contradict earlier models of a 13-16 stranded pore that implied loop dependent gating. [28]

Table 23: X-ray and NMR structures of VDACs and special achievements.[190]

Isoform	Origin	Method	Resolution	PDB code	Reference
VDAC1	mouse	X-ray	2.3 Å	3EMN	Ujwal *et al* (2008)
VDAC1	human	X-ray / NMR	4.1 Å	2JK4	Bayrhuber *et al* (2008)
VDAC1	human	solution NMR	rmsd: 3.6 Å	2K4T	Hiller et al (2008)
VDAC2	zebra fish	X-ray	2.8 Å	4BUM	Paz et al (2014)
			Achievements		
VDAC1	human	NMR/LDAO micelles	direct interaction between VDAC1 and Bcl-xL		Malia, Wagner (2007)
VDAC1	human	NMR/DMPC nanodiscs	VDAC1 in nanodiscs adopts native fold		Raschle et al (2009)
VDAC2	human	NMR/LDAO & DMPC nanodiscs	sequence-specific resonance assignments		Yu et al (2012)

The N-terminal region in the pores interior fuelled further debates about the gating mechanism of VDAC. [191, 192] VDACs, as other porins, are capable to switch between a high and several low conductance states, representing the open and closed channel, respectively. [7, 22, 31, 158, 178, 193] NMR-spectroscopic analyses indicate that the N-terminal helix exhibits an increased mobility favouring it as a tentative regulatory part. [25, 33, 194] Brownian dynamics calculations and molecular dynamics simulations have revealed the dependence of the channel's ion selectivity on salt concentration, with low salt concentrations favouring the gating of anions in the open state. [181, 182, 188, 195]

Having in mind that porins gating is mostly achieved by loops the situation in VDACs is less straight-forward. First, no major loop appears to be a prominent candidate in occluding the channel, and secondly, although the N-terminal α helix appears position-wise to exert control on the flux of metabolites [196], latest NMR studies [197] revealed distinct mobility only for strands β2-β7. Here, the N-terminal helix appeared relatively rigid, raising doubts in its involvement in controlling gating transitions.

Several studies suppose different types of conformational rearrangements to explain the complexity of the switching events. An early model by Hiller and Wagner suggested a movement of the N-terminal α-helix within the pore region.[33] In general, they propose two modes for channel closure. The first mode is based on movement of the whole N-terminal part (residues 1-20) from the wall to the middle, with the hinge region displaying flexibility. The second mode was explained by a twist/turn motion of only the helical stretch G11-K20 within the pore. The problem with the latter mechanism is its failure to explain the changing preferences of anions and cations in the open and closed state as demonstrated by *in silico* approaches of Choudary *et al*. [34]

Choudary claimed a mechanism, where the helix moves out of the barrel to induce an electric field capable of accounting for the changing ion preferences. In addition several other groups provided evidence that the N-terminus may have just a local, stabilizing effect but is not the final cause for VDAC gating.[198, 199] As indicated by solid-state NMR, the β-barrel mobility itself may be responsible for the switching.[198] This observation was strengthened by spectroscopic data from electron impedance and surface-enhanced infrared absorption, where the observed results were interpreted as a sign for an overall barrel deformation that correlates to the different closed states.[199]

Furthermore, Teijido *et al*.[189] reported that the mVDAC1-L10C-C127A-A170C-C232A mutant displayed native-like channel activity under oxidative conditions, and concluded that

voltage gating did not involve and/or require rearrangements of the covalently linked N-terminal fragment.

Geula *et al* proposed an N-terminal fragment detachment from the pore wall and subsequent translocation to the cytoplasmic side ("paddle" movement) upon VDACs opening.[200] All possible switching modes are summarised in Figure 67.

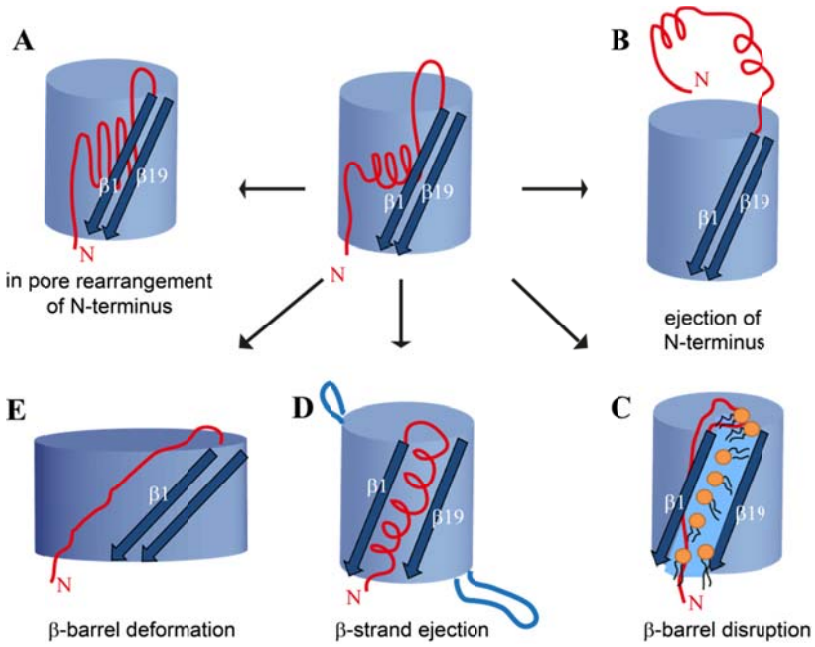

Figure 67:[190] Overview of proposed switching modes to achieve both, ion selectivity and subconductance states in VDACs. Switching is achieved by conformational changes of the N-terminal region either staying inside the barrel (**A**) [33] or moving outside (**B**) [34]. **C**: disruption of the continuous β-barrel at β1 and β19 followed by lipid inversion. Overall deformation of the pore by strand ejection causes a smaller remaining β-barrel (**D**) [28] or squeezing the pore to inhibit ion flux (**E**).[199]

None of the proposed suggestions for VDAC´s gating mechanism was able to explain all biochemical and electrophysiological findings on VDACs. Accordingly, the following chapter will highlight mVDAC1s N-terminus as a crucial element for gating.

5.2.2.1 Gating mechanism of VDAC1

In this work, the crystal structure of mVDAC1 (pdb code 3EMN [22]) was used as a template for the design and construction of all double-cysteine variants. All observed results like disulphide-bridge-formation, BLM measurements as well as EPR measurements, are in accordance to the crystal structure. Consequently, this work provides further support to the proposed 19-β-stranded 3D-structure and the proposed biologically relevant open state. [192]

To address the N-terminus as crucial element for the gating mechanism a setup of different experiments was performed. Like previous BLM and patch-clamp measurements [22, 32, 35, 158, 160-162, 188] reconstituted mVDAC1 exhibits a 3.94 ± 0.04 nS conductance in the open state (S0), whereas the average conductance of the closed state is 2.34 ± 0.06 nS, differing significantly ($P = 10^{-4}$) from previously published values (Table 24). Usually, VDAC1 is described as having one open and multiple closed states, where the overall conductance of the closed state is 50% of the open state. By analysis of previously published data, it is obvious, that the closed state is not just suffering 50% reduction of the overall current but adopts multiple states ranging from 35-65% of the open state. Additionally, there were at least two previously recognized but not well defined major states (S1, S2) [201]. In our setup, we could define the two closed states exhibiting 60% and 40% conductance compared to the open state. Furthermore, the S2 state itself splits into two further sub-states, S2A and S2B, in a 2.4:1 ratio. S2B exhibits a 1.52 ± 0.04 nS conductance almost the half of the S1 state. This precise description of the closed states is not only important to decipher the channels functionality but also to explain the switching mechanism of different VDAC variants with potentially subtle gating phenotypes. In addition, the overall flexibility of the N-terminus and the high variety of the closed states of VDAC could be an explanation, why VDAC interacts with a range of pro- and anti-apoptotic proteins by adopting structural substates.

Table 24: Conductance values for mVDAC1 variants following their reconstitution in planar lipids. Adapted from [99]

Protein	Reference	Open State (nS)	Closed state (nS)	Salt composition
mVDAC1	Ujwal *et al.* [22]	3.70 ± 0.40[a]	1.70 ± 0.20[a]	1 M KCl 5 mM $CaCl_2$
mVDAC1	Abu-Hamad *et al.* [35]	4.00	ND	
Δ 1-26-mVDAC1	Abu-Hamad *et al.* [35]	4.00	-	
hVDAC1	Hiller *et al.*[32]	3.90 ± 1.50[a]	ND	1 M KCl
hVDAC1	Shanmugavadivu *et al.* [162]	4.50 ± 0.50[a]	ND	1 M NaCl
hVDAC1	Engelhardt *et al.* [160]	~ 5.00	2.00	1 M KCl
NcVDAC1	Popp *et al.* [161]	4.0	2.00	
rVDAC	Colombini *et al.* [158]	4.50	ND	
ScVDAC	Colombini *et al.* [158]	4.50	ND	
mVDAC1	Mertins *et al.* [99]	3.94 ± 0.04[b] (S0)	2.61 ± 0.01[b](S1) 1.90 ± 0.06[b] (S2)	1 M KCl 5 mM $CaCl_2$
Δ1-21mVDAC1-Y22C		4.00 ± 0.04[b] (S0)	-	
mVDAC1-C127A-C232A		3.78 ± 0.09[b] (S0)	2.50 ± 0.12[b] (S1) 1.78 ± 0.09[b](S2)	
mVDAC1-CL-A14C- S193C (oxidized)		3.74 ± 0.05[b] (S0)	1.85 ± 0.07[b](S2) low probability	
mVDAC1-A14C-C127A- S193C -C232A (reduced)		3.70 ± 0.01[b] (S0)	1.95 ± 0.08[b] (S1) 1.67 ± 0.09[b] (S2)	
mVDAC1-CL-V3C-K119C (oxidized)		3.28 ± 0.04[b] (S0)	1.77 ± 0.09[b] (S2)	
mVDAC1-V3C-K119C- C127A-C232A (reduced)		3.98 ± 0.04[b] (S0)	~2.70 (S1) 2.05 ± 0.13[b] (S2)	

[a] values given with their standard deviations; [b] values given with their standard error; ND, not determined.

5.2.2.2 The N-terminal α-helix of mVDAC1 affects its gating characteristics

By characterizing the N-terminally truncated deletion variant Δ21-mVDAC1 an evident arrest in the open state was found, sharing similar characteristics with the Δ26-mVDAC1 deletion variant described by Abu-Hamad *et al* (Table 24). This indicates that the N-terminus of VDAC is at least involved in gating (Figure 68).[35] In agreement with previous observations [161, 163], current recordings of the Δ21-mVDAC1 deletion variant were characterized by some flickering corroborating the notion of a stabilizing effect of the N-terminal fragment for the whole pore as well. The lasting flickering can be explained by rapid transitions between different channel's sub-states not solely attributed to the mobility of the N-terminal fragment, but also to other structural components of mVDAC1. Additionally, NMR data also suggest a stabilising effect of the N-terminus on the pore´s conformation.[202] Nevertheless, the role of the helix seems to be more important than just ensuring overall stability.

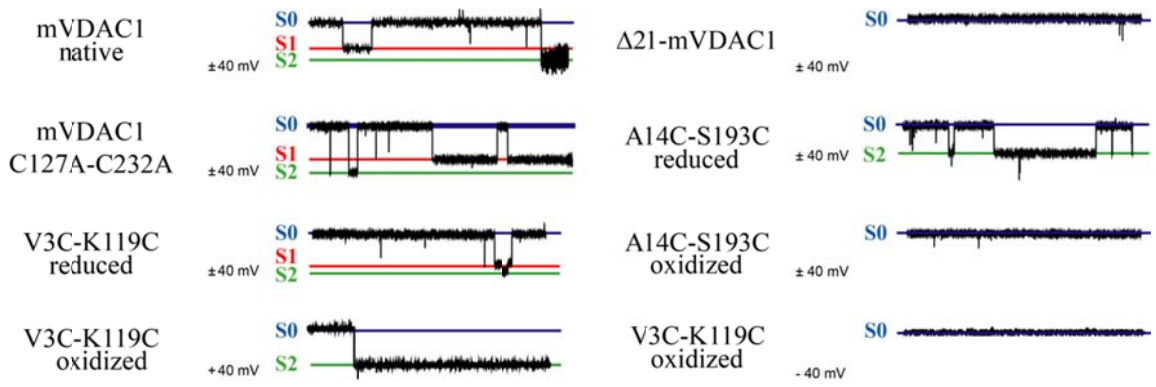

Figure 68: Overview of the gating profiles of VDAC1 variants, all variants adopt the high conductance state (S0 (blue)). The two distinct closed states (S1 (red) and S2 (green)) can only be achieved when full flexibility of the N-terminus is available.

To address the flexibility of the N-terminus during the switching mechanism, we engineered and characterized double-cysteine variants for immobilising different parts of the N-terminus within the β-barrel. The cross-linked mVDAC1-A14C-S193C channel exhibits a clear preference for the open state (average dwell time 30.6 min) and switches hence to the S2 state only with a strongly reduced probability (Table 24, Figure 68). Having achieved the closed state, this variant fails to re-open. The residual switching of mVDAC1-A14C-S193C could be explained by the mobility of residues 1-13 and the subsequent hinge region (KGFGYG) that is highly conserved in *metazoa*. The observed arrest in the open state of this variant for ~30 min indicates that the middle of the helix is involved in the opening of the native channel.

In mVDAC1-A14C-S193C the hinge region remains free and is therefore able to undergo conformational changes that could cause the channel's closure.

Surprisingly, the oxidized and subsequently reconstituted mVDAC1-V3C-K119C variant, exhibits an asymmetric gating characteristics. It conducts in the open state at both negative and positive potentials, and closes only upon application of a reversed potential. Furthermore, the transitions between open and closed states were mediated *via* a series of substates (Figure 69). This behaviour was never described before for a VDAC variant. The final closed state of mVDAC1-V3C-K119C was comparable to wild type´s S2 state (Table 24, Figure 68).

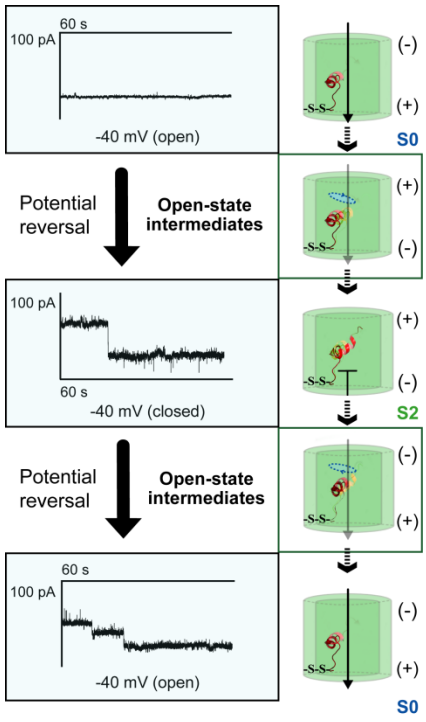

Figure 69: [99] CuX_2Ph pre-treated and subsequently reconstituted V3C-K119C-mVDAC1 conducted in the open state upon application of both negative and positive potentials (e.g. −40 mV) but closed only at one set of potentials (e.g. +40 mV), depending on its orientation in the lipid layer. As indicated in the corresponding traces (one step closing, two-step opening) and the adjacent cartoons, the gating behaviour was dynamic in both directions, and was probably mediated by a series of short-lived intermediates. The probable movement of the 5–14 residue part is sketched (dashed blue ellipticity). Cross-linking at the base of the channel is designated –S-S-. Polarity of the membrane is indicated.

The open-to-closed state transitions of mVDAC1-V3C-K119C occur slower than in the wild type, extending the dwell time of the cross-linked channel in the open state to 78.6 s. As the switching activity surprisingly lacks the expected symmetrical behaviour of the native channel one can postulate that only one direction of the applied electric field relative to the membrane-

embedded VDAC porin destabilizes its fixed helix. Furthermore, the behaviour of this channel upon potential reversal suggests that the residue 4-26 stretch is still capable to undergo structural reorganizations allowing for slower S0-to-S2 transitions.

Taken together, the results of the cross-linked VDAC1-variants demonstrate the importance of the flexibility of the N-terminus. Affixing of residue 14 to the barrel wall locks the pore in an open state and tends to be more effective than affixing residue 3. Switching was not completely blocked for both variants probably because of an incomplete oxidation of these variants or a higher flexibility of the N-terminus as previously assumed. BLM findings for both variants were providing new phenotypes for gating, suggesting that the full flexibility of the N-terminal fragment is required for achieving transitions to and/or from the S1 state, and that S0-to-S2 can occur independently of S0-to-S1 transitions, probably *via* meta-stable intermediates of an alternative route (Figure 70).

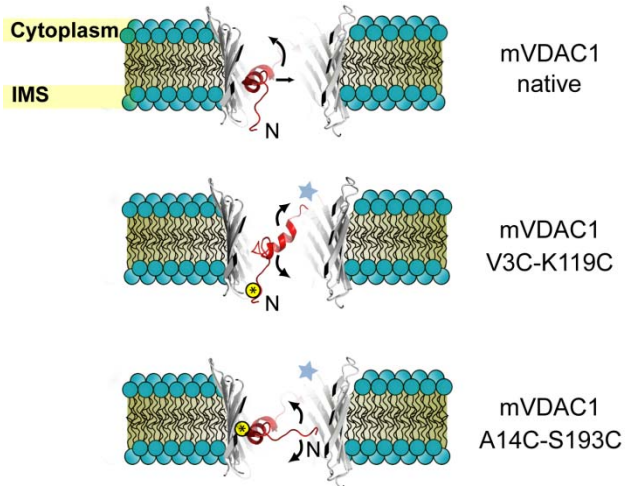

Figure 70:[99] Cross section of a 3D-model of mVDAC1, based on the 3EMN structure, parallel to the membrane plane. Cross-linking at the base and midpoint of the pore is indicated (yellow circled asterisk). Possible dynamic movements of the α-helix and the 1-4 residue N-terminal part are described for the two cross-linked mutants relative to the native channel. Arrows indicate possible directions of movement.

As mentioned above, Teijido *et al* [189] reported that the mVDAC1-L10C-C127A-A170C-C232A mutant displayed native-like channel activity under oxidative conditions, and concluded that voltage gating did not involve and/or require rearrangements of the covalently linked N-terminal fragment. Contrary to that, both our mVDAC1 double cysteine variants show distinct gating profiles under oxidative conditions, avoiding the S1 and relaxing only to the S2 state. The reasons for the observed behaviour of the mVDAC1-L10C-A170C variant can be manifold. For example, *in situ* oxidation as performed by Teijido *et al* [189] failed for all

of our mVDAC1 variants under the chosen BLM conditions. Only *in vitro* oxidation provided a complete oxidation as verified by ESI-MS. Furthermore, in all our variants the use of a charged N-terminal affinity tag for purification was refrained, to guarantee the absence of any side effects. As demonstrated by Weichbrodt [203] even a slightly prolonged N-terminus leads to a higher mobility of the very N-terminus and thus to flickering in BLM measurement. The characterisation of a VDAC1 variant with such a prolonged N-terminus (RGS) revealed accordingly a new gating phenotype.

5.2.2.3 A model for mVDAC1 closure involving local unfolding/refolding events

Based on the results, a model of VDACs closure mediated by the concurrence of 1) a flipping motion of the far N-terminal part into the middle of the channel and 2) a local unfolding/refolding event of the α-helix can be proposed (Figure 71). Compared to the literature it is obvious that this model can explain both, the ion selectivity and the observed substates. The closure of the cross-linked VDAC variants could be explained by another model based on the flexibility of the N-terminus. Here, the closure is mediated by mechanical strain effects, stemming from the movement of the hinge region, which can further induce either a) the structural collapse of the barrel wall b) the irreversible unfolding of the N-terminal helix or c) a combination of the two. All scenarios could result in permanent channel closure as observed for the oxidized mutant.

In conclusion, I have demonstrated that conformational restriction of the N-terminal α-helix dynamics strongly affects the gating characteristics of mVDAC1. Therefore, the question has to be addressed whether the substates and the observed flexibility can be linked to a biological relevance. It is known that VDACs are capable to interact with a plethora of different effectors and therefore it is highly plausible that the different substates relate to the achievable states after effector binding (Figure 71). Surely, and as suggested by molecular dynamics simulations, [34, 197] the N-terminal segment is not the only determinant of the channel's activity and selectivity, but it plays, however, an essential part, supported undoubtedly by the structural plasticity of the barrel wall.

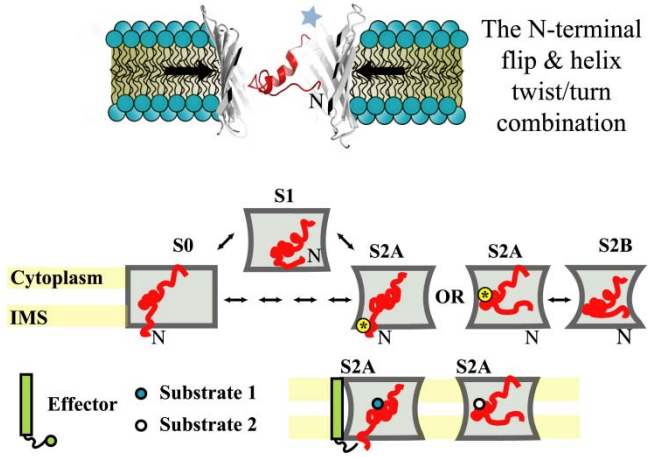

Figure 71:[99] Native channel voltage gating involves concurrent movement of the very N-terminal part into the pore and induction of channel narrowing by partial wall collapse**.** In the open S0 state, the helix is located at the mid-point of the pore with the far N-terminus facing the IMS. Switching to the S1 closed state is initiated upon movement of the far N-terminus into the pore and corroborating movements of the pore's wall. Oxidized mutants (yellow circled asterisk) become immobilized in an S2A state, exhibiting restricted N-terminal fragment flexibility and impeded barrel wall movement. In the S2B state movements of both the barrel wall and the N-terminus are most complete. Effectors could control S1↔S2 transitions enabling or prohibiting interactions with substrates thus regulating apoptotic responses. Note that transitions to the S2 state can be S1-independent.

5.2.2.4 Gating behaviour of VDAC2s - the involvement of salt bridges and cysteines

VDAC2 is highly homologous to VDAC1 (sequence identity 71 %) and hence shares a common overall structure (Figure 72). Therefore, the same gating mechanism was assumed. Recently, the 3D crystal structure of VDAC2 from zebra fish was published showing the same overall structure as mVDAC1 and hVDAC1.[204] As VDACs were initially numbered according to the order of their discovery, a comparison of isoforms from different species can be however misleading. While structural predictions of β-strands in the transmembrane β-barrel proteins are generally difficult, a classification upon VDACs N-terminal sequence seems to be more rewarding.[190] VDACs' N-termini vary in length between different isoforms, *e.g.* human VDAC2 has a prolonged N-terminus compared to hVDAC1. The N-terminus of VDAC2 from zebra fish is shorter than hVDAC2 and therefore more comparable to hVDAC1.

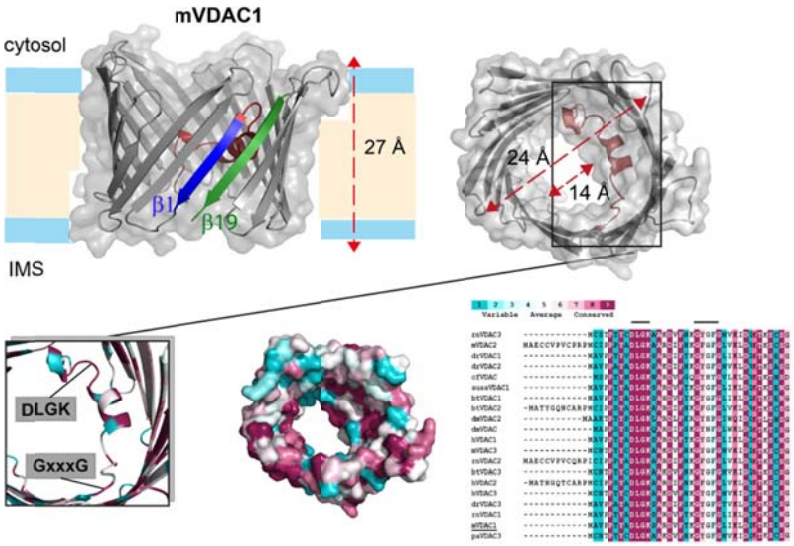

Figure 72:[190] Overall structure of VDACs, including a comparison of structural similarities of VDACs in *metazoa*, Multiple sequence alignments (MSA) were analysed for conservation by the CONSURF server (http://consurf.tau.ac.il). Colours indicate the levels of conservation; from highly conserved (maroon) to highly variable (light-blue) residues (as classified by CONSURF). Top: crystal structure of mVDAC1 as side view (left) and top view (right) β1 (blue) and β19 (green) are closing the pore, the N-terminus is shown in red; lower left: detailed structural view on the N-terminal regions, lower middle: surface representations of VDACs showing the pore from the cytosolic side, lower right: MSA depicting the N-terminal region.

While all VDAC isoforms share significant sequence identity in *metazoa*, mammalian VDAC1 and VDAC2 show antagonist functions during apoptosis.[205, 206] While VDAC1 is believed to be able to induce or at least promote apoptosis, VDAC2 is described to be anti-apoptotic. In contrast to VDAC1, VDAC2 has a prolonged N-terminus and harbours 11 cysteines instead of two in VDAC1. The function of VDAC2 and its cysteines still remain elusive. One hypothesis is that VDAC2 is involved in neutralizing reactive oxygen species (ROS) that are generated in the IMS and are able to induce apoptosis.[206, 207] The cysteines in the VDAC2 structure are of special interest because a) cysteines are known to interact with metal ions and b) cysteines are pH- and redox-sensitive.

As expected, VDAC2 respond in lipid bilayer measurements to an applied voltage but with altered gating characteristics compared to VDAC1. As demonstrated above, the maximum conductivity of mVDAC1 was 3.94 nS in the open state and 2.61 and 1.90 nS in the closed state at pH 8.6. In contrast, VDAC2 showed a conductivity of only 0.86 nS in the "open" state and 0.02 nS in the "closed" state at pH 8.6. Both values are very low and differ significantly

from the observed values in VDAC1. Apparently VDAC2 is permanently impaired in term of conductance under these conditions although small transitions were observed. Interestingly, at pH 6.2 the channel restores a conductivity of 3.48 nS similar to VDAC1, although the closed state adopts still very low conductances of ~ 18% (0.63 nS). Having in mind how VDAC2 was prepared for BLM it is obvious, that this pH dependent gating behaviour is reversible. First, VDAC2 was refolded at pH 6.0, then the pH was raised to 8.5 for purification and finally, the pH was lowered again only during BLM measurements. Therefore, a denaturation of the VDAC2 structure during preparation can be excluded.

The effect of the strong pH dependency of VDAC2 is known from other β-barrels. OmpG is described to close not only by voltage application but also as a result of a pH shift.[56] At acidic pH loop 6 folds into the pore and thereby closes the whole channel as observed in electrophysiological measurements. The structural rearrangement of OmpG was also described by X-ray crystallography, where loop 6 was found to pleat into the pore.[45] Furthermore, pH-dependent closing was observed for OmpF where large extracellular loops fold into the channel at low pH or high voltages.[208] Another example for a strong pH dependency is the Bcl-2 family protein BAX.[209] BAX exhibits a conductance of 0.731 nS at pH 4.0, whereas the overall conductance drops to 0.329 nS when being shifted to pH 7.0. Especially this protein family is quite interesting when discussing pH-dependence of VDAC as many members of the family interact directly with VDACs. Therefore, a physiological regulatory effect of presumably all VDACs can be postulated upon pH changes.

In all given examples, pH-dependency is explained by a structural rearrangement of specific parts of the protein. Following this, the dominant structural rearrangement in VDAC2 upon pH shift has to be addressed. The most obvious structure in VDACs is the N-terminal α-helix that forms a dominant part for switching. Therefore, this region could be involved in structural rearrangements as consequence of a pH shift. Clearly, when discussing pH shifts existing salt bridges in the protein are influenced as well. In the crystal structure of VDAC1 (pdb: 3EMN) highly conserved salt bridges are observed between the positions K12-D16-K20. Recent studies on VDAC1 from rat liver, reported a pH dependency on VDAC1´s characteristics in lipid bilayer recordings.[210] Tejiido *et al* described an increased anion selectivity at acidic pH in combination with faster channel transitions. Furthermore, an influence on the existing salt bridges by pH shift was discussed. As indicated by MD simulations, alternating forming salt bridges at low pHs may explain the faster transitions,

since more salt bridges are susceptible to be disrupted at low pH. The same could have occurred during the BLM measurements of mVDAC2 as well. In accordance to Tejiido *et al*, VDAC2 shows an increased transition between the open and the closed state at acidic pH. It might be that upon pH 6.2 salt bridges are disrupted and an mVDAC1-like gating characteristic is restored. Studies of Törnroth-Horsefield and Neutze [211] conjectured K12 and K20 to be important selectivity determinants of the changing ion-selectivity. Interestingly, the salt-bridge region of VDACs as well as the hinge region is highly conserved in all *metazoas* corroborating its physiological importance (Figure 72). Accordingly, the observed pH dependence may be explained by the presence of the K12-D16-K20 salt bridge in combination with the hinge region.

Beside the pH dependence of VDAC2, a remarkable difference of VDAC1 and VDAC2 is the presence of 11 cysteines in mVDAC2. It has been demonstrated that the two cysteines in VDAC1 have no influence on the gating behaviour. [212, 213] In VDAC2 the impact of the cysteines remains unclear especially because 9 of the 11 cysteines are facing to the IMS (Figure 73). Recently, Marya and Mahalakshmi demonstrated the influence of the cysteine residues in hVDAC2 upon protein folding and thermal stability.[214] Although the thermal stability of the cysteineless hVDAC2 variant is increased, the overall protein structure is less stable towards lateral membrane pressure.

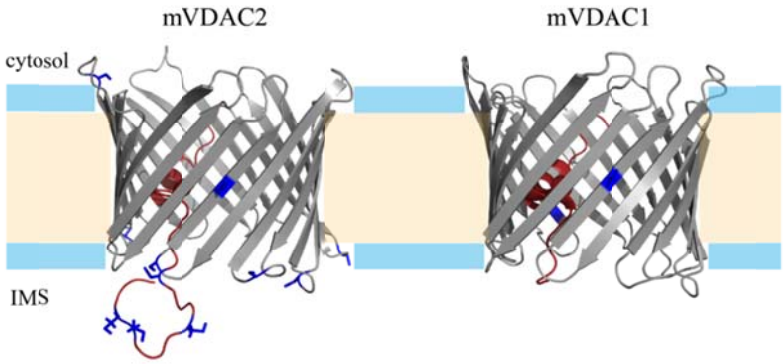

Figure 73: Cysteines of mVDAC2 are located at strategically important positions and may neutralize there ROS [214], Left: side view of mVDAC2, the N-terminus is highlighted in red and the 11 existing cysteines are displayed in blue, Model structure for VDAC2 was generated by SWISS-MODEL (http://swissmodel.expasy.org) using the murine VDAC1 structure (PDB code 3EMN) as template, Right: side view of mVDAC1, the N-terminus is highlighted in red and the two existing cysteines are displayed in blue.

An influence of the existing cysteines of mVDAC2 in BLM measurements cannot be excluded. It is unlikely, that disulphide bridges formation and disruption occurs under the BLM conditions as our BLM results for double-cysteine VDAC1 variants demonstrated that only a pre-oxidation was sufficient to provide disulphide-bond-formation. Still, the influence of cysteines VDAC2 demands further investigation.

Assuming that mVDAC2´s N-terminus is the crucial element of gating, there are three possibilities to explain the observed gating characteristics with respect to the pH dependence and existing cysteines: a) ionic interactions in the N-terminus that involves salt bridges, b) metal binding to the cysteines and c) interaction of the N-terminus with the barrel wall by disulphide-bridges or ionic interaction (Figure 74). Clearly, more experiments have to be performed to unravel VDAC2´s gating behaviour and biological function.

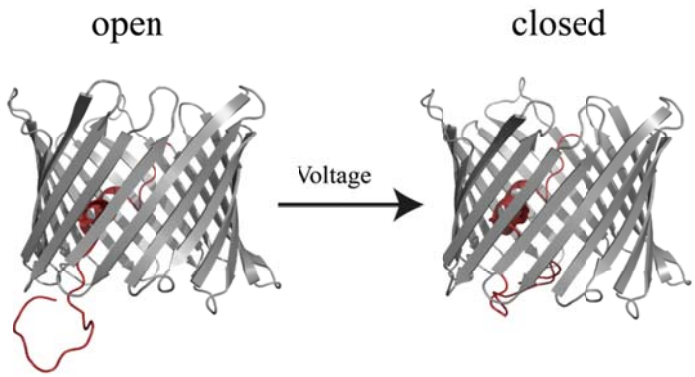

Figure 74: Proposed gating mechanism of mVDAC2, the N-terminus could close the pore as it is able to fold into the pore. The flexibility of the N-terminus could be influenced by a) ionic interactions in the N-terminus that involves salt bridges, b) metal binding to the cysteines and c) interaction of the N-terminus with the barrel wall by disulphide-bridges or ionic interaction.

5.2.3 EMP´s gating – an odd porin shows a novel kind of gating

In the past β-barrels were used for ion-channel engineering because of their robustness and defined switching behaviour. It has been demonstrated that OmpG is suitable for ion-channel engineering as OmpG shows a high tolerance against mutations and organic solvents. [60, 126, 215] The general aim of ion-channel engineering is to construct a pore with new features,

whether selectivity or enhanced gating characteristics. When using natural porins the influence of the natural switching regions cannot be excluded. For example, in OmpG the loop L6 was identified as region dominating the gating behaviour. In BLM measurements OmpG showed a high transition rate between open and closed states. This intrinsic feature makes it very difficult to control the gating of OmpG or provide new features within the pore. For this Grosse *et al* reduced gating by a loop 6 deletion variant resulting in a permanent open pore with very few transition rates.[59] With this in mind an artificial porin was constructed using the OmpG loop 6 deletion variant as template. By reducing the pore to the minimally required components we claimed to obtain an ideal template for ion-channel engineering. This template would be a simple, well-behaving pore without intrinsic gating characteristics and a high robustness against different lipids and detergents. In addition, a perfect template should be monomeric to facilitate the analyses of conductance changes.

In the first attempt to engineer such an improved template the enhanced minimal porin (EMP) was used. EMP consist only a β-barrel where all gating dependent structures are removed, namely all known loops that were identified of being responsible for gating (Figure 75).

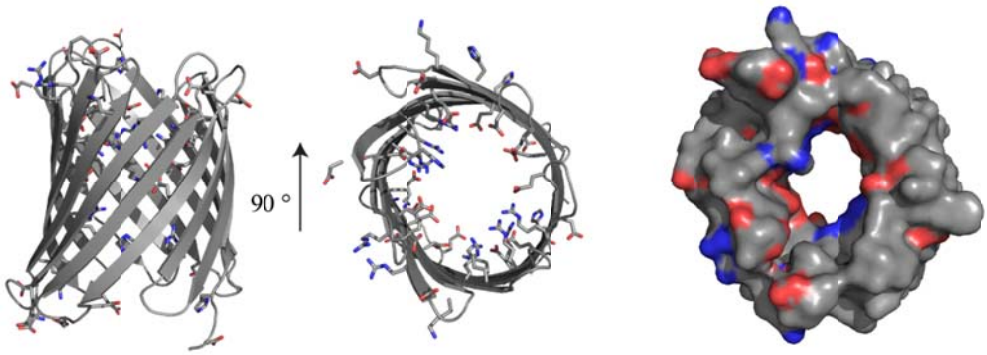

Figure 74: Overall structure of the artificial porin EMP, the overall structures represents a β-barrel; all charged amino acids are shown as sticks to highlight a potential role in a salt-bridge formation. Side view (left) and top view (middle) from the extracellular side including a surface representation (right) are shown as cartoons. The model structure for EMP was generated by SWISS-MODEL (http://swissmodel.expasy.org) using the OmpG structure (PDB code 21WW) as template.

Accordingly, EMP´s overall structural stability was examined in detergents as well in lipidic environments. CD and OCD measurements were performed providing information about the ability and stability upon EMPs reconstitution in lipids. CD analysis resulted in the expected overall β-barrel structure showing a high stability under thermally denaturing conditions. Most interestingly, the OCD spectra of EMP in DMPC bilayers showed significant

differences when the bilayer thickness changed upon going from the gel phase (20 °C) to the thinner liquid crystalline phase (35 °C) assuming that EMP reacts sensitive to the bilayer thickness. The change as visible by OCD can be interpreted in terms of an increased tilt angle of the β-strands in response to a compression by the bilayer. Most likely this sensitivity is caused by the very short β-turns instead of the loops present in EMP´s template OmpG. Therefore, it might be that the pore interacts with lipidic head groups resulting in a membrane-sensitive barrel. The observed increase of the tilt angle in lipid-bilayers is a phenomenon well known from other proteins. For example, helical membrane proteins were found to increase their tilt as response to membrane thickness. [216, 217] Until now, OCD in combination with solid phase NMR was used to identify mostly α-helical transmembrane elements such as the oncogenic E5 protein [145], the platelet derived growth factor receptor [218] and channel-forming peptides. [144, 219, 220] Therefore, this work provides a first example for the analysis of β-barrels with oriented CD measurements giving hints upon β-strand tilts in combination with biophysics to enhance the understanding on membrane protein dynamics. Only recently, Ruskamo *et al* described also an example for a β-barrel protein whose orientation was characterised by OCD spectroscopy.[221]

To address the gating characteristics of EMP, BLM measurements in different lipidic environments and two pH values were performed. As mentioned above porins exhibit gating mostly by the movement of flexible loops folding into the pore. Surprisingly, the loop-depleted EMP exhibits strong gating, though the only element still capable of closing the pore is the β-barrel itself. EMP channels were highly conductive with an open state in the range of 0.86 ± 0.02 – 1.06 ± 0.04 nS with two sub-conducting states (S1: 0.64 ±0.02 nS and S2: 0.38 ± 0.01 nS) comparable to the substates found in VDAC. In the less compact and charged asolectin at pH 7.4 EMP showed a 16.5% P_o with a 5-fold lower frequency of transitions than OmpG. In zwitterionic DPhPC EMP showed a 46% P_o and a 3-fold lower frequency in comparison to OmpG. At acidic conditions this behaviour is inverted, and EMP appears to have a higher P_o, albeit fewer transitions. The corresponding Ohm plots yield a high- and a low-conducting state at acidic pH in asolectin and DPhPC bilayers, respectively. Interestingly, EMP's current traces show remarkable similarities to current blockades resulting from modulators like polyethylene glycols [222] or polypeptide loops in α-HL.[223] Nevertheless, how EMP achieves its two distinct closed states is still elusive. OCD experiments suggest a β-strand tilt during insertion into bilayers. It is improbable if the two distinct close states can be explained by a tilt of the β-strands as a deletion of two β-strands of

human VDAC1 [224] lead to a 2- and 3.5-fold reduction in conductance whereas the smaller EMP only exhibited a 1.5- to 2-fold difference in conductance, depending on pH and lipid composition. Therefore, a gating by the restriction of the pore size alone can be excluded. Apart from an ejection of a β-turn substructure from the 16-stranded β-barrel, only a semi-collapsed, ellipsoidal EMP may be suitable to explain the closing events at 35 °C and at pH 7.4. Furthermore, and as mentioned above, not only loops can be responsible for switching events but salt bridges as well. Keeping in mind that strong lipid and pH dependences are found, EMP may follow a salt-bridge induced switching more comparable to OmpA´s gating then to parental OmpG´s. The interior of the pore shows a charge distribution so that various salt bridges between positive and negative charged amino acids can be adopted. Reorganisation of these interactions could enforce structural changes in the barrel, accounting for further reduction of the open probability at pH 5.0. Lowering the pH allows the barrel to acquire a more stretched conformation, due to a shift in the asolectin lipid-phase transition to higher temperatures, or due to the formation of stabilising electrostatic interactions (Figure 76).

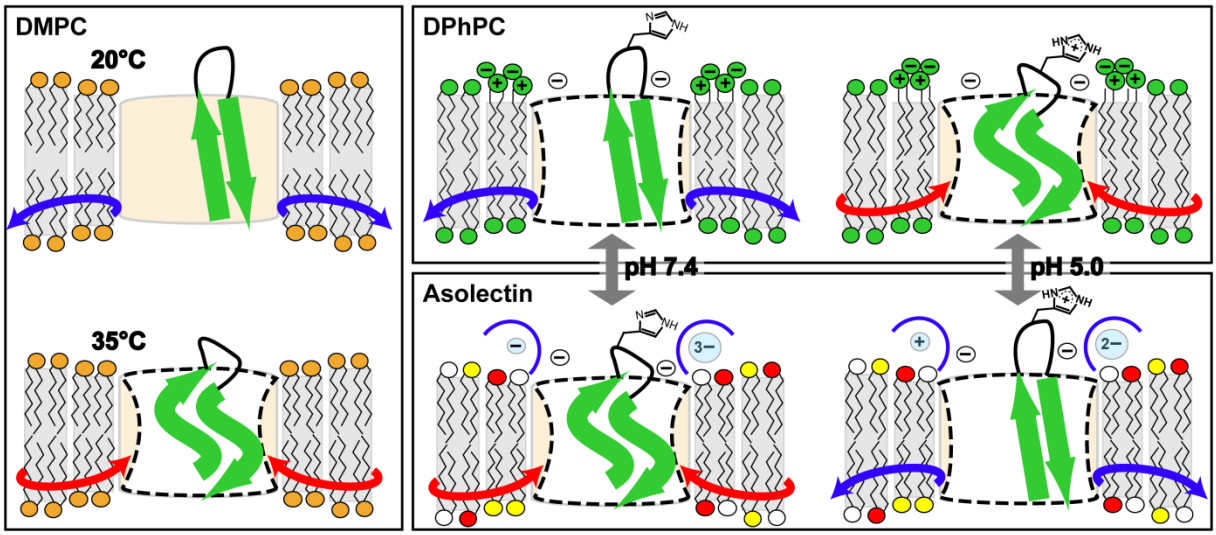

Figure 76:[59] Hypothetical model on the elastic movements of the EMP barrel. In the gel phase of DMPC (20 °C), the height of the β-barrel matches the thickness of the bilayer. At 35 °C, where the liquid crystalline membrane is thinner, the pore becomes compressed (red arrow) and the β-strands acquire a more tilted structure. In response to the membrane charge and fluidity, EMP shows inverted gating behaviour in DPhPC and asolectin at pH 7.4 and pH 5.0.

Taken together, EMP and its characteristics may serve as a model system to resolve general issues of porins in terms of folding, gating behaviour and the role of structural and functional dynamics.

5.3 VDAC and its role in mitochondrial related apoptosis

VDACs are the most abundant proteins of the outer mitochondrial membrane and form thousands of pores in each mitochondrion's outer membrane. The high number of VDAC-channels explains the permeability of the membrane indicated by osmotic unresponsiveness in isolated intact mitochondria. Additionally, the rapid rates of respiration as well as the porous appearance of outer membranes in electron micrographs of isolated mitochondria (Figure 77) corroborates the importance of this membrane porin.

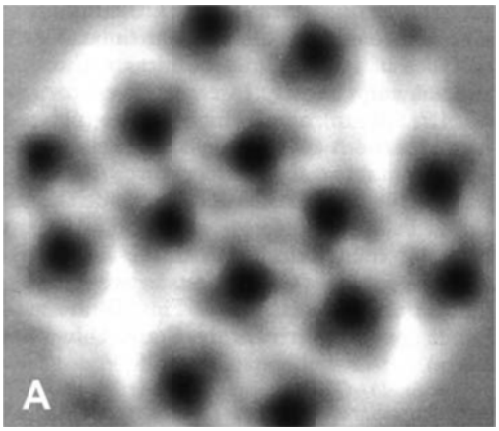

Figure 77:[225] Structure of VDAC pores in the mitochondrial outer membrane isolated from fungal mitochondria imaged by low dose electron microscopy. Each pore (black) is 2 nm in diameter.

VDACs are known to be involved in mitochondrial processes such as ATP-, calcium or ROS-transport. Beside this, they were identified as key players of mitochondrial physiology such as being involved in the mitochondrial related apoptotic pathway. In the regulation of the intrinsic or mitochondrial apoptotic pathway VDAC was identified to interact directly with a plethora of pro- or anti-apoptotic proteins. The participation of VDACs in the apoptotic cascade are discussed as a) a minor component incorporated into the mitochondrial transition pore (MTP) complex, b) a major *a priori* component that creates the huge outer membrane pore itself by homo- or hetero-oligomerisation, c) an indirect trigger for pore formation, *e.g.* by chaperoning its assembly within the membrane, or d) an inducer for the formation of lipidic pores. It is well accepted that the molecular mechanisms of mitochondrial apoptosis is initiated through induction of protein-permeable pores by multi-domain pro-apoptotic

members of the B-cell lymphoma-2 (Bcl-2) family, such as Bcl-2-associated protein X (Bax) and Bcl-2 homologous antagonist killer (Bak) as well as Bcl-2 homology domain 3 (BH3)-only proteins, such as Bid or Bcl-2 like protein 11 (Bim), that directly activate Bax or Bak.[226-228] However, the precise mechanisms how Bcl-2 family proteins initiate the apoptotic cascade is still not fully understood. As a model, it was proposed that VDACs are directly involved in in the apoptotic cascade by providing a proteinaceous docking platform for either members of the Bcl-2 protein family such as Bcl-xL [168, 169], Bid/tBid [170], Bax/Bak [171] or Bnip3 [173] as well as hexokinases. [172]

In this work, I focused on the pro-apoptotic VDAC-effector Bid/tBid. Recent studies imply that Bid is a key player in neuronal cell death pathways. Accordingly, Bid seems to promote mitochondrial demise by release of death promoting proteins in the cytosol and the acceleration of oxidative stress.[229-233] Furthermore, Bid-deficient neurons are highly resistant to cell death stimuli including oxygen-glucose deprivation (OGD) and glutamate-induced excitotoxicity *in vitro*[231, 234] and show reduced damage after cerebral ischemia and brain trauma *in vivo*.[234-236] Recent studies revealed that inhibition of Bid by small-molecules as well as Bid gene silencing using small interfering RNA (siRNA) is suitable for neuroprotection by averting mitochondrial dysfunction and neuronal cell death.[229-232, 237]

Thus, I address the question whether Bid or its active truncated form Bid (tBid) is interacting in a direct and specific manner with VDAC1. Although a close interplay between VDAC and Bid has been proposed,[170] a quantitative description of the electrophysiological and the structural effect of Bid/tBid on VDAC has not yet been demonstrated. Accordingly, I provide new insights of the intrinsic cell death in neurons that might mirror the emerging non-neuronal concepts of apoptosis.

5.3.1 The VDAC1-tBid complex: insights to a neuronal cell death control point

VDACs are able to interact with a plethora of pro- and anti-apoptotic proteins as well with small compounds as the VDAC inhibitor DIDS.[238] Although the interactions were phenomenologically analysed, the interaction patterns as well as the structures of these

complexes remain largely unclear. Recently, various structural models for VDAC2/apoptotic factor complexes have been proposed trying to define such interaction patterns (Figure 78). [174]

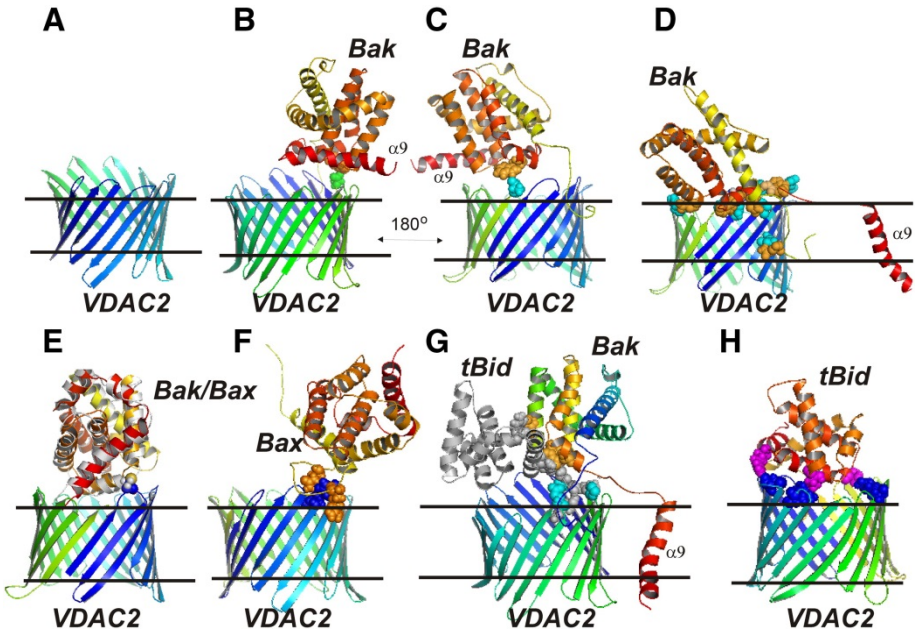

Figure 78: Speculative models of VDAC2 in complexes with Bak, Bax, and tBid as analysed by molecular dynamics simulation and docking experiments, **A** Structural model of MOM-integrated VDAC2, **B**, **C**, **D** structural models of the VDAC2/Bak complex, **D** Bak integrates by helix 9 (red) into the membrane after VDAC2 binding; intermolecular polar contacts are shown as cyan (VDAC2) and orange (tBid) spheres **E** superimposition of Bax onto Bak in the best-scored VDAC2/Bak complex, **F** the best-scored complex VDAC2/Bax **G** *S*tructural model of the complex VDAC2/Bak-tBid **H** structural model of the complex VDAC2/tBid*;* Intermolecular polar contacts are shown as blue (VDAC2) and magenta (tBid) spheres. [174]

Beside these speculative models there were attempts to characterise VDAC1´s gating behaviour in the presence of effectors. As mentioned above, VDAC1 is adopting one high (referred to as open) and several low (referred to as closed) states. I quantified these closed states into at least three major states; S1, S2A and S2B (section 5.2.2). [99] It is still under debate, whether the variety of closed substates can be connected to a biological function in the effector response and thus to different output-signals in mitochondrial-related apoptosis. Accordingly, closed or partially-closed VDAC1 states can be induced by either high voltages or interaction with pro- and anti-apoptotic proteins. [38, 158, 168, 170, 207, 239, 240] Interestingly, both the anti-apoptotic protein Bcl-xL and the pro-apoptotic protein tBid similar promote channel closure.[168, 170] This is surprising, as prevention and induction of apoptosis should be subject to different input signals and may have distinct signatures in BLM measurements. A

quantification of the BLM data for channel closure was missing in these reports and thus it was not possible to connect the loss of conductivity to the observed S1, S2A and S2B substates

In my work with the pro-apoptotic VDAC effector Bid/tBid I demonstrated not only a protein-protein interaction but quantified the tBid-induced closed state by BLM measurements and defined for the first time potential interaction patterns. I will discuss these findings in the next sections.

5.3.1.1 VDAC1 and Bid/tBid are interacting in a direct manner undergoing structural changes

The first hints for a stable and direct interaction of VDAC1 and Bid/tBid was gained by SEC and thermofluor measurements. In SEC a shift in the elution pattern was observed and SDS-PAGE analysis revealed the co-elution of VDAC1 and Bid/tBid. Surprisingly, the protein complex eluted later thus indicating that the hydrodynamic diameter was reduced compared to VDAC1. Apparently, the VDAC1 surrounding micelle became altered by effector-binding. Accordingly, the observed apparent molecular mass is explained by Bid/tBid-induced reduction of the VDAC1 surrounding micelle, thus generating the impression of a smaller VDAC1-Bid/tBid complex compared to VDAC1 alone.
An additional hint to a stable VDAC1-Bid/tBid-complex was given by thermofluor measurements. Here the thermic analysis revealed a 12° C higher melting temperature of the VDAC1-Bid and a 17° C higher melting temperature of the VDAC1-tBid-complex compared to VDAC1 alone. Both SEC and thermofluor are providing first hints; not proving or excluding a direct interaction.

These hints of a direct and stable interaction between VDAC1 and Bid/tBid could be corroborated by CD and OCD measurements. By CD analyses, I demonstrated that the structure of the VDAC1-tBid complex differs significantly from the structure of the isolated proteins. Interestingly, the observed structural effect only appeared in a molar ratio of 1:2 (VDAC:tBid). Furthermore, OCD analyses indicate that the β-strands of VDAC1 rearrange upon tBid binding as calculations from the minimum maximum relation of the CD signal shows the β-strands more tilted in the membrane. The difference-spectrum of the calculated

and recorded mVDAC1-tBid complex reveals a random coil-like structure, suggesting a partial unfolding of at least one component. Additionally, the negative signal at 208 nm indicates that an α-helix inserts into the membrane in a vertical fashion.

5.3.1.2 VDAC1´s gating is permanently affected by Bid/tBid binding

In electrophysiological measurements such as BLM, VDAC1 shows unique gating characteristics including at least three major states; S1, S2A and S2B (section 5.2.2).[99] Although, an electrophysiological influence of tBid was demonstrated before,[170] a quantification of the BLM data for channel closure with respect to the previous observed S1, S2A and S2B states was missing. In my work I quantified for the first time the tBid-induced closed state by BLM measurements.

The maximum conductivity of mVDAC1 was 3.94 nS in the open state and 2.61 and 1.90 nS in the closed state. After tBid addition the channel suffered a 23% reduction of the overall current leading to a permanent semi-closed pore with a conductivity of 3.05 nS. This semi-closed state is significantly different from the previously observed S1 and S2 states. Additionally, VDAC1 arrested in this semi-closed state and no transitions were observed after tBid binding. As we know from our previous reports on mVDAC1´s gating characteristics, the flexibility of the N-terminus is required for channel transitions.[99] Furthermore, these transitions are mandatory for VDAC1´s functionality. Accordingly, tBid is affecting VDAC1´s gating characteristics and leads to a permanent semi-closed pore. As a hypothesis, the N-terminus might be involved in the binding as a full flexibility of the N-terminus was required before to obtain the full set of closed channel substates.

5.3.1.3 VDAC´s barrel is sufficient for Bid/tBid binding

Following the BLM analyses of the VDAC1-tBid complex, I addressed the elucidation of a potential binding pattern. Because of VDAC´s particular structure there might be two potential areas that can be attacked by pro- or anti-apoptotic factors. The parallel β1 and β19 strands close the barrel and hinder intrusion of the lipid phase into the pore interior. Hence β1 is the shortest β-strand in the structure of VDAC1 it might represent an unstable site of VDAC´s barrel, *i.e.* a putative breaking point of barrel integrity which may be influenced by

structural changes at the N-terminus. Interestingly, the β1/β19 interface had been identified by mutational studies to be crucial for VDAC oligomerisation.[213] Furthermore, under apoptotic conditions the author reports a tendency of VDAC1 to form higher oligomers using a new dimer interface along the β16-strands. The other potential breaking point is the conserved membrane-facing acidic residue E73. It has been demonstrated that this residue is crucial for the interaction with the anti-apoptotic hexokinase I.[197] This interaction causes mainly the intrinsic structural plasticity of VDAC1 with its μsec–msec dynamics as shown by NMR-spectroscopy.[241] Furthermore, it was demonstrated that E73 is important for the interaction with the anti-apoptotic Bcl-xL protein as well.[168]

To define the crucial structural elements required for tBid binding, I performed thermophoresis and EPR measurements. In thermophoresis measurements, a clear preference of tBid for VDAC1 was found compared to the inactive Bid. tBid binds with a 52 fold higher affinity to VDAC1 (K_D = 26.9 μM) than Bid (K_D = 1.4 mM), thus demonstrating the high affinity of tBid towards the mitochondrial target VDAC1. Furthermore and to address an involvement of the N-terminus in tBid binding, thermophoresis analysis with N-terminal deletion VDAC1-variants were performed. Here I could clearly demonstrate that the N-terminus is not required per se for tBid binding. In the deletion variant Δ26-mVDAC1 the whole N-terminus is deleted and only the VDAC1 barrel remains. Indeed, the affinity suffered only a 2.6 fold reduction where tBid still binds in a specific and direct manner. Surprisingly, the deletion variant Δ11-mVDAC1, where just half of the N-terminal helix remains, showed a 14-fold increased affinity towards tBid binding as compared to full-length VDAC1 thus hinting to a supporting role of the N-terminus in effector binding. In addition, tBid binding to VDAC2 revealed a 3.4 weaker affinity compared to VDAC1. Accordingly, these results hint to a common binding pattern in VDAC1 and VDAC2, although VDAC1 most likely is the preferred target of tBid (see also Oppermann 2014 [20]). Overall, I demonstrated that the VDAC1 barrel is sufficient for tBid binding with the N-terminus exerting a supportive role.

A more detailed view upon structural changes of VDAC upon tBid binding was gained by EPR-analysis. In accordance to the thermophoresis results, an influence on the flexibility of the β-barrel structure as well as the N-terminal α-helix was found. Interestingly, the N-terminus loses some of its flexibility after tBid binding, whereas the overall β-barrel structure just suffered small structural changes as indicated in the form factors of the DEER measurements. Especially, the cytosol-facing side of VDAC1 is influenced by tBid binding.

Furthermore, EPR-analysis revealed the existence of stable VDAC1 oligomers in LDAO-containing buffer. Surprisingly, these oligomers were disrupted as indicated by the disappearance of longer distances in the DEER measurements by tBid-binding.

5.3.2 Hypothetical models for the VDAC1-tBid interaction

In summary, my results clearly demonstrate that a) tBid interacts with mVDAC1 in a direct and specific manner, b) a reduction of the overall current is observed in BLM measurements, c) VDAC1 and tBid interact in a 1:2 molar ratio with a structural rearrangement, d) the formed VDAC1-tBid complex has an increased thermal stability and e) tBid binding might disrupt stable VDAC1 oligomers. To combine all these observations, three different models are put forward (Figure 79).

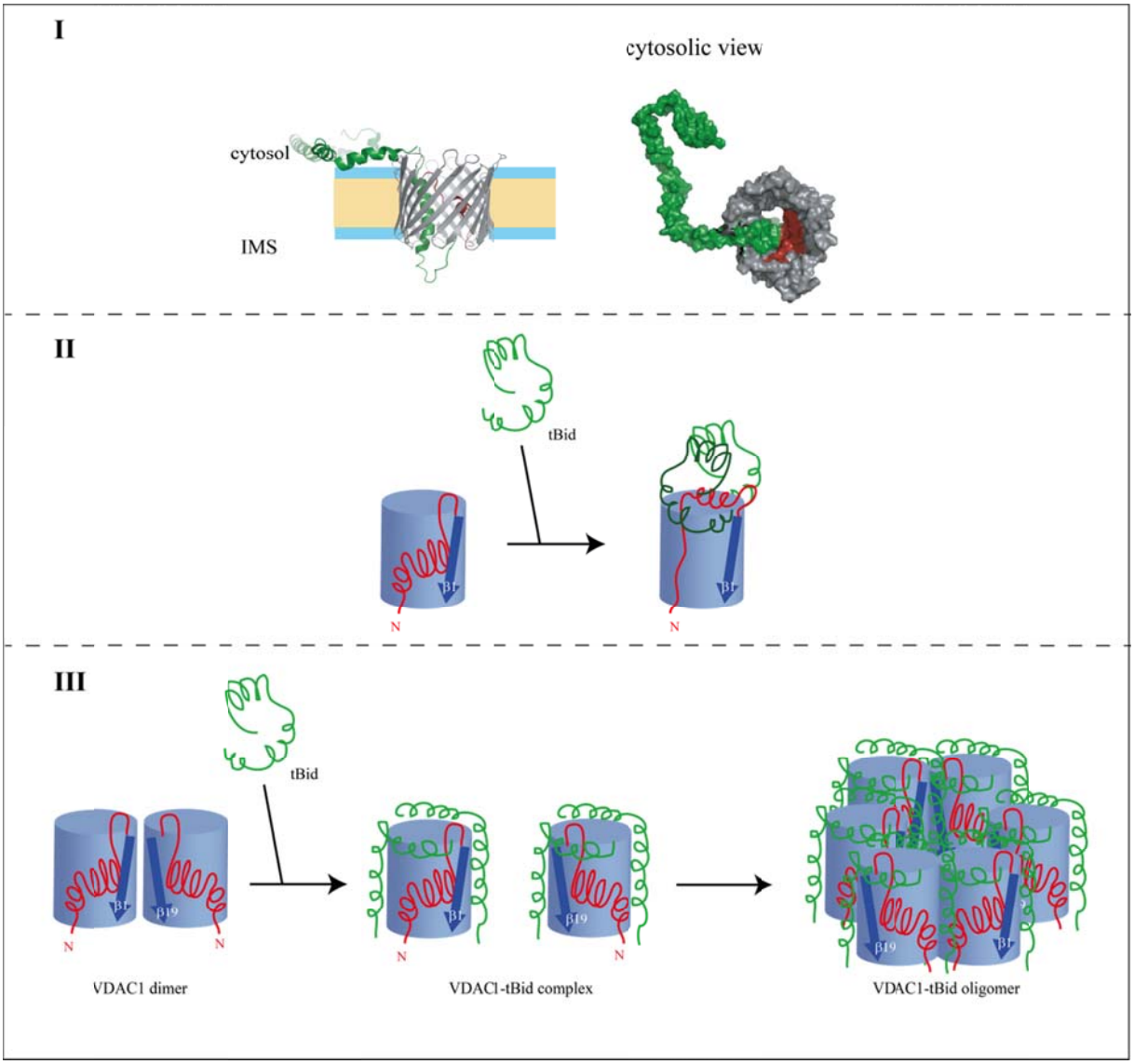

Figure 79: Hypothetical models for the VDAC1-tBid interaction. **I** The Invasionmodel: As a result of the HEX-docking server analyses, one helix of tBid incorporates into the pore and thereby partly close the pore, mVDAC1 is shown as cartoon in grey with its N-terminus in red, tBid is shown as green cartoon; left side view of the best fitting result, right: cytosolic view with surface. **II** Representation of the Periphery-bindingmodel: Following computational analyses of Veresov and Davidovskii tBid (green) binds to the top of VDAC1, the N-terminal helix (red) is pulled out of the barrel thus forming a strong interaction to the tBid dimer. This interaction is predicted to depend on the flexibility of VDACs N-terminus. **III** The Monomerisationmodel: A VDAC1 dimer is formed between β1 and β19 (blue arrows); upon tBid (green) binding the interface of the dimer is blocked by two tBid molecules. The formation of higher oligomers as observed in literature could occur because of an interaction between β16 strands.

Model I, was achieved by simple docking analyses performed with the HEX server. The computational docking analysis between mVDAC1 (crystal structure pdb: 3EMN) and tBid (NMR structure pdb: 25MI) was performed by a "shape only" search. In this model, one α-helix of tBid invades the channel´s pore and thereby constricts the channel. With this

invasionmodel the reduced conductivity as well as the arrest in a semi-closed state can be explained. The model fails to explain the found stoichiometry and gives no hint to explain the thermophoresis results, where just VDAC´s barrel is essential for tBid binding.

Model II is based on the structural predictions by Veresov and Davidovskii [242] Here tBid binds to the extramembranous, cytosolic periphery area VDAC1. Two tBid effectors crown VDAC1, so that the N-terminal helix is exposed to the pore´s surface. The helix provides more attainable interactions to enhance effector binding. This periphery-bindingmodel explains the reduced conductivity, the arrest in a semi-closed state by interaction with distinct parts of the N-terminus, the stoichiometry and the thermophoresis results, where dominant binding pattern exerted by the barrel alone. In addition it might give an explanation for the increased affinity of tBid towards Δ11-mVDAC1. Presumably, the promoting influence of the N-terminus as found in thermophoresis is located between residues 11-26 because these are the remaining residues in Δ11-mVDAC1. Because of the shortened N-terminus of this variant it could be that the remaining helix shows an increased flexibility as interactions between the very N-terminus and the barrel are deleted. This flexibility as well as the cytosolic-exposed remains of the N-terminus may lead to increased affinity. Nevertheless, this model fails to explain the disappearance of VDAC1 oligomers as observed in EPR measurements.

Modell III rationalised the observed VDAC1 dimer-monomer-equilibrium change upon tBid-binding. As demonstrated by Geula *et al* [213] VDACs are able to form dimers in detergent- and lipid-containing buffer. These dimers are formed in the interface of the strands β1, β2 and β19, one of the weak areas in the VDAC1 structure. Interestingly, the $\alpha-\beta_{19}$ architecture as well as the dimerization tendency reminds on other, structurally not yet characterized mitochondrial outer membrane proteins like the TOM40 component of the pre-protein translocase.[243] Here, upon tBid binding the dimer interface is disrupted as a helix of tBid incorporates into the membrane. The recently published NMR structure of amphiphilic tBid reveals that only helices 3 and 5 have distinct membrane contacts whereas the others remain unaligned in relation to the membrane surface.[105] Nevertheless, an incorporation of a helix into the lipid bilayer cannot be excluded because several NOE signals are missing in the NMR structure. Accordingly, a helix of tBid may be involved in membrane anchoring as BLM measurements revealed the incorporation tendency of tBid or parts of it into lipid bilayers (Culmsee, unpublished data).The incorporation of helices into a membrane are known for pore-forming toxins such as the diphtheria and anthrax toxins.[244] A hint for the

incorporation of an α-helix of the tBid–VDAC1-complex is given by the OCD data, where a positive signal at 208 nm indicates the incorporation of an helix in an upright manner. As consequence of the VDAC1-dimer-disruption the VDAC1-tBid complex could be stabilized by higher oligomers. In accordance to Geula *et al*,[213] a tendency for VDAC1 for higher oligomers under apoptotic conditions can be assumed, where these oligomers are formed along the β16-strands and involve tBid as intervening component. Model III can explain the reduced conductivity, the arrest in a semi-closed state by constricting VDAC1 from the outside and thereby arresting the N-terminus, the stoichiometry, the thermophoresis results that the dominant binding pattern is found in the barrel and the disappearance of VDAC1 oligomers. In addition, by constricting the pore it might be that the N-terminus is exposed to the barrels cytosolic surface thus exposing the previously discussed residues 11-26 generating the higher affinity of Δ11-mVDAC1 for tBid binding.

Taken together, Model II and III are consistent with the obtained results. To decide between these two models, more experiments, including structural analyses have to be done to unveil the exact mechanism of pro-apoptotic binding.

6. Outlook

In the past five years ~ 600 articles about VDACs have been published, highlighting the high impact of mitochondrial porins on biomedical and physiological aspects. Nevertheless, VDAC´s function and its certain role in mitochondrial-related apoptosis raises several questions.

Although members of the VDAC family are clearly involved in the mitochondrial mediated apoptosis, the precise molecular mechanism is still elusive. It is known that in the intrinsic pathway cytochrome c is released from the IMS to the cytosol. Accordingly, there are now eight competing models, how cytochrome c (cyt c) is released and how VDAC is involved in this (Figure 79). Briefly, these models are described as a) rupture of the OMM and release of cyt c caused by osmotic matrix swelling as consequence of VDAC closure, b) cyt c release by the formation of a large permeability transition pore where VDAC is a part of it – this pore is formed as reply of ROS or Ca^{2+} overproduction, c) formation of Bax/Bak oligomers releasing cyt c after their activation of tBid, d) cyt c-release by Bax oligomers without the involvement of VDAC, e) formation of VDAC1 and Bax oligomers to release cyt c, f) release of cyt c by a supramolecular high-conductance channel (mitochondrial apoptosis-inducing channel), g) the release of cyt c by lipidic channels and g) VDAC homo-oligomers forming a cyt c releasing channel. By elucidation of the distinct mechanism of apoptosis it should be possible to find crucial control points and thereby better strategies to induce or prevent apoptosis.

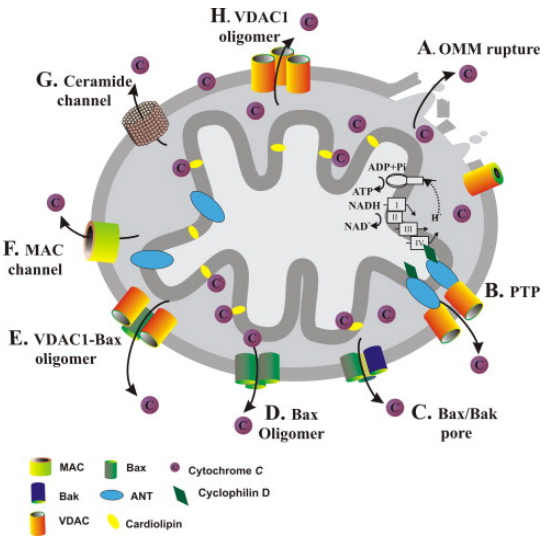

Figure 79:[38] Schematic representation of proposed models for the release of cytochrome c from the IMS to the cytosol. a) rupture of the OMM by osmotic matrix swelling, b) formation of a large permeability transition pore (PTP), c) formation of Bax/Bak oligomers, d) by Bax oligomers, e) by VDAC1-Bax oligomers, f) supramolecular high-conductance channel (mitochondrial apoptosis-inducing channel) g) lipidic channels h) VDAC homo-oligomers.

Once the mechanism of apoptosis and the involvement of VDAC are known, one may put more effort into the development of new pharmaceutical agents involving VDAC as target. Interestingly, many chemotherapeutical reagents act as mitochondrial-apoptosis inducers. These reagents act either indirectly with VDAC by the production of ROS (furanoaphthoquinones or erastin) or directly by interaction with VDAC (G3139 (oblimersen), floxetin (prozac), cis-platin or endostatin). Especially G3139 seems to be an interesting and rewarding lead for the VDAC targets. G3139 is an oligonucleotide that was developed to target initiation codons of Bcl-2 mRNA but interacts directly with VDAC and reduces its channel activity. Having this in mind other biocompatible reagents such as small peptides can be assumed to affect VDACs activity. If it becomes possible to trigger VDAC in a specific way, a huge influence on all mitochondria-related diseases can be assumed.

Furthermore, I have demonstrated the relevance of direct VDAC-effector interactions. Although many VDAC effectors have been identified, the binding patterns or the overall structures of the VDAC1-effector complexes remain elusive. In future studies one has to focus to unravel the biochemical and structural basis for the VDAC-effector interactions and to understand how they modulate the channel's gating characteristics. With this a deeper understanding in cell survival will be given. Clearly, satisfying answers about VDAC-effector complexes can only be given on the basis of crystal-structures.

While mVDAC1 and mVDAC3 share high sequence identity and are capable of signalling in similar ways, mVDAC2 appears to deviate from these two other isoforms because of its prolonged N-terminus, the presence of 11 internal cysteines, an antagonist function in apoptosis and the deviating gating characteristics when compared to VDAC1. Future studies highly will unravel the unique functions of VDAC2 with respect to the role of its prolonged N-terminus and the abundance of cysteines facing the IMS.

7. Literature

1. Voet, D., Voet, J. G., Pratt, C. W., *Lehrbuch der Biochemie*, ed. A.G. Beck-Sickinger, Hahn, U. 2002, Leipzig: Wiley-VCH.
2. Löffler, G., Petrides, P., *Biochemie und Patobiochemie*. Vol. 7. Auflage. 2003, Heidelberg: Springer-Verlag.
3. Schmidtke, K., et al., *Hartnup syndrome, progressive encephalopathy and allo-albuminaemia.* European journal of Pediatrics, 1992. **151**(12): p. 899-903.
4. Miller, D.S., *Regulation of P-glycoprotein and other ABC drug transporters at the blood–brain barrier.* Trends in pharmacological Sciences, 2010. **31**(6): p. 246-254.
5. http://medcell.med.yale.edu/lectures/introduction_cell_membrane.php.
6. Higgins, C.F., *ABC transporters: from microorganisms to man.* Annual review of Cell Biology, 1992. **8**(1): p. 67-113.
7. Doring, C. and M. Colombini, *Voltage dependence and ion selectivity of the mitochondrial channel, VDAC, are modified by succinic anhydride.* Journal of Membrane Biology, 1985. **83**(1): p. 81-86.
8. Liu, H. and E.M. Wintour, *Aquaporins in development-a review.* Reprod Biol Endocrinol, 2005. **3**(1): p. 18.
9. Zeth, K. and M. Thein, *Porins in prokaryotes and eukaryotes: common themes and variations.* Biochem. J, 2010. **431**: p. 13-22.
10. http://philschatz.com/anatomy-book/resources/0315_Mitochondrion_new.jpg.
11. Behnke, H.D., Münchener Medizinische Wochenschrift, 1977. **119**: p. 317-318.
12. Colombini, M., *STRUCTURE AND MODE OF ACTION OF A VOLTAGE DEPENDENT ANION SELECTIVE CHANNEL (VDAC) LOCATED IN THE OUTER MITOCHONDRIAL MEMBRANE DEPENDENT ANION SELECTIVE CHANNEL (VDAC)*.* Annals of the New York Academy of Sciences, 1980. **341**(1): p. 552-563.
13. Welsch, U., *Lehrbuch Histologie: Zytologie, Histologie, mikroskopische Anatomie*. 2003: Urban & Fischer Bei Elsevier.
14. Lemeshko, S.V. and V.V. Lemeshko, *Metabolically derived potential on the outer membrane of mitochondria: a computational model.* Biophysical journal, 2000. **79**(6): p. 2785-2800.
15. Lemeshko, V.V., *Model of the outer membrane potential generation by the inner membrane of mitochondria.* Biophysical journal, 2002. **82**(2): p. 684-692.
16. Lemeshko, V.V., *Theoretical evaluation of a possible nature of the outer membrane potential of mitochondria.* European Biophysics Journal, 2006. **36**(1): p. 57-66.
17. Lemeshko, V.V., *VDAC electronics: 1. VDAC-hexo (gluco) kinase generator of the mitochondrial outer membrane potential.* Biochimica et Biophysica Acta (BBA)-Biomembranes, 2014. **1838**(5): p. 1362-1371.
18. Lemeshko, V.V., *VDAC electronics: 2. A new, anaerobic mechanism of generation of the membrane potentials in mitochondria.* Biochimica et Biophysica Acta (BBA)-Biomembranes, 2014. **1838**(7): p. 1801-1808.
19. Fulda, S. and K. Debatin, *Extrinsic versus intrinsic apoptosis pathways in anticancer chemotherapy.* Oncogene, 2006. **25**(34): p. 4798-4811.
20. Oppermann, S., *Targeting Bid for mitoprotection-Bid crystallization, new mechanisms and inhibitory compounds*, 2014, Philipps-Universität Marburg.
21. Diekert, K., et al., *Apocytochrome c requires the TOM complex for translocation across the mitochondrial outer membrane.* The EMBO journal, 2001. **20**(20): p. 5626-5635.
22. Ujwal, R., et al., *The crystal structure of mouse VDAC1 at 2.3 Å resolution reveals mechanistic insights into metabolite gating.* Proceedings of the National Academy of Sciences, 2008. **105**(46): p. 17742.

23. Vander Heiden, M.G., et al., *Bcl-x L promotes the open configuration of the voltage-dependent anion channel and metabolite passage through the outer mitochondrial membrane.* Journal of Biological Chemistry, 2001. **276**(22): p. 19414.
24. Shoshan-Barmatz, V., et al., *The voltage-dependent anion channel (VDAC): function in intracellular signalling, cell life and cell death.* Current pharmaceutical Design, 2006. **12**(18): p. 2249-2270.
25. Bayrhuber, M., et al., *Structure of the human voltage-dependent anion channel.* Proceedings of the National Academy of Sciences, 2008. **105**(40): p. 15370.
26. Schein, S.J., M. Colombini, and A. Finkelstein, *Reconstitution in planar lipid bilayers of a voltage-dependent anion-selective channel obtained from paramecium mitochondria.* Journal of Membrane Biology, 1976. **30**(1): p. 99-120.
27. Homblé, F., E.-M. Krammer, and M. Prévost, *Plant VDAC: Facts and speculations.* Biochimica et Biophysica Acta (BBA)-Biomembranes, 2012. **1818**(6): p. 1486-1501.
28. Colombini, M., *VDAC structure, selectivity, and dynamics.* Biochimica et Biophysica Acta (BBA)-Biomembranes, 2012. **1818**(6): p. 1457-1465.
29. Shoshan-Barmatz, V. and D. Ben-Hail, *VDAC, a multi-functional mitochondrial protein as a pharmacological target.* Mitochondrion, 2012. **12**(1): p. 24-34.
30. Takahashi, Y. and C. Tateda, *The functions of voltage-dependent anion channels in plants.* Apoptosis, 2013. **18**(8): p. 917-924.
31. Rostovtseva, T. and M. Colombini, *VDAC channels mediate and gate the flow of ATP: implications for the regulation of mitochondrial function.* Biophysical journal, 1997. **72**(5): p. 1954-1962.
32. Hiller, S., et al., *Solution structure of the integral human membrane protein VDAC-1 in detergent micelles.* Science, 2008. **321**(5893): p. 1206.
33. Hiller, S. and G. Wagner, *The role of solution NMR in the structure determinations of VDAC-1 and other membrane proteins.* Current opinion in structural biology, 2009. **19**(4): p. 396-401.
34. Choudhary, O.P., et al., *The electrostatics of VDAC: implications for selectivity and gating.* Journal of molecular biology, 2010. **396**(3): p. 580-592.
35. Abu-Hamad, S., et al., *The VDAC1 N-terminus is essential both for apoptosis and the protective effect of anti-apoptotic proteins.* Journal of Cell Science, 2009. **122**(11): p. 1906.
36. Lemasters, J.J. and E. Holmuhamedov, *Voltage-dependent anion channel (VDAC) as mitochondrial governator—thinking outside the box.* Biochimica et Biophysica Acta (BBA)-Molecular Basis of Disease, 2006. **1762**(2): p. 181-190.
37. Han, D., et al., *Voltage-dependent anion channels control the release of the superoxide anion from mitochondria to cytosol.* Journal of Biological Chemistry, 2003. **278**(8): p. 5557-5563.
38. Shoshan-Barmatz, V., et al., *VDAC, a multi-functional mitochondrial protein regulating cell life and death.* Molecular Aspects of Medicine, 2010. **31**(3): p. 227-285.
39. Sampson, M.J., et al., *Immotile sperm and infertility in mice lacking mitochondrial voltage-dependent anion channel type 3.* Journal of Biological Chemistry, 2001. **276**(42): p. 39206-39212.
40. Weeber, E.J., et al., *The role of mitochondrial porins and the permeability transition pore in learning and synaptic plasticity.* Journal of Biological Chemistry, 2002. **277**(21): p. 18891-18897.
41. Rosenbusch, J.P., *Characterization of the major envelope protein from Escherichia coli.* Journal of Biological Chemistry, 1974. **249**(24): p. 8019.
42. Benz, R., *Porin from bacterial and mitochondrial outer membranes.* CRC critical reviews in biochemistry, 1985. **19**(2): p. 145.
43. Reitz, S., *Strukturelle und funktionelle Charakterisierung von hybriden OmpF-Poren*, in *Fachbereich Chemie*2009, Philipps Universität: Marburg.
44. Schulz, G.E., *β-Barrel membrane proteins.* Current opinion in structural biology, 2000. **10**(4): p. 443-447.

45. Yildiz, Ö., et al., *Structure of the monomeric outer-membrane porin OmpG in the open and closed conformation.* The EMBO journal, 2006. **25**(15): p. 3702-3713.
46. Deisenhofer, J., et al., *X-ray structure analysis of a membrane protein complex:: Electron density map at 3 Å resolution and a model of the chromophores of the photosynthetic reaction center from Rhodopseudomonas viridis.* Journal of molecular biology, 1984. **180**(2): p. 385-398.
47. Cowan, S., et al., *The structure of OmpF porin in a tetragonal crystal form.* Structure, 1995. **3**(10): p. 1041-1050.
48. Reitz, S., et al., *On the function and structure of synthetically modified porins.* Angewandte Chemie International Edition, 2009. **48**(26): p. 4853-4857.
49. Phale, P.S., et al., *Stability of trimeric OmpF porin: the contributions of the latching loop L2.* Biochemistry, 1998. **37**(45): p. 15663-15670.
50. Schirmer, T., et al., *Structural basis for sugar translocation through maltoporin channels at 3.1 A resolution.* Science, 1995. **267**(5197): p. 512-514.
51. Bölter, B., et al., *Ion channels in the outer membranes of chloroplasts and mitochondria: open doors or regulated gates?* The EMBO journal, 2001. **20**: p. 935-940.
52. Misra, R. and S.A. Benson, *A novel mutation, cog, which results in production of a new porin protein (OmpG) of Escherichia coli K-12.* Journal of bacteriology, 1989. **171**(8): p. 4105-4111.
53. Van Gelder, P., et al., *Voltage sensing in the PhoE and OmpF outer membrane porins of Escherichia coli: role of charged residues1.* Journal of molecular biology, 1997. **269**(4): p. 468-472.
54. Behlau, M., et al., *Projection structure of the monomeric porin OmpG at 6 å resolution1.* Journal of molecular biology, 2001. **305**(1): p. 71-77.
55. Conlan, S. and H. Bayley, *Folding of a monomeric porin, OmpG, in detergent solution.* Biochemistry, 2003. **42**(31): p. 9453-9465.
56. Conlan, S., et al., *Biochemical and biophysical characterization of OmpG: a monomeric porin.* Biochemistry, 2000. **39**(39): p. 11845-11854.
57. Grosse, W., et al., *Structural and functional characterization of a synthetically modified OmpG.* Bioorganic & medicinal chemistry, 2010. **18**(22): p. 7716-7723.
58. Subbarao, G.V. and B. van den Berg, *Crystal structure of the monomeric porin OmpG.* Journal of molecular biology, 2006. **360**(4): p. 750-759.
59. Grosse, W., et al., *Structure-Based Engineering of a Minimal Porin Reveals Loop-Independent Channel Closure.* Biochemistry, 2014. **53**(29): p. 4826-4838.
60. Chen, M., et al., *Outer membrane protein G: Engineering a quiet pore for biosensing.* Proceedings of the National Academy of Sciences of the United States of America, 2008. **105**(17): p. 6272-7.
61. Grosse, W., L.O. Essen, and U. Koert, *Strategies and Perspectives in Ion-Channel Engineering.* Chembiochem, 2011. **12**(6): p. 830-839.
62. Beckstein, O., et al., *Ion channel gating: insights via molecular simulations.* FEBS letters, 2003. **555**(1): p. 85-90.
63. Pautsch, A. and G.E. Schulz, *Structure of the outer membrane protein A transmembrane domain.* Nature Structural & Molecular Biology, 1998. **5**(11): p. 1013-1017.
64. Bond, P.J., J.D. Faraldo-Gómez, and M.S. Sansom, *OmpA: a pore or not a pore? Simulation and modeling studies.* Biophysical journal, 2002. **83**(2): p. 763-775.
65. Song, L., et al., *Structure of staphylococcal α-hemolysin, a heptameric transmembrane pore.* Science, 1996. **274**(5294): p. 1859-1865.
66. Cavalieri, S.J., G.A. Bohach, and I. Snyder, *Escherichia coli alpha-hemolysin: characteristics and probable role in pathogenicity.* Microbiological reviews, 1984. **48**(4): p. 326.
67. Channon, K., E.H.C. Bromley, and D.N. Woolfson, *Synthetic biology through biomolecular design and engineering.* Current opinion in structural biology, 2008. **18**(4): p. 491-498.
68. Grünberg, R. and L. Serrano, *Strategies for protein synthetic biology.* Nucleic Acids Research, 2010. **38**(8): p. 2663.

69. Fisher, M., et al., *De Novo Designed Proteins from a Library of Artificial Sequences Function in Escherichia coli and enable cell growth*, Plos one, 2011 **6**(1): e15364
70. Essen, L.O. and U. Koert, *Ion-channel engineering.* Annu. Rep. Prog. Chem., Sect. C: Phys. Chem., 2008. **104**: p. 165-188.
71. An, N., et al., *Crown ether–electrolyte interactions permit nanopore detection of individual DNA abasic sites in single molecules.* Proceedings of the National Academy of Sciences, 2012. **109**(29): p. 11504-11509.
72. Banghart, M.R., M. Volgraf, and D. Trauner, *Engineering light-gated ion channels.* Biochemistry, 2006. **45**(51): p. 15129-15141.
73. Hall, A.R., et al., *Hybrid pore formation by directed insertion of [alpha]-haemolysin into solid-state nanopores.* Nature Nanotechnology, 2010. **5**(12): p. 874-877.
74. Woodhouse, G., et al., *The ion channel switch biosensor.* Journal of Molecular Recognition, 1999. **12**(5): p. 328-334.
75. Mourot, A., I. Tochitsky, and R.H. Kramer, *Light at the end of the channel: optical manipulation of intrinsic neuronal excitability with chemical photoswitches.* Frontiers in molecular Neuroscience, 2013. **6**.
76. Busskamp, V. and B. Roska, *Optogenetic approaches to restoring visual function in retinitis pigmentosa.* Current opinion in Neurobiology, 2011. **21**(6): p. 942-946.
77. Gradinaru, V., et al., *Optical deconstruction of parkinsonian neural circuitry.* Science, 2009. **324**(5925): p. 354-359.
78. Taylor, R.G., D.C. Walker, and R.R. Mclnnes, *E. coli host strains significantly affect the quality of small scale plasmid DNA preparations used for sequencing.* Nucleic Acids Research, 1993. **21**(7): p. 1677.
79. Prilipov, A., et al., *Coupling site directed mutagenesis with high level expression: large scale production of mutant porins from E. coli.* FEMS microbiology letters, 1998. **163**(1): p. 65-72.
80. Prilipov, A., et al., *Identification and characterization of two quiescent porin genes, nmpC and ompN, in Escherichia coli BE.* Journal of bacteriology, 1998. **180**(13): p. 3388.
81. Novy, R., et al., *Overcoming the codon bias of E. coli for enhanced protein expression.* Innovations, 2001. **12**: p. 1-3.
82. Dubendorf, J.W. and F.W. Studier, *Controlling basal expression in an inducible T7 expression system by blocking the target T7 promoter with lac repressor.* Journal of Molecular Biology, 1991. **219**(1): p. 45-59.
83. Dubendorff, J.W. and F.W. Studier, *Creation of a T7 autogene: Cloning and expression of the gene for bacteriophage T7 RNA polymerase under control of its cognate promoter.* Journal of Molecular Biology, 1991. **219**(1): p. 61-68.
84. https://eu.idtdna.com/analyzer/Applications/OligoAnalyzer/.
85. Salisowski, A., *Herstellung und Charakterisierung von Deletionsmutanten des mitochondrialen Membranproteins mVDAC1*, in *Departement of chemistry*2010, Philipps-University: Marburg.
86. Back, K., *Funktionelle Charakterisierung von mVDAC1- Basis für Ion Channel Engineering*, in *Fachbereich Chemie*2010, Philipps Universität: Marburg.
87. Bertani, G., *Studies on lysogenesis I.: The mode of phage liberation by lysogenic Escherichia coli.* Journal of Bacteriology, 1951. **62**(3): p. 293.
88. http://sevierlab.vet.cornell.edu/resources/Stratagene-QuikchangeManual.pdf.
89. Müllhardt, C., *Der Experimentator: Molekularbiologie / Genomics*. Vol. 6. Auflage. 2008, Heidelberg: Spektrum Akademischer Verlag.
90. http://delliss.people.cofc.edu/virtuallabbook/LabReadings/CompCellsTransf/CompCells_PlasmidTransf.pdf .
91. Kushner, S.R., *An improved method for transformation of Escherichia coli with ColEl derived plasmids.* 1978.
92. Morrison, D., *Transformation in Escherichia coli: cryogenic preservation of competent cells.* Journal of bacteriology, 1977. **132**(1): p. 349-351.

93. Mandel, M. and A. Higa, *Calcium-dependent bacteriophage DNA infection.* Journal of Molecular Biology, 1970. **53**(1): p. 159-162.
94. Dower, W.J., J.F. Miller, and C.W. Ragsdale, *High efficiency transformation of E. coli by high voltage electroporation.* Nucleic acids Research, 1988. **16**(13): p. 6127-6145.
95. Calvin, N. and P. Hanawalt, *High-efficiency transformation of bacterial cells by electroporation.* Journal of Bacteriology, 1988. **170**(6): p. 2796-2801.
96. QIAGEN, *QIAprep® Miniprep Handbook, 2$_{end}$ Ed.*, 2006.
97. Feliciello, I. and G. Chinali, *A Modified Alkaline Lysis Method for the Preparation of Highly Purified Plasmid DNA from Escherichia Coli.* Analytical Biochemistry, 1993. **212**(2): p. 394-401.
98. Mülhardt, C., *Der Experimentator: Molekularbiologie, Genomics*. 2009: Springer.
99. Mertins, B., et al., *Flexibility of the N-terminal mVDAC1 segment controls the channel's gating behavior.* PloS one, 2012. **7**(10): p. e47938.
100. Brookman, G. and S. James, *Mechanism of cell disintegration in a high pressure homogenizer.* Biotechnology and Bioengineering, 1974. **16**(3): p. 371-383.
101. De Bernardez Clark, E., E. Schwarz, and R. Rudolph, *Inhibition of aggregation side reactions during in vitro protein folding.* Methods in Enzymology, 1999. **309**: p. 217-236.
102. Middelberg, A.P., *Preparative protein refolding.* TRENDS in Biotechnology, 2002. **20**(10): p. 437-443.
103. http://expassy.org/tools/protparam.html.
104. Li, H., et al., *Cleavage of BID by caspase 8 mediates the mitochondrial damage in the Fas pathway of apoptosis.* Cell, 1998. **94**(4): p. 491-501.
105. Wang, Y. and N. Tjandra, *Structural insights of tBid, the caspase-8-activated Bid, and its BH3 domain.* Journal of Biological Chemistry, 2013. **288**(50): p. 35840-35851.
106. Mertins, B., *Strukturelle und funktionelle Charakterisierung von mVDAC1-Biohybriden; Diplomarbeit Philipps-Universität Marburg.* 2011.
107. Gaberc-Porekar, V. and V. Menart, *Perspectives of immobilized-metal affinity chromatography.* Journal of Biochemical and Biophysical Methods, 2001. **49**(1): p. 335-360.
108. Hunte, C., G. von Jagow, and H. Schagger, *Membrane protein purification and crystallization: a practical guide*. 2003: Academic press.
109. Chen, M., et al., *Outer membrane protein G: Engineering a quiet pore for biosensing.* Proceedings of the National Academy of Sciences, 2008. **105**(17): p. 6272.
110. Klammt, C., et al., *Cell-free production of integral membrane proteins on a preparative scale.* Methods in Molecular Biology, 2007. **375**: p. 57-78.
111. Neves, P., et al., *Characterization of membrane protein reconstitution in LUVs of different lipid composition by fluorescence anisotropy.* Journal of pharmaceutical and biomedical analysis, 2009. **49**(2): p. 276-81.
112. Eriks, L.R., J.A. Mayor, and R.S. Kaplan, *A strategy for identification and quantification of detergents frequently used in the purification of membrane proteins.* Analytical Biochemistry, 2003. **323**(2): p. 234-41.
113. Laemmli, U.K., *Cleavage of structural proteins during the assembly of the head of bacteriophage T4.* Nature, 1970. **227**(5259): p. 680-685.
114. Oakley, B.R., D.R. Kirsch, and N.R. Morris, *A simplified ultrasensitive silver stain for detecting proteins in polyacrylamide gels.* Analytical Biochemistry, 1980. **105**(1): p. 361-363.
115. Wittig, I., H.-P. Braun, and H. Schägger, *Blue native PAGE.* Nature protocols, 2006. **1**(1): p. 418-428.
116. Pappin, D., P. Hojrup, and A. Bleasby, *Rapid identification of proteins by peptide-mass fingerprinting.* Current Biology, 1993. **3**(6): p. 327-332.
117. Henzel, W.J., et al., *Identifying proteins from two-dimensional gels by molecular mass searching of peptide fragments in protein sequence databases.* Proceedings of the National Academy of Sciences, 1993. **90**(11): p. 5011.
118. Marshall, A.G., C.L. Hendrickson, and G.S. Jackson, *Fourier transform ion cyclotron resonance mass spectrometry: a primer.* Mass spectrometry reviews, 1998. **17**(1): p. 1-35.

119. Rose, F., *Über die Verbindungen des Eiweiss mit Metalloxyden.* Annalen der Physik, 1833. **104**(5): p. 132-142.
120. Smith, P., et al., *Measurement of protein using bicinchoninic acid.* Analytical Biochemistry, 1985. **150**(1): p. 76-85.
121. Benz, R., et al., *Formation of large, ion-permeable membrane channels by the matrix protein (porin) of Escherichia coli.* Biochimica et Biophysica Acta (BBA)-Biomembranes, 1978. **511**(3): p. 305-319.
122. Sakmann, B. and E. Neher, *Single-channel recording*. 2009: Springer New York.
123. Mueller, P., et al., *Methods for the formation of single bimolecular lipid membranes in aqueous solution.* The Journal of Physical Chemistry, 1963. **67**(2): p. 534-535.
124. Bean, R., et al., *Discrete conductance fluctuations in lipid bilayer protein membranes.* The Journal of General Physiology, 1969. **53**(6): p. 741-757.
125. Hladky, S. and D. Haydon, *Discreteness of conductance change in bimolecular lipid membranes in the presence of certain antibiotics.* 1970.
126. Grosse, W., et al., *Structural and functional characterization of a synthetically modified OmpG.* Bioorganic & Medicinal Chemistry, 2010. **18**(22): p. 7716-23.
127. Ericsson, U.B., et al., *Thermofluor-based high-throughput stability optimization of proteins for structural studies.* Analytical biochemistry, 2006. **357**(2): p. 289-298.
128. Alexandrov, A.I., et al., *Microscale fluorescent thermal stability assay for membrane proteins.* Structure, 2008. **16**(3): p. 351-359.
129. Ludwig, C., K.H.-u. Staatsdruckerei, and W. Braumüller, *Diffusion zwischen ungleich erwärmten Orten gleich zusammengesetzter Lösung*. 1856: Aus der KK Hof-und Staatsdruckerei, in Commission bei W. Braumüller, Buchhändler des KK Hofes und der K. Akademie der Wissenschaften.
130. Würger, A., *Temperature dependence of the soret motion in colloids.* Langmuir, 2009. **25**(12): p. 6696-6701.
131. Jerabek-Willemsen, M., et al., *Molecular interaction studies using microscale thermophoresis.* Assay and drug development technologies, 2011. **9**(4): p. 342-353.
132. Seidel, S.A., et al., *Microscale thermophoresis quantifies biomolecular interactions under previously challenging conditions.* Methods, 2013. **59**(3): p. 301-315.
133. Wienken, C.J., et al., *Protein-binding assays in biological liquids using microscale thermophoresis.* Nature Communications, 2010. **1**: p. 100.
134. Ranjbar, B. and P. Gill, *Circular Dichroism Techniques: Biomolecular and Nanostructural Analyses-A Review.* Chemical Biology & Drug design, 2009. **74**(2): p. 101-120.
135. http://www.photophysics.com/tutorials/circular-dichroism-cd-spectroscopy/4-cd-spectrometer-operating-principles.
136. Kelly, S.M. and N.C. Price, *The use of circular dichroism in the investigation of protein structure and function.* Current Protein and Peptide Science, 2000. **1**(4): p. 349-384.
137. van Stokkum, I.H., et al., *Estimation of protein secondary structure and error analysis from circular dichroism spectra.* Analytical biochemistry, 1990. **191**(1): p. 110-8.
138. Provencher, S.W. and J. Glockner, *Estimation of globular protein secondary structure from circular dichroism.* Biochemistry, 1981. **20**(1): p. 33-7.
139. Whitmore, L. and B.A. Wallace, *DICHROWEB, an online server for protein secondary structure analyses from circular dichroism spectroscopic data.* Nucleic acids research, 2004. **32**(Web Server issue): p. W668-73.
140. Lobley, A., L. Whitmore, and B.A. Wallace, *DICHROWEB: an interactive website for the analysis of protein secondary structure from circular dichroism spectra.* Bioinformatics, 2002. **18**(1): p. 211-2.
141. Sreerama, N. and R.W. Woody, *Estimation of protein secondary structure from circular dichroism spectra: comparison of CONTIN, SELCON, and CDSSTR methods with an expanded reference set.* Analytical Biochemistry, 2000. **287**(2): p. 252-60.

142. Abdul-Gader, A., A.J. Miles, and B.A. Wallace, *A reference dataset for the analyses of membrane protein secondary structures and transmembrane residues using circular dichroism spectroscopy.* Bioinformatics, 2011. **27**(12): p. 1630-1636.
143. Lees, J.G., et al., *A reference database for circular dichroism spectroscopy covering fold and secondary structure space.* Bioinformatics, 2006. **22**(16): p. 1955-1962.
144. Burck, J., et al., *Conformation and membrane orientation of amphiphilic helical peptides by oriented circular dichroism.* Biophysical journal, 2008. **95**(8): p. 3872-81.
145. Windisch, D., et al., *Structural role of the conserved cysteines in the dimerization of the viral transmembrane oncoprotein E5.* Biophysical journal, 2010. **99**(6): p. 1764-72.
146. Wu, Y., H.W. Huang, and G.A. Olah, *Method of oriented circular dichroism.* Biophysical journal, 1990. **57**(4): p. 797-806.
147. Klare, J.P. and H.-J. Steinhoff, *Spin labeling EPR.* Photosynthesis research, 2009. **102**(2-3): p. 377-390.
148. Bordignon, E. and H.-J. Steinhoff, *Membrane protein structure and dynamics studied by site-directed spin-labeling ESR*, in *ESR spectroscopy in membrane biophysics*. 2007, Springer. p. 129-164.
149. Steinhoff, H.-J., et al., *Two dimensional diffusion of small molecules on protein surfaces: an EPR study of the restricted translational diffusion of protein-bound spin labels.* European Biophysics Journal, 1991. **20**(5): p. 293-303.
150. Steinhoff, H.-J., et al., *Determination of interspin distances between spin labels attached to insulin: comparison of electron paramagnetic resonance data with the X-ray structure.* Biophysical Journal, 1997. **73**(6): p. 3287.
151. Berliner, L.J., *From spin-labeled proteins to in vivo EPR applications.* European Biophysics Journal, 2010. **39**(4): p. 579-588.
152. Pannier, M., et al., *Dead-time free measurement of dipole–dipole interactions between electron spins.* Journal of Magnetic Resonance, 2000. **142**(2): p. 331-340.
153. Jeschke, G. and Y. Polyhach, *Distance measurements on spin-labelled biomacromolecules by pulsed electron paramagnetic resonance.* Physical Chemistry Chemical Physics, 2007. **9**(16): p. 1895-1910.
154. Polyhach, Y., E. Bordignon, and G. Jeschke, *Rotamer libraries of spin labelled cysteines for protein studies.* Physical Chemistry Chemical Physics, 2011. **13**(6): p. 2356-2366.
155. Jancarik, J. and S.-H. Kim, *Sparse matrix sampling: a screening method for crystallization of proteins.* Journal of Applied Crystallography, 1991. **24**(4): p. 409-411.
156. Landau, E.M. and J.P. Rosenbusch, *Lipidic cubic phases: a novel concept for the crystallization of membrane proteins.* Proceedings of the National Academy of Sciences, 1996. **93**(25): p. 14532-14535.
157. Sanders, C.R. and J.H. Prestegard, *Magnetically orientable phospholipid bilayers containing small amounts of a bile salt analogue, CHAPSO.* Biophysical journal, 1990. **58**(2): p. 447-460.
158. Colombini, M., *Voltage gating in the mitochondrial channel, VDAC.* Journal of Membrane Biology, 1989. **111**(2): p. 103-111.
159. Meng, F.-G., Y.-D. Park, and H.-M. Zhou, *Role of proline, glycerol, and heparin as protein folding aids during refolding of rabbit muscle creatine kinase.* The International Journal of Biochemistry & Cell Biology, 2001. **33**(7): p. 701-709.
160. Engelhardt, H., et al., *High-level expression, refolding and probing the natural fold of the human voltage-dependent anion channel isoforms I and II.* Journal of Membrane Biology, 2007. **216**(2): p. 93-105.
161. Popp, B., et al., *The role of the N and C termini of recombinant Neurospora mitochondrial porin in channel formation and voltage-dependent gating.* Journal of Biological Chemistry, 1996. **271**(23): p. 13593-13599.
162. Shanmugavadivu, B., et al., *Correct Folding of the [beta]-Barrel of the Human Membrane Protein VDAC Requires a Lipid Bilayer.* Journal of Molecular Biology, 2007. **368**(1): p. 66-78.

163. De Pinto, V., et al., *Structure of the voltage dependent anion channel: state of the art.* Journal of Bioenergetics and Biomembranes, 2008. **40**(3): p. 139-147.
164. Kienker, P., et al., *Transmembrane insertion of the colicin Ia hydrophobic hairpin.* Journal of Membrane Biology, 1997. **157**(1): p. 27-37.
165. Krasilnikov, O., et al., *A novel approach to study the geometry of the water lumen of ion channels: colicin Ia channels in planar lipid bilayers.* Journal of Membrane Biology, 1998. **161**(1): p. 83-92.
166. Marques, E.J., et al., *Does VDAC insert into membranes in random orientation?* Biochimica et Biophysica Acta (BBA)-Biomembranes, 2004. **1661**(1): p. 68-77.
167. Zizi, M., et al., *Oriented channel insertion reveals the motion of a transmembrane beta strand during voltage gating of VDAC.* Journal of Membrane Biology, 1995. **144**(2): p. 121-129.
168. Arbel, N., D. Ben-Hail, and V. Shoshan-Barmatz, *Mediation of the antiapoptotic activity of Bcl-xL protein upon interaction with VDAC1 protein.* Journal of Biological Chemistry, 2012. **287**(27): p. 23152-23161.
169. Malia, T.J. and G. Wagner, *NMR structural investigation of the mitochondrial outer membrane protein VDAC and its interaction with antiapoptotic Bcl-xL.* Biochemistry, 2007. **46**(2): p. 514-525.
170. Rostovtseva, T.K., et al., *Bid, but not Bax, regulates VDAC channels.* Journal of Biological Chemistry, 2004. **279**(14): p. 13575-13583.
171. Shimizu, S., et al., *Essential role of voltage-dependent anion channel in various forms of apoptosis in mammalian cells.* The Journal of Cell Biology, 2001. **152**(2): p. 237-250.
172. Godbole, A., et al., *Mitochondrial VDAC and hexokinase together modulate plant programmed cell death.* Protoplasma, 2013. **250**(4): p. 875-884.
173. Chaanine, A.H., et al., *Potential Role of BNIP3 in Cardiac Remodeling, Myocardial Stiffness, and Endoplasmic Reticulum Mitochondrial Calcium Homeostasis in Diastolic and Systolic Heart Failure.* Circulation: Heart Failure, 2013. **6**(3): p. 572-583.
174. G.Veresov, V. and A.I. Davidovskii, *Structural insights into proapoptotic signaling mediated by MTCH2, VDAC2, TOM40 and TOM22.* Cellular Signalling, 2014. **26**(2): p. 370-382.
175. Sina Oppermann, B.M., Lilja Meissner, Cornelius Krasel, Georgios Psakis, Philipp Reiß, Amalia M. Dolga, Nikolaus Plesnila, Moritz Bünemann, Lars-Oliver Essen, Carsten Culmsee, *Interaction of Bid and VDAC1 determines mitochondrial demise and cell death in neurons.* submitted, 2014.
176. Gao, Z., Y. Shao, and X. Jiang, *Essential roles of the Bcl-2 family of proteins in caspase-2-induced apoptosis.* Journal of Biological Chemistry, 2005. **280**(46): p. 38271-38275.
177. Abu-Hamad, S., et al., *The VDAC1 N-terminus is essential both for apoptosis and the protective effect of anti-apoptotic proteins.* Journal of Cell Science, 2009. **122**(11): p. 1906-1916.
178. Gincel, D., S.D. Silberberg, and V. Shoshan-Barmatz, *Modulation of the voltage-dependent anion channel (VDAC) by Glutamate1.* Journal of bioenergetics and biomembranes, 2000. **32**(6): p. 571-583.
179. Hiller, S., et al., *Solution structure of the integral human membrane protein VDAC-1 in detergent micelles.* Science, 2008. **321**(5893): p. 1206-1210.
180. Krammer, E.-M., F. Homble, and M. Prévost, *Concentration dependent ion selectivity in VDAC: a molecular dynamics simulation study.* PloS one, 2011. **6**(12): p. e27994.
181. Lee, K.I., et al., *Brownian dynamics simulations of ion transport through the VDAC.* Biophysical Journal, 2011. **100**(3): p. 611-619.
182. Rui, H., et al., *Molecular dynamics studies of ion permeation in VDAC.* Biophysical Journal, 2011. **100**(3): p. 602-610.
183. Ujwal, R., et al., *The crystal structure of mouse VDAC1 at 2.3 Å resolution reveals mechanistic insights into metabolite gating.* Proceedings of the National Academy of Sciences, 2008. **105**(46): p. 17742-17747.

184. Windisch, D., et al., *Structural characterization of a C-terminally truncated E5 oncoprotein from papillomavirus in lipid bilayers.* Biological Chemistry, 2014. **395**(12): p. 1443-1452.
185. Benz, R., *Structure and function of porins from gram-negative bacteria.* Annual Reviews in Microbiology, 1988. **42**(1): p. 359-393.
186. Lou, K.-L., et al., *Structural and functional characterization of OmpF porin mutants selected for larger pore size I. Crystallographic analysis.* Journal of Biological Chemistry, 1996. **271**(34): p. 20669-20675.
187. Phale, P.S., et al., *Voltage gating of Escherichia coli porin channels: role of the constriction loop.* Proceedings of the National Academy of Sciences, 1997. **94**(13): p. 6741-6745.
188. Pavlov, E., et al., *The mitochondrial channel VDAC has a cation-selective open state.* Biochimica et Biophysica Acta (BBA)-Bioenergetics, 2005. **1710**(2-3): p. 96-102.
189. Teijido, O., et al., *Affixing the N-terminal alpha helix of the voltage dependent anion channel to the channel' s wall does not prevent its voltage gating.* Journal of Biological Chemistry, 2012.
190. Mertins, B., G. Psakis, and L.-O. Essen, *Voltage-dependent anion channels: the wizard of the mitochondrial outer membrane.* Biological chemistry, 2014. **395**(12): p. 1435-1442.
191. Colombini, M., *The published 3D structure of the VDAC channel: native or not?* Trends in Biochemical Sciences, 2009. **34**(8): p. 382-389.
192. Hiller, S., et al., *The 3D structures of VDAC represent a native conformation.* Trends in Biochemical Sciences, 2010.
193. Colombini, M., E. Blachly-Dyson, and M. Forte, *VDAC, a channel in the outer mitochondrial membrane.* Ion channels, 1996. **4**: p. 169-202.
194. Hiller, S., et al., *Solution structure of the integral human membrane protein VDAC-1 in detergent micelles.* Science's STKE, 2008. **321**(5893): p. 1206.
195. Krammer, E.M., F. Homblé, and M. Prévost, *Concentration Dependent Ion Selectivity in VDAC: A Molecular Dynamics Simulation Study.* PLoS ONE, 2011. **6**(12): p. e27994.
196. Thomas, L., et al., *Mapping of residues forming the voltage sensor of the voltage-dependent anion-selective channel.* Proceedings of the National Academy of Sciences, 1993. **90**(12): p. 5446.
197. Villinger, S., et al., *Functional dynamics in the voltage-dependent anion channel.* Proceedings of the National Academy of Sciences, 2010. **107**(52): p. 22546.
198. Zachariae, U., et al., *β-Barrel mobility underlies closure of the voltage-dependent anion channel.* Structure, 2012. **20**(9): p. 1540-1549.
199. Kozuch, J., et al., *Voltage-dependent structural changes of the membrane-bound anion channel hVDAC1 probed by SEIRA and electrochemical impedance spectroscopy.* Physical Chemistry Chemical Physics, 2014.
200. Geula, S., D. Ben-Hail, and V. Shoshan-Barmatz, *Structure-based analysis of VDAC1: N-terminus location, translocation, channel gating and association with anti-apoptotic proteins.* 2012.
201. Rostovtseva, T.K., et al., *Voltage gating of VDAC is regulated by nonlamellar lipids of mitochondrial membranes.* Journal of Biological Chemistry, 2006. **281**(49): p. 37496.
202. Schneider, R., et al., *The native conformation of the human VDAC1 N terminus.* Angewandte Chemie International Edition, 2010. **49**(10): p. 1882-1885.
203. Weichbrodt, C., *Elektrophysiologische Charakterisierung des mitochondrialen Porins VDAC1 und des antimikrobiellen Peptids Dermcidin in lösungsmittelfreien Modellmembranen*, 2013, Niedersächsische Staats-und Universitätsbibliothek Göttingen.
204. Schredelseker, J., et al., *High Resolution Structure and Double Electron-Electron Resonance of the Zebrafish Voltage-dependent Anion Channel 2 Reveal an Oligomeric Population.* Journal of Biological Chemistry, 2014. **289**(18): p. 12566-12577.
205. Cheng, E.H.-Y., et al., *VDAC2 inhibits BAK activation and mitochondrial apoptosis.* Science, 2003. **301**(5632): p. 513-517.

206. Messina, A., et al., *VDAC isoforms in mammals.* Biochimica et Biophysica Acta (BBA)-Biomembranes, 2012. **1818**(6): p. 1466-1476.
207. Colombini, M., *VDAC: the channel at the interface between mitochondria and the cytosol.* Molecular and cellular biochemistry, 2004. **256**(1-2): p. 107-115.
208. Müller, D.J. and A. Engel, *Voltage and pH-induced channel closure of porin OmpF visualized by atomic force microscopy.* Journal of molecular biology, 1999. **285**(4): p. 1347-1351.
209. Schlesinger, P.H., et al., *Comparison of the ion channel characteristics of proapoptotic BAX and antiapoptotic BCL-2.* Proceedings of the National Academy of Sciences, 1997. **94**(21): p. 11357-11362.
210. Teijido, O., et al., *Acidification affects voltage-dependent anion channel functioning asymmetrically: role of salt bridges.* Journal of Biological Chemistry, 2014: p. jbc. M114. 576314.
211. Törnroth-Horsefield, S. and R. Neutze, *Opening and closing the metabolite gate.* Proceedings of the National Academy of Sciences, 2008. **105**(50): p. 19565-19566.
212. Aram, L., et al., *VDAC1 cysteine residues: topology and function in channel activity and apoptosis.* Biochem. J, 2010. **427**: p. 445-454.
213. Geula, S., et al., *Structure-based Analysis of VDAC1 Protein DEFINING OLIGOMER CONTACT SITES.* Journal of Biological Chemistry, 2012. **287**(3): p. 2179-2190.
214. Maurya, S.R. and R. Mahalakshmi, *Influence of Protein–Micelle Ratios and Cysteine Residues on the Kinetic Stability and Unfolding Rates of Human Mitochondrial VDAC-2.* PloS one, 2014. **9**(1): p. e87701.
215. Korkmaz-Ozkan, F., et al., *Correlation between the OmpG secondary structure and its pH-dependent alterations monitored by FTIR.* Journal of molecular biology, 2010. **401**(1): p. 56-67.
216. Ramakrishnan, M., et al., *Orientation of beta-barrel proteins OmpA and FhuA in lipid membranes. Chain length dependence from infrared dichroism.* Biochemistry, 2005. **44**(9): p. 3515-23.
217. Muhle-Goll, C., et al., *Hydrophobic matching controls the tilt and stability of the dimeric platelet-derived growth factor receptor (PDGFR) β transmembrane segment.* Journal of Biological Chemistry, 2012. **287**(31): p. 26178-26186.
218. Muhle-Goll, C., et al., *Hydrophobic matching controls the tilt and stability of the dimeric platelet-derived growth factor receptor (PDGFR) beta transmembrane segment.* The Journal of Biological Chemistry, 2012. **287**(31): p. 26178-86.
219. Vogel, H., *Comparison of the conformation and orientation of alamethicin and melittin in lipid membranes.* Biochemistry, 1987. **26**(14): p. 4562-72.
220. Qian, S., et al., *Structure of transmembrane pore induced by Bax-derived peptide: evidence for lipidic pores.* Proceedings of the National Academy of Sciences of the United States of America, 2008. **105**(45): p. 17379-83.
221. Ruskamo, S., et al., *Atomic resolution view into the structure-function relationships of the human myelin peripheral membrane protein P2.* Acta Crystallographica Section D, 2014. **70**(1): p. 165-176.
222. Movileanu, L., S. Cheley, and H. Bayley, *Partitioning of individual flexible polymers into a nanoscopic protein pore.* Biophysical Journal, 2003. **85**(2): p. 897-910.
223. Jung, Y., H. Bayley, and L. Movileanu, *Temperature-responsive protein pores.* Journal of the American Chemical Society, 2006. **128**(47): p. 15332-40.
224. Reina, S., et al., *Deletion of beta-strands 9 and 10 converts VDAC1 voltage-dependence in an asymmetrical process.* Biochimica et biophysica acta, 2013. **1827**(6): p. 793-805.
225. Mannella, C.A. and K.W. Kinnally, *Reflections on VDAC as a voltage-gated channel and a mitochondrial regulator.* Journal of Bioenergetics and Biomembranes, 2008. **40**(3): p. 149-155.

226. Chipuk, J., L. Bouchier-Hayes, and D. Green, *Mitochondrial outer membrane permeabilization during apoptosis: the innocent bystander scenario.* Cell Death & Differentiation, 2006. **13**(8): p. 1396-1402.
227. Desagher, S. and J.-C. Martinou, *Mitochondria as the central control point of apoptosis.* Trends in Cell Biology, 2000. **10**(9): p. 369-377.
228. Green, D.R. and G. Kroemer, *The pathophysiology of mitochondrial cell death.* Science, 2004. **305**(5684): p. 626-629.
229. Barho, M.T., et al., *N-Acyl Derivatives of 4-Phenoxyaniline as Neuroprotective Agents.* ChemMedChem, 2014. **9**(10): p. 2260-2273.
230. Grohm, J., et al., *Inhibition of Drp1 provides neuroprotection in vitro and in vivo.* Cell Death & Differentiation, 2012. **19**(9): p. 1446-1458.
231. Landshamer, S., et al., *Bid-induced release of AIF from mitochondria causes immediate neuronal cell death.* Cell Death & Differentiation, 2008. **15**(10): p. 1553-1563.
232. Oppermann, S., et al., *Novel N-phenyl substituted thiazolidinediones protect neural cells against glutamate-and tBid-induced toxicity.* Journal of Pharmacology and Experimental Therapeutics, 2014: p. jpet. 114.213777.
233. Tobaben, S., et al., *Bid-mediated mitochondrial damage is a key mechanism in glutamate-induced oxidative stress and AIF-dependent cell death in immortalized HT-22 hippocampal neurons.* Cell Death & Differentiation, 2010. **18**(2): p. 282-292.
234. Culmsee, C., et al., *Apoptosis-inducing factor triggered by poly (ADP-ribose) polymerase and Bid mediates neuronal cell death after oxygen-glucose deprivation and focal cerebral ischemia.* The Journal of Neuroscience, 2005. **25**(44): p. 10262-10272.
235. Bermpohl, D., et al., *Traumatic brain injury in mice deficient in Bid: effects on histopathology and functional outcome.* Journal of Cerebral Blood Flow & Metabolism, 2005. **26**(5): p. 625-633.
236. Yin, X.-M., et al., *Bid-mediated mitochondrial pathway is critical to ischemic neuronal apoptosis and focal cerebral ischemia.* Journal of Biological Chemistry, 2002. **277**(44): p. 42074-42081.
237. Becattini, B., et al., *Targeting apoptosis via chemical design: inhibition of bid-induced cell death by small organic molecules.* Chemistry & biology, 2004. **11**(8): p. 1107-1117.
238. Lepke, S., et al., *A study of the relationship between inhibition of anion exchange and binding to the red blood cell membrane of 4, 4'-diisothiocyano stilbene-2, 2'-disulfonic acid (DIDS) and its dihydro derivative (H2DIDS).* The Journal of membrane biology, 1976. **29**(1): p. 147-177.
239. Benz, R., *Permeation of hydrophilic solutes through mitochondrial outer membranes: review on mitochondrial porins.* Biochimica et Biophysica Acta (BBA)-Reviews on Biomembranes, 1994. **1197**(2): p. 167-196.
240. Shoshan-Barmatz, V., N. Keinan, and H. Zaid, *Uncovering the role of VDAC in the regulation of cell life and death.* Journal of bioenergetics and biomembranes, 2008. **40**(3): p. 183-191.
241. Villinger, S., et al., *Functional dynamics in the voltage-dependent anion channel.* Proceedings of the National Academy of Sciences, 2010. **107**(52): p. 22546-22551.
242. G Veresov, V. and A.I. Davidovskii, *Structural insights into proapoptotic signaling mediated by MTCH2, VDAC2, TOM40 and TOM22.* Cellular signalling, 2014. **26**(2): p. 370-382.
243. Wojtkowska, M., et al., *Phylogenetic analysis of mitochondrial outer membrane β-barrel channels.* Genome Biology and Evolution, 2012. **4**(2): p. 110-125.
244. Mueller, M., et al., *The structure of a cytolytic &agr;-helical toxin pore reveals its assembly mechanism.* Nature, 2009. **459**(7247): p. 726-730.

8. Acknowledgment

First and foremost, I would like to thank Prof. Dr Lars-Oliver Essen for the interesting and challenging work with membrane proteins. As a membrane protein scientist has to be a bit "special", he always supported and helped me through troubled times. His understanding and clear advices helped me to become a better scientist and for this I would like to thank him the most.

I would also like to thank Professor Norbert Hampp for kindly taking up the secondary supervision of this work.

A special thank goes to Sophie, Silke, Katrin and George for correcting and line editing of this thesis.

Many thanks to all my collaboration partners who helped me to think outside the "biochemical" box. I thank Dr Philipp Reiß for performing the BLM measurements, Dr Dirk Windisch for analysing the CD and OCD data, Dr Johann Klare and Katharina Rudi for the EPR measurements. Furthermore, I would like to thank Dr Sina Oppermann for providing the cell line experiments, which helped to bring my work to a next level.

A special thank goes to Dr Georgios Psakis and Dr Louisa Tsougaraki. You are good friends in good and bad times and you helped me to settle after all the things that have happened. George I would like to thank you for all the inspiring discussion and the priceless evenings in the Quod.

Dr Wolfgang Grosse and Dr Manuel Maestre-Reyna helped me in the early stage of my scientific career. Beside the work, both of you were good friends and I have to thank you for the great time.

To all the former and actual members of the Essen group Ankan, Elisabeth, Katrin, Maik, Manuel, Michael, Petra, Ralf, Silke, Sophie, Stephan, Timo, Wolfgang, Vitali and Yann go my most heartful thanks for having provided for such a great time.

To all friends in Germany, Spain, Italy, Taiwan, Canada, UK and everywhere else, please feel acknowledged. Without you, life would have been less colourful.

I like to thank my boyfriend Johannes Gleisinger for the mental and moral support and all the midnight dinners. Thank you for all the small and big things and all hot-water bags when I was freezing cold.

Finally, I would like to thank my parents, my brother Christof and my sister Susanne, their unconditional support, love and intelligence have always been an inspiration to me, even if I did not show it all the time. A special thanks to my brother. He as a sociologist draws my attention to the scientific system in natural science and human discipline. Through this I became a much better scientist as I learned that formation of hypotheses is more than just having ideas. Thank you for make me think instead of having thoughts. Suse, there is a special connection between us and no words are needed to express how important you are for me.

9. Appendix

9.1 Abbreviations

Å	angstrom
A	ampere
Amp	ampicillin
APS	ammoniumperoxidisulfate
AU	absorption units
BLM	black-lipid-membrane
bp	basepair
CHAPSO	3-[(3-cholamidopropyl)-dimethylammonio]-2-hydroxy-1-propanesulfonate
CMC	critical micellar concentration
Da	dalton
dH_2O (dest. H_2O)	distilled water
ddH_2O(bidest.H_2O)	double distilled water
DMF	dimethylformamide
DMPC	1,2-dimyristoyl-sn-glycero-3-phosphocholine
DMSO	dimethyl sulfoxide
DNA	desoxyribonucleic acid
dNTPs	2'-desoxynucleotide
DTT	dithiothreitol
EDTA	ethylenediaminetetraacetic acid
EPR	electron paramagnetic resonance
EtOH	ethanol
g	gram
h	hour
HPLC	high pressure liquid chromatography
IB	inclusion bodies
IEC	ion exchange chromatography
IPTG	isopropyl-β-D-thiogalactopyranoside

L	litre
LDAO	lauryldimethylamine-N-oxide
TOF	time of flight
m	meter
M	molar (mol/L)
MCS	multiple cloning side
min	minutes
mVDAC	murine voltage dependent anion channel
MWCO	molecular weight cut off
NMR	nucleic magnetic resonance
NaOAc	sodiumacetate
OD	optical denisity
OG	*n*-octyl-β-*D*-glucopyranoside
Omp	outer membrane protein
PCR	polymerase chain reaction
rpm	rotations per minute
RNA	ribonucleic acid
RT	room temperature
S	Siemens
SDS	sodiumdodecylsulfate
SDS-PAGE	sodiumdodecylsulfate poly-acrylamide gel electrophoresis
TCA	trichloroacetic acid
TCEP	tris(2-carboxyethyl)phosphinhydrochloride
TMEDA	tetramethylenethylenediamine
Tris	tris(hydroxymethyl)-aminomethane
UV	ultraviolett
V	Volt

9.2 Abbreviations of amino acids

Amino acid	Three letter code	One letter code
Alanin	Ala	A
Arginin	Arg	R
Asparagin	Asn	N
Aspartat	Asp	D
Cystein	Cys	C
Glutamat	Glu	E
Glutamin	Gln	Q
Glycin	Gly	G
Histidin	His	H
Isoleucin	Ile	I
Leucin	Leu	L
Lysin	Lys	K
Methionin	Met	M
Phenylalanin	Phe	F
Prolin	Pro	P
Serin	Ser	S
Threonin	Thr	T
Tryptophan	Trp	W
Tyrosin	Tyr	Y
Valin	Val	V

9.3 nucleotide and amino acid sequence of the used proteins

mVDAC1

nucleotide sequence:

ATGGCCGTGCCTCCCACATACGCCGATCTTGGCAAGTCCGCCAGGGATGTCTTCACCAAGGGCTACGGCTTTGGC
TTAATAAAACTTGATTTGAAAACGAAGTCAGAGAATGGATTGGAATTTACCAGCTCAGGCTCTGCCAACACGGAA
ACCACCAAAGTGAACGGCAGCCTGGAAACCAAGTACAGATGGACTGAGTATGGGCTGACGTTTACAGAGAAGTGG
AACACAGACAACACCCTGGGCACTGAGATCACTGTGGAAGACCAGCTTGCTCGTGGACTGAAGCTCACCTTTGAT
TCGTCATTCTCGCCGAACACTGGGAAAAAAAATGCTAAAATCAAGACAGGGTACAAGAGGGAGCACATCAACCTC
GGCTGTGACGTGGACTTTGACATCGCTGGGCCCTCGATCCGGGGCGCTCTGGTGCTTGGCTATGAGGGTTGGCTG
GCTGGCTACCAGATGAATTTTGAGACCTCGAAGTCCCGAGTGACCCAGAGCAACTTCGCAGTTGGCTATAAGACG
GATGAATTCCAGCTTCATACTAATGTGAATGACGGGACAGAGTTTGGTGGCTCCATTTACCAGAAGGTGAACAAG
AAGTTGGAGACTGCTGTCAATCTCGCCTGGACTGCAGGAAACAGTAACACTCGCTTCGGAATAGCAGCCAAGTAT
CAGGTCGACCCTGATGCCTGCTTTTCGGCCAAAGTGAACAACTCTAGCCTGATTGGCTTAGGGTACACTCAGACC
CTAAAACCAGGTATCAAACTGACGTTGTCAGCCCTGCTCGATGGCAAGAACGTCAATGCGGGTGGCCACAAGCTT
GGCCTAGGACTGGAATTTCAAGCATAA

amino acid sequence:

MAVPPTYADLGKSARDVFTKGYGFGLIKLDLKTKSENGLEFTSSGSANTETTKVNGL
ETKYRWTEYGLTFTEKWNTDNTLGTEITVEDQLARGLKLTFDSSFSPNTGKKNAKIK
TGYKREHINLGCDVDFDIAGPSIRGALVLGYEGWLAGYQMNFETSKSRVTQSNFAVG
YKTDEFQLHTNVNDGTEFGGSIYQKVNKKLETAVNLAWTAGNSNTRFGIAAKYQVD
PDACFSAKVNNSSLIGLGYTQTLKPGIKLTLSALLDGKNVNAGGHKLGLGLEFQA

mVDAC2

nucleotide sequence:

ATGGCCGAATGTTGTGTTCCGGTTTGTCCGCGTCCGATGTGTATTCCGCCTCCGTATGCAGATCTGGGTAAAGCA
GCACGTGATATTTTCAATAAAGGTTTTGGTTTCGGCCTGGTGAAACTGGATGTTAAAACCAAAAGCTGTAGCGGT
GTTGAATTTAGCACCAGCGGTAGCAGCAATACCGATACCGGTAAAGTTAGCGGCACCCTGGAAACCAAATACAAA
TGGTGTGAATATGGTCTGACCTTCACCGAAAAATGGAATACAGATAATACCCTGGGCACCGAAATTGCCATTGAA
GATCAGATTTGTCAGGGTCTGAAACTGACCTTTGATACCACCTTTAGCCCGAATACCGGCAAAAAAAGCGGTAAA
ATCAAAAGCGCCTATAAACGCGAATGCATTAATCTGGGTTGTGATGTGGATTTTGATTTCGCAGGTCCGGCAATT
CATGGTAGCGCAGTTTTTGGTTATGAAGGTTGGCTGGCAGGTTATCAGATGACATTTGATAGCGCAAAAAGCAAA
CTGACCCGTAGCAATTTTGCAGTTGGTTATCGTACCGGTGATTTTCAGCTGCATACCAATGTTAATAACGGCACC
GAATTTGGTGGTAGCATTTATCAGAAAGTGTGCGAAGATTTTGACACCAGCGTTAATCTGGCATGGACCAGCGGC
ACCAATTGTACCCGTTTTGGTATTGCAGCAAAATATCAGCTGGATCCGACCGCAAGCATTAGCGCCAAAGTGAAT
AATTCAAGCCTGATTGGTGTTGGTTATACCCAGACCCTGCGTCCGGGTGTTAAACTGACACTGAGCGCACTGGTT
GATGGTAAAAGCTTTAATGCCGGTGGTCATAAACTGGGTCTGGCACTGGAACTGGAAGCATAA

amino acid sequence:

MAECCVPVCPRPMCIPPPYADLGKAARDIFNKGFGFGLVKLDVKTKSCSGVEFSTSGS
SNTDTGKVSGTLETKYKWCEYGLTFTEKWNTDNTLGTEIAIEDQICQGLKLTFDTTFS
PNTGKKSGKIKSAYKRECINLGCDVDFDFAGPAIHGSAVFGYEGWLAGYQMTFDSA
KSKLTRSNFAVGYRTGDFQLHTNVNNGTEFGGSIYQKVCEDFDTSVNLAWTSGTNC
TRFGIAAKYQLDPTASISAKVNNSSLIGVGYTQTLRPGVKLTLSALVDGKSFNAGGHK
LGLALELEA.

mVDAC1-C127A-C232A

nucleotide sequence:

ATGGCCGTGCCTCCCACATACGCCGATCTTGGCAAGTCCGCCAGGGATGTCTTCACCAAGGGCTACGGCTTTGGC
TTAATAAAACTTGATTTGAAAACGAAGTCAGAGAATGGATTGGAATTTACCAGCTCAGGCTCTGCCAACACGGAA
ACCACCAAAGTGAACGGCAGCCTGGAAACCAAGTACAGATGGACTGAGTATGGGCTGACGTTTACAGAGAAGTGG
AACACAGACAACACCCTGGGCACTGAGATCACTGTGGAAGACCAGCTTGCTCGTGGACTGAAGCTCACCTTTGAT
TCGTCATTCTCGCCGAACACTGGGAAAAAAAATGCTAAAATCAAGACAGGGTACAAGAGGGAGCACATCAACCTC
GGGGCTGACGTGGACTTTGACATCGCTGGGCCCTCGATCCGGGGCGCTCTGGTGCTTGGCTATGAGGGTTGGCTG
GCTGGCTACCAGATGAATTTTGAGACCTCGAAGTCCCGAGTGACCCAGAGCAACTTCGCAGTTGGCTATAAGACG
GATGAATTCCAGCTTCATACTAATGTGAATGACGGGACAGAGTTTGGTGGCTCCATTTACCAGAAGGTGAACAAG
AAGTTGGAGACTGCTGTCAATCTCGCCTGGACTGCAGGAAACAGTAACACTCGCTTCGGAATAGCAGCCAAGTAT
CAGGTGGATCCTGATGCCGCCTTTTCGGCCAAAGTGAACAACTCTAGCCTGATTGGCTTAGGGTACACTCAGACC
CTAAAACCAGGTATCAAACTGACGTTGTCAGCCCTGCTCGATGGCAAGAACGTCAATGCGGGTGGCCACAAGCTT
GGCCTAGGACTGGAATTTCAAGCATAA

amino acid sequence:

MAVPPTYADLGKSARDVFTKGYGFGLIKLDLKTKSENGLEFTSSGSANTETTKVNGS
LETKYRWTEYGLTFTEKWNTDNTLGTEITVEDQLARGLKLTFDSSFSPNTGKKNAKI
KTGYKREHINLGADVDFDIAGPSIRGALVLGYEGWLAGYQMNFETSKSRVTQSNFAV
GYKTDEFQLHTNVNDGTEFGGSIYQKVNKKLETAVNLAWTAGNSNTRFGIAAKYQV
DPDAAFSAKVNNSSLIGLGYTQTLKPGIKLTLSALLDGKNVNAGGHKLGLGLEFQA

Δ 1-11-mVDAC1-K12C

nucleotide sequence:

ATGTGTTCCGCCAGGGATGTCTTCACCAAGGGCTACGGCTTTGGCTTAATAAAACTTGATTTGAAAACGAAGTCA
GAGAATGGATTGGAATTTACCAGCTCAGGCTCTGCCAACACGGAAACCACCAAAGTGAACGGCAGCCTGGAAACC
AAGTACAGATGGACTGAGTATGGGCTGACGTTTACAGAGAAGTGGAACACAGACAACACCCTGGGCACTGAGATC
ACTGTGGAAGACCAGCTTGCTCGTGGACTGAAGCTCACCTTTGATTCGTCATTCTCGCCGAACACTGGGAAAAAA
AATGCTAAAATCAAGACAGGGTACAAGAGGGAGCACATCAACCTCGGCTGTGACGTGGACTTTGACATCGCTGGG
CCCTCGATCCGGGGCGCTCTGGTGCTTGGCTATGAGGGTTGGCTGGCTGGCTACCAGATGAATTTTGAGACCTCG
AAGTCCCGAGTGACCCAGAGCAACTTCGCAGTTGGCTATAAGACGGATGAATTCCAGCTTCATACTAATGTGAAT
GACGGGACAGAGTTTGGTGGCTCCATTTACCAGAAGGTGAACAAGAAGTTGGAGACTGCTGTCAATCTCGCCTGG
ACTGCAGGAAACAGTAACACTCGCTTCGGAATAGCAGCCAAGTATCAGGTCGACCCTGATGCCTGCTTTTCGGCC
AAAGTGAACAACTCTAGCCTGATTGGCTTAGGGTACACTCAGACCCTAAAACCAGGTATCAAACTGACGTTGTCA
GCCCTGCTCGATGGCAAGAACGTCAATGCGGGTGGCCACAAGCTTGGCCTAGGACTGGAATTTCAAGCATAA

amino acid sequence:

MCSARDVFTKGYGFGLIKLDLKTKSENGLEFTSSGSANTETTKVNGSLETKYRWTEY
GLTFTEKWNTDNTLGTEITVEDQLARGLKLTFDSSFSPNTGKKNAKIKTGYKREHINL
GCDVDFDIAGPSIRGALVLGYEGWLAGYQMNFETSKSRVTQSNFAVGYKTDEFQLH
TNVNDGTEFGGSIYQKVNKKLETAVNLAWTAGNSNTRFGIAAKYQVDPDACFSAKV
NNSSLIGLGYTQTLKPGIKLTLSALLDGKNVNAGGHKLGLGLEFQA

Δ 1-21-mVDAC-Y22C

nucleotide sequence:

ATGTGCGGCTTTGGCTTAATAAAACTTGATTTGAAAACGAAGTCAGAGAATGGATTGGAATTTACCAGCTCAGGC
TCTGCCAACACGGAAACCACCAAAGTGAACGGCAGCCTGGAAACCAAGTACAGATGGACTGAGTATGGGCTGACG
TTTACAGAGAAGTGGAACACAGACAACACCCTGGGCACTGAGATCACTGTGGAAGACCAGCTTGCTCGTGGACTG
AAGCTCACCTTTGATTCGTCATTCTCGCCGAACACTGGGAAAAAAAATGCTAAAATCAAGACAGGGTACAAGAGG
GAGCACATCAACCTCGGCTGTGACGTGGACTTTGACATCGCTGGGCCCTCGATCCGGGGCGCTCTGGTGCTTGGC
TATGAGGGTTGGCTGGCTGGCTACCAGATGAATTTTGAGACCTCGAAGTCCCGAGTGACCCAGAGCAACTTCGCA
GTTGGCTATAAGACGGATGAATTCCAGCTTCATACTAATGTGAATGACGGGACAGAGTTTGGTGGCTCCATTTAC
CAGAAGGTGAACAAGAAGTTGGAGACTGCTGTCAATCTCGCCTGGACTGCAGGAAACAGTAACACTCGCTTCGGA
ATAGCAGCCAAGTATCAGGTCGACCCTGATGCCTGCTTTTCGGCCAAAGTGAACAACTCTAGCCTGATTGGCTTA
GGGTACACTCAGACCCTAAAACCAGGTATCAAACTGACGTTGTCAGCCCTGCTCGATGGCAAGAACGTCAATGCG
GGTGGCCACAAGCTTGGCCTAGGACTGGAATTTCAAGCATAA

amino acid sequence:

MCGFGLIKLDLKTKSENGLEFTSSGSANTETTKVNGSLETKYRWTEYGLTFTEKWNT
DNTLGTEITVEDQLARGLKLTFDSSFSPNTGKKNAKIKTGYKREHINLGCDVDFDIAG
PSIRGALVLGYEGWLAGYQMNFETSKSRVTQSNFAVGYKTDEFQLHTNVNDGTEFG
GSIYQKVNKKLETAVNLAWTAGNSNTRFGIAAKYQVDPDACFSAKVNNSSLIGLGYT
QTLKPGIKLTLSALLDGKNVNAGGHKLGLGLEFQA

Δ1- 25-mVDAC1-L26C

nucleotide sequence

ATGTGTATAAAACTTGATTTGAAAACGAAGTCAGAGAATGGATTGGAATTTACCAGCTCAGGCTCTGCCAACACG
GAAACCACCAAAGTGAACGGCAGCCTGGAAACCAAGTACAGATGGACTGAGTATGGGCTGACGTTTACAGAGAAG
TGGAACACAGACAACACCCTGGGCACTGAGATCACTGTGGAAGACCAGCTTGCTCGTGGACTGAAGCTCACCTTT
GATTCGTCATTCTCGCCGAACACTGGGAAAAAAAATGCTAAAATCAAGACAGGGTACAAGAGGGAGCACATCAAC
CTCGGCTGTGACGTGGACTTTGACATCGCTGGGCCCTCGATCCGGGGCGCTCTGGTGCTTGGCTATGAGGGTTGG
CTGGCTGGCTACCAGATGAATTTTGAGACCTCGAAGTCCCGAGTGACCCAGAGCAACTTCGCAGTTGGCTATAAG
ACGGATGAATTCCAGCTTCATACTAATGTGAATGACGGGACAGAGTTTGGTGGCTCCATTTACCAGAAGGTGAAC
AAGAAGTTGGAGACTGCTGTCAATCTCGCCTGGACTGCAGGAAACAGTAACACTCGCTTCGGAATAGCAGCCAAG
TATCAGGTCGACCCTGATGCCTGCTTTTCGGCCAAAGTGAACAACTCTAGCCTGATTGGCTTAGGGTACACTCAG
ACCCTAAAACCAGGTATCAAACTGACGTTGTCAGCCCTGCTCGATGGCAAGAACGTCAATGCGGGTGGCCACAAG
CTTGGCCTAGGACTGGAATTTCAAGCATAA

amino acid sequence:

MCIKLDLKTKSENGLEFTSSGSANTETTKVNGSLETKYRWTEYGLTFTEKWNTDNTL
GTEITVEDQLARGLKLTFDSSFSPNTGKKNAKIKTGYKREHINLGCDVDFDIAGPSIRG
ALVLGYEGWLAGYQMNFETSKSRVTQSNFAVGYKTDEFQLHTNVNDGTEFGGSIYQ
KVNKKLETAVNLAWTAGNSNTRFGIAAKYQVDPDACFSAKVNNSSLIGLGYTQTLK
PGIKLTLSALLDGKNVNAGGHKLGLGLEFQA

mVDAC1-A2C-E121C-C127A-C232A

nucleotide sequence

ATGTGCGTGCCTCCCACATACGCCGATCTTGGCAAGTCCGCCAGGGATGTCTTCACCAAGGGCTACGGCTTTGGC
TTAATAAAACTTGATTTGAAAACGAAGTCAGAGAATGGATTGGAATTTACCAGCTCAGGCTCTGCCAACACGGAA
ACCACCAAAGTGAACGGCAGCCTGGAAACCAAGTACAGATGGACTGAGTATGGGCTGACGTTTACAGAGAAGTGG
AACACAGACAACACCCTGGGCACTGAGATCACTGTGGAAGACCAGCTTGCTCGTGGACTGAAGCTCACCTTTGAT
TCGTCATTCTCGCCGAACACTGGGAAAAAAAATGCTAAAATCAAGACAGGGTACAAGAGGTGCCACATCAACCTC
GGGGCTGACGTGGACTTTGACATCGCTGGGCCCTCGATCCGGGGCGCTCTGGTGCTTGGCTATGAGGGTTGGCTG
GCTGGCTACCAGATGAATTTTGAGACCTCGAAGTCCCGAGTGACCCAGAGCAACTTCGCAGTTGGCTATAAGACG
GATGAATTCCAGCTTCATACTAATGTGAATGACGGGACAGAGTTTGGTGGCTCCATTTACCAGAAGGTGAACAAG
AAGTTGGAGACTGCTGTCAATCTCGCCTGGACTGCAGGAAACAGTAACACTCGCTTCGGAATAGCAGCCAAGTAT
CAGGTGGATCCTGATGCCGCCTTTTCGGCCAAAGTGAACAACTCTAGCCTGATTGGCTTAGGGTACACTCAGACC

CTAAAACCAGGTATCAAACTGACGTTGTCAGCCCTGCTCGATGGCAAGAACGTCAATGCGGGTGGCCACAAGCTT
GGCCTAGGACTGGAATTTCAAGCATAA

amino acid sequence:

MCVPPTYADLGKSARDVFTKGYGFGLIKLDLKTKSENGLEFTSSGSANTETTKVNGS
LETKYRWTEYGLTFTEKWNTDNTLGTEITVEDQLARGLKLTFDSSFSPNTGKKNAKI
KTGYKRCHINLGADVDFDIAGPSIRGALVLGYEGWLAGYQMNFETSKSRVTQSNFA
VGYKTDEFQLHTNVNDGTEFGGSIYQKVNKKLETAVNLAWTAGNSNTRFGIAAKYQ
VDPDAAFSAKVNNSSLIGLGYTQTLKPGIKLTLSALLDGKNVNAGGHKLGLGLEFQA

mVDAC1-V3C-K119C-C127A-C232A

nucleotide sequence

ATGGCCTGCCCTCCCACATACGCCGATCTTGGCAAGTCCGCCAGGGATGTCTTCACCAAGGGCTACGGCTTTGGC
TTAATAAAACTTGATTTGAAAACGAAGTCAGAGAATGGATTGGAATTTACCAGCTCAGGCTCTGCCAACACGGAA
ACCACCAAAGTGAACGGCAGCCTGGAAACCAAGTACAGATGGACTGAGTATGGGCTGACGTTTACAGAGAAGTGG
AACACAGACAACACCCTGGGCACTGAGATCACTGTGGAAGACCAGCTTGCTCGTGGACTGAAGCTCACCTTTGAT
TCGTCATTCTCGCCGAACACTGGGAAAAAAAAATGCTAAAATCAAGACAGGGTACAAGAGGGAGCACATCAACCTC
GGCTGTGACGTGGACTTTGACATCGCTGGGCCCTCGATCCGGGGCGCTCTGGTGCTTGGCTATGAGGGTTGGCTG
GCTGGCTACCAGATGAATTTTGAGACCTCGAAGTCCCGAGTGACCCAGAGCAACTTCGCAGTTGGCTATAAGACG
GATGAATTCCAGCTTCATACTAATGTGAATGACGGGACAGAGTTTGGTGGCTCCATTTACCAGAAGGTGAACAAG
AAGTTGGAGACTGCTGTCAATCTCGCCTGGACTGCAGGAAACAGTAACACTCGCTTCGGAATAGCAGCCAAGTAT
CAGGTCGACCCTGATGCCTGCTTTTCGGCCAAAGTGAACAACTCTAGCCTGATTGGCTTAGGGTACACTCAGACC
CTAAAACCAGGTATCAAACTGACGTTGTCAGCCCTGCTCGATGGCAAGAACGTCAATGCGGGTGGCCACAAGCTT
GGCCTAGGACTGGAATTTCAAGCATAA

amino acid sequence:

MACPPTYADLGKSARDVFTKGYGFGLIKLDLKTKSENGLEFTSSGSANTETTKVNGS
LETKYRWTEYGLTFTEKWNTDNTLGTEITVEDQLARGLKLTFDSSFSPNTGKKNAKI
KTGYCREHINLGCDVDFDIAGPSIRGALVLGYEGWLAGYQMNFETSKSRVTQSNFAV
GYKTDEFQLHTNVNDGTEFGGSIYQKVNKKLETAVNLAWTAGNSNTRFGIAAKYQV
DPDACFSAKVNNSSLIGLGYTQTLKPGIKLTLSALLDGKNVNAGGHKLGLGLEFQA.

mVDAC1-K12C-C127A-C232A

nucleotide sequence

ATGGCCGTGCCTCCCACATACGCCGATCTTGGCTGCTCCGCCAGGGATGTCTTCACCAAGGGCTACGGCTTTGGC
TTAATAAAACTTGATTTGAAAACGAAGTCAGAGAATGGATTGGAATTTACCAGCTCAGGCTCTGCCAACACGGAA
ACCACCAAAGTGAACGGCAGCCTGGAAACCAAGTACAGATGGACTGAGTATGGGCTGACGTTTACAGAGAAGTGG
AACACAGACAACACCCTGGGCACTGAGATCACTGTGGAAGACCAGCTTGCTCGTGGACTGAAGCTCACCTTTGAT
TCGTCATTCTCGCCGAACACTGGGAAAAAAAAATGCTAAAATCAAGACAGGGTACAAGAGGGAGCACATCAACCTC
GGGGCTGACGTGGACTTTGACATCGCTGGGCCCTCGATCCGGGGCGCTCTGGTGCTTGGCTATGAGGGTTGGCTG
GCTGGCTACCAGATGAATTTTGAGACCTCGAAGTCCCGAGTGACCCAGAGCAACTTCGCAGTTGGCTATAAGACG
GATGAATTCCAGCTTCATACTAATGTGAATGACGGGACAGAGTTTGGTGGCTCCATTTACCAGAAGGTGAACAAG
AAGTTGGAGACTGCTGTCAATCTCGCCTGGACTGCAGGAAACAGTAACACTCGCTTCGGAATAGCAGCCAAGTAT
CAGGTGGATCCTGATGCCGCCTTTTCGGCCAAAGTGAACAACTCTAGCCTGATTGGCTTAGGGTACACTCAGACC
CTAAAACCAGGTATCAAACTGACGTTGTCAGCCCTGCTCGATGGCAAGAACGTCAATGCGGGTGGCCACAAGCTT
GGCCTAGGACTGGAATTTCAAGCATAA

amino acid sequence:

MAVPPTYADLGCSARDVFTKGYGFGLIKLDLKTKSENGLEFTSSGSANTETTKVNGS
LETKYRWTEYGLTFTEKWNTDNTLGTEITVEDQLARGLKLTFDSSFSPNTGKKNAKI
KTGYKREHINLGADVDFDIAGPSIRGALVLGYEGWLAGYQMNFETSKSRVTQSNFAV
GYKTDEFQLHTNVNDGTEFGGSIYQKVNKKLETAVNLAWTAGNSNTRFGIAAKYQV
DPDAAFSAKVNNSSLIGLGYTQTLKPGIKLTLSALLDGKNVNAGGHKLGLGLEFQA.

mVDAC1-K12C-D30C-C127A-C232A

nucleotide sequence

ATGGCCGTGCCTCCCACATACGCCGATCTTGGCTGCTCCGCCAGGGATGTCTTCACCAAGGGCTACGGCTTTGGC
TTAATAAAACTTTGTTTGAAAACGAAGTCAGAGAATGGATTGGAATTTACCAGCTCAGGCTCTGCCAACACGGAA
ACCACCAAAGTGAACGGCAGCCTGGAAACCAAGTACAGATGGACTGAGTATGGGCTGACGTTTACAGAGAAGTGG
AACACAGACAACACCCTGGGCACTGAGATCACTGTGGAAGACCAGCTTGCTCGTGGACTGAAGCTCACCTTTGAT
TCGTCATTCTCGCCGAACACTGGGAAAAAAAAATGCTAAAATCAAGACAGGGTACAAGAGGGAGCACATCAACCTC
GGGGCTGACGTGGACTTTGACATCGCTGGGCCCTCGATCCGGGGCGCTCTGGTGCTTGGCTATGAGGGTTGGCTG
GCTGGCTACCAGATGAATTTTGAGACCTCGAAGTCCCGAGTGACCCAGAGCAACTTCGCAGTTGGCTATAAGACG
GATGAATTCCAGCTTCATACTAATGTGAATGACGGGACAGAGTTTGGTGGCTCCATTTACCAGAAGGTGAACAAG
AAGTTGGAGACTGCTGTCAATCTCGCCTGGACTGCAGGAAACAGTAACACTCGCTTCGGAATAGCAGCCAAGTAT
CAGGTGGATCCTGATGCCGCCTTTTCGGCCAAAGTGAACAACTCTAGCCTGATTGGCTTAGGGTACACTCAGACC
CTAAAACCAGGTATCAAACTGACGTTGTCAGCCCTGCTCGATGGCAAGAACGTCAATGCGGGTGGCCACAAGCTT
GGCCTAGGACTGGAATTTCAAGCATAA

amino acid sequence:

MAVPPTYADLGCSARDVFTKGYGFGLIKLCLKTKSENGLEFTSSGSANTETTKVNGS
LETKYRWTEYGLTFTEKWNTDNTLGTEITVEDQLARGLKLTFDSSFSPNTGKKNAKI
KTGYKREHINLGADVDFDIAGPSIRGALVLGYEGWLAGYQMNFETSKSRVTQSNFAV
GYKTDEFQLHTNVNDGTEFGGSIYQKVNKKLETAVNLAWTAGNSNTRFGIAAKYQV
DPDAAFSAKVNNSSLIGLGYTQTLKPGIKLTLSALLDGKNVNAGGHKLGLGLEFQA.

mVDAC1-K12C-K32C-C127A-C232A

nucleotide sequence

ATGGCCGTGCCTCCCACATACGCCGATCTTGGCTGCTCCGCCAGGGATGTCTTCACCAAGGGCTACGGCTTTGGC
TTAATAAAACTTGATTTGTGCACGAAGTCAGAGAATGGATTGGAATTTACCAGCTCAGGCTCTGCCAACACGGAA
ACCACCAAAGTGAACGGCAGCCTGGAAACCAAGTACAGATGGACTGAGTATGGGCTGACGTTTACAGAGAAGTGG
AACACAGACAACACCCTGGGCACTGAGATCACTGTGGAAGACCAGCTTGCTCGTGGACTGAAGCTCACCTTTGAT
TCGTCATTCTCGCCGAACACTGGGAAAAAAAATGCTAAAATCAAGACAGGGTACAAGAGGGAGCACATCAACCTC
GGGGCTGACGTGGACTTTGACATCGCTGGGCCCTCGATCCGGGGCGCTCTGGTGCTTGGCTATGAGGGTTGGCTG
GCTGGCTACCAGATGAATTTTGAGACCTCGAAGTCCCGAGTGACCCAGAGCAACTTCGCAGTTGGCTATAAGACG
GATGAATTCCAGCTTCATACTAATGTGAATGACGGGACAGAGTTTGGTGGCTCCATTTACCAGAAGGTGAACAAG
AAGTTGGAGACTGCTGTCAATCTCGCCTGGACTGCAGGAAACAGTAACACTCGCTTCGGAATAGCAGCCAAGTAT
CAGGTGGATCCTGATGCCGCCTTTTCGGCCAAAGTGAACAACTCTAGCCTGATTGGCTTAGGGTACACTCAGACC
CTAAAACCAGGTATCAAACTGACGTTGTCAGCCCTGCTCGATGGCAAGAACGTCAATGCGGGTGGCCACAAGCTT
GGCCTAGGACTGGAATTTCAAGCATAA

amino acid sequence:

MAVPPTYADLGCSARDVFTKGYGFGLIKLDLCTKSENGLEFTSSGSANTETTKVNGS
LETKYRWTEYGLTFTEKWNTDNTLGTEITVEDQLARGLKLTFDSSFSPNTGKKNAKI
KTGYKREHINLGADVDFDIAGPSIRGALVLGYEGWLAGYQMNFETSKSRVTQSNFAV
GYKTDEFQLHTNVNDGTEFGGSIYQKVNKKLETAVNLAWTAGNSNTRFGIAAKYQV
DPDAAFSAKVNNSSLIGLGYTQTLKPGIKLTLSALLDGKNVNAGGHKLGLGLEFQA.

mVDAC1-K12C-S57C-C127A-C232A

nucleotide sequence

ATGGCCGTGCCTCCCACATACGCCGATCTTGGCTGCTCCGCCAGGGATGTCTTCACCAAGGGCTACGGCTTTGGC
TTAATAAAACTTGATTTGAAAACGAAGTCAGAGAATGGATTGGAATTTACCAGCTCAGGCTCTGCCAACACGGAA
ACCACCAAAGTGAACGGCTGCCTGGAAACCAAGTACAGATGGACTGAGTATGGGCTGACGTTTACAGAGAAGTGG
AACACAGACAACACCCTGGGCACTGAGATCACTGTGGAAGACCAGCTTGCTCGTGGACTGAAGCTCACCTTTGAT
TCGTCATTCTCGCCGAACACTGGGAAAAAAAAATGCTAAAATCAAGACAGGGTACAAGAGGGAGCACATCAACCTC
GGGGCTGACGTGGACTTTGACATCGCTGGGCCCTCGATCCGGGGCGCTCTGGTGCTTGGCTATGAGGGTTGGCTG
GCTGGCTACCAGATGAATTTTGAGACCTCGAAGTCCCGAGTGACCCAGAGCAACTTCGCAGTTGGCTATAAGACG
GATGAATTCCAGCTTCATACTAATGTGAATGACGGGACAGAGTTTGGTGGCTCCATTTACCAGAAGGTGAACAAG
AAGTTGGAGACTGCTGTCAATCTCGCCTGGACTGCAGGAAACAGTAACACTCGCTTCGGAATAGCAGCCAAGTAT
CAGGTGGATCCTGATGCCGCCTTTTCGGCCAAAGTGAACAACTCTAGCCTGATTGGCTTAGGGTACACTCAGACC
CTAAAACCAGGTATCAAACTGACGTTGTCAGCCCTGCTCGATGGCAAGAACGTCAATGCGGGTGGCCACAAGCTT
GGCCTAGGACTGGAATTTCAAGCATAA

amino acid sequence:

MAVPPTYADLGCSARDVFTKGYGFGLIKLDLKTKSENGLEFTSSGSANTETTKVNGC
LETKYRWTEYGLTFTEKWNTDNTLGTEITVEDQLARGLKLTFDSSFSPNTGKKNAKI
KTGYKREHINLGADVDFDIAGPSIRGALVLGYEGWLAGYQMNFETSKSRVTQSNFAV
GYKTDEFQLHTNVNDGTEFGGSIYQKVNKKLETAVNLAWTAGNSNTRFGIAAKYQV
DPDAAFSAKVNNSSLIGLGYTQTLKPGIKLTLSALLDGKNVNAGGHKLGLGLEFQA.

mVDAC1- K12C -E59C-C127A-C232A

nucleotide sequence

ATGGCCGTGCCTCCCACATACGCCGATCTTGGCTGCTCCGCCAGGGATGTCTTCACCAAGGGCTACGGCTTTGGC
TTAATAAAACTTGATTTGAAAACGAAGTCAGAGAATGGATTGGAATTTACCAGCTCAGGCTCTGCCAACACGGAA
ACCACCAAAGTGAACGGAAGCTTGTGCACCAAGTACAGATGGACTGAGTATGGGCTGACGTTTACAGAGAAGTGG
AACACAGACAACACCCTGGGCACTGAGATCACTGTGGAAGACCAGCTTGCTCGTGGACTGAAGCTCACCTTTGAT
TCGTCATTCTCGCCGAACACTGGGAAAAAAAAATGCTAAAATCAAGACAGGGTACAAGAGGGAGCACATCAACCTC
GGGGCTGACGTGGACTTTGACATCGCTGGGCCCTCGATCCGGGGCGCTCTGGTGCTTGGCTATGAGGGTTGGCTG
GCTGGCTACCAGATGAATTTTGAGACCTCGAAGTCCCGAGTGACCCAGAGCAACTTCGCAGTTGGCTATAAGACG
GATGAATTCCAGCTTCATACTAATGTGAATGACGGGACAGAGTTTGGTGGCTCCATTTACCAGAAGGTGAACAAG
AAGTTGGAGACTGCTGTCAATCTCGCCTGGACTGCAGGAAACAGTAACACTCGCTTCGGAATAGCAGCCAAGTAT
CAGGTGGATCCTGATGCCGCCTTTTCGGCCAAAGTGAACAACTCTAGCCTGATTGGCTTAGGGTACACTCAGACC
CTAAAACCAGGTATCAAACTGACGTTGTCAGCCCTGCTCGATGGCAAGAACGTCAATGCGGGTGGCCACAAGCTT
GGCCTAGGACTGGAATTTCAAGCATAA

amino acid sequence:

MAVPPTYADLGCSARDVFTKGYGFGLIKLDLKTKSENGLEFTSSGSANTETTKVNGS
LCTKYRWTEYGLTFTEKWNTDNTLGTEITVEDQLARGLKLTFDSSFSPNTGKKNAKI
KTGYKREHINLGADVDFDIAGPSIRGALVLGYEGWLAGYQMNFETSKSRVTQSNFAV
GYKTDEFQLHTNVNDGTEFGGSIYQKVNKKLETAVNLAWTAGNSNTRFGIAAKYQV
DPDAAFSAKVNNSSLIGLGYTQTLKPGIKLTLSALLDGKNVNAGGHKLGLGLEFQA.

mVDAC1- A14C -C127A- S193C-C232A

nucleotide sequence

ATGGCCGTGCCTCCCACATACGCCGATCTTGGCAAGTCCTGCAGGGATGTCTTCACCAAGGGCTACGGCTTTGGC
TTAATAAAACTTGATTTGAAAACGAAGTCAGAGAATGGATTGGAATTTACCAGCTCAGGCTCTGCCAACACGGAA
ACCACCAAAGTGAACGGCAGCCTGGAAACCAAGTACAGATGGACTGAGTATGGGCTGACGTTTACAGAGAAGTGG
AACACAGACAACACCCTGGGCACTGAGATCACTGTGGAAGACCAGCTTGCTCGTGGACTGAAGCTCACCTTTGAT
TCGTCATTCTCGCCGAACACTGGGAAAAAAAATGCTAAAATCAAGACAGGGTACAAGAGGGAGCACATCAACCTC
GGGGCTGACGTGGACTTTGACATCGCTGGGCCCTCGATCCGGGGCGCTCTGGTGCTTGGCTATGAGGGTTGGCTG
GCTGGCTACCAGATGAATTTTGAGACCTCGAAGTCCCGAGTGACCCAGAGCAACTTCGCAGTTGGCTATAAGACG
GATGAATTCCAGCTTCATACTAATGTGAATGACGGGACAGAGTTTGGTGGCTGCATTTACCAGAAGGTGAACAAG
AAGTTGGAGACTGCTGTCAATCTCGCCTGGACTGCAGGAAACAGTAACACTCGCTTCGGAATAGCAGCCAAGTAT
CAGGTGGATCCTGATGCCGCCTTTTCGGCCAAAGTGAACAACTCTAGCCTGATTGGCTTAGGGTACACTCAGACC
CTAAAACCAGGTATCAAACTGACGTTGTCAGCCCTGCTCGATGGCAAGAACGTCAATGCGGGTGGCCACAAGCTT
GGCCTAGGACTGGAATTTCAAGCATAA

amino acid sequence:

MAVPPTYADLGKSCRDVFTKGYGFGLIKLDLKTKSENGLEFTSSGSANTETTKVNGS
LETKYRWTEYGLTFTEKWNTDNTLGTEITVEDQLARGLKLTFDSSFSPNTGKKNAKI
KTGYKREHINLGADVDFDIAGPSIRGALVLGYEGWLAGYQMNFETSKSRVTQSNFAV
GYKTDEFQLHTNVNDGTEFGGCIYQKVNKKLETAVNLAWTAGNSNTRFGIAAKYQV
DPDAAFSAKVNNSSLIGLGYTQTLKPGIKLTLSALLDGKNVNAGGHKLGLGLEFQA.

mVDAC1-K28C -C127A-Q154C -C232A

nucleotide sequence

ATGGCCGTGCCTCCCACATACGCCGATCTTGGCAAGTCCGCCAGGGATGTCTTCACCAAGGGCTACGGCTTTGGC
TTAATATGTCTTGATTTAAAAACGAAGTCAGAGAATGGATTGGAATTTACCAGCTCAGGCTCTGCCAACACGGAA
ACCACCAAAGTGAACGGCAGCCTGGAAACCAAGTACAGATGGACTGAGTATGGGCTGACGTTTACAGAGAAGTGG
AACACAGACAACACCCTGGGCACTGAGATCACTGTGGAAGACCAGCTTGCTCGTGGACTGAAGCTCACCTTTGAT
TCGTCATTCTCGCCGAACACTGGGAAAAAAAAATGCTAAAATCAAGACAGGGTACAAGAGGGAGCACATCAACCTC
GGGGCTGACGTGGACTTTGACATCGCTGGGCCCTCGATCCGGGGCGCTCTGGTGCTTGGCTATGAGGGTTGGCTA
GCTGGCTACTGTATGAATTTTGAGACCTCGAAGTCCCGAGTGACCCAGAGCAACTTCGCAGTTGGCTATAAGACG
GATGAATTCCAGCTTCATACTAATGTGAATGACGGGACAGAGTTTGGTGGCTCCATTTACCAGAAGGTGAACAAG
AAGTTGGAGACTGCTGTCAATCTCGCCTGGACTGCAGGAAACAGTAACACTCGCTTCGGAATAGCAGCCAAGTAT
CAGGTGGATCCTGATGCCGCCTTTTCGGCCAAAGTGAACAACTCTAGCCTGATTGGCTTAGGGTACACTCAGACC
CTAAAACCAGGTATCAAACTGACGTTGTCAGCCCTGCTCGATGGCAAGAACGTCAATGCGGGTGGCCACAAGCTT
GGCCTAGGACTGGAATTTCAAGCATAA

amino acid sequence:

MAVPPTYADLGKSARDVFTKGYGFGLICLDLKTKSENGLEFTSSGSANTETTKVNGS
LETKYRWTEYGLTFTEKWNTDNTLGTEITVEDQLARGLKLTFDSSFSPNTGKKNAKI
KTGYKREHINLGADVDFDIAGPSIRGALVLGYEGWLAGYCMNFETSKSRVTQSNFAV
GYKTDEFQLHTNVNDGTEFGGSIYQKVNKKLETAVNLAWTAGNSNTRFGIAAKYQV
DPDAAFSAKVNNSSLIGLGYTQTLKPGIKLTLSALLDGKNVNAGGHKLGLGLEFQA.

mVDAC1-K32C- C127A-C232A

nucleotide sequence

ATGGCCGTGCCTCCCACATACGCCGATCTTGGCTGCTCCGCCAGGGATGTCTTCACCAAGGGCTACGGCTTTGGC
TTAATAAAACTTGATTTGTGCACGAAGTCAGAGAATGGATTGGAATTTACCAGCTCAGGCTCTGCCAACACGGAA
ACCACCAAAGTGAACGGCAGCCTGGAAACCAAGTACAGATGGACTGAGTATGGGCTGACGTTTACAGAGAAGTGG
AACACAGACAACACCCTGGGCACTGAGATCACTGTGGAAGACCAGCTTGCTCGTGGACTGAAGCTCACCTTTGAT
TCGTCATTCTCGCCGAACACTGGGAAAAAAAAATGCTAAAATCAAGACAGGGTACAAGAGGGAGCACATCAACCTC
GGGGCTGACGTGGACTTTGACATCGCTGGGCCCTCGATCCGGGGCGCTCTGGTGCTTGGCTATGAGGGTTGGCTG
GCTGGCTACCAGATGAATTTTGAGACCTCGAAGTCCCGAGTGACCCAGAGCAACTTCGCAGTTGGCTATAAGACG
GATGAATTCCAGCTTCATACTAATGTGAATGACGGGACAGAGTTTGGTGGCTCCATTTACCAGAAGGTGAACAAG
AAGTTGGAGACTGCTGTCAATCTCGCCTGGACTGCAGGAAACAGTAACACTCGCTTCGGAATAGCAGCCAAGTAT
CAGGTGGATCCTGATGCCGCCTTTTCGGCCAAAGTGAACAACTCTAGCCTGATTGGCTTAGGGTACACTCAGACC
CTAAAACCAGGTATCAAACTGACGTTGTCAGCCCTGCTCGATGGCAAGAACGTCAATGCGGGTGGCCACAAGCTT
GGCCTAGGACTGGAATTTCAAGCATAA

amino acid sequence:

MAVPPTYADLGKSARDVFTKGYGFGLIKLDLCTKSENGLEFTSSGSANTETTKVNGS
LETKYRWTEYGLTFTEKWNTDNTLGTEITVEDQLARGLKLTFDSSFSPNTGKKNAKI
KTGYKREHINLGADVDFDIAGPSIRGALVLGYEGWLAGYQMNFETSKSRVTQSNFAV
GYKTDEFQLHTNVNDGTEFGGSIYQKVNKKLETAVNLAWTAGNSNTRFGIAAKYQV
DPDAAFSAKVNNSSLIGLGYTQTLKPGIKLTLSALLDGKNVNAGGHKLGLGLEFQA.

mVDAC1-E36C -C127A-D176C -C232A

nucleotide sequence

ATGGCCGTGCCTCCCACATACGCCGATCTTGGCAAGTCCGCCAGGGATGTCTTCACCAAGGGCTACGGCTTTGGC
TTAATAAAACTTGATTTGAAAACGAAGTCATGTAATGGATTGGAATTCACCAGCTCAGGCTCTGCCAACACGGAA
ACCACCAAAGTGAACGGCAGCCTGGAAACCAAGTACAGATGGACTGAGTATGGGCTGACGTTTACAGAGAAGTGG
AACACAGACAACACCCTGGGCACTGAGATCACTGTGGAAGACCAGCTTGCTCGTGGACTGAAGCTCACCTTTGAT
TCGTCATTCTCGCCGAACACTGGGAAAAAAAATGCTAAAATCAAGACAGGGTACAAGAGGGAGCACATCAACCTC
GGGGCTGACGTGGACTTTGACATCGCTGGGCCCTCGATCCGGGGCGCTCTGGTGCTTGGCTATGAGGGTTGGCTG
GCTGGCTACCAGATGAATTTTGAGACCTCGAAGTCCCGAGTGACCCAGAGCAACTTCGCAGTTGGCTATAAGACA
TGTGAATTCCAGCTTCATACTAATGTGAATGACGGGACAGAGTTTGGTGGCTCCATTTACCAGAAGGTGAACAAG
AAGTTGGAGACTGCTGTCAATCTCGCCTGGACTGCAGGAAACAGTAACACTCGCTTCGGAATAGCAGCCAAGTAT
CAGGTGGATCCTGATGCCGCCTTTTCGGCCAAAGTGAACAACTCTAGCCTGATTGGCTTAGGGTACACTCAGACC
CTAAAACCAGGTATCAAACTGACGTTGTCAGCCCTGCTCGATGGCAAGAACGTCAATGCGGGTGGCCACAAGCTT
GGCCTAGGACTGGAATTTCAAGCATAA

amino acid sequence:

MAVPPTYADLGKSARDVFTKGYGFGLIKLDLKTKSCNGLEFTSSGSANTETTKVNGS
LETKYRWTEYGLTFTEKWNTDNTLGTEITVEDQLARGLKLTFDSSFSPNTGKKNAKI
KTGYKREHINLGADVDFDIAGPSIRGALVLGYEGWLAGYQMNFETSKSRVTQSNFAV
GYKTCEFQLHTNVNDGTEFGGSIYQKVNKKLETAVNLAWTAGNSNTRFGIAAKYQV
DPDAAFSAKVNNSSLIGLGYTQTLKPGIKLTLSALLDGKNVNAGGHKLGLGLEFQA.

mVDAC1-E59C- C127A-C232A

nucleotide sequence

ATGGCCGTGCCTCCCACATACGCCGATCTTGGCAAGTCCGCCAGGGATGTCTTCACCAAGGGCTACGGCTTTGGC
TTAATAAAACTTGATTTGAAAACGAAGTCAGAGAATGGATTGGAATTTACCAGCTCAGGCTCTGCCAACACGGAA
ACCACCAAAGTGAACGGAAGCTTGTGCACCAAGTACAGATGGACTGAGTATGGGCTGACGTTTACAGAGAAGTGG
AACACAGACAACACCCTGGGCACTGAGATCACTGTGGAAGACCAGCTTGCTCGTGGACTGAAGCTCACCTTTGAT
TCGTCATTCTCGCCGAACACTGGGAAAAAAAAATGCTAAAATCAAGACAGGGTACAAGAGGGAGCACATCAACCTC
GGGGCTGACGTGGACTTTGACATCGCTGGGCCCTCGATCCGGGGCGCTCTGGTGCTTGGCTATGAGGGTTGGCTG
GCTGGCTACCAGATGAATTTTGAGACCTCGAAGTCCCGAGTGACCCAGAGCAACTTCGCAGTTGGCTATAAGACG
GATGAATTCCAGCTTCATACTAATGTGAATGACGGGACAGAGTTTGGTGGCTCCATTTACCAGAAGGTGAACAAG
AAGTTGGAGACTGCTGTCAATCTCGCCTGGACTGCAGGAAACAGTAACACTCGCTTCGGAATAGCAGCCAAGTAT
CAGGTGGATCCTGATGCCGCCTTTTCGGCCAAAGTGAACAACTCTAGCCTGATTGGCTTAGGGTACACTCAGACC
CTAAAACCAGGTATCAAACTGACGTTGTCAGCCCTGCTCGATGGCAAGAACGTCAATGCGGGTGGCCACAAGCTT
GGCCTAGGACTGGAATTTCAAGCATAA

amino acid sequence:

MAVPPTYADLGKSARDVFTKGYGFGLIKLDLKTKSENGLEFTSSGSANTETTKVNGS
LCTKYRWTEYGLTFTEKWNTDNTLGTEITVEDQLARGLKLTFDSSFSPNTGKKNAKI
KTGYKREHINLGADVDFDIAGPSIRGALVLGYEGWLAGYQMNFETSKSRVTQSNFAV
GYKTDEFQLHTNVNDGTEFGGSIYQKVNKKLETAVNLAWTAGNSNTRFGIAAKYQV
DPDAAFSAKVNNSSLIGLGYTQTLKPGIKLTLSALLDGKNVNAGGHKLGLGLEFQA.

mVDAC1-E59C -C127A-S193C -C232A

nucleotide sequence

ATGGCCGTGCCTCCCACATACGCCGATCTTGGCAAGTCCGCCAGGGATGTCTTCACCAAGGGCTACGGCTTTGGC
TTAATAAAACTTGATTTGAAAACGAAGTCAGAGAATGGATTGGAATTTACCAGCTCAGGCTCTGCCAACACGGAA
ACCACCAAAGTGAACGGAAGCTTGTGCACCAAGTACAGATGGACTGAGTATGGGCTGACGTTTACAGAGAAGTGG
AACACAGACAACACCCTGGGCACTGAGATCACTGTGGAAGACCAGCTTGCTCGTGGACTGAAGCTCACCTTTGAT
TCGTCATTCTCGCCGAACACTGGGAAAAAAAAATGCTAAAATCAAGACAGGGTACAAGAGGGAGCACATCAACCTC
GGGGCTGACGTGGACTTTGACATCGCTGGGCCCTCGATCCGGGGCGCTCTGGTGCTTGGCTATGAGGGTTGGCTG
GCTGGCTACCAGATGAATTTTGAGACCTCGAAGTCCCGAGTGACCCAGAGCAACTTCGCAGTTGGCTATAAGACG
GATGAATTCCAGCTTCATACTAATGTGAATGACGGGACAGAGTTTGGTGGCTGCATTTACCAGAAGGTGAACAAG
AAGTTGGAGACTGCTGTCAATCTCGCCTGGACTGCAGGAAACAGTAACACTCGCTTCGGAATAGCAGCCAAGTAT
CAGGTGGATCCTGATGCCGCCTTTTCGGCCAAAGTGAACAACTCTAGCCTGATTGGCTTAGGGTACACTCAGACC
CTAAAACCAGGTATCAAACTGACGTTGTCAGCCCTGCTCGATGGCAAGAACGTCAATGCGGGTGGCCACAAGCTT
GGCCTAGGACTGGAATTTCAAGCATAA

amino acid sequence:

MAVPPTYADLGKSARDVFTKGYGFGLIKLDLKTKSENGLEFTSSGSANTETTKVNGS
LCTKYRWTEYGLTFTEKWNTDNTLGTEITVEDQLARGLKLTFDSSFSPNTGKKNAKI
KTGYKREHINLGADVDFDIAGPSIRGALVLGYEGWLAGYQMNFETSKSRVTQSNFAV
GYKTDEFQLHTNVNDGTEFGGCIYQKVNKKLETAVNLAWTAGNSNTRFGIAAKYQV
DPDAAFSAKVNNSSLIGLGYTQTLKPGIKLTLSALLDGKNVNAGGHKLGLGLEFQA.

mVDAC1-D78C -C127A-N214C -C232A

nucleotide sequence

ATGGCCGTGCCTCCCACATACGCCGATCTTGGCAAGTCCGCCAGGGATGTCTTCACCAAGGGCTACGGCTTTGGC
TTAATAAAACTTGATTTGAAAACGAAGTCAGAGAATGGATTGGAATTTACCAGCTCAGGCTCTGCCAACACGGAA
ACCACCAAAGTGAACGGCAGCCTGGAAACCAAGTACAGATGGACTGAGTATGGGCTGACGTTTACAGAGAAGTGG
AACACATGCAACACCCTGGGCACTGAGATCACTGTGGAAGACCAGCTTGCTCGTGGACTGAAGCTCACCTTTGAT
TCGTCATTCTCGCCGAACACTGGGAAAAAAAATGCTAAAATCAAGACAGGGTACAAGAGGGAGCACATCAACCTC
GGGGCTGACGTGGACTTTGACATCGCTGGGCCCTCGATCCGGGGCGCTCTGGTGCTTGGCTATGAGGGTTGGCTG
GCTGGCTACCAGATGAATTTTGAGACCTCGAAGTCCCGAGTGACCCAGAGCAACTTCGCAGTTGGCTATAAGACG
GATGAATTCCAGCTTCATACTAATGTGAATGACGGGACAGAGTTTGGTGGCTCCATTTACCAGAAGGTGAACAAG
AAGTTGGAGACTGCTGTCAATCTCGCCTGGACGGCAGGATGCAGTAACACTCGCTTCGGAATAGCAGCCAAGTAT
CAGGTGGATCCTGATGCCGCCTTTTCGGCCAAAGTGAACAACTCTAGCCTGATTGGCTTAGGGTACACTCAGACC
CTAAAACCAGGTATCAAACTGACGTTGTCAGCCCTGCTCGATGGCAAGAACGTCAATGCGGGTGGCCACAAGCTT
GGCCTAGGACTGGAATTTCAAGCATAA

amino acid sequence:

MAVPPTYADLGKSARDVFTKGYGFGLIKLDLKTKSENGLEFTSSGSANTETTKVNGS
LETKYRWTEYGLTFTEKWNTCNTLGTEITVEDQLARGLKLTFDSSFSPNTGKKNAKI
KTGYKREHINLGADVDFDIAGPSIRGALVLGYEGWLAGYQMNFETSKSRVTQSNFAV
GYKTDEFQLHTNVNDGTEFGGSIYQKVNKKLETAVNLAWTAGCSNTRFGIAAKYQV
DPDAAFSAKVNNSSLIGLGYTQTLKPGIKLTLSALLDGKNVNAGGHKLGLGLEFQA.

mVDAC1-E88C -K119C-C127A -C232A

nucleotide sequence

ATGGCCGTGCCTCCCACATACGCCGATCTTGGCAAGTCCGCCAGGGATGTCTTCACCAAGGGCTACGGCTTTGGC
TTAATAAAACTTGATTTGAAAACGAAGTCAGAGAATGGATTGGAATTTACCAGCTCAGGCTCTGCCAACACGGAA
ACCACCAAAGTGAACGGCAGCCTGGAAACCAAGTACAGATGGACTGAGTATGGGCTGACGTTTACAGAGAAGTGG
AACACAGACAACACCCTGGGCACTGAGATCACTGTGTGTGACCAGCTTGCTCGTGGACTGAAGCTCACCTTTGAT
TCGTCATTCTCGCCGAACACTGGGAAAAAAAAATGCTAAAATCAAGACAGGGTACTGCAGGGAGCACATCAACCTC
GGCGCCGACGTGGACTTTGACATCGCTGGGCCCTCGATCCGGGGCGCTCTGGTGCTTGGCTATGAGGGTTGGCTG
GCTGGCTACCAGATGAATTTTGAGACCTCGAAGTCCCGAGTGACCCAGAGCAACTTCGCAGTTGGCTATAAGACG
GATGAATTCCAGCTTCATACTAATGTGAATGACGGGACAGAGTTTGGTGGCTCCATTTACCAGAAGGTGAACAAG
AAGTTGGAGACTGCTGTCAATCTCGCCTGGACTGCAGGAAACAGTAACACTCGCTTCGGAATAGCAGCCAAGTAT
CAGGTGGATCCTGATGCCGCCTTTTCGGCCAAAGTGAACAACTCTAGCCTGATTGGCTTAGGGTACACTCAGACC
CTAAAACCAGGTATCAAACTGACGTTGTCAGCCCTGCTCGATGGCAAGAACGTCAATGCGGGTGGCCACAAGCTT
GGCCTAGGACTGGAATTTCAAGCATAA

amino acid sequence:

MAVPPTYADLGKSARDVFTKGYGFGLIKLDLKTKSENGLEFTSSGSANTETTKVNGS
LETKYRWTEYGLTFTEKWNTDNTLGTEITVCDQLARGLKLTFDSSFSPNTGKKNAKI
KTGYCREHINLGADVDFDIAGPSIRGALVLGYEGWLAGYQMNFETSKSRVTQSNFAV
GYKTDEFQLHTNVNDGTEFGGSIYQKVNKKLETAVNLAWTAGNSNTRFGIAAKYQV
DPDAAFSAKVNNSSLIGLGYTQTLKPGIKLTLSALLDGKNVNAGGHKLGLGLEFQA.

mVDAC1 -C127A-A134C -C232A–D264C

nucleotide sequence

ATGGCCGTGCCTCCCACATACGCCGATCTTGGCAAGTCCGCCAGGGATGTCTTCACCAAGGGCTACGGCTTTGGC
TTAATAAAACTTGATTTGAAAACGAAGTCAGAGAATGGATTGGAATTTACCAGCTCAGGCTCTGCCAACACGGAA
ACCACCAAAGTGAACGGCAGCCTGGAAACCAAGTACAGATGGACTGAGTATGGGCTGACGTTTACAGAGAAGTGG
AACACAGACAACACCCTGGGCACTGAGATCACTGTGGAAGACCAGCTTGCTCGTGGACTGAAGCTCACCTTTGAT
TCGTCATTCTCGCCGAACACTGGGAAAAAAAAATGCTAAAATCAAGACAGGGTACAAGAGGGAGCACATCAACCTC
GGGGCTGACGTGGACTTTGACATCTGTGGGCCCTCGATCCGCGGCGCTCTGGTGCTTGGCTATGAGGGTTGGCTG
GCTGGCTACCAGATGAATTTTGAGACCTCGAAGTCCCGAGTGACCCAGAGCAACTTCGCAGTTGGCTATAAGACG
GATGAATTCCAGCTTCATACTAATGTGAATGACGGGACAGAGTTTGGTGGCTCCATTTACCAGAAGGTGAACAAG
AAGTTGGAGACTGCTGTCAATCTCGCCTGGACTGCAGGAAACAGTAACACTCGCTTCGGAATAGCAGCCAAGTAT
CAGGTGGATCCTGATGCCGCCTTTTCGGCCAAAGTGAACAACTCTAGCCTGATTGGCTTAGGGTACACTCAGACC
CTAAAACCAGGTATCAAACTGACGTTGTCAGCCCTGCTCTGTGGCAAGAACGTCAACGCGGGTGGCCACAAGCTT
GGCCTAGGACTGGAATTTCAAGCATAA

amino acid sequence:

MAVPPTYADLGKSARDVFTKGYGFGLIKLDLKTKSENGLEFTSSGSANTETTKVNGS
LETKYRWTEYGLTFTEKWNTDNTLGTEITVEDQLARGLKLTFDSSFSPNTGKKNAKI
KTGYKREHINLGADVDFDICGPSIRGALVLGYEGWLAGYQMNFETSKSRVTQSNFAV
GYKTDEFQLHTNVNDGTEFGGSIYQKVNKKLETAVNLAWTAGNSNTRFGIAAKYQV
DPDAAFSAKVNNSSLIGLGYTQTLKPGIKLTLSALLCGKNVNAGGHKLGLGLEFQA.

Enhanced minimal porin (EMP)

nucleotide sequence

ATGGAAGAACGCAATGATTGGCACTTTAACATTGGCGCCATGTATGAAATTGATAATGGTGTTGCAGAACCGAGC
GTGTATTTTAACGCAGCAAATGGTCCGTGGCGTATTGCGCTAGCCTATTATCAAGAAGGTAATTTTGATCGTCCG
GAACTGGAAGTGCATTATCAGTTCCTCGAGAATGATGATTTTAGCTTTGGCCTGACAGGCGGTTTTCGTAATTAT
GGTAATACACAGCGCTGGAAAATTGCACCGGATTGGGATGTTAAACTGACCGATGATCTGCGTTTTAATGGTTGG
TTATCGATGTACAAATTTGCCGGTGATACCCGTGTTGAAACCGAAACCGGTCTGCAGTATACCTTTAATGAAACC
GTTGCACTGCGCGTGAACTATTATCTGGAACGTGGTGGTGAATTTAGCACCCAAGAAATTCGTGCATATCTGCCG
CTGACCCTGGGTAACCACAGCGTGACCCCGTATACCCGTATTGGTCTTGATCAGGCAGGCCATGATTTTAATCGT
GTTGGTCTGTTTTATGGCTACGATTTTCAGAATGGTCTGTCCGTCTCGCTGGAATACGCGTTTGAATGGAATGAT
AGCGATAAATTCCATTATGCAGGTGTGGGTGTGAACTATAGCTTTCATCATCATCACCATCATTAA

amino acid sequence:

MEERNDWHFNIGAMYEIDNGVAEPSVYFNAANGPWRIALAYYQEGNFDRPELEVHY
QFLENDDFSFGLTGGFRNYGNTQRWKIAPDWDVKLTDDLRFNGWLSMYKFAGDTR
VETETGLQYTFNETVALRVNYYLERGGEFSTQEIRAYLPLTLGNHSVTPYTRIGLDQA
GHDFNRVGLFYGYDFQNGLSVSLEYAFEWNDSDKFHYAGVGVNYSFHHHHHH.

Bid

nucleotide sequence

ATGGGCAGCAGCCATCATCATCATCATCACAGCAGCGGCCTGGTGCCGCGCGGCAGCCATATGGACTCTGAGGTC
AGCAACGGTTCCGGCCTGGGGGCCAAGCACATCACAGACCTGCTGGTGTTCGGCTTTCTCCAAAGCTCTGGCTGT
ACTCGCCAAGAGCTGGAGGTGCTGGGTCGGGAACTGCCTGTGCAAGCTTACTGGGAGGCAGACCTCGAAGACGAG
CTGCAGACAGACGGCAGCCAGGCCAGCCGCTCCTTCAACCAAGGAAGAATAGAGCCAGATTCTGAAAGTCAGGAA
GAAATCATCCACAACATTGCCAGACATCTCGCCCAAATAGGCGATGAGATGGACCACAACATCCAGCCCACACTG
GTGAGACAGCTAGCCGCACAGTTCATGAATGGCAGCCTGTCGGAGGAAGACAAAAGGAACTGCCTGGCCAAAGCC
CTTGATGAGGTGAAGACAGCCTTCCCCAGAGACATGGAGAACGACAAGGCCATGCTGATAATGACAATGCTGTTG
GCCAAAAAAGTGGCCAGTCACGCACCATCTTTGCTCCGTGATGTCTTCCACACGACTGTCAACTTTATTAACCAG
AACCTATTCTCCTATGTGAGGAACTTGGTTAGAAACGAGATGGACTGA

amino acid sequence:

MGSSHHHHHHSSGLVPRGSHMDSEVSNGSGLGAKHITDLLVFGFLQSSGCTRQELEV
LGRELPVQAYWEADLEDELQTDGSQASRSFNQGRIEPDSESQEEIIHNIARHLAQIGDE
MDHNIQPTLVRQLAAQFMNGSLSEEDKRNCLAKALDEVKTAFPRDMENDKAMLIM
TMLLAKKVASHAPSLLRDVFHTTVNFINQNLFSYVRNLVRNEMD.

9.4 Calibration of the size exclusion chromatography column

Molecular weight determination by gel fi ltration is carried out by comparing an elution volume parameter, of the protein of interest, with the values obtained for several known calibration standards. The calibration of the used size exclusion chromatography columns was carried out by the GE Healthcare Calibration Kit after manufactors instructions. The result is shown in the figure below.

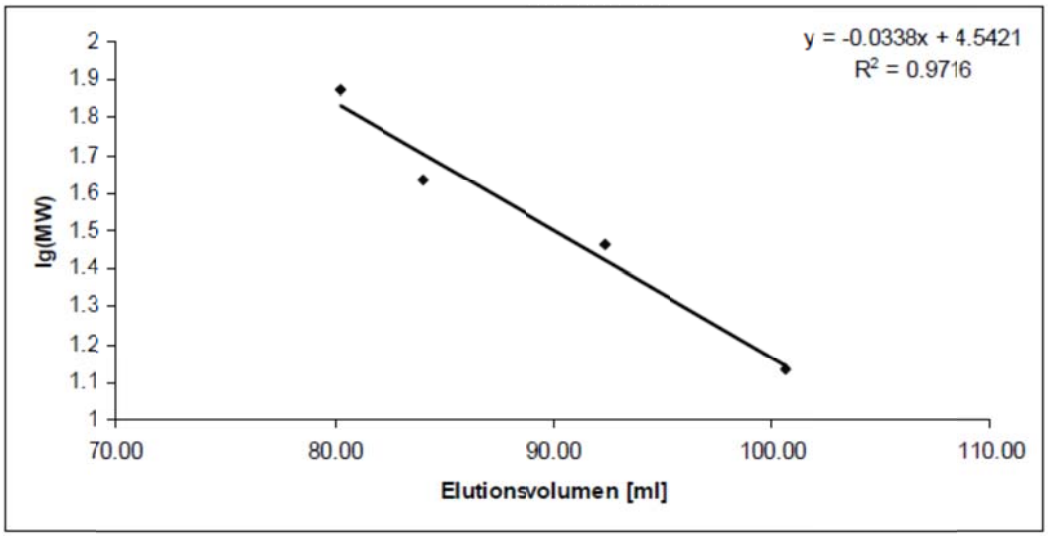

Figure: Calibration of the used Superdex 200 size-exclusion column 16/60.

9.5 SEC chromatograms of the VDAC1- and Δ11-mVDAC1-Bid/tBid complex

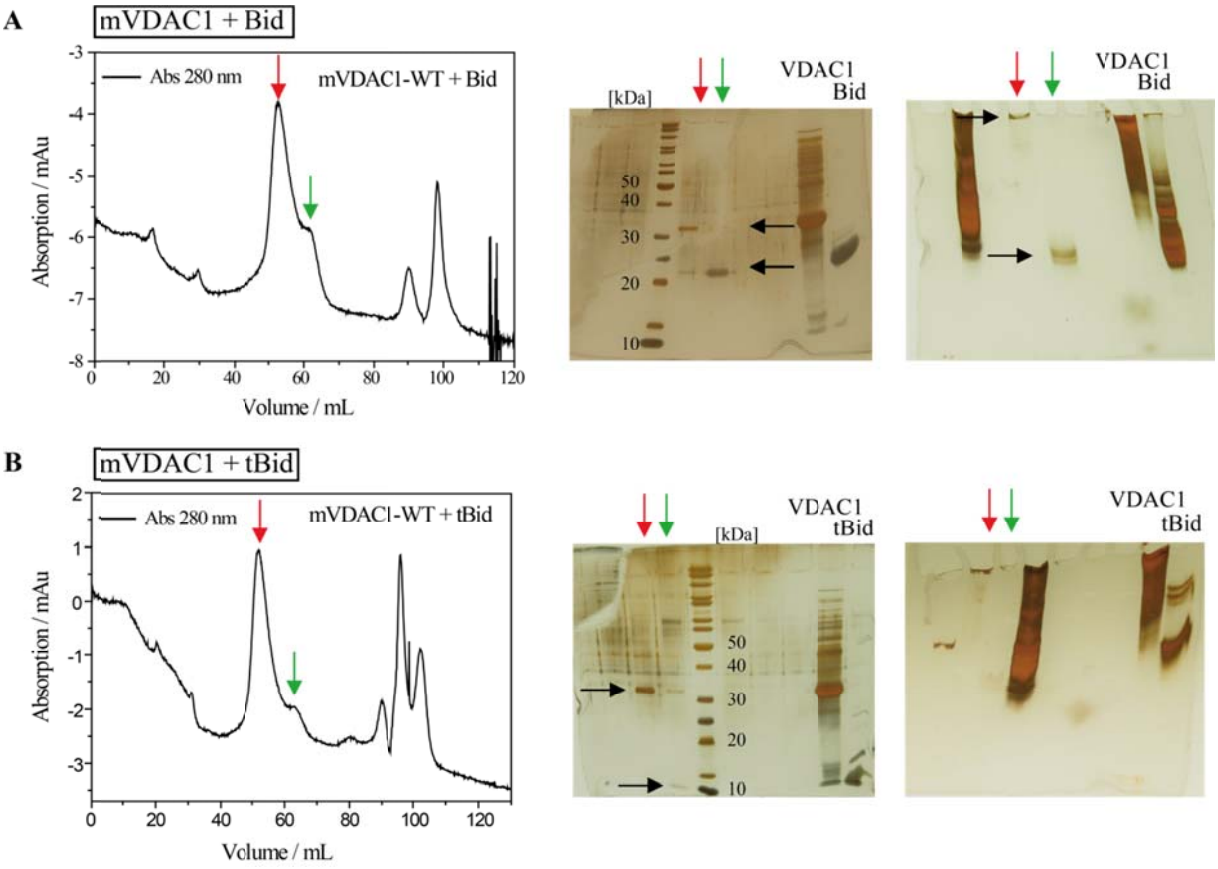

(**A**) Chromatogram and corresponding 12% silver stained SDS-PAGE (middle) and silver stained native PAGE (right) analysis of VDAC1 and Bid complex, red and green arrow indicates the fractions, black arrows marks the position of VDAC1 or Bid in the PAGE, (**B**) Chromatogram and corresponding 12% silver stained SDS-PAGE (middle) and silver stained native PAGE (right**)** analysis of VDAC1 and tBid complex, red and green arrow indicates the fractions, black arrows marks the position of VDAC1 or tBid in the PAGE,

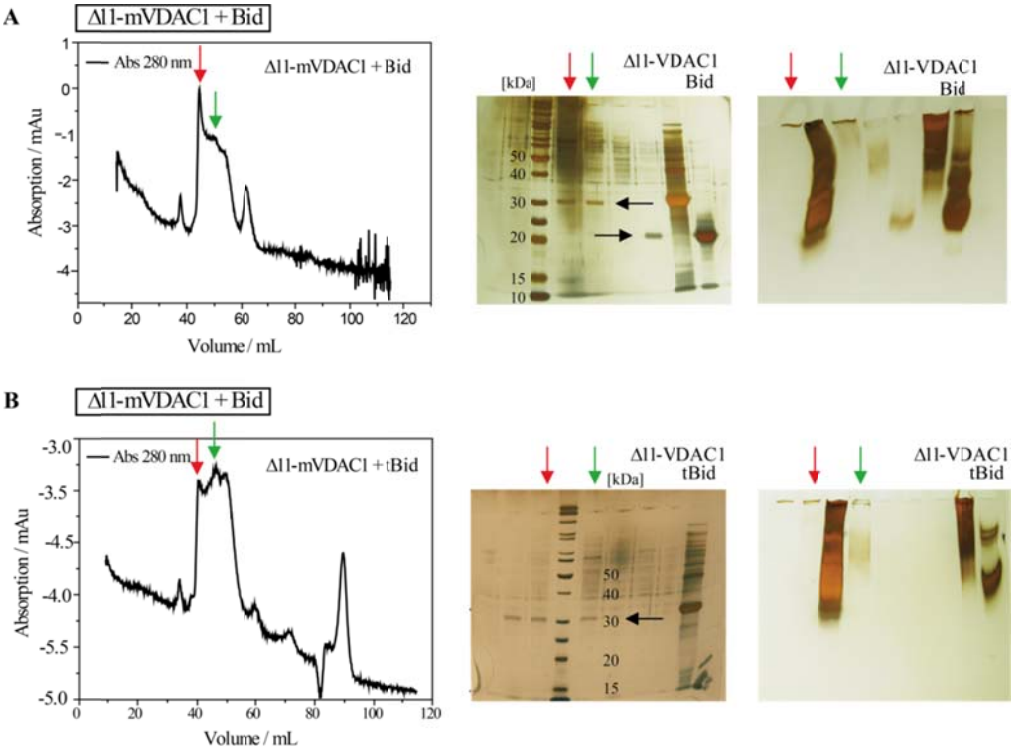

(**A**) Chromatogram and corresponding 12% silver stained SDS-PAGE (middle) and silver stained native PAGE (right) analysis of Δ11-VDAC1 and Bid complex, red and green arrow indicates the Fractions, (**B**) Chromatogram and corresponding 12% silver stained SDS-PAGE (middle) and silver stained native PAGE (right) analysis of Δ11-VDAC1 and tBid complex, red and green arrow indicates the Fractions,

9.6 Crystallisation conditions of the VDAC1 fine screening

Table S1: Fine screening of VDAC-variants

	1	2	3	4	5	6	7	8	9	10	11	12
A	HEPES 0.1 Na3Citr 0.2 Prop.10 %	HEPES 0.1 Na3Citr 0.1 Prop.10 %	HEPES 0.1 Na3Citr 0.1 Prop.15 %	HEPES 0.1 Na3Citr 0.1 Prop.20 %	HEPES 0.1 MgCl 0.2 EtOH 10 %	HEPES 0.1 Na3Cit 0.1 EtOH 10 %	HEPES 0.1 Na3Cit 0.1 EtOH 10 %	NaSCN 0.2 PEG 3350 20%	HEPES 0.1 Na3Citr 0.1 Prop.10 % PEG 3350 20%	HEPES 0.1 Na3Citr 0.1 Prop.15 % PEG 3350 20%	HEPES 0.1 MgCl 0.1 EtOH 10 % PEG 3350 20%	HEPES 0.1 Na3Cit 0.1 EtOH 10 % PEG 3350 20%
B	HEPES 0.1 Na3Citr 0.2 Prop.12 %	HEPES 0.1 Na3Cit 0.15 Prop.10 %	HEPES 0.1 Na3Citr 0.1 Prop.15 %	HEPES 0.1 Na3Cit 0.15 Prop.20 %	HEPES 0.1 MgCl 0.2 EtOH 12 %	HEPES 0.1 MgCl 0.15 EtOH 10 %	HEPES 0.1 Na3Cit 0.15 EtOH 10 %	NaSCN 0.1 PEG 3350 20%	HEPES 0.1 Na3Cit 0.15 Prop.10 % PEG 3350 20%	HEPES 0.1 Na3Cit 0.15 Prop.15 % PEG 3350 20%	HEPES 0.1 MgCl 0.15 EtOH 10 % PEG 3350 20%	HEPES 0.1 Na3Cit 0.15 EtOH 10 % PEG 3350 20%
C	HEPES 0.1 Na3Citr 0.2 Prop.14 %	HEPES 0.1 Na3Cit 0.25 Prop.10 %	HEPES 0.1 Na3Cit 0.25 Prop.15 %	HEPES 0.1 Na3Cit 0.25 Prop.20 %	HEPES 0.1 MgCl 0.2 EtOH 14 %	HEPES 0.1 MgCl 0.25 EtOH 10 %	HEPES 0.1 Na3Cit 0.25 EtOH 10 %	NaSCN 0.2 PEG 3350 10%	HEPES 0.1 Na3Cit 0.25 Prop.10 % PEG 3350 20%	HEPES 0.1 Na3Cit 0.25 Prop.15 % PEG 3350 20%	HEPES 0.1 MgCl 0.25 EtOH 10 % PEG 3350 20%	HEPES 0.1 Na3Cit 0.25 EtOH 10 % PEG 3350 20%
D	HEPES 0.1 Na3Citr 0.2 Prop.16%	HEPES 0.1 MgCl 0.1 Prop.10 %	HEPES 0.1 MgCl 0.1 Prop.15 %	HEPES 0.1 MgCl 0.1 Prop.20 %	HEPES 0.1 MgCl 0.2 EtOH 16 %	HEPES 0.1 MgCl 0.1 EtOH 15 %	HEPES 0.1 Na3Cit 0.1 EtOH 15 %	NaSCN 0.2 PEG 3350 15%	HEPES 0.1 MgCl 0.1 Prop.10 % PEG 3350 20%	HEPES 0.1 MgCl 0.1 Prop.15 % PEG 3350 20%	HEPES 0.1 MgCl 0.1 EtOH 15 % PEG 3350 20%	HEPES 0.1 Na3Cit 0.1 EtOH 15 % PEG 3350 20%
E	HEPES 0.1 Na3Citr 0.2 Prop.18 %	HEPES 0.1 MgCl 0.15 Prop.10 %	HEPES 0.1 MgCl 0.15 Prop.15 %	HEPES 0.1 MgCl 0.15 Prop.20 %	HEPES 0.1 MgCl 0.2 EtOH 18 %	HEPES 0.1 MgCl 0.15 EtOH 15 %	HEPES 0.1 Na3Cit 0.15 EtOH 15 %	NaSCN 0.2 PEG 3350 25%	HEPES 0.1 MgCl 0.15 Prop.10 % PEG 3350 20%	HEPES 0.1 MgCl 0.15 Prop.15 % PEG 3350 20%	HEPES 0.1 MgCl 0.15 EtOH 15 % PEG 3350 20%	HEPES 0.1 Na3Cit 0.15 EtOH 15 % PEG 3350 20%
F	HEPES 0.1 Na3Citr 0.2 Prop.20%	HEPES 0.1 MgCl 0.25 Prop.10 %	HEPES 0.1 MgCl 0.25 Prop.15 %	HEPES 0.1 MgCl 0.25 Prop.20 %	HEPES 0.1 MgCl 0.2 EtOH 20 %	HEPES 0.1 MgCl 0.25 EtOH 15 %	HEPES 0.1 Na3Cit 0.25 EtOH 15 %	NaSCN 0.1 PEG 3350 15%	HEPES 0.1 MgCl 0.25 Prop.10 % PEG 3350 20%	HEPES 0.1 MgCl 0.25 Prop.15 % PEG 3350 20%	HEPES 0.1 MgCl 0.25 EtOH 15 % PEG 3350 20%	HEPES 0.1 Na3Cit 0.25 EtOH 15 % PEG 3350 20%
G	HEPES 0.1 Na3Citr 0.2 Prop.22 %	Tris pH 8.5 0.1M 15% MDP	Tris pH 7.5 0.1M Prop 15% NaCl 0.3	Tris pH 7.5 0.1M MDP 18% PEG 3.350 10%	HEPES 0.1 MgCl 0.2 EtOH 22 %	HEPES 0.1 MgCl 0.15 EtOH 20%	HEPES 0.1 Na3Cit 0.15 EtOH 20%	NaSCN 0.1 PEG 3350 10%	Tris pH 8.5 0.1M 15% MDP PEG 3350 20%	Tris pH 7.5 0.1M Prop 15% NaCl 0.3 PEG 3350 20%	HEPES 0.1 MgCl 0.15 EtOH 20% PEG 3350 20%	HEPES 0.1 Na3Cit 0.15 EtOH 20% PEG 3350 20%
H	HEPES 0.1 Na3Citr 0.2 Prop.24 %	Tris pH 8.0 0.1M 15% MDP	Tris pH 7.0 0.1M Prop 15% NaCl 0.3	Tris pH 7.0 0.1M MDP 18% PEG 3.350 10%	HEPES 0.1 MgCl 0.2 EtOH 24 %	HEPES 0.1 MgCl 0.25 EtOH 20%	HEPES 0.1 Na3Cit 0.25 EtOH 20%	NaSCN 0.1 PEG 3350 25%	Tris pH 8.0 0.1M 15% MDP PEG 3350 20%	Tris pH 7.0 0.1M Prop 15% NaCl 0.3 PEG 3350 20%	HEPES 0.1 MgCl 0.25 EtOH 20% PEG 3350 20%	HEPES 0.1 Na3Cit 0.25 EtOH 20% PEG 3350 20%

9.7 EMP design

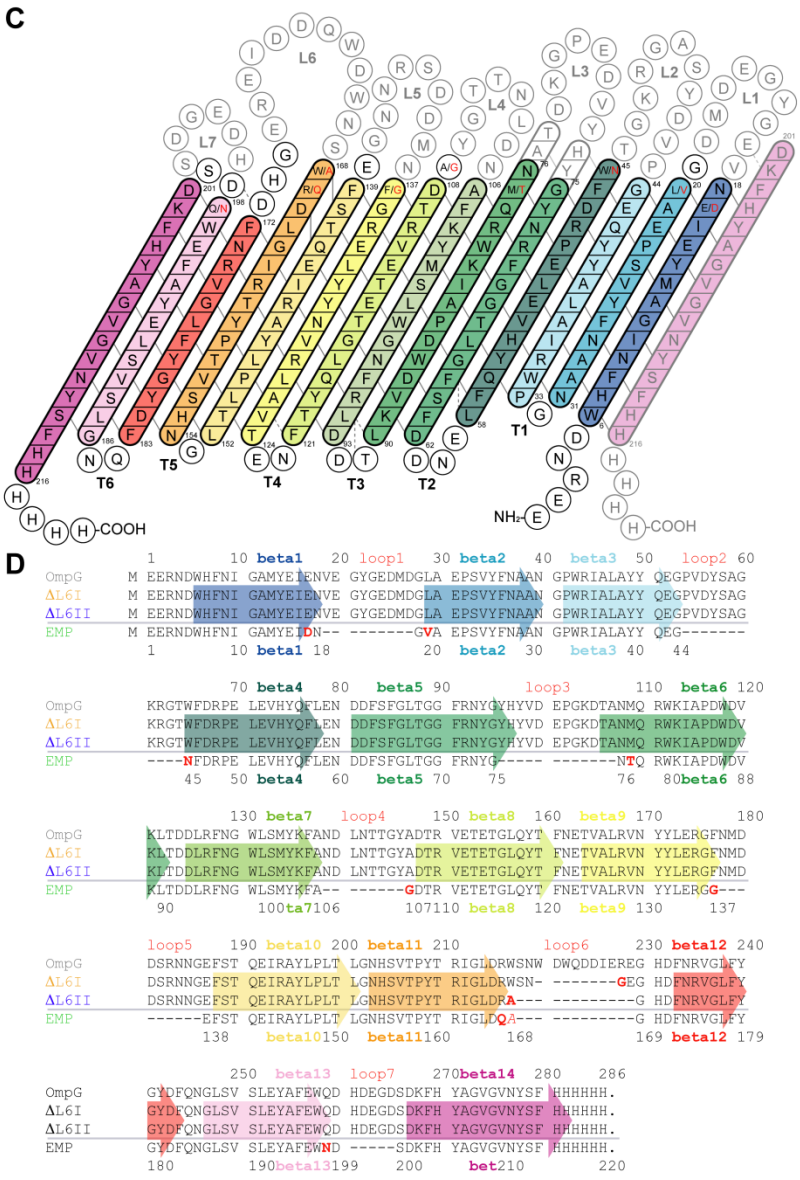

(**C**) The topology of OmpG (opaque) with rainbow coloured transmembrane β-strands. Strand β14 is repeated on the N-terminal side reflecting the β-barrel assembly. Grey lines between strands indicate the H-bonding network; topology of EMP is in black, introduced mutations in red. (**D**) Sequence alignment of OmpG and its variants, strands coloured according to (**C**).